Università degli Studi della Basilicata

Ph.D. Program

"Chemical Sciences"

"Synthesis of Nanostructured Metal-Chitosan Hybrids by Laser Ablation in Liquid"

Scientific Disciplinary Sector
"Physical chemistry – CHIM/02"

Ph.D. Coordinator

Prof. Patrizia Falabella

Ph.D. Candidate

Michela Marsico

Tutor

Prof. Angela De Bonis

Cycle XXXVII

Contents

Glossary

Laser Ablation in Liquid (LAL): a technique that uses laser pulses to remove material from a solid target immersed in a liquid, generating nanoparticles through vaporization, condensation, and interactions with the surrounding medium.

Adsorption: a physicochemical phenomenon in which molecules or ions accumulate on the surface of a solid or liquid material without penetrating its internal structure.

Antibacterial: any substance, coating, or material capable of inhibiting bacterial growth or destroying bacteria through chemical, physical, or biological interactions.

Atomic Force Microscopy (AFM): an imaging technique that uses a nanometric probe to analyse the topography and mechanical properties of surfaces with ultra-high resolution.

Biodegradability: the ability of a material to naturally decompose into simpler compounds through the action of microorganisms or environmental chemical reactions.

Biocompatibility: the property of a material that allows it to interact with a biological environment without causing toxic, inflammatory, or immune rejection responses.

Biopolymer: a macromolecule of biological origin, derived from living organisms or natural materials, characterized by biodegradability and eco-sustainability.

Cavitation: a phenomenon where gas or vapor bubbles form and rapidly collapse in a liquid due to pressure fluctuations, generating shock waves, high temperatures, and chemical reactions.

Colloidal Suspension: a stable dispersion of fine particles or nanoparticles in a liquid medium, maintained by electrostatic or steric stabilization.

Controlled Release: a technique used in drug delivery systems to regulate the release rate of an active compound, enhancing efficacy and minimizing side effects.

Crystallinity: a measure of the degree of structural order in a solid material, influencing properties such as hardness, rigidity, mechanical strength, and thermal stability.

Degree of Deacetylation (DDA): a parameter that measures the percentage of deacetylated units in chitosan, influencing its solubility and biological properties.

Electrical Conductivity: the ability of a material to transport electric current through the movement of electrons or ions.

Electrophoretic Deposition (EPD): a technique that exploits an electric field to deposit charged particles onto a surface, forming uniform coatings with industrial and biomedical applications.

Electrostatic Interactions: forces of attraction or repulsion between charged particles, fundamental in colloidal stability and nanoparticle dispersion.

Fourier Transform Infrared Spectroscopy (FTIR): an analytical technique that measures the absorption of infrared radiation by a material, providing information about its chemical composition.

Functionalization: a chemical modification of a material's surface to impart new properties, such as hydrophobicity, biocompatibility, or the ability to bind specific biomolecules.

Hydrophobicity: the tendency of a material to repel water, often achieved through chemical treatments or specialized coatings.

Hydrophilicity: the property of a material that enhances its interaction with water, often due to the presence of polar functional groups on its surface.

Hydrogen Bonding: a weak interaction between a hydrogen atom bonded to an electronegative element (oxygen, nitrogen, or fluorine) and another molecule containing an electronegative atom.

Localized Surface Plasmon Resonance (LSPR): an optical phenomenon occurring when metallic nanoparticles interact with light, generating collective oscillations of surface electrons and modifying the material's optical properties.

Nanocomposite: a material composed of a polymeric, ceramic, or metallic matrix in which nanoparticles are dispersed to enhance mechanical, thermal, or electrical properties.

Nanoparticle: a particle ranging from 1 to 100 nanometres in size, characterized by unique physicochemical properties due to its high surface area and quantum effects.

Nanostructured Material: a material with an organized structure at the nanoscale, providing superior physical and chemical properties compared to conventional materials.

Photocatalysis: a light-activated chemical process in which a semiconductor material accelerates a reaction, commonly used for the degradation of pollutants and water purification

Plasma: the fourth state of matter, consisting of an ionized gas with free electrons and ions, exhibiting high electrical conductivity.

Scanning Electron Microscopy (SEM): an imaging technique that uses electron beams to provide high-resolution images of a material’s surface morphology.

Surface Reactivity: the ability of a material to chemically interact with other substances, often influenced by particle size and the presence of functional groups.

X-ray Diffraction (XRD): a technique used to determine the crystalline structure of materials by analyzing the diffraction pattern of X-rays.

Abstract

The growing focus on environmental sustainability, together with the need to improve technological performance in various industrial sectors, has led to an increasing interest in the development of innovative materials. In this scenario, composite materials are emerging as protagonists, thanks to their ability to combine superior properties through the synergistic interaction of different components. Among composites, biopolymers stand out as a particularly promising class, because they combine characteristics of biodegradability and biocompatibility with a reduced environmental impact compared to traditional materials. In particular, chitosan, a polysaccharide derived from chitin, is noted for its exceptional biological and chemical properties, making it an ideal candidate for applications ranging from biomedical to agri-food, environmental to industrial. At the same time, nanomaterial production techniques have been developing rapidly in recent decades, with a particular focus on sustainable and toxic-free methods. Among these techniques, laser ablation in liquid (LAL) has attracted interest as a versatile and eco-friendly approach to the synthesis of nanomaterials. The LAL allows for the control of the properties of nanoparticles produced without the use of harmful chemicals, thus minimising waste and environmental emissions.

This work aims to explore the integration of chitosan with LAL technology for the production of advanced composite materials. Moreover, the possibility to consider chitosan obtained from alternative sources such as Hermetia illucens will be explored. The main objective is twofold: on the one hand, to use the LAL to prepare nanocomposite polymer/metal materials in a one-step approach and to understand how chitosan affects the nucleation and growth processes of nanoparticles and the stability of the colloidal solutions obtained; on the other hand, to assess the effectiveness of a renewable and circular approach to new materials production.

Introduction

The following PhD thesis explores the innovative field of nanostructured composite materials, with a particular focus on the integration of metal nanoparticles into biocompatible and biodegradable materials such as chitosan, through the use of liquid laser ablation (LAL). This approach not only opens new frontiers in materials science but also underlines a strong commitment to environmental sustainability, an increasingly crucial aspect of modern scientific research. The introductory chapter sets out the research context, highlighting the growing importance of nanostructured materials in different fields, from biomedicine to industry. Provides a detailed overview of the unique properties of chitosan, a natural polymer chosen for its biocompatibility and biodegradability, In addition, the chapter discusses the role of metal nanoparticles, with particular emphasis on silver and copper nanoparticles, highlighting their applications in antimicrobial, catalytic and biomedical fields.

The next chapter provides an in-depth description of the materials used and the experimental methodologies adopted. The theory behind liquid laser ablation (LAL), the dynamics of the cavitation bubble and the temporal evolution of the ablation process are described in detail, as well as the influence of laser parameters on the production of nanoparticles. The final part of the chapter is dedicated to the description of the preparation and characterization of chitosan derived from alternative source Hermetia illucens, including a comparative evaluation between traditional marine sources and alternative sources such as Hermetia illucens, to promote greater sustainability.

In the third chapter, the effect of LAL parameters on the characteristics of metal nanoparticles and metal composites is analyzed, showing how the presence of Chitosan affects the formation, growth and stability of nanoparticles. In addition, the antibacterial properties of both copper and silver enriched composites are discussed, with a particular focus on the antimicrobial activity of chitosan-silver composites and their biocompatibility with fibroblast cell lines.

The fourth chapter explores the application of chitosan-based materials in bone implant coatings. The electrophoretic deposition (EPD) process is analysed, a technique that allows thin and uniform films to be obtained on metal surfaces, improving the biocompatibility and antibacterial properties of implants. Experiments show that chitosan coatings and silver nanoparticles are able to inhibit the growth of bacteria such as Staphylococcus aureus and Escherichia coli, without compromising the viability of human bone cells. The results indicate the potential of these materials for the construction of antibacterial and bioactive implants.

The fifth chapter is devoted to the environmental applications of the synthesised materials, in particular to the photocatalytic degradation of organic dyes present in industrial waste water. Silver-based and chitosan nanocomposites are tested as catalysts for photodegradation of methylene blue, demonstrating high pollutant abatement capabilities under UV and visible lighting. The chapter concludes with a discussion of degradation mechanisms and prospects for using these materials to purify water in film form.

In the concluding chapter, it is pointed out how the integration of sustainable technologies and biocompatible materials can lead to the development of innovative solutions for biomedical and environmental applications. The use of laser ablation in liquid for the synthesis of metal nanoparticles, combined with the use of chitosan from alternative sources, represents a significant step towards more environmentally friendly and responsible production. Future research prospects are also outlined, including possible developments in the production of multi-functional composite materials and the optimisation of their properties for specific applications. The importance of further studies to assess the long-term safety of developed materials is stressed and to explore new applications in emerging fields.

Chapter 1 Biocomposite nanostructured materials

1.1 Composite materials

Composite materials are a class of heterogeneous materials obtained by combining two or more phases with different chemical-physical properties. This synergy allows materials to be designed with superior performance compared to individual components. A composite is generally made up of a matrix, which acts as a binder, and a reinforcement, which gives strength and rigidity.[1] The matrix, typically a polymer, metal or ceramic, has the function of distributing loads and protecting reinforcement. The latter, consisting of fibres or particles, determines the mechanical properties of the composite. Composite materials are classified according to the materials that make up them.[1], [2]

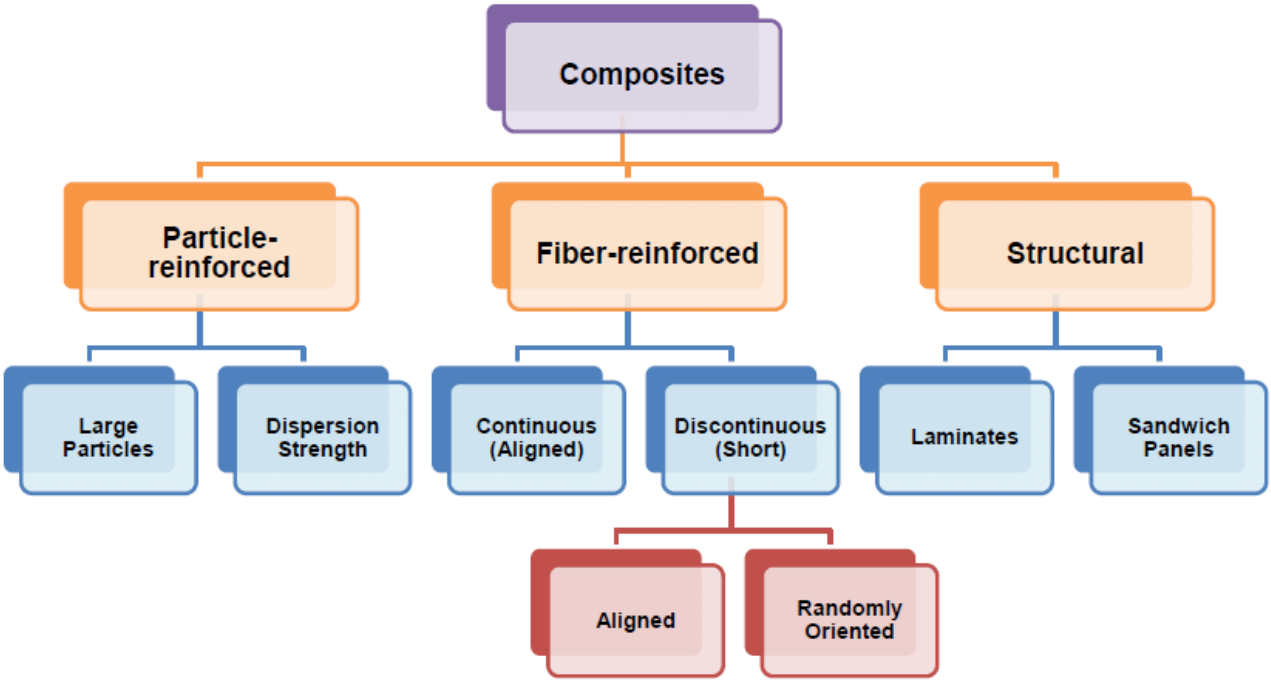

Figure 1.1 Composite materials classification.

1.1.1 Fiber-reinforced composites

Fiber-reinforced composites (FRC) are an advanced class of materials with a high strength/weight ratio and stiffness. This combination of properties is obtained by the integration of high-performance mechanical fibres (glass, carbon, aramid) into a polymer matrix (epoxy, polyester or vinyl ester). The synergy between the two phases gives FRC excellent corrosion resistance and makes them ideal for engineering applications requiring lightness and strength. The wide range of matrices and fibres available allows to customize the properties of the FRCs, adapting them to specific application needs. These features make FRCs widely used in

industries such as aerospace, automotive and construction.[3] Beyond their traditional applications, FRCs have also found significant use in biomedical engineering. For instance, carbon fiber composites have been employed in the creation of dental and orthopedic implants, where they must withstand high mechanical loads while maintaining excellent biocompatibility. [4] . One example is the so-called "green composites", derived from biodegradable plant fibres and matrices. [5], [6] The ability of these materials to mimic the mechanical properties of natural bone has made them a cornerstone in regenerative medicine. [4]

1.1.2 Particle reinforced composites

Particle reinforced composites (PRC) are a class of advanced materials obtained by combining a continuous matrix (polymer, metal or ceramic) and particles dispersed within it. This synergy allows to obtain materials with superior mechanical, thermal and electrical properties compared to the individual components.[7] The nature of the matrix and particles (size, shape, composition) significantly influences the final properties of the composite. According to the matrix, polymer matrix composites (PMC), metal matrix composites (MMC) and ceramic matrix composites (CMC) are distinguished. PMCs, for example, combine the processability of polymers with the resistance of ceramic particles, while MMCs offer a high strength/weight ratio and good thermal conductivity. The CMC, on the other hand, are used in high temperature environments due to their chemical inertia. The applications of CRPs are wide ranging, from automotive to aerospace and biomedical. [7], [8] The biomedical applications of PRCs are vast; polymer matrix composites, for example, have been explored for drug delivery systems and tissue engineering scaffolds. Their biocompatibility and tunable properties make them suitable for controlled release of therapeutic agents and for creating environments that promote tissue regeneration.[9]

1.1.3 Laminated composites

Laminated composites are a class of advanced materials characterized by a layered structure obtained by stacking and gluing together thin sheets, called sheets. The typical polymer matrix and the reinforced fibres (carbon, glass, aramid) specifically oriented inside each sheet give the laminate anisotropic mechanical properties.[10] This feature allows the material to be optimized for strength and rigidity in the desired directions. The high strength/weight ratio and versatility of laminated composites make them ideal for applications that require lightness and strength, such as in aerospace, automotive, construction and also biomedical.[11] In the biomedical field, laminated composites have been used to create custom-made orthopedic implants and prostheses. The ability to tailor the mechanical properties of these materials to

match those of the surrounding bone tissue has improved the long-term performance and patient outcomes of these implants.[12]

1.1.4 Nanocomposite

Nanocomposites are an advanced class of composite materials in which at least one of the reinforcement phases has nanometric dimensions, typically between 1 and 100 nanometres. As with other composites, they are made of a matrix, different according to the characteristics of the desired application: polymer matrices are the most common in nanocomposites and include thermoplastic polymers such as polypropylene (PP) and polyethylene (PE), and thermosetting materials such as epoxy resins and polyester.[13] Metal matrices are used in nanocomposites for applications requiring high thermal conductivity and mechanical strength; finally ceramic matrices are used to improve wear resistance, the hardness and thermal stability of nanocomposites. The nanoparticles integrated in the material, which are very small in size, differ in species and characteristic, ranging from carbon in the form of graphene, known for its excellent electrical, thermal and mechanical properties, to carbon nanotubes with extraordinary mechanical strength and electrical conductivity, leading to the use of clay nanoparticles, of metals or metal oxides.[13], [14] Nanocomposites have many properties, including mechanical properties such as mechanical strength, hardness and wear resistance compared to traditional composites, due to the high specific surface area and strong interaction between nanoparticles and matrix; thermal properties, with greater thermal stability and consequently lower susceptibility to thermal deformation; electrical properties, the inclusion of carbon nanotubes or graphene can significantly improve the electrical conductivity of polymers, making nanocomposites useful in electronic and electromagnetic shielding applications; optical properties and ultimately antibacterial properties, particularly nanocomposites composed of nanoparticles of metal oxides such as titanium dioxide or silver; show antibacterial properties.[13]

In addition to the automotive and aerospace fields already mentioned, nanocomposites are used in electronics, advanced electronic devices such as printed circuits, flexible displays and electromagnetic shielding materials.

Particular interest has been aroused in the field of life sciences and biomedicine, where these materials are emerging as materials of choice for a wide range of applications. This is due to their unique properties in which for example there are biocompatibility, antimicrobial activity or anti-cancer activity. Biocompatibility of composite materials is essential to ensure safe interaction with biological tissues without causing adverse reactions. For example, chitin-based composites, widely studied for their integration with living tissues, have been used in

applications such as scaffold for bone and tissue regeneration, as well as advanced wound dressings.[5], [6] The ability of these materials to promote cell growth, minimizing the risk of inflammation or rejection, makes them particularly suitable for biomedical applications. [4] Biodegradability is a further key advantage, particularly relevant in applications where the material needs to gradually dissolve in the body after it has performed its function. Materials such as polyhydroxybutyrate (PHB) or natural polymer composites have been widely used in regenerative surgery, as they avoid secondary removal and reduce environmental impact.[4], [6] These materials are also made from renewable resources, which contributes to greater sustainability.[5] Some nanocomposite materials, especially those combined with metal nanoparticles, show significant antimicrobial properties. For example, chitin combined with silver nanoparticles has demonstrated effective antibacterial activity against pathogens, making these composites ideal for use in medical devices such as catheters or surgical implant coatings. [5], [6] In addition, it has been seen that the inclusion of zinc oxide nanoparticles has expanded the possibilities for use in clinical environments, providing safe and protective coatings against infection. [5] The anti-cancer properties of some nanocomposites represent an emerging area of research. The combination of biocompatible materials with therapeutic agents or specific nanoparticles allows the development of intelligent systems for the release of anti-cancer drugs. For example, graphene oxide composites or other nanostructured have been used to transport and release chemotherapy drugs directly into cancer cells, maximising their effectiveness and reducing systemic side effects.[4], [6] Another application of great interest is the use as biosensors. These devices exploit the sensitivity of materials to chemical, biological or physical stimuli to detect specific biomarkers or molecules of interest. Conductive polymer composites, such as polyaniline combined with carbon nanotubes, have demonstrated high sensitivity in the detection of glucose, DNA and proteins. This makes them particularly useful for real-time monitoring of clinical conditions such as diabetes or neurodegenerative diseases.[4], [5]

Finally, the food industry and more specifically food packaging uses nanocomposites in packaging to extend the shelf life of foods and improve product protection. [15]

To conclude, the composite materials, due to their characteristic properties are fundamental in high-tech sectors such as aerospace, automotive, biomedical and renewable energy, where they offer superior performance compared to traditional materials. The ability to design materials with specific properties makes them ideal for advanced applications requiring light weight, corrosion resistance, and high durability.

1.2 Composite biopolymers

Composite biopolymers are a subgroup of composite materials, consisting of a natural polymer matrix reinforced with other materials, often in the form of fibres or nanoparticles. These materials combine the favourable properties of biopolymers, such as biodegradability and sustainability, with the improved characteristics of reinforcement, such as mechanical strength and thermal stability. [16], [17] As with other composite materials, they are made of a matrix, in this case exclusively polymeric, which differs by origin, or be of natural origin such as polysaccharides (cellulose, starch, chitin, chitosan), proteins (Gelatin, soy, collagen, silk fibrin) or polymers derived from micro-organisms (Poly-hydroxyalkanoates (PHA), poly-hydroxybutyrate (PHB)) or be of synthetic origin such as polymers of modified natural origin (Polylactic acid (PLA), polyglycolic acid (PGA), poly(caprolactone) (PCL)) or polymers derived from renewable sources (biodegradable polyurethanes, aliphatic polyesters). Reinforcing materials may include natural fibres (e.g. flax fibre, hemp), nanoparticles (e.g. modified clays, cellulose nanocrystals, metals or metal oxides) and also biodegradable synthetic materials.[16], [18]

Composite biopolymers have a range of properties improved over pure polymers, including improved mechanical property, the inclusion of reinforcements significantly improves the mechanical strength of biopolymers, due to the stress transfer facilitated by nanofillers interacting with the polymer matrix; the presence of reinforcements can also improve the thermal stability of biopolymers, making them suitable for use in high temperature environments. Finally, they maintain the biodegradability typical of the polymer matrix they are made despite the addition of reinforcing materials that usually do not have this property, which makes them environmentally sustainable materials.[17], [18]

Composite biopolymers are produced using a variety of techniques, the choice of the appropriate one depends on the polymer and the reinforcing material used. The main techniques include in situ polymerization, fusion intercalation and solution intercalation. In situ polymerization, a technique that allows an effective dispersion of the nanofiller in the polymer monomer used. The polymerization reaction is facilitated by the incorporation of a thermal or photo-catalytic initiator or catalyst, which allows for even distribution of the nanofiller in the matrix. However, this technique has some limitations, such as the difficulty of curing between layers.[19] The fusion intercalation, dispersion takes place directly in the molten state of the thermoplastic polymer through conventional techniques such as injection moulding and extrusion. This technique does not require the use of solvents and allows to obtain a good dispersion of the nanofiller in the polymeric matrix, finally the intercalation in solution, which

involves the use of a solvent in which both the polymer and the nanofiller are dissolved. Once the dispersion is obtained, the solvent is removed, leaving a well dispersed nanocomposite in the polymer matrix. This technique is particularly useful for polymers which cannot be processed in the molten state. [19]

1.2.1 Applications Composite biopolymers

Applications of biopolymers cover a wide range of sectors, from the food industry to biomedicine, agriculture, automotive, aerospace and construction.

Biopolymers have many applications in the food industry, especially as biodegradable packaging materials. For example, starch is widely studied for its low cost, availability and renewability, and is used in food packaging applications. However, to improve mechanical strength and thermal stability, starch is often combined with nanofillers, creating suitable materials for edible packaging that offer high strength and improved barrier properties.[16], [17]

In the biomedical field, biopolymers are used to develop bio-compatible and biodegradable materials for a variety of applications. Chitosan and alginate are two prominent examples. Chitosan, derived from the deacetylation of chitin, is known for its biocompatibility and antibacterial activity, and is used in biosensors, supercapacitors, hydrogels and controlled release of drugs. [17] Alginate, a natural polysaccharide with good fibre-forming properties, is used in pharmaceuticals, tissue manufacturing and biomedical applications due to its unique gelling properties. [17], [19]

Biopolymers such as poly(ε-caprolactone) (PCL) are also used in agriculture, due to their biodegradability and ease of processing. PCL, when combined with nanofillers, can be used to create materials used in agricultural and biomedical applications. [19]

In the automotive industry, biopolymers are increasingly used to reduce environmental impact. Automotive components must be made of 95% recyclable materials, with 85% of these being mechanically recycled and reused. For example, blends of recycled PLA and virgin PLA with chain extenders are used for 3D printing and injection moulding, showing good flow properties and ease of processing. [17]

Biopolymers are also used in the aerospace industry to develop self-healing materials that can replace carbon-based composites. These self-healing materials can repair structural damage, defects or cracks, showing exceptional physical, mechanical, thermal and rheological properties. [17]

In conclusion, biopolymers can be used in the construction industry to create self-healing materials that improve durability and reduce maintenance. These materials can repair damage such as cracks and structural defects on their own, extending the useful life of structures. [17]

These examples demonstrate the versatility of biopolymers and their potential in various industrial sectors, promoting sustainability and technological innovation.

1.3 Chitosan

Chitosan, the main derivative of chitin, belongs to the family of polysaccharides, specifically is a copolymer formed by alternating units of N-acetylglucosamine and N-glucosamine linked by β-(1-4) binding along the polymer chain. Chitin is mainly found in the exoskeletons of marine animals such as crabs and shrimps, insect exoskeletons, and fungi. Chitosan is produced by the deacetylation process: the process involves the almost total removal of acetyl groups by using a strong concentrated base, usually NaOH; the most significant challenge is to obtain the highest percentage of deacetylation possible without going against side effects such as depolymerization or formation of reactive species. In contrast to chitin, the partial deacetylation of chitosan allows it to dissolve in slightly acidic solutions, making this biopolymer of interest for many applications. Today's uses range from the adsorption of heavy metals or organic dyes in wastewater to the use as contact lens materials for its film forming and optical transparency properties. [20], [21]

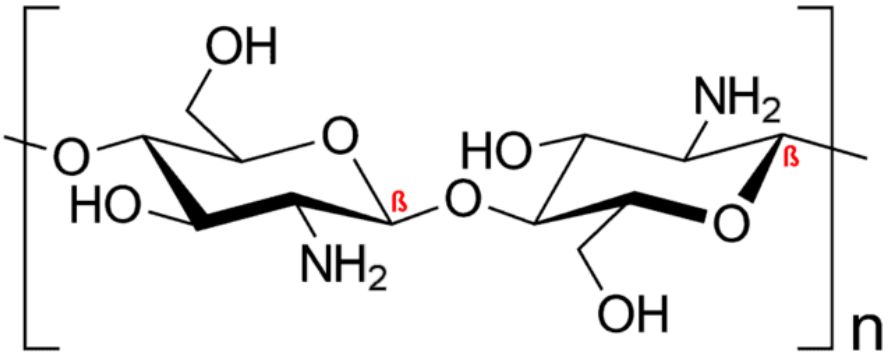

Figure 1.2 Chitosan unit molecular structure.

1.3.1 Physico-chemical properties

The main parameters that affect the properties of chitosan are the deacetylation degree and molecular weight. The deacetylation degree (DDA) determines not only physical chemical

properties but also biological ones such as biodegradability and biocompatibility. DDA can be defined as:

$$\mathrm{DDA} = \frac{n(\mathrm{GlcN})}{n(\mathrm{GlcN}) + n(\mathrm{GlcNAc})} \times 100\%$$

Where n(GlcN) is the average of the N-glucosamine units and n(GlcNAc) is the average of the N-acetylglucosamine units. DDA strongly influences biological properties, many studies have shown that a high degree of deacetylation allows a better interaction between positively charged amine and negatively charged cell membrane surface, promoting attachment and proliferation.[21], [22]

Chitosan has a rather complex and fascinating solubility behaviour. Its ability to dissolve in a solvent depends on a set of interrelated factors which influence the structure and interactions of the polymer in solution. Among the factors influencing solubility, the degree of deacetylation plays a fundamental role; the greater the amount of acetyl groups removed from the molecule, the greater the tendency of chitosan to form strong intra- and intermolecular hydrogen bonds. Not only the degree of deacetylation but also the distribution of the acetyl groups along the chain of chitosan has an impact on its solubility; an uneven distribution of acetyl groups can affect the shape of the molecule and its ability to interact with solvent molecules. Another crucial factor is the pH of the solution, chitosan is a weak base and consequently its solubility increases in acidic environments. Under these conditions, the amino groups of chitosan are protonated, acquiring a positive charge that makes them more water-like and less likely to form hydrogen bonds with each other. In contrast, in basic environments, chitosan tends to precipitate. The ionic strength of the solution also affects the solubility of chitosan, the addition of salts can screen the positive charges of protonated amino groups, reducing electrostatic repulsions and promoting aggregate formation. Finally, temperature can influence solubility; an increase in temperature tends to favour solubility, since it provides energy to the molecules, facilitating the break-up of hydrogen bonds and increasing the mobility of polymer chains. [23], [24]

The viscosity of chitosan is closely related to the molecular conformation of the polymer in solution, and significantly influences its rheological characteristics and, consequently, the behaviour in the processing processes and polymeric matrices. [25] This can be influenced by numerous factors, first of all the degree of deacetylation (DD): a high DD promotes the formation of intermolecular hydrogen bonds, increasing the viscosity of solutions. [25] Another very important factor is the molecular weight, this is directly proportional to the viscosity,

longer molecules and therefore heavier, form larger three-dimensional lattices in solution, which greatly increases their viscosity.[26] The pH of the solution also influences its viscosity, in fact in an acid environment the protonated polymer chains, acquiring a positive charge and increasing the electrostatic repulsions, which tend to expand the molecules and increase the viscosity, on the contrary, under basic conditions, viscosity decreases due to shielding of positive charges. [26] Another factor that can influence the viscosity of chitosan is temperature, the viscosity decreases with increasing temperature, according to Arrhenius's law. Finally, increasing concentration of chitosan solutions strongly influences viscosity, due to increased interactions among polymer chains. [25]

Chitosan has interesting optical properties, this is due to the presence of amino and acetylamine groups, which give the polymer a weak absorption in the ultraviolet and visible region of the electromagnetic spectrum, making it transparent in this wavelength range. This feature is particularly useful for applications where transparency is critical, such as in optical sensors. [27] In addition to absorption, chitosan can also exhibit fluorescence properties, although to a lesser extent than other fluorophores, this fluorescence is due to the presence of chromophore groups within its molecular structure.[28] The intensity and position of fluorescent emission peaks can be modulated by varying the pH of the environment or introducing chemical changes in the polymer. The pH of the medium plays a crucial role in the optical properties of chitosan, at acid pH, the amino groups of chitosan are protonated, modifying the interaction of the polymer with other molecules and with light, influencing both light absorption and emission.[29] The optical properties of chitosan can be further modulated through interaction with other molecules. For example, the formation of complexes with metal ions can induce significant variations in the absorption and emission spectrum. Similarly, the addition of dyes or nanoparticles can give chitosan new optical properties such as photoluminescence or colour changes in response to external stimuli.[30]

1.3.2 Biological properties

In nature chitin and chitosan are degraded first in oligosaccharides and then in units of n-acetylglucosamine and n-glucosamine by enzymes such as chitinase and chitosanases. [31] Lysozyme and enzymes of enteric bacterial colonies play a major role in the human body, but many studies have identified other enzymes that can degrade chitosan such as chitinase, glucosidases and proteases.[32], [33] Moreover, it has been shown that DDA also affects degradability, DDA>50% are less easily degradable due to progressive reduction in the number of n-acetylglucosamine units and to increased crystallinity, characterized by polymer chains that are arranged in a regular and repetitive way. [32]

In the past decades many studies have been concerned with the biocompatibility of chitosan, which emerged not only the lack of toxicity of the polymer for cell lines such as osteoblasts, hepatocyte endothelial and other cells but also the ability to act as a support for cell adhesion and proliferation.[34] The study of in vivo models showed that chitosan does not trigger pathological inflammation responses. [34] The biocompatibility of this polymer can be explained by considering the structural and functional similarity of chitosan with glycosaminoglycans present in the extracellular matrix; the DDA has been shown to affect biocompatibility, in fact, high degrees of deacetylation have shown to provide better cellular support and trigger less inflammation.[35]

Chitosan has demonstrated remarkable antimicrobial properties and although numerous studies have been devoted to understanding the molecular mechanisms underlying this activity, a complete and unambiguous picture has not yet been achieved.[36], [37]

One of the main mechanisms proposed involves the direct interaction of chitosan with bacterial cell membrane. The cationic nature of chitosan, or its positive electric charge, allows it to interact electrostatically with bacterial cell membranes, which have a negative net charge due to the presence of lipopolysaccharides and phospholipids. This interaction can lead to membrane destabilization, resulting in pore formation and loss of essential cellular components. Impairment of cell membrane integrity is a lethal event for the bacterium.[38]

In addition to damaging the membrane, chitosan can penetrate into the bacterial cell, interfering with numerous vital processes. Chitosan has been shown to inhibit protein synthesis by binding to ribosomes or other components of the protein synthesis machinery. Chitosan can also interact with the bacterial genetic material, DNA and RNA, inhibiting replication and transcription processes, thus compromising the ability of the bacterium to multiply and survive.[39]

Another mechanism of action of chitosan is its ability to chelate metal ions essential for bacterial growth, such as iron and magnesium. The chelation of these ions by chitosan prevents their availability for bacterial metabolic processes, inhibiting the activity of numerous enzymes and compromising cell viability.[40]

The antimicrobial activity of chitosan is thus a complex set of mechanisms of action, involving interaction with the cell membrane, penetration into the cell and interference with essential cellular processes. Thorough understanding of these mechanisms is crucial for the development of new antimicrobial strategies based on the use of chitosan and its derivatives.

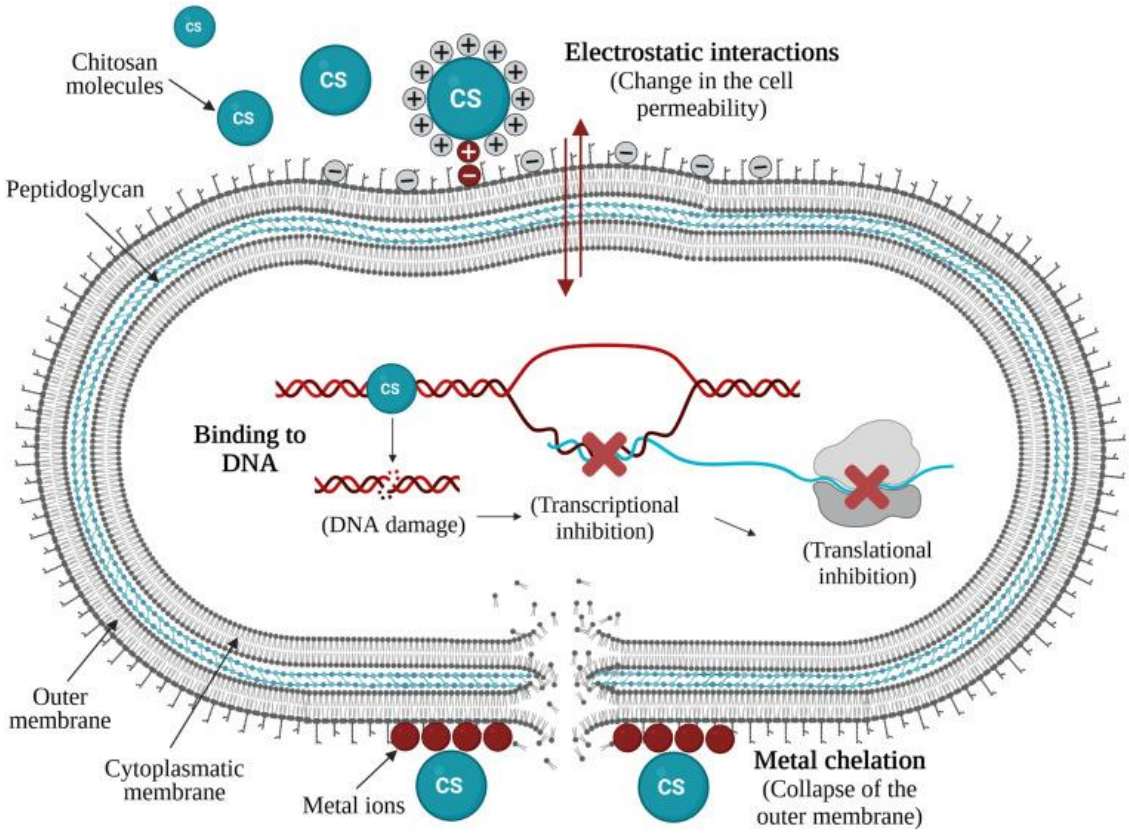

Figure 1.3 Chitosan antimicrobial mechanisms.[38]

1.3.3 Applications

Chitosan, thanks to its unique properties, has applications in various fields, even very different from each other. In the biomedical field, chitosan is widely used as a carrier in drug delivery systems for its ability to improve the bioavailability of drugs.[41] Protects drugs from degradation in the gastrointestinal tract and promotes better absorbency. [42] Some examples of this type of application include the inclusion of chitosan nanoparticles for targeted cancer therapy and chitosan-based hydrogels for controlled drug release.[41], [42] Also in the health sector, chitosan promotes wound healing by supporting cell proliferation, angiogenesis and modulating inflammatory responses, it is therefore used in wound dressings, hydrogels and films that can provide a wet environment conducive to healing, while offering antimicrobial protection.[43] In tissue engineering, chitosan serves as scaffold material for the regeneration of bones, cartilage and nerve tissues due to its ability to support cell adhesion and growth. It is often combined with other materials to improve its mechanical properties and biocompatibility. [44] Referring to the health field but more specifically cosmetic-pharmaceutical chitosan is appreciated for its moisturizing and film forming properties. It is used in hair care products, skin creams and lotions to provide a protective barrier on skin and hair. [45] Due to its mucoadesive properties it is suitable for use in nasal sprays and other mucosal delivery systems.

It is also explored for its potential in oral care products such as toothpastes and mouthwashes due to its antibacterial effects.[46]

In agriculture, chitosan is used as a plant growth promoter due to its ability to induce defence mechanisms in plants, improving resistance to pathogens and pests. Applied as a seed treatment, soil improver or foliar spray to promote healthier crop growth. It is also used in coatings to extend the shelf life of fruits and vegetables by forming a barrier against microbial contamination and moisture loss. The additional advantage of these coatings is that they are biodegradable and can be easily removed by washing.[47]

In the environmental field, chitosan is used for water treatment, it is effective in removing heavy metals, dyes and other pollutants from wastewater due to its ability to bind with contaminants. It is used in filtration systems and as an adsorbent in environmental cleaning processes.[48]

In the food industry its property is exploited and chitosan is used as a natural preservative, applied to meat, fish and dairy products to inhibit the growth of organisms that cause deterioration and prolong shelf life.[49], [50]

In the textile industry, chitosan is used to give antimicrobial and deodorant finishes to textiles, making them ideal for use in medical and sports clothing, where it is important to prevent bacterial growth and bad odors. [51] Also, thanks to its free primary amine, chitosan can easily bind with various reagents to improve resistance to washes, making the treatment durable over time. [51] Chitosan is also used as a natural stain in the dyeing of fabrics, improving colour absorption and fade resistance. [52] This is particularly useful for fibres such as wool, where chitosan can improve the effectiveness of reactive dyes.[53] In addition, chitosan can be applied in combination with other chemicals to achieve more sharp and defined print results. [52]

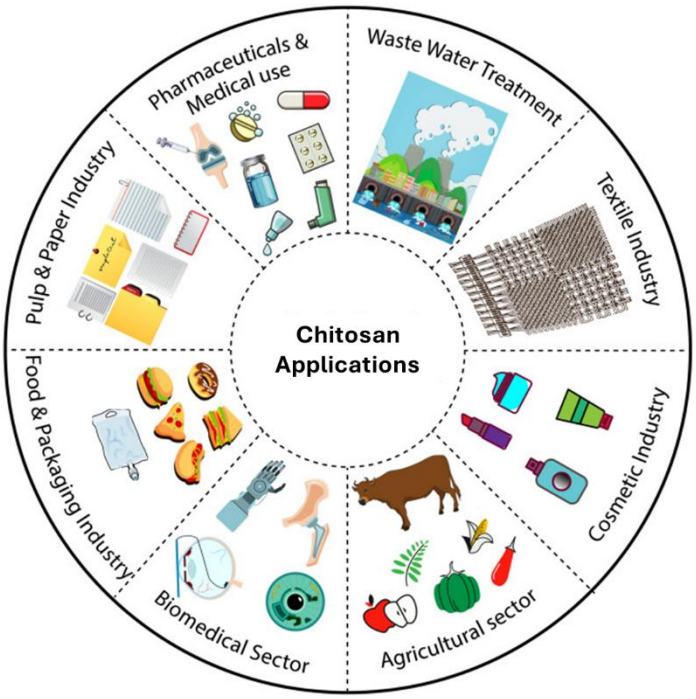

Figure 1.4 Chitosan applications.[54]

1.4 Nanoparticles

Nanoparticles are particles of nanometric size, generally between 1 and 100 nanometres (nm). At this scale, the physical, chemical and biological properties of particles may differ significantly from those of their larger counterparts due to quantum effects and the large specific surface area in relation to volume, providing new opportunities for technological innovations due to their unique features. These particles can be made of various materials, such as metals, oxides, polymers or composites.[55], [56]

The properties of nanoparticles are closely related to particle size which is strongly influenced by the synthesis method; synthesis methods can be classified into physical, chemical or green methods. [57]

The methods which can be classified as physical synthesis include evaporation-condensation and laser ablation. The first involves nanoparticles being synthesised by converting the material of interest into a gas using a tubular furnace, then the steam is condensed, forming nuclei that easily grow into nanoparticles, the variation of the parameters of this process allows to influence size and yield of nanoparticles. The second method allows nanoparticles to be obtained in air or solution without the use of additional reagents; the factors influencing the properties of the nanoparticles thus obtained are the laser wavelength, the duration of irradiation and the nature of the liquid medium used.[56], [57]

In chemical synthesis, the most widely used technique is chemical reduction, where a precursor is reduced by chemicals to nanoparticle; This method has the advantage of obtaining an excellent yield in a relatively short time but the disadvantage of leaving residues of reagents on the nanoparticles, potentially toxic and not eco-compatible.[55]

Alongside chemical and physical methods, biological synthesis techniques or "green" are gaining attention, as they use natural reducing agents derived from plants, bacteria and fungi. These approaches are considered more sustainable and less toxic than traditional chemical methods. For example, plant extracts containing flavonoids, polyphenols and terpenes can act as both reducing agents and stabilising agents, offering a "green" path to produce highly biocompatible nanoparticles. [56], [57]

1.4.1 Silver nanoparticles

Among the metal nanoparticles, the research interest has focused on silver nanoparticles (AgNPs) whose unique properties, surface plasmon resonance, electrical and thermal conductivity and optical properties have allowed its application in a wide range of fields, from wastewater treatment to medical devices for anti-cancer or antibacterial therapies.[58], [59]

AgNPs are particularly known for their strong localized surface plasmonic resonance (LSPR) effects due to their high electron density and relatively low damping compared to other metals. LSPR occurs when the collective oscillations of free electrons in a metal nanoparticle resonate with incident light. This resonance is strongly localized on the surface of the nanoparticle. The resonance condition for LSPR is met when the frequency of the incident light corresponds to the natural oscillation frequency of the surface electrons in the nanoparticle. This causes an increase in the electromagnetic field around the nanoparticle.[60], [61]

Moreover, AgNPs have emerged as promising alternative antibacterial agents, able to overcome the resistance developed by some bacterial strains to traditional antibiotics. Their antimicrobial efficacy is closely related to particle size, AgNPs with less than 10 nm diameter demonstrating greater bactericidal activity.[62], [63]

The mechanisms of action underlying this effectiveness are multiple and synergistic. First, AgNPs release silver ions (Ag+) into the surrounding environment. These highly reactive ions interact with the sulphidyl (-SH) groups of bacterial proteins, inhibiting their function and thus compromising vital cellular processes. In particular, interaction with enzymes involved in cellular respiration and DNA replication leads to cell death.[63]

In addition, AgNPs are able to adhere to the surface of bacterial cell membranes, altering their permeability and causing structural damage. This impairment of the cell barrier causes essential cellular components to escape and ultimately leads to cell lysis.[63]

An additional mechanism of action is linked to the production of reactive oxygen species (ROS) induced by AgNPs. ROS, such as hydroxyl radicals (OH•) and hydrogen peroxide (H_2O_2), are powerful oxidants that can damage DNA, proteins and cell lipids, triggering oxidative processes that compromise the integrity and vitality of the bacterial cell.[62], [63]

Finally, AgNPs can interact directly with bacterial DNA and proteins, inhibiting replication and transcription processes. This interaction alters gene expression and inhibits protein synthesis, thereby impairing cell growth and proliferation.[62]

The wide range of action of AgNPs is probably due to the multiple mechanisms of action involved, making them promising candidates for the development of new antimicrobial strategies.

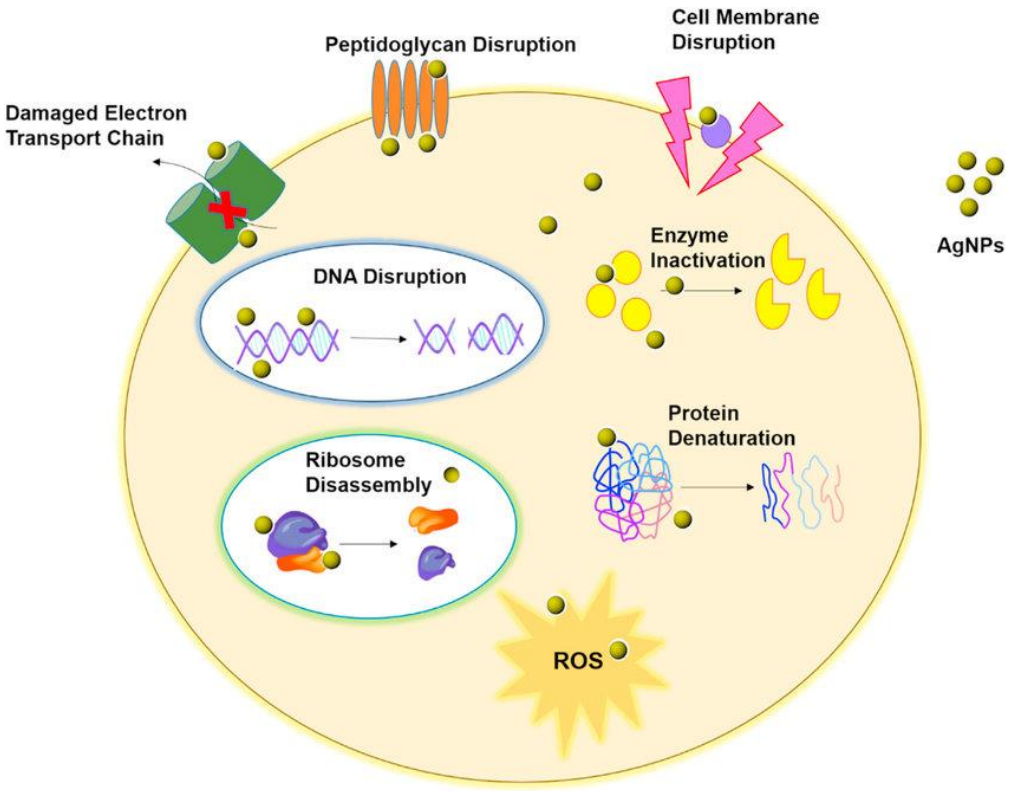

Figure 1.5 Silver nanoparticles antimicrobial mechanisms.[64]

AgNPs have been studied for their potential as antifungal agents, studies have revealed several mechanisms that contribute to the fungicidal effect, some are similar to those operated in bacterial cells. The oxidation and production of ROS, resulting in the production of reactive

oxygen species, free radicals and hydrogen peroxide which are highly toxic to micro-organisms and can damage cell membranes, proteins and the DNA of the fungus. The interaction with cell membranes, specifically with lipids and membrane proteins, compromises the integrity of the membrane and leads to cell death. The inhibition of protein synthesis and DNA damage, causing mutations or other forms of genetic damage. And the interaction with enzymes and metabolites key elements of fungal metabolism, disrupting the biochemical processes necessary for growth and reproduction of fungi.[65], [66]

A mechanism implemented only in fungal cells is that where silver nanoparticles inhibit the production of ergosterol, an essential component of the cell membrane of fungi. Ergosterol plays a role similar to cholesterol in animal cells which is crucial for the functionality and integrity of fungal cell membranes, the lack of this essential component leads to the formation of a no optimal membrane which therefore tends to break more easily, leading to cell death.[65]

Silver nanoparticles possess a high specific surface area, thanks to this characteristic, they accumulate in high concentrations in the contact zones with fungi, amplifying the effectiveness of the antifungal action.[66]

AgNPs have shown antiviral activity in several studies, due to different mechanisms through which they can affect viruses. The main antiviral mechanisms include concentration and surface effect, AgNPs have a high specific surface area, which allows them to interact effectively with viral particles. AgNPs interfere with the ability of the virus to adhere and penetrate into host cells, this interference can occur through direct binding between nanoparticles and viral glycoproteins or cellular receptors, preventing the virus from entering the host cell. AgNPs can also cause direct damage to the viral structure by interacting with components of the viral lining, such as proteins in the capsule, altering its structure and impairing the virus's ability to infect cells. Within the host cell, silver nanoparticles can interfere with viral replication by interacting with cellular components involved in virus replication or damaging viral RNA or DNA, Preventing the replication process. AgNPs can interfere with the assembly process of virions within the infected cell, preventing the formation of new virus particles ready for exit and infection of other cells. Finally, by producing reactive oxygen species (ROS), AgNPs can damage viral proteins and nucleic acids, negatively affecting the ability of the virus to replicate.[67]

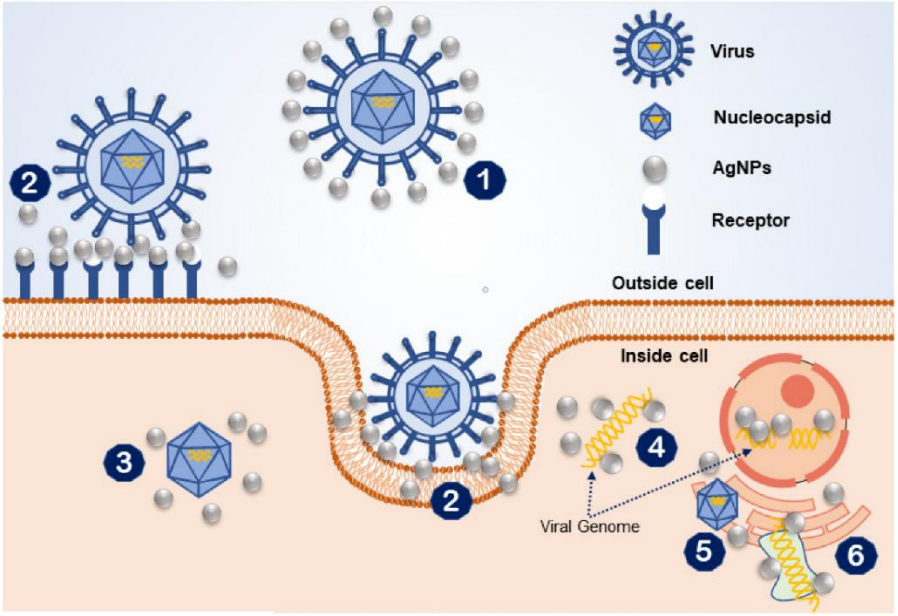

Figure 1.6. Silver nanoparticles antiviral mechanisms: (1) interaction of AgNPs with the viral surface; (2) interface with the cell membrane while blocking the viral attachment; (3) inhibition of cellular pathways of the virus; (4) interaction with viral genome; (5) interaction to inhibit viral genome replication; (6) inhibition of cellular factors (i.e., protein synthesis) necessary for viral replication. [67]

1.4.1.1 Applications

The optical properties and antimicrobial activity of Ag-NPs have allowed their wide use in the field of sewage purification. The purification of water from hazardous materials is very important, especially when it comes to heavy materials and pathogenic microorganisms. [63] Mercury, for example, is one of the highly toxic heavy metals that requires very selective selection and sensitive techniques to be detected. In a study conducted by Abdel-Lateef, a technique was developed to detect Hg^{+2} in water samples with high sensitivity and selectivity on different anions and minerals Al^{+3}, Ba^{+2}, Ni^{+2} and Co^{+2}. AgNPs can detect other metals that may be present in the water, such as Cu^{+2}, Fe^{+3}, Zn^{+2}, Pb^{+2}, and Al^{+3}. [68] In addition to the detection of AgNPs, through antimicrobial activity can operate a water disinfection.[63]

AgNPs, because their antimicrobial properties are widely studied for use in the food industry, such as active packaging materials that release AgNPs to prevent the growth of bacteria such as E. coli and Salmonella, prolonging the shelf life of food. One practical example is the use of plastic films containing AgNPs, which have shown to significantly reduce microbial contamination in fresh products such as fruit and vegetables.[69], [70]

AgNPs are used as nano sensors in the food industry to monitor food quality and safety. These nano sensors exploit the unique optical properties of AgNPs, such as surface plasmon resonance

(SPR), which changes in the presence of contaminants, allowing rapid and sensitive detection of harmful substances.[71]

Studies have looked at the production of nanosensors based on AgNPs, which can detect the presence of pesticides or pathogens such as E. coli in real time, ensuring that food is safe for consumption before reaching the consumer; the use of AgNPs-based nanosensors for detection of pesticides and other chemical contaminants in fruit and vegetables not only provides a rapid response, but is also highly sensitive, allowing the detection of contaminants at very low concentrations.[72]

Despite the benefits, further research is needed to assess the long-term safety of AgNPs in food and food contact materials, to assess the potential migration of nanoparticles into food and to understand their potential effects on human health.[72]

Finally, the AgNPs have established as promising tools in the biomedical field, thanks to their wide range of biological activities. Particularly appreciated for their antimicrobial properties, AgNPs have shown significant efficacy against a wide range of pathogens, including Gram-positive and Gram-negative bacteria, as well as certain viruses and fungi. The integration of AgNPs into medical devices has led to significant advances in the prevention of healthcare-related infections. For example, coatings with integrated AgNPs for vascular catheters have dramatically reduced the incidence of nosocomial infections, improving patient safety. [73] Similarly, AgNPs-impregnated dressings have shown an acceleration of healing processes and a reduction in infections in acute and chronic wounds such as burns.[74] AgNPs have also been explored as vectors for targeted drug delivery.[75] The EPR effect, which allows nanoparticles to accumulate preferentially in cancer tissues, has made AgNPs particularly interesting for chemotherapy. Preclinical studies have shown that AgNPs loaded with chemotherapy agents, such as doxorubicin, can improve therapeutic efficacy while reducing systemic toxicity. [76] In addition to therapeutic applications, AgNPs are also used in imaging. Their unique optical properties, particularly the SPR, make them ideal tools for developing highly sensitive and specific biosensors.[77] For example, functionalized AgNPs with specific cancer biomarker ligands can be used to visualize cancer lesions using optical imaging techniques, contributing to the early diagnosis and staging of neoplasia.[78]

1.4.2 Copper nanoparticles

Copper nanoparticles (CuNPs) are objects of increasing interest in scientific research and industry due to their unique physical and chemical properties. The nanometric size, typically

10 to 100 nm, gives these particles different characteristics than massive copper, such as higher chemical reactivity, antibacterial properties and electrical conductivity.

Copper nanoparticles, as well as those of silver and gold, show a localized surface plasmonic resonance (LSPR), specifically the range in which this occurs from the ultraviolet-visible to the near infrared, according to particle size. Unlike other precious metals, copper is easily susceptible to oxidation, with the formation of a surface layer of copper oxide, which impairs its optical properties and consequently LSPR.

CuNPs exhibited antibacterial, antifungal and antiviral activities. The mechanism behind the antimicrobial capabilities of CuNPs is still being studied, as these nanoparticles interact with micro-organisms at various cellular levels. The main interactions take place at the level of nucleic acids and proteins, resulting in denaturation of these elements. The plasma membrane is also a target of copper, causing depolarization and loss of membrane integrity. In addition to these direct damages, copper releases ions that reducing from Cu^{+} to Cu^{2+} promote the formation of reactive oxygen species (ROS); ROS cause oxidative stress on membrane lipids, a phenomenon known as lipid peroxidation, and on protein amino acids and nucleic acids. [79] [80]

The antifungal mechanism of CuNPs involves several processes, from first a structural damage to hyphae to conidia, nanoparticles cause rupture or deformation of surface structures with consequent impairment of cellular structural integrity; secondly, the released Cu^{+} ions promote the formation of ROS resulting in accumulation of oxidative stress on proteins, lipids and nucleic acids, which can cause cell death. Another important fungal toxicity mechanism involves the synthesis of ergosterol, ergosterol is a fundamental component of the fungal membrane, CuNPs interferes with the biosynthesis of this sterol limiting its synthesis, resulting in not good assemble of plasma membrane and cell death. [79],[81]

The antiviral mechanism of action involves various aspects, the ions released by nanoparticles promote the formation of ROS, which damage lipid, proteins and viral nucleic acids leading to inactivation of the virus; nanoparticles can limit binding and subsequent entry into the host cell of the virus in two ways, either by interacting with viral protein coatings and causing alterations that limit its binding to the host cell or by acting directly on cellular receptors , responsible for the binding and subsequent entry of the virus, hindering cellular absorption and penetration. [79]

All the mechanisms described above are summarised in Figure 1.7

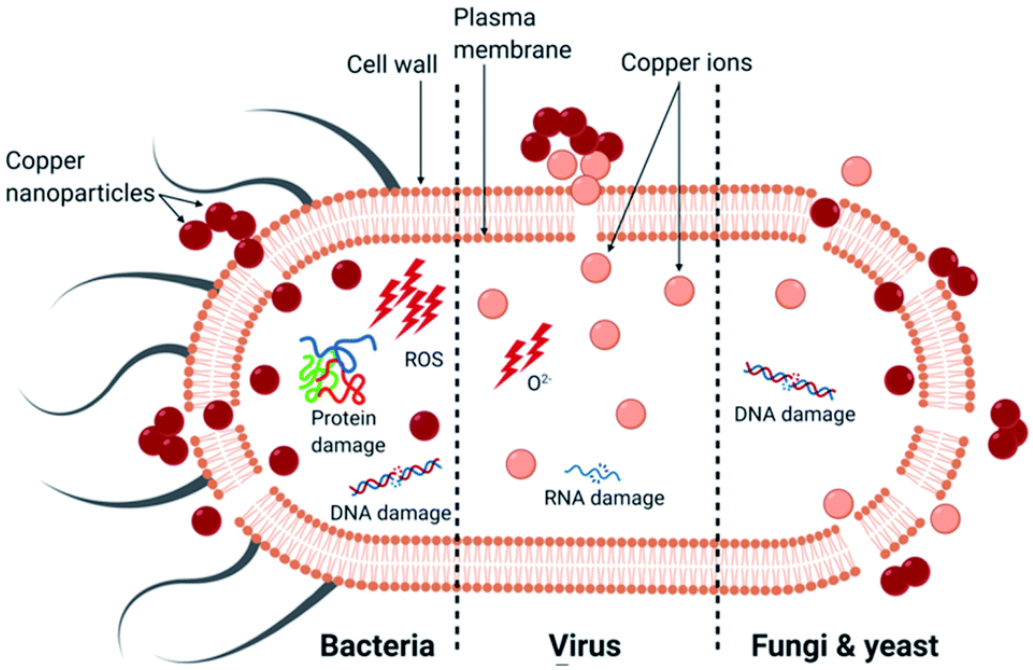

Figure 1.7 CuNPs interaction with bacteria, fungi and virus.[79]

1.4.2.1 Applications

In the biomedical and biotechnology sector, copper nanoparticles are exploited for their antibacterial and antifungal properties, incorporated into health products such as bandages and surface coatings to reduce the risk of infection. [82] The CuNPs are also explored as contrast agents for medical imaging and as vehicles for targeted drug administration. Nanoparticles offer a site-specific drug delivery system, due to their small size, large absorption surface for drug transport and also show an improvement in therapeutic efficacy with less toxicity.[83] Breast cancer was targeted using chitin-coated copper nanoparticles at different pH for the drug doxorubicin, on cell line MCF-7 studying its apoptotic activity.[84]

In the textile sector, several studies have evaluated the design of fabrics containing nano copper into polymer fibres such as nylon by hot extrusion process, thus developing antimicrobial fabrics. [85] Other studies have analysed the incorporation of CuNPs in cotton fibres and antimicrobial evaluation was carried out against E. coli, S. aureus, P. vulgaris and K. Pneumoniae, encouraging results suggest its use in tissues to produce PEPs (Personal Protective Equipment)[86] In the field of environmental protection, copper has been considered as a low-cost and low-toxicity metal, and copper and copper-based catalysts can be recycled and reused. [87] Bioremediation of pollutants such as dyes has become important for treating polluted waters, which can lead to changes in aquatic life and dangerous results. Therefore, the properties of CuNPs have been applied for the remediation of water polluted by textile effluents. The degradation activity of CuONPs is evaluated against organic dyes such as Congo red, methylene blue and rhodamine B, the results of the studies have shown a strong catalytic

capacity of the dyes under consideration, laying the foundations for a possible use of CuNPs and CuONPs for textile wastewater treatment.[88]

Chapter 2 Sustainable strategies for the synthesis of composite materials: laser assisted technology and alternative sources of biopolymers

In recent years, growing awareness of environmental issues and the need to develop sustainable technologies have catalysed a profound change in scientific and technological research. The transition to "green" methods is a crucial response to the challenges posed by climate change, pollution and depletion of natural resources. In this context, innovation has focused on techniques and materials that can reduce environmental impact, limit the use of hazardous chemicals and optimise the use of renewable resources.

One methodology that is gaining increasing attention is laser ablation in liquid (LAL), a technique that allows nanomaterials to be produced in a clean and sustainable manner. This methodology does not require the use of toxic chemicals or complicated purification processes, offering an environmentally friendly alternative to traditional chemical synthesis methods. The principle behind LAL is to use a laser beam focused on a solid surface immersed in a liquid, where the laser energy vaporises a small portion of the solid material, creating nanoparticles that disperse into the surrounding liquid. As well as being highly versatile and scalable, this technique makes it possible to modulate the composition and properties of nanomaterials, opening up new perspectives for industrial, biomedical and environmental applications.

Another key aspect in the search for sustainable solutions is biocompatible and biodegradable materials, including chitosan. Traditionally, this polysaccharide is obtained from the shells of crustaceans such as shrimps and crabs, an abundant source but not without ethical and environmental limitations related to intensive fishing and impact on marine ecosystems. As a result, research is exploring alternative and sustainable sources of chitosan, such as waste from the food industry or insects. The use of alternative sources not only reduces the exploitation of marine resources, but also promotes a circular economy, in which waste from one production sector can become resources for another.

This chapter aims to explore in depth the integration of sustainable technologies into nanomaterial production and the use of chitosan from alternative sources. The laser ablation in liquid in the production of nanoparticles will be analysed. In parallel, the properties and prospects of chitosan from alternative sources will be discussed, highlighting its potential. This integrated approach, which combines technological innovations and sustainable materials, is a key to addressing future challenges related to sustainability and responsible innovation.

2.1 Laser ablation in liquid (LAL)

Laser ablation (LA) refers to the removal of material by complex physico-chemical processes induced by the absorption of high-power laser light by a solid target [89]. The interaction of the laser beam with the target causes the expulsion of atoms, ions, molecules, electrons and clusters [89]. These components form a plasma, which is a neutral and highly ionized gas, which expands three-dimensionally with a variable speed depending on the type of particles, the wavelength and power of the ablation laser, and can range from 10^4 to 10^6 cm/s. [90] The process characteristics of LA depend on several parameters, including laser (pulsed or continuous wave), wavelength, fluence, target (solid or liquid) and the surrounding environment (vacuum, gas or liquid).

Pulsed laser systems are most frequently used for LA experiments and pulse duration (τ) is a crucial parameter. In fact, very different laser-matter interaction mechanisms occur with short or ultra-short pulsed lasers [89].

Laser ablation in liquid is a simple and versatile technique used to synthesize nanoparticles (NPs) of various materials. This method was introduced less than two decades ago to create colloidal solutions of nanoparticles. [91] The standard experimental setup for nanoparticle production is illustrated in Figure 2.1

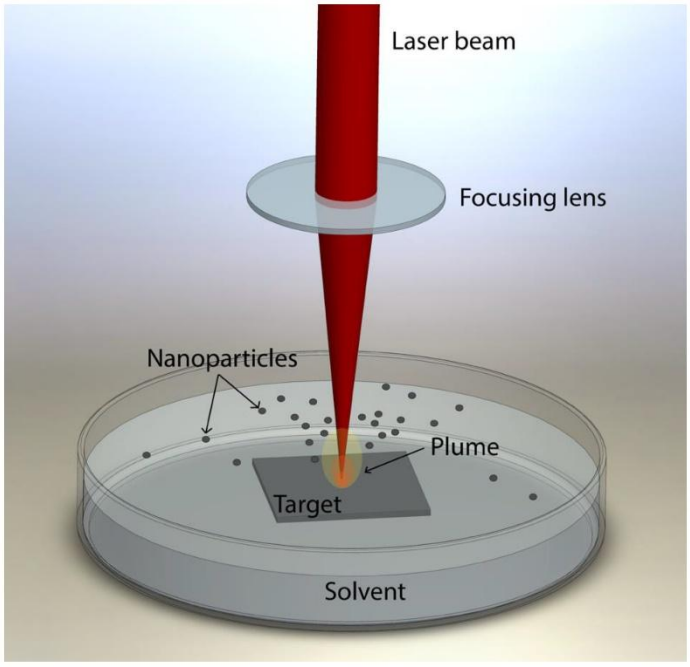

Figure 2.1 Schematic representation of the experimental set up used during laser ablation in liquids experiments.

In laser ablation in liquid (LAL), the liquid medium not only provides control parameters for fabrication but also influences the morphology and microstructure of the resulting products. Additionally, modifications in the shape and size of NPs prepared by laser post-irradiation have been observed. [91]

The most significant difference between laser ablation of solids in vacuum or diluted gas and in liquids is that liquids confine the dynamics of the plasma plume produced after the laser-target interaction. [92] Consequently, a series of processes, including the generation, transformation, and condensation of the plasma resulting from the ablation of solids in liquid environments, occur under the condition of liquid confinement. This confinement can significantly influence the characteristics of the plasma plume's evolution. [92]

When an incident laser pulse interacts with a solid target in a liquid, the formation of a laser induced plasma take place. The plasma confined by the liquid reaches a thermodynamic state that is markedly different from that of plasma generated in gas or vacuum. Specifically, plasma generated in a liquid, due to the confinement of the liquid, has a much higher density than that generated in gas or vacuum , the presence of liquid also allows faster heat dissipation through the interactions that absorb thermal energy.[92] In gas or vacuum ablation, the plasma tends to expand without any or almost no, in the case of gas, half-confined, leading to a plasma of low density and very high temperatures which are not dissipated. Finally, the further difference in the time it takes for the plasma to lose energy and return to the non-ionized state, in the liquid, heat dissipation by the medium leads to a rapid relaxation time whereas in gaseous or vacuum environments the times are longer because of the high temperatures reached by the plasma which persist due to lack of dissipation.[92] The evolution of the plasma plume generated in liquid is depicted in Figure 2.2.

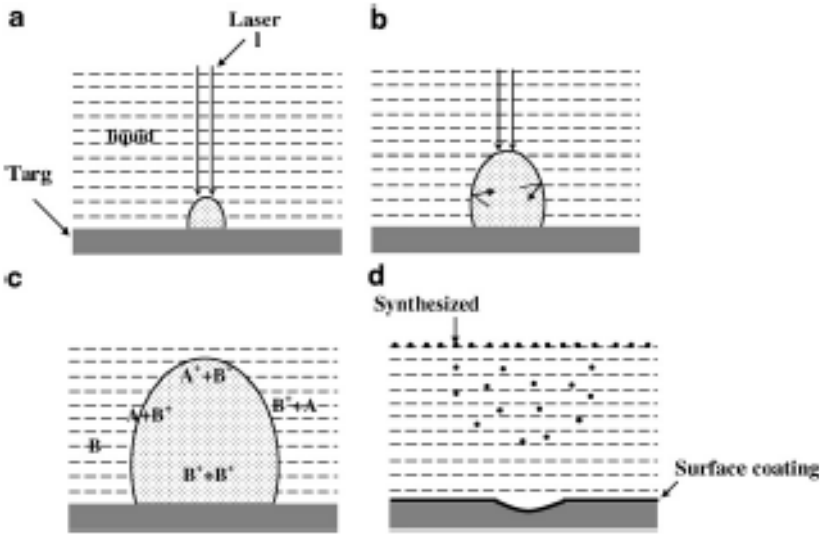

Figure 2.2 Evolution of the plasma plume generated in liquid environment. (a) Generation of the laser – induced plasma. (b) Expansion of the plasma plume in liquid. (c) Four type of chemical reactions which occur inside the plasma and liquid, and at the interface between the plasma and liquid. (d) Condensations of the plasma plume in liquid (surface coating on the target and nanoparticles fabrication in liquid).

As demonstrated by Fabbro and colleagues, a shock wave is induced following plasma formation and expansion in the liquid. [92],[93] This shock wave generates additional pressure, resulting in a temperature increase within the plasma. Consequently, the shock wave pushes the laser-induced plasma into a thermodynamic state characterized by higher temperature, higher pressure, and higher density than the initially generated plasma. [92] This thermodynamic state favours the formation of metastable phases which can only be achieved under high temperature and high pressure conditions. [92]

Four types of chemical reactions can occur in the plasma and at the liquid-plasma interface, as illustrated schematically in Figure 2.2 C. The first type of reaction occurs within the laser-induced plasma, where the high-pressure and high-temperature conditions facilitate the formation of new phases, particularly metastable ones, through high-temperature chemical reactions. The second type of reaction also occurs within the plasma but involves reactant species from both the target and the liquid. The high temperature and pressure of the laser-induced plasma cause excitation and evaporation of liquid molecules at the plasma-liquid interface, creating a new plasma from the liquid molecules. [92] This new plasma can rapidly mix with the laser-induced plasma, leading to chemical reactions between species from the target and the liquid molecules.

The third type of chemical reaction occurs at the plasma-liquid interface, where the high-temperature, high-pressure, and high-density conditions of the laser-induced plasma facilitate chemical reactions between ablated species from the target and liquid molecules. The fourth type of reaction takes place within the liquid itself. The high pressure in front of the laser-induced plasma drives ablated species from the solid target into the liquid, leading to reactions between these species and liquid molecules. [92] These reactions enable the fabrication of new materials by combining elements from the target and the liquid.

The final stage of the evolution of the plasma plume generated in liquids involves cooling and condensation within the confining liquid, as shown in Figure 2.2 C. Part of the plasma plume

condenses and deposits back onto the surface of the solid target during plasma quenching due to the confining pressure from the liquid. This condensation and deposition process leads to surface coating formation, which has been developed as a new Pulsed Laser Deposition (PLD) method for preparing surface coatings with metastable phases. [94], [95] Another portion of the plasma plume disperses into the liquid during quenching, resulting in the formation of small particles in the liquid.[92]

In the following section, the mechanisms of LAL of metal targets will be analysed in detail.

2.1.1 The mechanism of laser ablation

When a laser beam heats a metal target, various species such as plasma, vapor, and metal micro- or nano-sized droplets can be initially generated. These products can further react with the liquid medium to form nanoparticles (NPs).[96] Among these three possible products, vapor and plasma are typically obtained using short pulse-width lasers with high power density, such as nanosecond pulsed lasers with pulse widths of several nanoseconds and power densities ranging from 10^8 to 10^{10} W cm^{-2}.[96] In contrast, nanodroplets tend to be the principal product when low-power density lasers, such as millisecond lasers, are employed.[91]

The most important mechanisms for the formation of laser-ablated nanostructures are thermal evaporation and the formation of vapor or plasma phases (with subsequent interaction with the liquid), as well as the explosive ejection of nanodroplets .[96]

For the thermal evaporation mechanism, Zeng and colleagues conducted a comprehensive study of the laser ablation of Fe, Si, and Zn targets in water using a (Nd:YAG) pulsed laser with a wavelength of 1064 nm, a frequency of 10 Hz, and a pulse duration of 10 ns. The power was 80 mJ per pulse, and the spot size on the target was 2 mm in diameter.[97], [98]

In the case of a solid target, such as an Fe target, a high-temperature and high-pressure Fe plasma is produced at the solid-liquid interface after the initial laser shot. This is followed by the ultrasonic adiabatic expansion of the hot plasma, which leads to rapid cooling of the plume area and the formation of Fe clusters. These clusters interact with the surrounding aqueous solution, resulting in the formation of FeO nanoparticles.

Yang et al. [99] also utilized a Nd:YAG laser with a wavelength of 532 nm, a pulse duration of 10 ns, and a power density of 10^{10} W cm^{-2}. They proposed a different thermal evaporation model involving two types of plasma: a laser-induced plasma from the target and a plasma-induced plasma from the liquid medium. Following the interaction between the laser pulse and

the target, it is suggested that the target is heated and evaporated into a plasma state. This plasma then evaporates the surrounding liquid, converting it into plasma. These two plasmas can mix and react, ultimately cooling and condensing to produce compound nanomaterials (NMs). [99]

Four main parameters can be identified, whose trends in time and space determine the phase and structure of the produced NMs: pressure (P), temperature (T), concentration of the ablated material (CM), and concentration of solution species (CS). [100]

The second proposed mechanism is the explosive ejection model, Figure 2.3 [96], which was suggested to elucidate the formation of various nanostructures of metal oxides and sulfides with diverse morphologies when using a long-pulse laser (such as a millisecond pulsed laser).

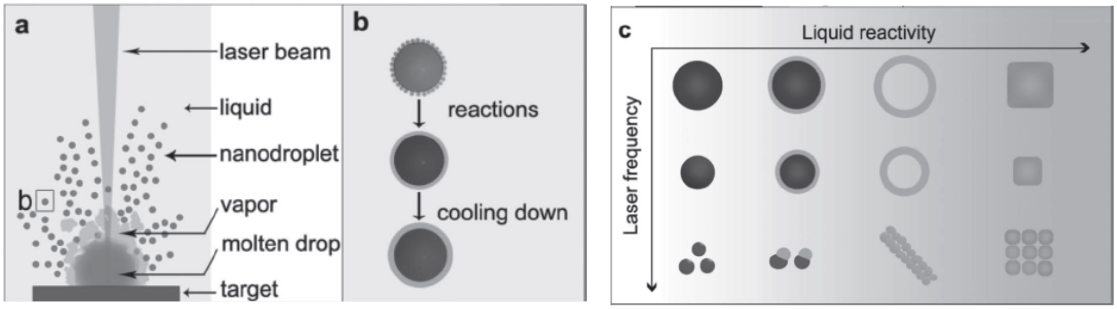

Figure 2.3 Sketch depicting the process of nanodroplet ejection and formation of nanostructures during the LAL process with a low-energy millisecond laser. a) Formation of nanodroplets. b) Reactions of an ejected metal nanodroplet in the surrounding liquid. c) Influence of liquid reactivity and laser frequency on the morphology of nanostructures obtained by ablating a Pb target in liquids. [96]

Due to its lower power density (10^6–10^7 W cm^{-2}), the ablation products mainly consist of metal nanodroplets, which are expelled into the liquid at high speed.[101] These hot metal nanodroplets are compact and therefore react with the liquid medium starting from their surface. The reactivity of the liquid and laser parameters determine the extent and rate of these reactions, resulting in products with varying morphologies and chemical compositions. [101] Thus, the reactions and final products can be tailored by selecting appropriate targets, liquids, and laser parameters. [101], [102]

This study employed a nanosecond laser source; therefore, the chronological sequence of ablation steps when a single laser pulse impacts the target will be explained.

2.1.2 Temporal evolution

In this section, will be analyse the temporal evolution of physical and chemical phenomena occurring in LAL. The laser fluence is assumed to be above the ablation threshold (typically 10-10^3 J cm^{-2}), and time (t) is defined as t = 0 when the laser pulse impacts the target. [100] The first phenomenon to occur is the penetration of the laser pulse into the liquid, Figure 2.4. This occurs before reaching the target, for t < 0. It is essential that the laser energy is directed solely towards the target and not dispersed into the surrounding liquid environment.

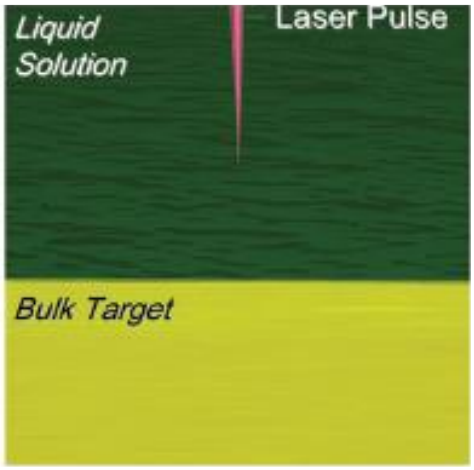

Figure 2.4 laser pulse penetration in the liquid before reaching the target.

For this reason, it is crucial to avoid liquid breakdown. [93], [103], [104] The laser fluence must remain below a threshold value (Fth) to prevent nonlinear optical effects such as multiphoton absorption by the liquid. [104] It is important that the liquid solution does not absorb the laser radiation. [100] Generally, under typical LAL conditions for NP production, solvent absorption is negligible because the energy delivered to the target is orders of magnitude greater than that absorbed by the liquid. Only under specific circumstances can the liquid solution significantly absorb or scatter laser light, such as when absorbing solutes or already formed NPs are present in the solution, leading to reduced energy transfer to the target. [100]

After passing through the liquid, various time-resolved phenomena occur. First is (I) the absorption of the laser pulse, occurring in the temporal range t = 0 to τ. Next, from t = 10^{-12} s to 10^{-10} s, (II) detachment of the ablated material occurs. From t = 10^{-10} to 10^{-7} s, (III) expansion and quenching of the plasma plume occur, followed by (IV) the expansion and collapse of the cavitation bubble, which takes place in the temporal range t = 10^{-6} s to 10^{-4} s. The final step,

observed for $t > 10^{-4}$ s, is (V) the slow growth and agglomeration of nanomaterials. These steps from II to VI are described in more detail below.

(I) Absorption of the laser pulse (from $t = 0$ to τ) is illustrated in Figure 2.5. The high photon density induces both linear and nonlinear absorption processes. Light is absorbed into the target until a depth approximately equivalent to the material's skin depth is reached. [105] Nonlinear optical processes are influenced by the intensity of the electromagnetic field, which is proportional to the pulse fluence (F) divided by the laser pulse duration (τ) .[106]

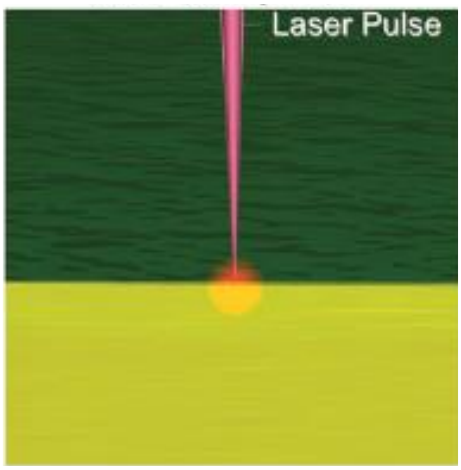

Figure 2.5 Absorption of the laser pulse within the target.

(II) Detachment of the ablated material (from $t = 10^{-12}$ s to 10^{-10} s) (Figure 2.6). The creation of locally induced space-charge separation and electron-ion collisions occur. These phenomena result in the detachment of material from the target on a timescale of approximately 10^{-12} seconds. [100]

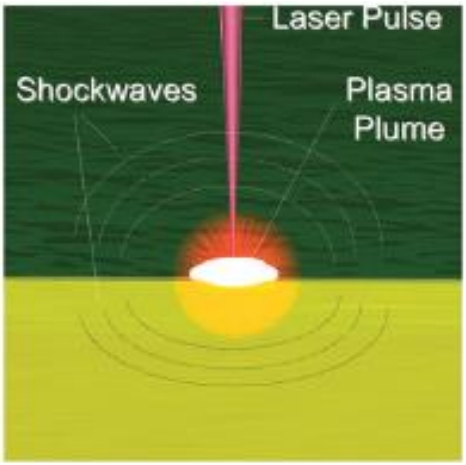

Figure 2.6 Detachment of the ablated material from the target.

The irradiated zone and the rest of the system exhibit significant temperature differences, with the solid target being highly efficient at dissipating heat. Consequently, material detachment occurs through both thermal and Coulombic mechanisms within a region that closely aligns with the laser spot. The physical properties of the detached material are crucial for understanding the subsequent steps of nanomaterial formation, such as nucleation, growth, and reactivity with solution species. The exact description of the ablation mechanism is complex, as multiple fragmentation processes can occur simultaneously within different zones of the laser spot, depending on laser parameters. [100] The most widely accepted theory employs classical thermodynamics as a first approximation to describe laser ablation. In this framework, three thermal processes can lead to material detachment from a laser-irradiated target: vaporization, normal boiling, and explosive boiling. [107] Explosive boiling, also known as phase explosion, is considered the primary thermodynamic mechanism for material detachment from the crater under typical LAL conditions with laser pulses shorter than 10^{-7} seconds.

Thermodynamics and molecular dynamics (MD) provide valuable insights into the initial stages of material detachment from the target. However, many aspects remain unclear, particularly regarding the effects of photoionization, photomechanical stress, and plasma confinement on the crater surface due to the surrounding liquid. Photoionization may cause material detachment through Coulombic explosion, similar to what has been observed during laser irradiation of particle suspensions. [108], [109]

During ablation, the recoil pressure of the ablated material generates two shockwaves: one propagating into the target and a specular one propagating into the liquid solution at supersonic speeds, around 10^3 m/s. A shockwave is a pressure wave that travels through a medium, causing abrupt discontinuities in density and temperature along its front. The energy of a shockwave generated by laser ablation is typically between 10%-50% of the absorbed pulse energy. [110] The propagation of the shockwave heats both the liquid and the target, potentially promoting further material detachment from the crater.[111], [112]

The high temperature and direct photoionization lead to the formation of highly ionized species within the ablated material, forming a non-equilibrium plasma plume. Inside the plasma, the temperature, pressure, and density are extremely high, on the order of 10^3 K, 10^9–10^{10} Pa, and 10^{22}-10^{23} atoms/cm^3, respectively.[100]

After the laser pulse ends, the plasma plume persists for about tens of nanoseconds. The rapid cooling of the plasma plume occurs due to its expansion and heat exchange with the solvent, resulting in a fast evolution of the plume. Additionally, the plasma may contain melted droplets and solid fragments.

The nanosecond laser pulse and the plasma plume overlap both temporally and spatially, allowing the plume to absorb energy from the laser. This effect, known as "plasma shielding," reduces the amount of laser energy reaching the target. Simultaneously, the absorption of laser energy by the plasma increases the temperature and lifetime of the plasma plume.

(III)Expansion and quenching of plasma plume (from t = 10^{-10} to 10^{-7} s) (Figure 2.7).

For t = 10^{-10} – 10^{-9} s, the liquid strongly confines the plasma plume onto the crater region. [100]

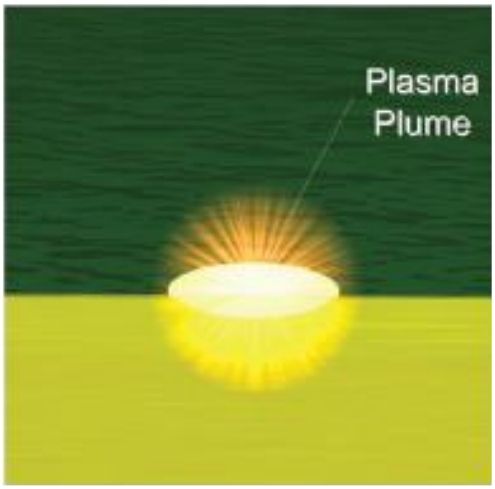

Figure 2.7 representation of the expansion and quenching of plasma plume.

One consequence of confinement is the slowed cooling rate at the interface between the ablated material and the target. This occurs because the hot ablated material can transfer thermal energy to the underlying target. As a result, laser ablation in liquid yields a higher output than in gas, as a larger portion of the target reaches the energy threshold for detachment. [100]

The spatial gradients of temperature (T), pressure (P), concentration of ablated material (C_M), and concentration of solution species (C_S) are very steep for times shorter than 10^{-10} seconds, making it possible to distinguish three distinct regions: the solid target, the expanding plasma plume, and the liquid solution. The plasma plume begins to expand after about 10^{-10} seconds, cooling down as it transfers its energy to both the liquid environment and the solid target. The liquid can reach temperatures around 10^3 K, comparable to the plasma plume temperature, leading to the degradation, ionization, and pyrolysis of solution molecules.[100] At this stage, the spatial gradients of T, P, C_M, and C_S become smoother and rapidly change over time and space as target and solvent species begin to merge. Experimental and theoretical studies have provided only semi-quantitative estimates of these gradients, while a quantitative evaluation is not yet available.[100]

The timescale of nucleation and growth processes remains not completely clear, which is a crucial aspect of laser ablation in liquid (LAL). Different hypotheses have been proposed: some suggest nucleation begins in about 10^{-9} seconds, while others propose longer times, up to 10^{-5} seconds.[100], [113] Studies show that in the early stages of ablation, before a complete mixing between the ablated species and the surrounding liquid occurs, intense condensation of atoms takes place within the confined plasma. This process, known as nucleation, is characterised by the rapid formation of stable atomic aggregates, the nuclei, which act as seeds for the subsequent growth of nanoparticles.[114], [115] Rapid cooling of the plasma, induced by contact with liquid, promotes condensation and the formation of critical-sized nuclei. [114] The high degree of ionisation present in plasma plays a crucial role in nucleation and early growth. Newly formed nuclei, accumulating a negative charge through the acquisition of electrons, become centers of attraction for positive ions in the plasma. [114], [115] This electrostatic interaction is crucial for the initial growth of nanoparticles, favouring the continued adhesion of ions to newly formed nuclei. Thus, nucleation can be considered a phenomenon dominated by the initial conditions of the plasma, in particular by the state of ionization and the density of the species cultured. [114] Mixing with the liquid, while influencing the later stages of growth and aggregation, has a minor impact on nucleation, which occurs mainly in a confined plasma environment.[115]

Optical emission spectroscopy (OES) has confirmed that reactions between target and solvent species can occur within the plasma. However, obtaining quantitative information on the extent of such phenomena has been difficult.

Preferential sites for growth and coalescence of nanoparticles may include liquid drops, solid fragments, and molecular clusters within the ablated material.[100], [116] Nanomaterials produced by LAL are typically polycrystalline, indicating that nuclei coalescence occurs. The nanoparticles usually have a spherical shape, suggesting that nuclei coalescence happens when interface energy is minimized through lattice rearrangement. This can be explained by considering that during the coalescence step, the nuclei are either melted or have a temperature high enough to allow interface atoms to be mobile.[92]

(IV)Expansion and collapse of cavitation bubble (from t = 10^{-6} s to 10^{-4} s) (Figure 2.8).

The cavitation bubble formation is due to the energy release by the plasma plume to the surrounding liquid. The plasma usually lasts until a time of 10^{-8} – 10^{-7} s [100]. The cavitation bubble growth occurs on a timescale of 10^{-7} – 10^{-6} s, and it expands up to times of the order of 10^{-4} s. [100], [117]

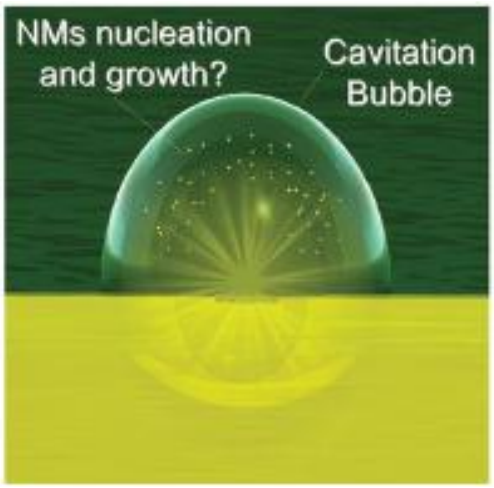

Figure 2.8 Representation of the cavitation bubble expansion and collapse.

The bubble moves through the liquid at supersonic speeds, exceeding 10^3 m/s, and can expand to a maximum radius of about a few millimeters. As the bubble expands, its temperature and pressure decrease, with the internal pressure dropping below that of the surrounding liquid.

Upon the bubble's collapse, a shockwave is emitted, marking the final physical phenomenon in the process of laser ablation of a target in liquid.[100]

(V) Slow growth and agglomeration of NMs (for t > 10^{-4}s) (figure 2.9). There are different hypothesis about nanomaterials formation, one of this is that they form inside the bubble during its expansion, and that process would occurs on a time scale of 10^{-6} – 10^{-4} s. [100] To think that nanomaterials are inside the bubble is a logical suggestion because they create from the originally hot plasma area, and the cavitation bubble forms by the heat release from this area to the surrounding liquid. [100]

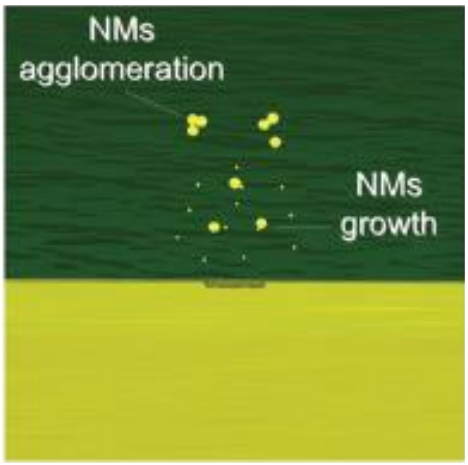

Figure 2.9 Representation of the slow growth and agglomeration of nanomaterials.

Experimental evidence confirms that excited species from the target remain within the cavitation bubble; however, there is no clear proof regarding the spatial distribution of the ablated material. This means it is possible that a significant portion of nanomaterials have been already formed and is located elsewhere in the liquid.[118]

Within the bubble, the concentration of solution species is much lower than in the surrounding liquid, and these species are in a higher energetic state. Additionally, the temperature inside the bubble is higher than that of the surrounding liquid during its expansion. Because the thermal conductivity of gas is lower than that of liquid, nanoparticles formed within the bubble remain hot for a longer time than those in the liquid. [100]

The temperature gradient at the bubble-liquid interface can promote the nucleation and condensation of nanomaterials. [100], [119] After the bubble collapses, a significant amount of energy is released through the emission of a shockwave,[100], [120] and the temperature and

pressure at the collapse point reach levels comparable to those within the plasma (around 10^3 K and 10^{10} Pa, respectively). As a result, already-formed nanomaterials may aggregate, undergo phase transitions, or experience minor alterations due to the condensation of ablated atoms and molecular clusters still present in the solution.[100], [121], [122] Agglomeration begins when the dispersion of nanomaterials becomes unstable, leading to precipitation over a timescale of minutes for particles of micrometer and nanometer size.[100], [123][100], [123] Additionally, material detachment from the target can also occur during this process. [100]

Another proposed mechanism for nanoparticle formation is liquid droplet ejection. [124] In this scenario, the creation of nanoparticles could be due to instability at the interface between the metal melt and liquid vapor. [125] The expanding vapours eject the molten layer, which then solidifies. The possible steps of this mechanism are depicted schematically in Figure 2.10.[125], [126]

Figure 2.10 Sketch of different stages of melt expulsion from the target.

The final step involves the detachment of a molten droplet into vapor, which then remains in the surrounding liquid as a nanoparticle. [125], [126]

2.1.3 Cavitation bubble dynamics

One of the consequences of ablating a target in a liquid environment is the formation of cavitation bubbles. Cavitation is distinct from boiling; in cavitation, the liquid undergoes a phase change to vapor due to a decrease in pressure at a constant temperature below the liquid's vapor pressure. In contrast, boiling involves a phase change from liquid to vapor due to an increase in temperature at constant volume.[124], [127] Generally, cavitation bubbles can form mechanically, as seen in sono cavitation and turbines, or through energy transfer in a localized area, such as with focused laser radiation. [128] Regardless of the method, these bubbles are characterized by the oscillatory behaviour of their walls.

The first significant analysis of cavitation and bubble dynamics was conducted by Lord Rayleigh in 1917, who solved the problem of an empty cavity collapsing in a large liquid mass.[129] Neglecting surface tension, liquid viscosity, and assuming the liquid is incompressible, Rayleigh derived the following expression to describe bubble collapse [129]:

$$R\frac{d^2R}{dt^2}+\frac{3}{2}\left(\frac{dR}{dt}\right)^2=\frac{p(R,t)-p_\infty(t)}{\rho} \quad \text{(I)}$$

with R(t) the bubble radius, p (R, t) the pressure of the liquid on the bubble surface, $p_\infty(t)$ the pressure in the liquid far away from the bubble and ρ the density of the liquid. The energy of the bubble can be expressed as [124], [130]:

$$E_B=\frac{4}{3}\pi(p_\infty-p_V)R_{max}^3 \quad \text{(II)}$$

where p_V is the vapor pressure of the liquid. From this, the collapse time of a cavitation bubble with a maximum radius R_{max} can be calculated [130]:

$$t_C=\sqrt{\frac{3\rho}{2(p_\infty-p_V)}}\int_R^{R_{max}}\sqrt{\frac{y^3}{y^3-R_{max}^3}}dy=0.91468R_{max}\sqrt{\frac{\rho}{p_\infty-p_V}} \quad \text{(III)}$$

A more realistic model that accounts for vapor-filled bubbles has been proposed to describe cavitation dynamics. Plesset studied vapor-filled bubbles in liquids, leading to one of the most widely used expressions for cavitation, known as the Rayleigh-Plesset equation [131], [132]:

$$R\frac{d^2R}{dt^2}+\frac{3}{2}\left(\frac{dR}{dt}\right)^2=\frac{1}{\rho}\left(\left(p_\infty-p_V+\frac{2\sigma}{R_0}\right)\left(\frac{R_0}{R}\right)^{3\gamma}-p_\infty+p_V-\frac{4\eta}{R}\frac{dR}{dt}-\frac{2\sigma}{R}\right)$$

(IV)

where σ and η are the surface tension and the viscosity of the liquid, respectively, and γ is the polytrophic index. This equation assumes that the gas inside the bubble undergoes an adiabatic process.

$$R\frac{d^2R}{dt^2}+\frac{3}{2}\left(\frac{dR}{dt}\right)^2=\frac{1}{\rho}\left(\left(p_\infty-p_V+\frac{2\sigma}{R_0}\right)\left(\frac{R_0}{R}^{3\gamma}\right)\left(1-\frac{3\gamma}{c}\frac{dR}{dt}\right)-p_\infty+p_V-\frac{4\eta}{R}\frac{dR}{dt}-\frac{2\sigma}{R}\right)$$

(V)

As indicated by these equations, cavitation bubble dynamics depend on the liquid's density, viscosity, surface tension, and compressibility. These parameters vary with the liquid's temperature, suggesting that the dynamics of cavitation bubbles are also temperature dependent. Recent studies have confirmed this hypothesis [124], [133]. The temporal evolution of the bubble wall in water at different temperatures shows that the bubble radius and lifetime increase exponentially with temperature. During expansion, collapse, and rebound phases, the temperature and pressure inside the bubble change significantly.

2.1.4 LA of metals in polymeric (Chitosan) solutions

The presence of biocompatible polymers, such as chitosan, in the liquid medium during LAL experiments significantly changes the physical properties of the system,[26], [134] with the consequence of a directly impacting on the formation and dynamics of the cavitation bubble. Chitosan, due to its viscoelastic properties, is presumed to act as a stabilizing agent for the cavitation bubble. The increased viscosity of the liquid medium, induced by the presence of the polymer, [26], [134] probably causes a greater confinement of the plasma plume generated by laser ablation. This confinement results in a prolonged life of the cavitation bubble, characterized by a more spherical and stable shape. The longer bubble life promotes more efficient energy transfer to the target tissue, optimizing the ablation process.

The presence of chitosan also significantly affects the thermal profile of the laser-material interaction. The higher viscosity of the medium slows down the heat diffusion from the ablation region, creating a more pronounced thermal gradient. [26], [134] This condition can promote a more controlled and precise ablation.

In addition to increasing viscosity, chitosan can change the surface tension and density of the medium, [26], [134] probably affecting bubble formation and collapse. Nanoparticles generated during ablation can interact with the polymer chains of chitosan, forming complexes that modify the optical and thermal properties of the medium. These interactions can influence the diffusion of nanoparticles and their interaction with the laser beam.
Under the intense action of the laser beam, chitosan can undergo degradation and ionization processes. The nature of the chemical species generated during these processes can influence the dynamics of the cavitation bubble and the characteristics of the encased material. For example, the formation of free radicals can promote cross-linking reactions between polymer chains by changing the mechanical properties of the material being treated.

In conclusion, chitosan emerges as a powerful modulator of the dynamics of the cavitation bubble during laser ablation in liquid environment.

2.2 Alternative sources of chitosan

Most of the chitosan produced and used comes from the fish industry, but the ever-increasing focus on sustainability and the circular economy is pushing towards other sources, especially for the production of insect-derived chitosan. Unlike crustaceans, insect farming has a low environmental impact; it can be done in confined spaces and with low water and feed consumption. Feed may be partly formed from organic waste, of the agro-food industry, leading to an additional advantage of the transformation of waste into resources, in a perspective of circular economy. The insects have additional advantages, they grow incredibly fast and possess less protein and fat than crustaceans, which allows to obtain a purer product with a simplified extraction process. Various studies have focused on the extraction of chitin from different species of insects including , Domestic Cricket (*Acheta domesticus*)[135], Flour Warbler (*Tenebrio molitor*)[136], Oriental Cockroach (*Blatta orientalis*)[137], Black Soldier Fly (*Hemetia illucens*)[138], the Migratory locust (*Locusta migratoria*)[139], and the bee (A*pis mellifera*)[140]; the species mentioned have shown to represent a good source of chitin, in our study the species used as source of chitin subsequently converted into chitosan is *Hermetia illucens.*

2.2.1 The insect *Hermetia illucens*

Hermetia illucens, commonly known as the black soldier fly (BSF), is a member of the family Stratiomyidae that has gained increasing attention for its sustainable applications in various industrial sectors. This insect is primarily known for its ability to bioconvert organic waste into high-value biomass, making it a crucial element in waste management, feed production, biofuels and even cosmetics. *Hermetia illucens* life cycle includes four main stages: egg, larva, pupa and adult. Eggs, laid in organic substrates, hatch within a few days. Once hatched, the larvae grow rapidly and feed on a variety of organic materials including food waste, manure and compost. Larvae can increase their weight by more than 200 times during this period of 14-18 days. At the end of the larval begins the pupal phase lasting about 14 days, during which the larva turns into an adult; adults live for about 5-8 days and do not feed, since they use the energy reserves accumulated during the larval phase. [141], [142] During the larval phase, this insect is able to consume a wide range of organic waste, including food waste, manure and agricultural residues, converting them into biomass with high protein and lipid content. This makes it an ideal tool for bioreading and bio-waste recovery. The process of bioconversion carried out by the larvae is not only environmentally sustainable, but also economically advantageous, as it reduces the amount of waste going to landfill and produces valuable products *H. illucens* larvae are known to accumulate proteins and lipids that can be used as feed ingredients or for biodiesel production. The biomass produced by the larvae is particularly popular in the feed industry, where it is used as a sustainable substitute for fishmeal. [141], [142]

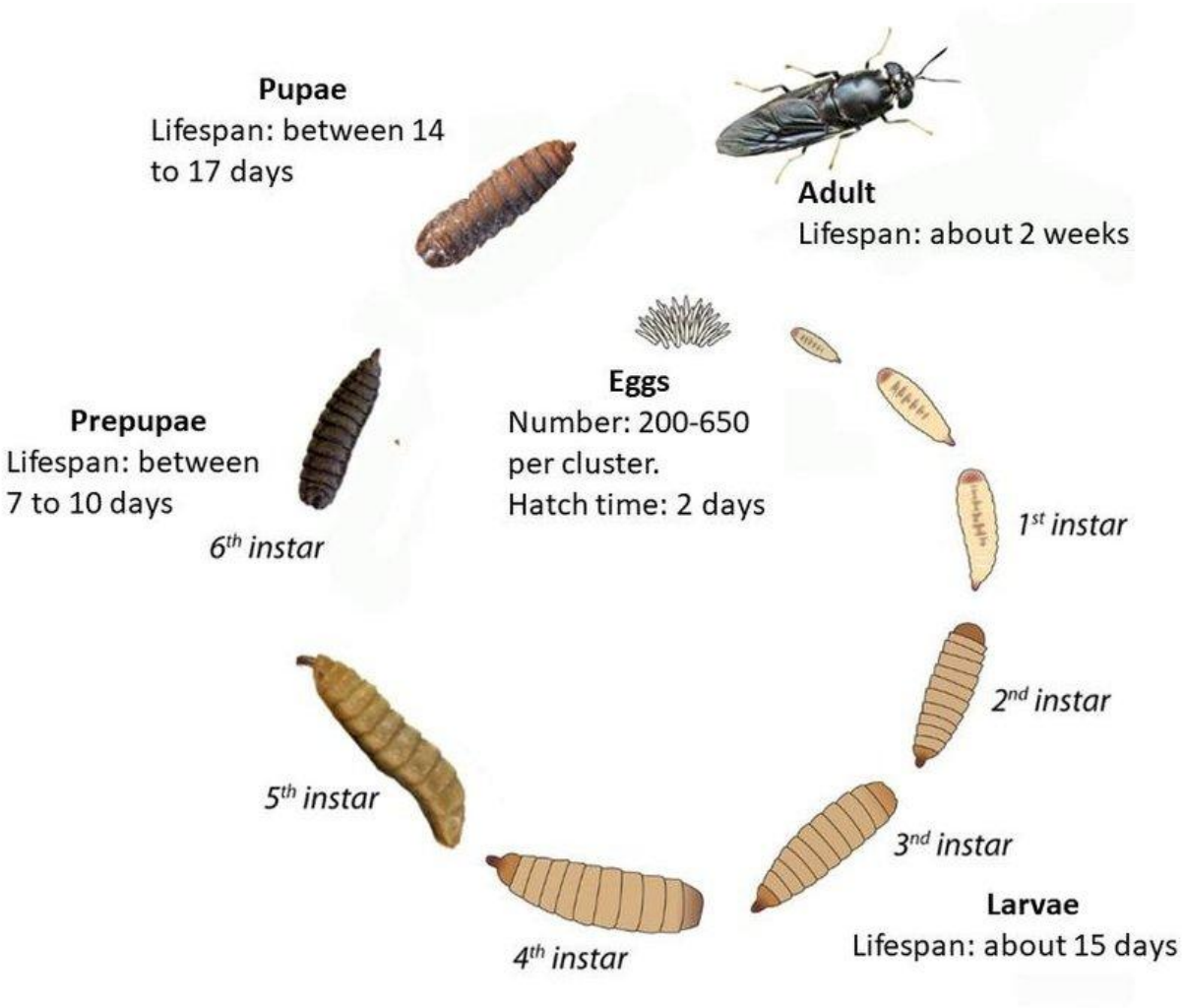

Figure 2.11 Life cycle illustration of *Hermetia illucens*

Hermetia illucens is particularly interesting for its sustainable applications, especially in waste management and biomass production. As already mentioned, the larvae of *H. illucens* are efficient in consuming organic waste, converting it into high protein and lipid biomass. This capacity is being used to reduce organic waste and produce feed for animals, particularly aquaculture and poultry. Larval biomass is a sustainable alternative to fish meal, often used in animal feed, reducing the pressure on fisheries.[143] The second field of application is that of biofuel production, due to their high lipid content, *H. illucens* larvae can be used for biodiesel production. The lipids extracted from larval biomass can be converted to methyl esters through the transesterification process, producing biodiesel that can be used as an alternative fuel.[144] Finally, residues not used in the applications listed above can be further recovered to produce Chitin and Chitosan; chitin, extracted from pupate exuviae and larval exoskeletons, can be converted into chitosan through a deacetylation process. Chitosan is a biopolymer with numerous applications in the food, pharmaceutical, cosmetic and agricultural sectors. [145] The

production of chitosan from *H. illucens* is a viable alternative to traditional production from crustaceans, offering a biocompatible and biodegradable product.

2.2.2 Chitin extraction and chitosan production from *Hermetia illucens*

The process of extracting chitin from *Hermetia illucens* is a topic of growing interest, given the sustainable and innovative applications of this insect-derived biopolymer. The following describes a detailed process which is divided into several key steps: demineralization, deproteinization, and deacetylation.

The first step in the process of chitin extraction is to collect larvae, pupal exuviae or the remains of dead adults of *Hermetia illucens*. The collected material is cleaned to remove any contaminants and then dried if necessary for easy storage and handling.

The next step consists of demineralization, it is the first chemical step, necessary to remove minerals, mainly calcium carbonate, present in the cuticle of insects. This is achieved by treatment with acids, such as dilute hydrochloric acid. The choice of acid concentration and reaction time depends on the quantity and type of minerals to be removed, as well as on the morphology of the starting material.

Once demineralization is complete, the material undergoes deproteinization, an alkaline treatment to remove any remaining proteins. This step involves the use of strong alkaline solutions, such as sodium hydroxide (NaOH), which degrade and solubilize proteins, separating them from chitin. Deproteinization is a crucial step, as the purity of the final chitosan depends on how effectively the proteins are removed.[146]

In some protocols, a further bleaching step is provided. This step serves to improve the aesthetic appearance of the final product by reducing the residual coloration that could result from pigments or other organic compounds present in the cuticle of insects. Bleaching can be performed using oxidizing agents such as hydrogen peroxide.

Finally, there is deacetylation, (Figure 2.12) this is the key step which transforms chitin, a hard polymer insoluble in water, into chitosan, which is soluble and has a wide range of applications.

This process is carried out by treating chitin with concentrated sodium hydroxide at high temperatures (usually between 90°C and 100°C) for a prolonged period. Alkaline treatment removes acetyl groups from chitin, increasing the solubility of the polymer and giving it the unique properties of chitosan, such as bioactivity and film forming ability. [147]

After deacetylation, the raw product is thoroughly washed with distilled water to remove any alkaline residues and impurities. The chitosan is then dried, usually at room temperature or under vacuum, to obtain a stable and preservable final product.

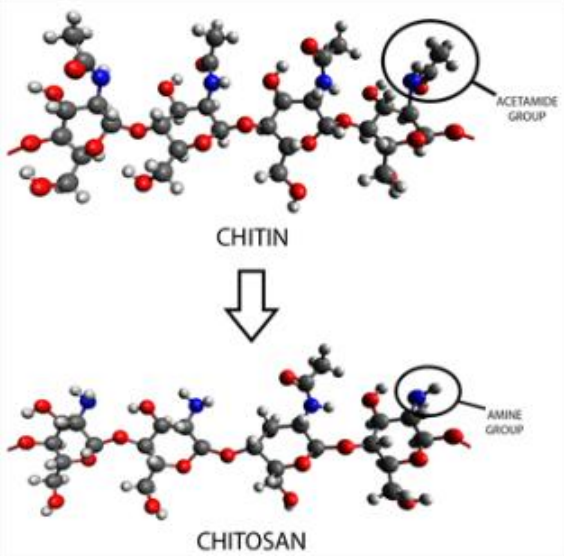

Figure 2.12 Graphical representation of the deacetylation process converting chitin to chitosan.

2.2.3 Degree of deacetylation

The most relevant parameter that affect some properties of chitosan, such as solubility, antimicrobial activity and biocompatibility is the degree of acetylation (DA). DA is defined as the proportion of glucosamine residues in the chitosan chain and affects the solubility of the polymer in dilute acid solutions. A higher DA, close to 80-85%, is essential for ensuring good solubility of chitosan, while a lower DA reduces this property, making chitosan less soluble and thus limiting its applications. The DA of chitosan also influences its biological properties, such as antimicrobial and anti-inflammatory activity.[148] For example, the ability of chitosan to inhibit pro-inflammatory cytokine production and to stimulate anti-inflammatory cytokines such as IL-10 is correlated with the molecular structure of chitosan, which is in turn influenced by DA.[29] Its antibacterial properties are also strongly influenced by DA. Chitosan with higher deacetylation degrees tend to have a higher density of free amino groups (NH_2), which when protonated at acidic pH become positively charged (NH^{3+}). These positively charged groups interact with the bacterial cell membranes, which are negatively charged, altering their permeability and causing intracellular material to escape, leading to the death of the

bacterium.[149] Finally, DA also affects the crystallinity and crystal size of chitosan. These parameters are crucial for determining the mechanical properties of the material, such as strength and flexibility, which are essential for applications in fields such as fabric engineering and biodegradable films.[150]

2.2.4 Experimental

2.2.4.1 Extraction of Chitin from Hermetia illucens and Chitosan production

Given the potential ecological potential of Hermetia illucens, in this work considered the chitosan obtained from this source was as a possible alternative to the commercial one. The samples of chitosan were provided by the team of Prof. Falabella, who deals with the breeding and production before chitin and finally the conversion of this into chitosan. From the Hermetia illucens it is possible to extract chitin from three different sources, from larvae, from eggshells, called esuvias and finally from adults at the end of their life cycle. As described in the previous paragraphs, the extraction of chitin consists of three main phases: demineralization, deproteinization and bleaching. The extraction protocol of all H. illucens samples was performed according to Hahn et al.[151]

To remove the minerals, mainly calcium carbonate, the insect samples were suspended in formic acid 0.5 M (solid ratio 1:10) and agitated at 350 rpm for 1 hour at room temperature. The demineralised material was then filtered through a mesh cloth (pore size 40-60 μm) and washed with deionised water until the filtrate reached a neutral pH. The washed demineralised samples were then dried overnight in an oven at 60 °C.

Proteins were removed from demineralised samples by treatment with sodium hydroxide (NaOH) 2 M (solid ratio 1:10) for 2 hours at 80 °C. The NaOH solution was initially placed in a flask on an agitated heating plate and heated to 80 °C. Once the temperature had been reached, the demineralised material was added to the flask and stirred at 350 rpm throughout the reaction. The temperature was checked with a thermometer. The deproteinization solution was then removed by filtering the suspension through a mesh cloth (pore size 40-60 μm) and the solid material was washed with deionized water until the filtrate reached a neutral pH. The washed deproteinized samples were dried in an oven at 60 °C overnight. After deproteinization, unbleached chitin was obtained.

Part of the purified unbleached chitin has been bleached. Hydrogen peroxide (H_2O_2) solution at 5% v/v was used (solid ratio 1:20 for larvae and pupal exuviae, 1:30 for adults), H_2O_2 solution was heated to 90 °C in a flask on a heating plate with stirring and then unbleached chitin was

added, stirred for 1 hour at 350 rpm. The temperature was checked with a thermometer. The bleached samples were filtered using filter paper (pore size 7-12 µm) and washed with deionised water until the filtrate reached a neutral pH. The washed samples were finally dried overnight in an oven at 60 °C. After this treatment, the bleached chitin was obtained.

The resulting chitosan was subjected to a series of analyses to determine its quality and properties. Fourier transform infrared spectroscopy (FTIR) was used to confirm the chemical structure of the polymer and its degree of deacetylation, whereas X-ray diffractometry (XRD) was used to analyze its crystallinity.

2.2.4.2 Crystallinity index by XRD analysis.

Analysis by X-ray diffraction (XRD) has been used to evaluate the crystallinity of chitosan. in particular, the crystallinity index (CrI) was used, calculated according to the Segal method.[152] CrI represents the ratio between the intensity of the most intense crystal peak (Ic) and the intensity of the amorphous region (Ia) of the diffractogram.

$$CrI\ (\%) = \frac{Ic - Ia}{Ic} \times 100$$

In addition, the size of crystallites was determined by applying the Scherrer equation.[153] This equation correlates the width at mid-height of a diffraction peak with the size of crystalline particles:

$$D\ (nm) = k\lambda/\beta cos\theta$$

where D is the size of the crystallites (nm), k is the form factor which depends on the nature of the crystallites and is 0.9, λ is the wavelength, β is the width at half height expressed in radians of the peak analysed, while θ is the corresponding diffraction angle. XRD analysis was conducted using an X'Pert PRO (Philips) diffractometer with Cu Kα radiation. The operating conditions were: 40 kV voltage, 32 mA current, scan interval from 2θ 5° to 60° and scan speed 0.04° s^{-1}.

2.2.4.3 Calculation of DD by FT-IR spectroscopy

FTIR spectroscopy is a valid methodology to calculate the degree of deacetylation of chitosan. Unlike the more complex and expensive 1H-NMR, the FT-IR technique has the advantage that it does not require a long and demanding sample preparation and does not need to dissolve the biopolymer in any solvent. [154] In addition, IR spectroscopy has the advantage of being high sensitivity technique.

Different chitosan dry and powdered samples (obtained from larvae, exuviae and adult) and commercial samples (chitosan LM, Chitosan HM and chitin) were considered. The powders were mixed with KBr (potassium bromide) and the mixture was pressed to obtain tablets with a diameter of 1 cm. The IR transmission spectra of chitin and chitosan samples were recorded using a Jasco 460Plus IR spectrometer. Samples were scanned with a resolution of 4 cm^{-1} and 64 accumulations and absorbance values were evaluated in the wavelength range 4000 - 400 cm^{-1}. The resulting spectra were processed using JASCO Spectra Manager software.

Several studies related to the calculation of the degree of residual acetylation of chitosan by IR spectroscopy have been carried out in recent years, which have led to the formulation of several equations, considered equally valid, for the DDA calculation. The equations are given in Figure 2.13 A and below in Figure 2.13 B are given the various baselines to be considered for the acquisition of the value of absorbance to be used in the equation. [154]

A

1 $$DA\ [\%]=\frac{A_{1655}}{A_{3450}} \times 100/1{,}33$$

2 $$DA\ [\%] = \frac{A_{1655}}{A_{2870}} \times 100/1{,}33$$

3 $$DA\ [\%] = \frac{A_{1655}}{A_{3450}} \times 115$$

4 $$DA\ [\%] = (\frac{A_{1320}}{A_{1420}} - 0{,}03822)/0{,}03133$$

B

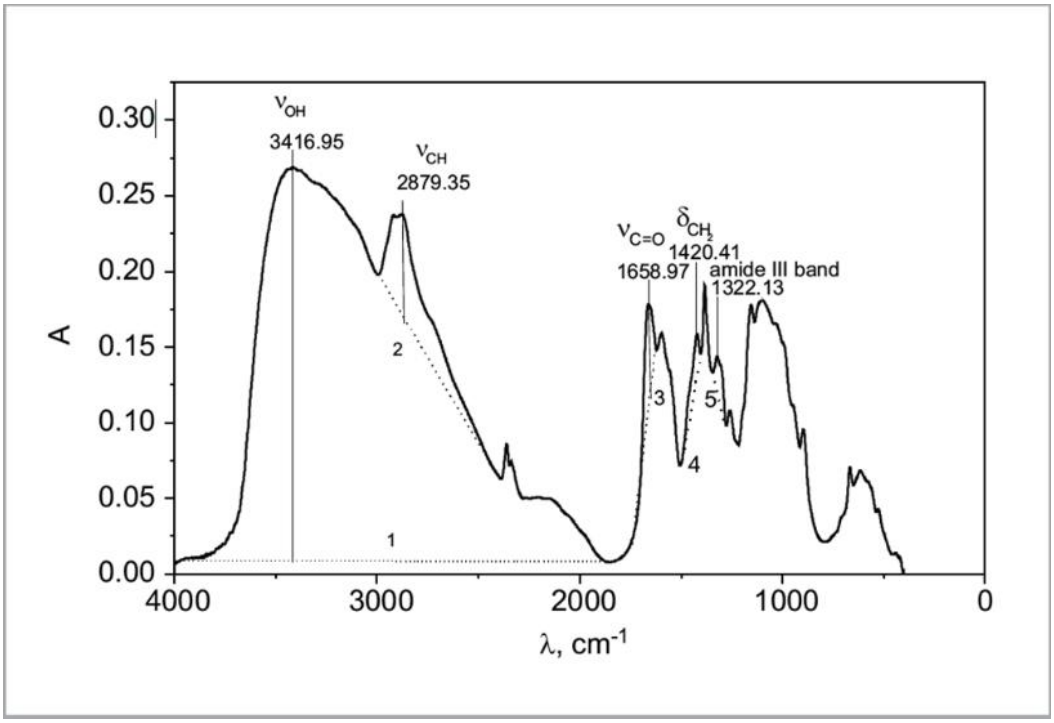

Figure 2.13 A) Equations for calculating the degree of acetylation; B) Graphical schema of the baseline to be used to identify the values to be used in the equations. [154]

2.2.5 Results and discussion

2.2.5.1 XRD analysis and crystallinity index

In Figure 2.14 are shown the XRD spectra of the samples of chitosan obtained from Hermetia illucens, both in the pre-bleaching stage and in the bleached. The image shows the presence of significant peaks around 10 and 20 degrees, which confirm the identity of the polymer. [138]

From the comparison between the respective bleached and non-bleached, the spectra show no significant differences except for the samples of chitosan larvae which has the peak at about 10° more intense after the bleaching.

A

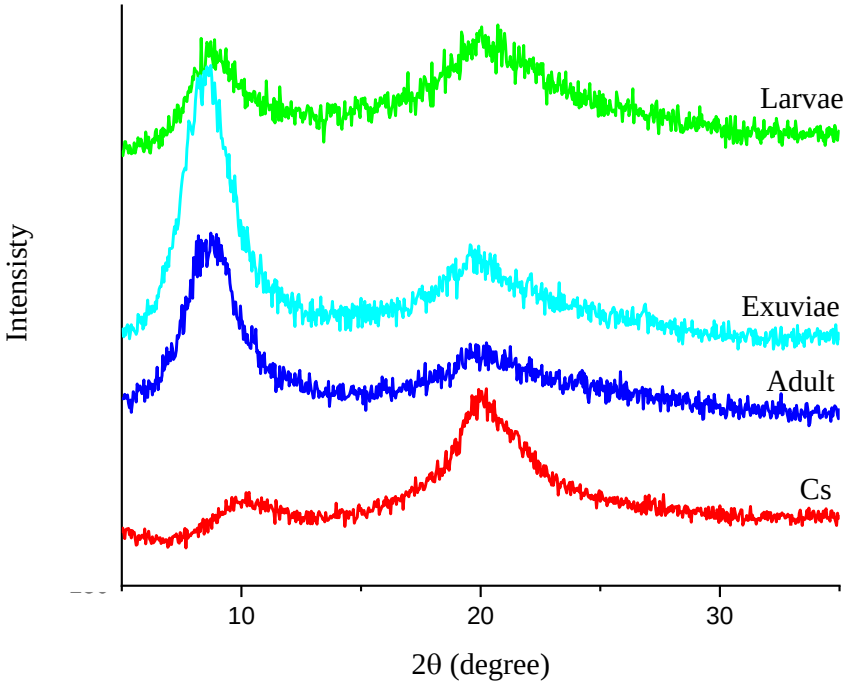
Intensisty
Larvae
Exuviae
Adult
Cs
10
20
30
2θ (degree)

B

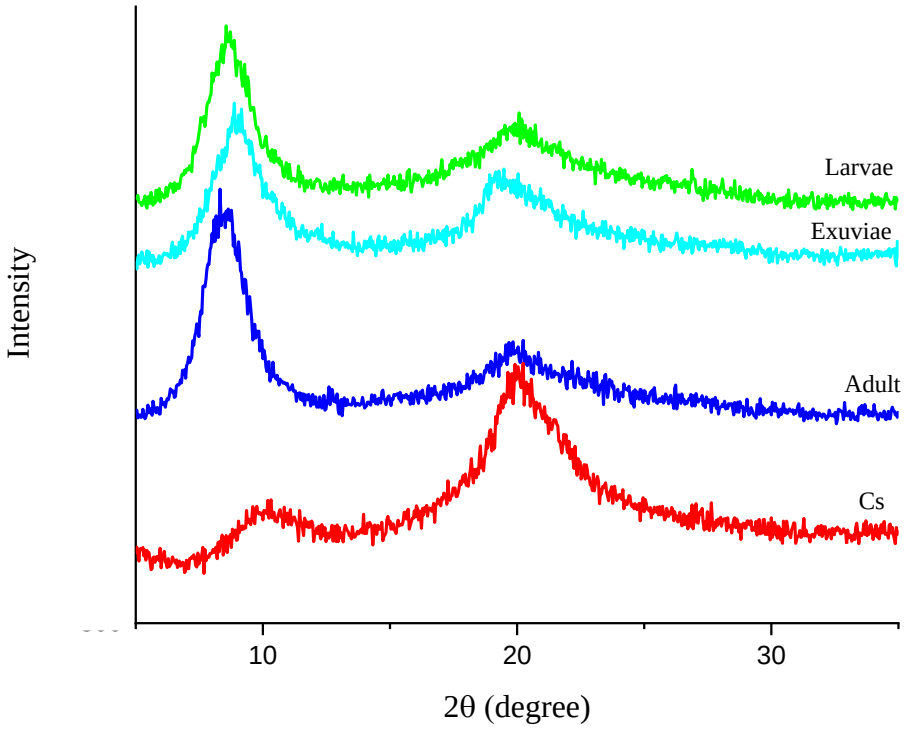
Intensity
Larvae
Exuviae
Adult
Cs
10
20
30
2θ (degree)

Figure 2.14 Spectra from XRD analysis A) chitosan samples produced by unbleached larvae, exuviae and adults of Hermetia illucens, B) chitosan samples produced by bleached larvae, exuviae and adults of Hermetia illucens compared to commercial chitosan.

From the diffractograms it was possible to determine the CrI value and the size of the crystallites from the chitosan samples, data presented in Table 2.1. While all CrI values and crystallite size were statistically similar, there were some minor differences between the samples. Both chitosans derived from larvae showed the lowest CrI values, although these were still comparable to those of the other samples, including the commercial chitosan. Analyzing the size of the crystallites, it is evident that all samples have similar values with the exception of pupal exuviae unbleached chitosan which has larger crystallites and comparable to commercial chitosan.

Table 2.1 Crystallinity index and crystalline size(nn-D_{100}) resulted from XRD analysis

Chitosan sample	CrI (%)	Crystallite size (nm)
Larvae unbleached	74±3.7	3±1
Larvae bleached	77±3.8	3±1
Pupal exuviae unbleached	78±3.9	4±1
Pupal exuviae bleached	80±4.1	3±1
Adults unbleached	79±4.0	3±1
Adults bleached	86±4.3	3±1
Commercial	79±4.0	4±1

2.2.5.2 FTIR analysis and evaluation of DA

From the FTIR spectra of the samples, shown in Figure 2.15, the absorbance values for the various peaks of the individual samples were calculated; the values were used to calculate the degree of acetylation using all the equations given.

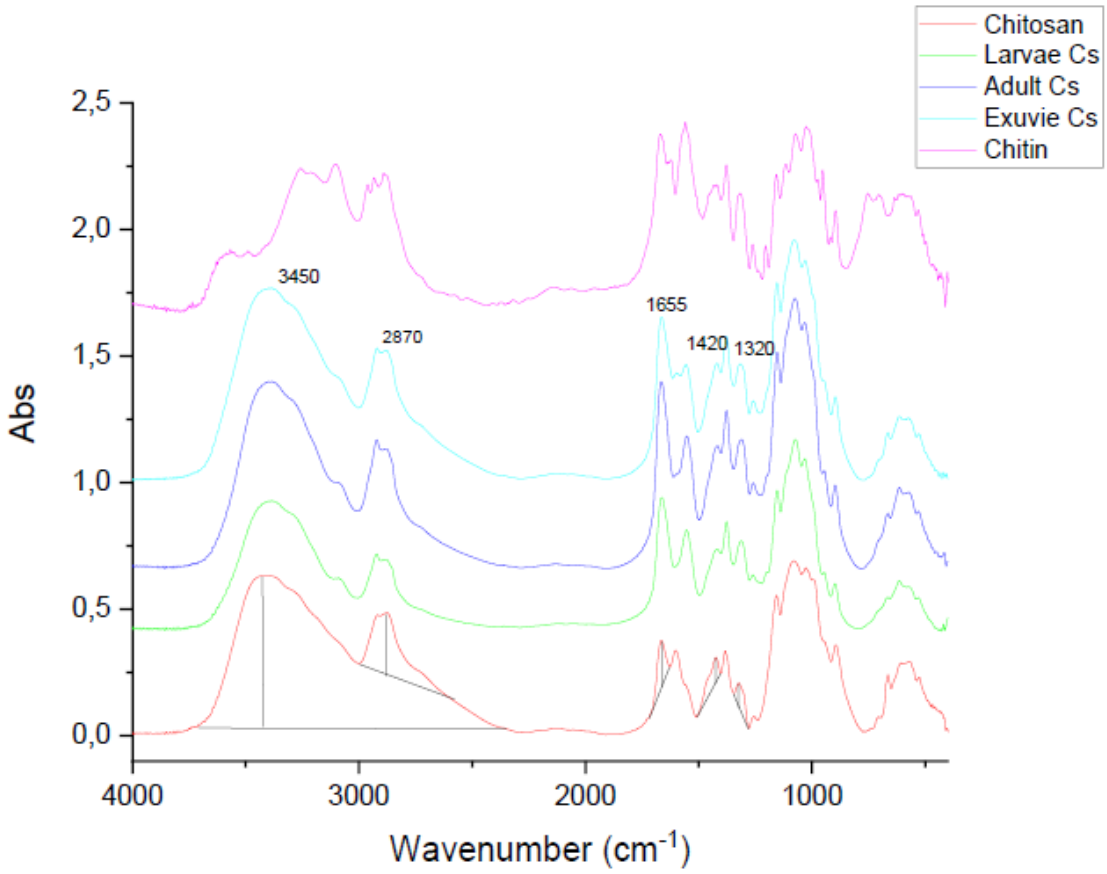

Figure 2.15 Spectra resulting from FTIR analysis of bleached chitosan samples produced from H. illucens comparing to commercial chitin and chitosan.

The IR spectra of two types of commercial chitosan (high molecular weight and low molecular weight) and commercial chitin (Figure 2.16), whose acetylation grades are released by the manufacturer, which were used as a control, to assess the quality of the method.

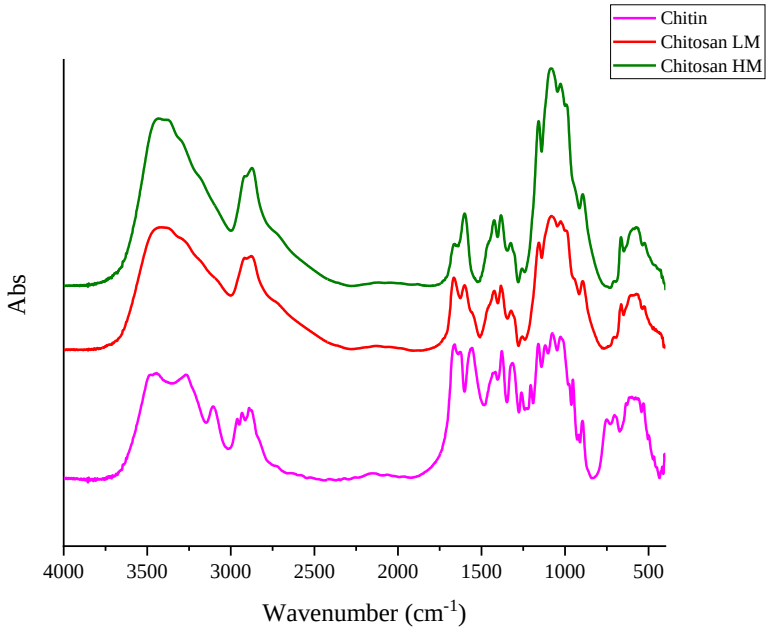

Figure 2.16 Spectra resulting from FTIR analysis of commercial chitosan high molecular weight (green), low molecular weight (red) and commercial chitin (purple)

The analysis of the control samples, data given in the table 2.2, shows that the equation whose result leads to the truest value is equation n 4; the values obtained for acetylation equal to 98%, 10% and 29% respectively for chitin, Chitosan HM and Chitosan LM are absolutely comparable with the reported, 99%, 10% and 30% respectively. The other equations lead to a result that overestimates or underestimates the actual degree of acetylation.

Table 2.2 degree of acetylation commercial samples

	1	**2**	**3**	**4**	**Reported**
Chitin	92%	87%	90%	98%	99%
Chitosan HM	4%	23%	6%	10%	10%
Chitosan LM	33%	50%	31%	29%	30%

For samples of chitosan extracted the values are given in table 2.3, considering the above mentioned, the values of degree of acetylation considered are those obtained by equation 4. Chitosan obtained from larvae and adults have a degree of acetylation of 50% while those extracted from exuviae with a residual degree of acetylation of 36% are the most similar to commercial. The degree of acetylation is indeed a fundamental characteristic of chitosan,

influencing its biological properties and applications. A lower degree of acetylation generally increases the solubility and biological activity of chitosan.

Table 2.3 degree of acetylation Hermetia illucens samples

	1	**2**	**3**	**4**
Larvae CS	53%	63%	77%	52%
Adult CS	48%	74%	76%	50%
Exuvie CS	38%	50%	37%	36%

The results of the analyses showed that chitosan produced from the biomass of pupal exuviae has structural and compositional characteristics highly comparable to those of commercial chitosan. In particular, samples of chitosan derived from exuviae showed a degree of crystallinity and crystallite size extremely similar to those of the commercial product. In addition, the degree of deacetylation of chitosan obtained from exuviae was found to be significantly higher than the other samples analysed and comparable with that of commercial chitosan. Based on this experimental evidence, chitosan produced from pupal exuviae is has been selected as reference material for subsequent experimental applications.

2.3 Conclusion

In conclusion, laser ablation in liquid and the use of insect-derived chitosan represent two innovative and sustainable strategies in green chemistry and biotechnology. Liquid laser ablation is an environmentally friendly technique, allowing the synthesis of nanomaterials without the use of toxic chemical reagents, reducing the environmental impact associated with conventional production processes. This approach not only minimises waste generation, but also promotes precise control of the size and morphology of nanoparticles, expanding their potential in biomedical, environmental and industrial applications. At the same time, the use of insect-derived chitosan offers a viable sustainable alternative to its extraction from marine sources, which has limitations related to the supply and conservation of marine ecosystems. Insects are an abundant and renewable source of chitosan, reducing pressure on ocean resources

and contributing to a more sustainable management of organic waste through insect farming. This approach aligns with the principles of the circular economy, promoting resource efficiency and reducing negative impacts on the environment.

Chapter 3 Chitosan/metal nanoparticles: synthesis and properties

3.1 Chitosan-based composite materials

Composite materials that combine chitosan and metal nanoparticles (NPs) represent a class of advanced materials of increasing interest for their applications in various fields, including biomedicine, environmental purification and catalysis.[155] Among the innovative synthesis methods used to obtain metal nanoparticles, Laser Ablation in Liquid (LAL) represents an innovative and sustainable technique for the synthesis of metal nanoparticles and is proposed as alternative to chemical synthesis that involves the use of toxic reagents, frequently. [156] When nanoparticles are generated in a solution containing a polymer, such as chitosan, the polymer can play a crucial role as a natural stabilizer, preventing the aggregation of the nanoparticles;[156] in particular, using chitosan, its cationic structure interacts electrostatically with negatively charged metal nanoparticles, coating them and preventing aggregation, effectively.[157] This interaction not only stabilises nanoparticles, but also gives them additional properties such as biocompatibility and biodegradability, making them particularly suitable for biomedical and environmental applications.[157] The literature shows that several metals and non-metals nanoparticles, including gold, silver, copper, zinc and selenium, have been synthesized, by laser ablation in chitosan solutions.[158]–[164] The resulting chitosan-stabilized nanoparticles offer a wide range of applications. Copper and selenium nanoparticles obtained in the chitosan matrix have been shown to be effective in treating drug-resistant bacterial and fungal infections. These nanoparticles can be used in the sterilisation of medical devices and in the protection of surfaces exposed to contamination.[162], [163] At the same time, copper nanoparticles, which inhibit microbial growth, are being used in food storage, helping to extend the shelf life of products.[158] Composite materials obtained from gold ablation in chitosan are useful in advanced diagnostic applications, such as the detection of tumour biomarkers and the localised treatment of cancer cells, thanks to the stability and biocompatibility conferred by the presence of chitosan.[159] Finally, zinc-chitosan and copper-chitosan composites have proved to be suitable catalysts in water purification processes and industrial chemical reactions, where particle size reduction and chitosan-induced stability improve the performances of the materials. [158], [162], [164]

The ability of forming film of chitosan has strongly attracted attention of both food industry and medical industry.[155],[165] In the food industry, the performances of these films has been analysed and demonstrated an extension of the shelf life of foods and the ability to preserve food quality by preventing bacterial or fungal contamination.[166], [167] Chitosan films designed for food packaging are synthesized by methods such as solvent melting,

electrospinning and layer-by-layer assembly.[168] They often require the addition of a plasticizer, such as glycerine, to improve their mechanical properties.[166] Many studies have been interested in the production and evaluation of the efficacy of chitosan films with metallic nanoparticles, such as silver, gold and copper, whose integration improves antimicrobial properties and also mechanical properties.[169]–[171] These films have been shown to be more effective than chitosan films in prolonging the life of food by inhibiting bacterial growth.

In the medical field, chitosan films are used for wound dressings, drug delivery and coatings of medical devices due to their antimicrobial, biocompatible and biodegradable properties. Chitosan based dressings facilitate the removal of exudates, promote skin regeneration and haemostasis and prevent infections by inhibiting bacterial growth. [172], [173] The moderate antibacterial activity can be improved by adding various active additives such as metal nanoparticles, metal oxides, graphene, fullerenes and derivatives, including plant extracts.[165] For example, the introduction of silver nanoparticles significantly improves antimicrobial activity and accelerates wound healing, creating a moist environment and reducing inflammation.[174], [175] These films protect against microbes such as *Staphylococcus aureus, Pseudomonas aeruginosa* and *Escherichia coli*. [176]Chitosan films with silver nanoparticles also show a slight anti-adhesive activity against *S. aureus*, useful for coating medical implants reducing bacterial contamination.[174]

This chapter describes, in the first part, the initial optimization of the process of liquid ablation of silver in commercial chitosan solution, the identification of optimal ablation parameters and the preparation of silver and copper nanoparticles in commercial chitosan and insect-derived chitosan solutions; their physico-chemical characterization and the evaluation of their biological activities. In the second part, similar experiments and characterizations were carried out on the prepared composite materials in the form of self-standing films.

3.2 Experimental

3.2.1 Nanoparticles synthesis in chitosan solution

Chitosan solutions at different concentrations were prepared by dissolving 0.1 g, 0.5 g and 1 g respectively of commercial chitosan (average molecular weight: 100,000-300,000 Da, deacetylation degree: 75%, purchased from Acros Organics) in 1 L of 0.1% aqueous acetic acid solution (v/v, Sigma-Aldrich). The suspensions were subjected to magnetic shaking at 40 °C for 4 hours in order to facilitate the complete dissolution of the polymer. In parallel, a solution of chitosan extracted from exuviae (CsE) was prepared by dissolving 1 g of CsE (35,000 Da,

deacetylation degree: 74%) [138] in 1 L of 0.1% (v/v) acetic acid aqueous solution. The system was subjected to magnetic stirring at 40 °C for 8 hours to ensure complete solubilisation of the polymer. At the end of the process, the solutions were filtered to remove any insoluble impurities. For laser ablation in liquid experiments, a nanosecond Nd:YAG laser source (λ: 532 nm; τ: 7 ns; repetition frequency 10 Hz, Power : 150 mW) was used. The laser beam was focused perpendicularly on a metal, silver or copper target, immersed in 50 ml of chitosan solution, contained in a 5 cm x 5 cm cuvette, continuously stirred, each ablation lasting 45 minutes. The concentration of the metal nanoparticles generated was determined indirectly by measuring the mass loss of the target before and after ablation.

Table 3.1 List of origin solution and related pH.

Solution	pH
Cs 1g/L	4.05
CsE 1g/L	4.04
Hac 0.1%	4.01

3.2.1.1 Physico-chemical characterization

The optical properties of the colloidal solutions were investigated by Uv-Vis spectroscopy. Spectra were acquired using a UV-Vis spectrophotometer (model Spercord 50/PLUS Analytic Jena) in the wavelength range from 200 to 800 nm with a spectral resolution of 0,2 nm.

The morphology, size distribution and crystalline domains of nanoparticles were determined using transmission electron microscopy (TEM) by using a G2 20 FEI Tecnai instrument, operating at 200kV. The colloidal solutions were dropped on carbon-coated copper grids (Agar Scientific) left to dry at room temperature.

The XRD diffractograms were obtained using SIEMENS D5000 X-ray diffractometer, using Cu-Kα radiation, operating at 40 kV and 32 mA. Diffraction patterns were acquired in the 2θ range of 5°-60°, with a step size of 0.040° and a time per step 4 s.

The FTIR spectroscopic analysis was carried out on a Jasco J-460 spectrophotometer. Absorption spectra were acquired in the spectral range between 4000 and 400 cm^{-1}, for each sample, three spectra were acquired and averaged. The solid samples (commercial chitosan and

chitosan extract from exuviae) were previously finely pulverized. Subsequently, a known quantity of each powder was carefully mixed with KBr, the resulting mixture was pressed to obtain a transparent tablet which was used directly for FTIR analysis. For the prepared colloidal solutions, an amount of the colloidal solutions was deposited on a Si (100) monocrystalline silicon wafer (Goodfellow). After evaporation of the solvent, the sample was analysed directly by FTIR. An uncoated silicon wafer was used as a reference.

XPS spectra are acquired with a Phoibos 100-MCD5 SPECS spectrometer, in medium area mode, with a spot of about 2 mm diameter, using an input and output slot of 7x20 mm and 20x39mm respectively. The samples to be analysed were deposited on monocrystalline silicon (Si (100) Goodfellow) wafer.

3.2.1.2 Biological test

Antibacterial activity

Bacterial colonies of *E. coli* and *M. flavus* were each inoculated into 10 ml of sterile Luria Bertani (LB) culture medium. The medium was prepared with 1% tryptone, 0.5% yeast extract, and 0.5% sodium chloride (all from Sigma-Aldrich, St. Louis, Missouri, USA). The cultures were then incubated in a water bath shaker at 37 °C and 150 rpm for 18 hours.

Agar Diffusion Test

The antimicrobial activity of various chitosan samples was evaluated using the agar diffusion test *E. coli* and *M. flavus* bacteria were evenly distributed on sterile Petri dishes containing 25 ml of solidified LB-Agar medium (LB with 1.5% bacteriological agar from Sigma-Aldrich, St. Louis, Missouri, USA) using a cotton swab. Subsequently, 5µl of each colloidal solution was applied onto the LB agar plates and incubated at 37 °C for 24 hours. For each plate, acetic acid and commercial chitosan solution at the same concentrations served as positive controls, while distilled water was used as a negative control. The antimicrobial activity was assessed by measuring the diameter of the inhibition zones (mm). Results were reported as mean and the relative standard deviations from three independent biological replicates.

Minimum Inhibitory Concentration (MIC) by Microdilution Assay

Serial dilutions of all chitosan samples were prepared in 96-well plates at the following concentrations: 1, 0,5, 0,25, 0,125, 0,06, 0,03, 0,0015, 0,006 and 0,003 g/L. Acetic acid solutions were also tested at equivalent concentrations (0,1, 0,05, 0,025, 0,0125,0,006, 0,003, 0,0015 0,0006 and 0,0003%, respectively), and each bacterial culture (*E. coli* and *M. flavus*) served as a negative control. The bacterial cultures were used at a concentration of 10^6 CFUs/ml for both species. The 96-well plates were incubated at 37 °C for 24 hours, and bacterial concentrations were measured as absorbance at 600 nm using a Multiskan Go

spectrophotometer (Thermo Scientific, Waltham, MA, USA). The minimum inhibitory concentration (MIC) was defined as the lowest concentration of chitosan at which no bacterial growth was observed.

3.2.2 Films

The chitosan and nanoparticles/chitosan films were prepared by drop-casting method.[177] The solutions were all cast on disposable weighing boats (3,5x3,5cm) and left to dry at room temperature. After drying, the films were neutralized by immersion in 0.05 M NaOH solution, then rinsed in distilled water until completely neutrality and left to dry.

Table 3.2 List of films produced, with name and origin solution.

Solution	**Film**
Cs	Cs
CsE	CsE
Cs-AgNPs	AgNPs-Cs
CsE-AgNPs	AgNPs-CsE
Cs-CuNPs	CuNPs-Cs
CsE-CuNPs	CuNPs-CsE

3.2.2.1 Physico-chemical characterization

A scanning electron microscopy (SEM) (Carl Zeiss Auriga with EDS, X-MaxN Oxford Instruments) was used to study the surface morphology. Before the observation the samples were coated with gold layer (around 15nm) by QUORUM model Q150T, to prevent sample charging during images acquisition.

The wetting behaviour of films was evaluated by contact angle measurement using the KRÜSS DSA30 drop shape analyser. Five drops of distilled water with a volume of 3 µl were dropped on the centre of each sample to avoid any effects from the edges. Then a mean value and the standard deviation of the contact angle were calculated.

To evaluate swelling index the films were immersed in distilled water at room temperature until they reached equilibrium. The weight of the wet samples (Ws) was measured after removing the surface water with absorbent paper. The bulge index (SI) was then calculated based on the weight of wet (Ws) and dry films (Wd) using the following equation.

$$SI = \left(\frac{Ws - Wd}{Wd}\right) x\ 100$$

3.2.2.2 Biological tests

Biological tests have been carried out at Institute of Biomaterials, Department of Materials Science and Engineering, University of Erlangen-Nuremberg, Heated Prof. Dr.-Ing. habil. Aldo R. Boccaccini.

Film Agar Diffusion test

The antimicrobial activity of the composite material in film form was assessed by means of an agar diffusion test. *Escherichia coli* and *Micrococcus flavus* were inoculated separately in 25 ml of LB culture medium (Sigma-Aldrich, St. Louis, Missouri, USA) enriched with agar (1.5% w/v) and homogenized. Then about 12 ml of inoculated soil were poured into sterile Petri dishes and allowed to solidify. The films to be tested were then placed on the surface of the agar and covered with the remaining inoculated soil. The plates were incubated at 37 °C for 24 hours. Antimicrobial activity was quantified by measuring the diameter of bacterial inhibition zones around films.

Viability: WST-8 test

NIH-3T3 cells, mouse embryonic fibroblasts, were cultured in dulbecco's modified eagle medium (Gibco) supplemented with 10% (v/v) heat inactivated FBS, 200mM L-glutamine, 100 units/mL penicillin and 100 µg/mL of streptomycin, at 37°C in a humidified atmosphere of 5% CO_2. The growth media was changed every 2 days. The cells were washed with PBS and isolated from the culture flask through trypsinization (0.25% trypsin-EDTA), suspended in fresh culture media, and used to access the bone cell viability on bare.

Prior to these assays, the samples were sterilized with UV 1h per side and wash with sterile PBS. In order to assess the cytotoxicity of the samples, the cells were seeded at a density of $1x10^4$ cells/well, and incubated for 24, 48 and 72h, at 37°C in a humidified atmosphere of 5% CO_2. Negative controls were assigned to cells cultured in the well without any sample. Each film has been tested in triplicate. At the end of the incubation time, the culture medium was removed and washed with phosphate buffer solution (PBS), then 300 µl of WST-8 reagent (1% reagent solution WST-8 (Sigma-Aldrich) and 99% complete fresh medium) have been added to each well and the cells have been incubated for ~2 hours at 37 ºC and 5% CO2. During the incubation WST-8 (water -soluble tertrazolium salt) is reduced to an orange-coloured formazan by mitochondria. After incubation, 100 µl of the solution was transferred from each well to a

96-well plate. The absorbance was measured at 450 nm using an Omega FLUO star microplate reader (BMG Labtech) Uv-Vis spectrometer.

Antimicrobial test

The antimicrobial activity of coatings against the gram-positive bacteria *S. aureus* and gram-negative *E. coli* was evaluated. A suspension of *S. aureus* and *E. coli* bacteria was inoculated into a sterile Lysogeny broth (LB) medium overnight. The optical density was then adjusted to 0.015. Aliquots of the bacterial suspensions were added to the samples, that were previously sterilized by UV, immersed in sterile LB. Growth control wells contained only bacteria in LB media. After a 24-hour incubation at 37 ºC, these extracts were completely homogenised and rates from 100 µl to 96 wells (n = 3) were added. The optical density measurements were performed on a microplate reader (PHOmo, anthos Mikrosysteme GmbH, Germany) at 600 nm.

Statistical analysis

All experiments were performed in triplicates and results of agar diffusion and microdilution assays were expressed as mean ± standard deviation. Data of the MIC determination was analyzed with Two-way ANOVA, With Bonferroni *post-hoc* test. All statistical analyses were performed using GraphPad Prism version 6.01 for Windows (GraphPad Software, La Jolla, California USA - www.graphpad.com).

3.3 Results and discussion

3.3.1 Laser ablation of silver in chitosan solution

A comparative analysis was conducted to optimize the laser ablation process of silver in aqueous solutions of chitosan at varying concentrations. Four solutions were prepared: a 0.1% v/v acetic acid, and three chitosan solution at different concentration: 0.1 g/L, 0.5 g/L and 1 g/L. The solutions obtained by the ablation of silver were characterized to quantify the concentration of AgNPs generated. (Table 3.3)

Table 3.3 solutions AgNPs concentrations.

Name sample	[Cs]	[Ag]
Cs-AgNPs	1g/l Cs	8.9±0.3 µg/ml
Cs5-AgNPs	0,5g/l Cs	8.5±0.9 µg/ml
Cs1-AgNPs	0,1g/l Cs	10.7±0.5 µg/ml
Hac-AgNPs	0,1% Hac	10.1±1 µg/ml

As expected, the ablation in the solution at higher chitosan concentration results a lower nanoparticles yield. This phenomenon can be attributed to a synergy of factors. Firstly, the increased viscosity of the solution resulting from the increase in polymer concentration could hinder the expulsion of newly formed nanoparticles from the laser interaction zone, by facilitating their reaggregation or adhesion to the target surface. Secondly, the attenuation of the laser beam within more concentrated solutions results in a reduction of the incident radiant energy on the target surface, thus compromising the efficiency of the ablation process and the formation and dispersion of nanoparticles.

The graph in Figure 3.1 shows the UV-Vis absorbance spectra of the samples prepared. In all spectra is observed a peak around 400 nm corresponding to the surface plasmon of silver nanoparticles. [178] Intensity of this peak varies according to the sample. In general, there is a decrease in peak intensity as the chitosan concentration increases, indicating a decrease in the amount of AgNPs present in the sample, consistent with the trend of the concentration. In addition, a slight peak shift towards longer wavelengths is observed for the Cs5-AgNPs and Cs-AgNPs samples. This shift could be due to variations in the size of nanoparticles or interactions between nanoparticles and the chitosan matrix.[179]–[181]

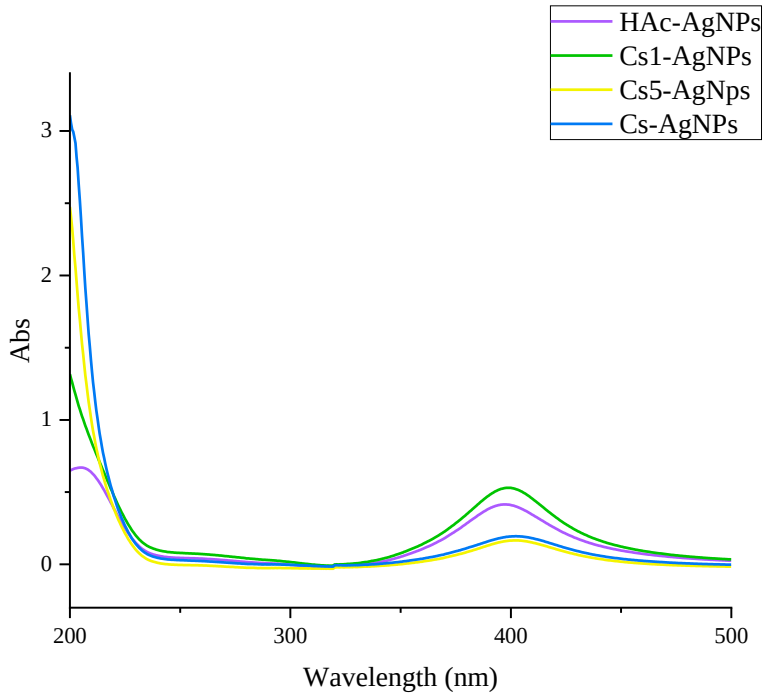

Figure 3.1 UV-Visible spectra of Hac-AgNPs (purple), Cs1-AgNPs (green), Cs5-AgNPs (yellow) and Cs-AgNPs (blue)

UV-Vis spectroscopy has also been used to evaluate the temporal stability of dispersed AgNPs in synthesized solutions. The results, shown in Figure 3.2, show a clear dependence of colloidal stability of AgNPs on polymer concentration. After 12 weeks from the synthesis, (Figure 3.3) it is observed that AgNPs dispersed in a solution of Cs1g/L maintain their characteristic absorption peak, indicating good colloidal stability over time, although slightly less effective, the same can be seen in the Cs5-AgNPs sample. In contrast, for Cs1-AgNPs and Hac-AgNPs there is a progressive decrease of the peak absorption intensity over time, specifically the decrease of the peak absorbance is 59%, 58%, 53% and 19% for Hac-AgNPs, Cs1-AgNPs, Cs5-AgNPs and Cs-AgNPs, respectively. (Figure 3.3)

These results suggest that a higher concentration of chitosan promotes the long-term stability of colloidal dispersions of AgNPs. The presence of the polymer causing a higher density of the colloidal solution, seems to provide a more protective environment for nanoparticles, preventing their aggregation and sedimentation. [159], [160] Conversely, at low concentrations of Cs, the interactions between nanoparticles could prevail over nanoparticle-polymer interactions, favouring the formation of aggregates and a consequent decrease in the intensity of the spectral signal.

A

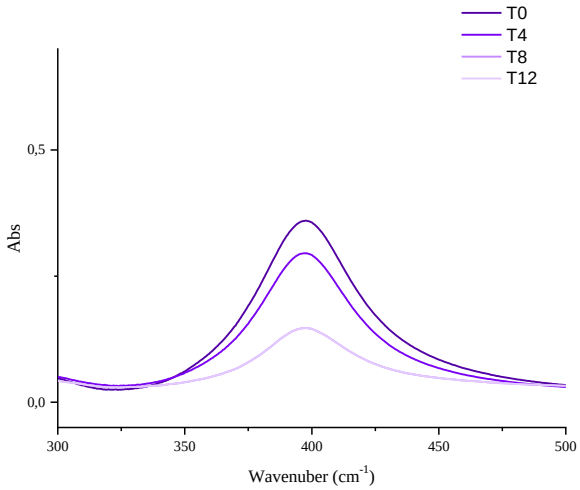

B

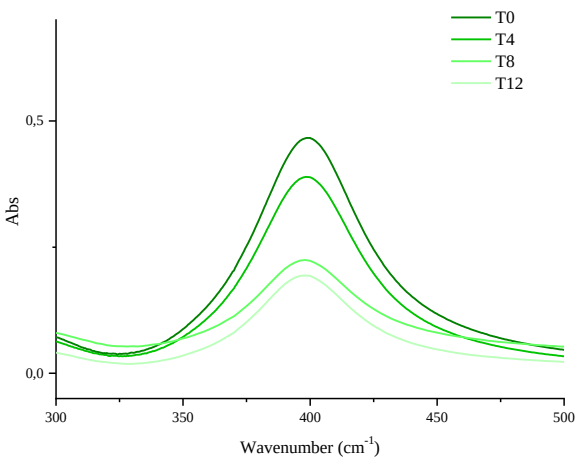

C

D

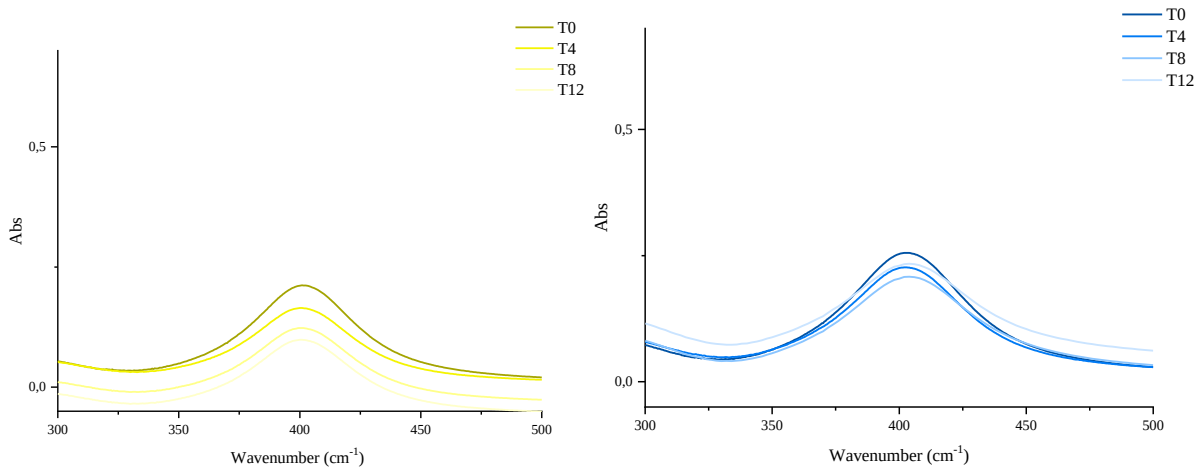

Figure 3.2 A) Hac-AgNPs B) Cs1-AgNPs C) Cs5-AgNPs D) Cs-AgNPs UV-visible spectra at different acquisition times (weeks)

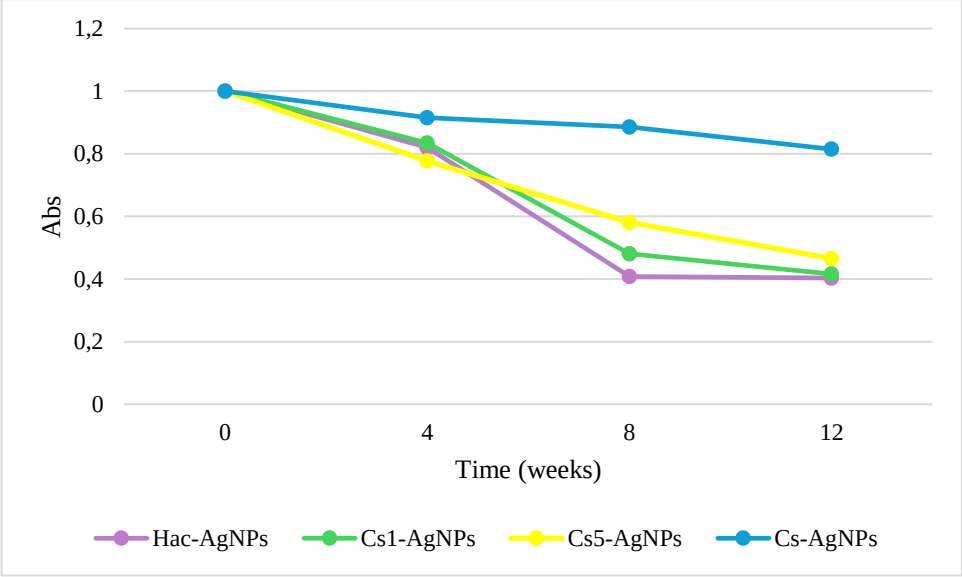

Figure 3.3 Graph that records the normalized maximum absorption of metal-polymer solutions, at around 400nm, at several times.

The analysis of TEM micrographs confirmed the formation of substantially spherical AgNPs. The presence of chitosan during the synthesis process has a significant influence on the size of the nanoparticles obtained. In particular, an increase of the average AgNPs diameter from 11.53 nm in Hac-AgNPs to 14.92 nm and 18.46 nm, respectively for Cs1-AgNPs and Cs-AgNPs was

observed. This dimensional heterogeneity could be attributed to coalescence phenomena induced by the laser ablation processes employed during synthesis, such as melting, which favour the formation of larger aggregates.[182] In addiction these results suggest that chitosan can influence the nucleation and growth mechanisms of nanoparticles even if the presence of a polymer shell on the metal nanoparticles cannot be excluded.

A

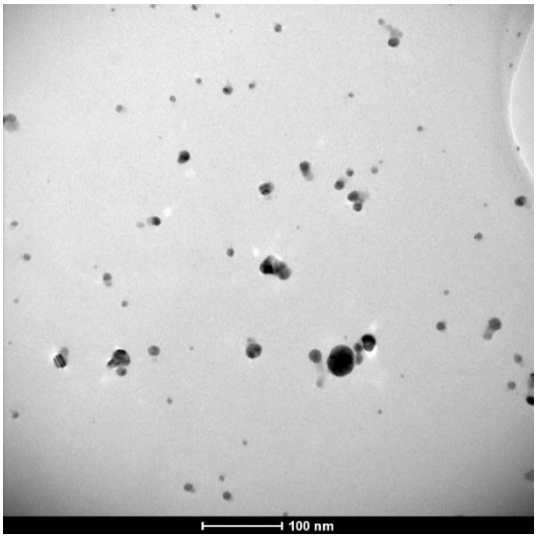

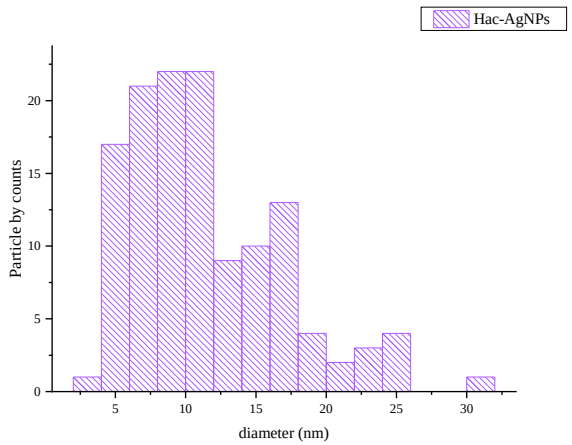

B

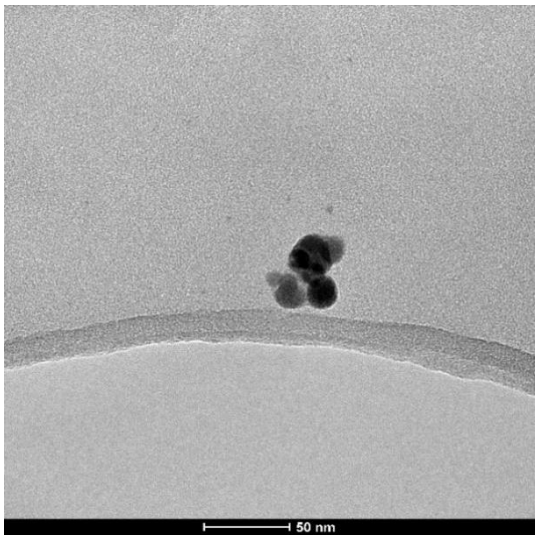

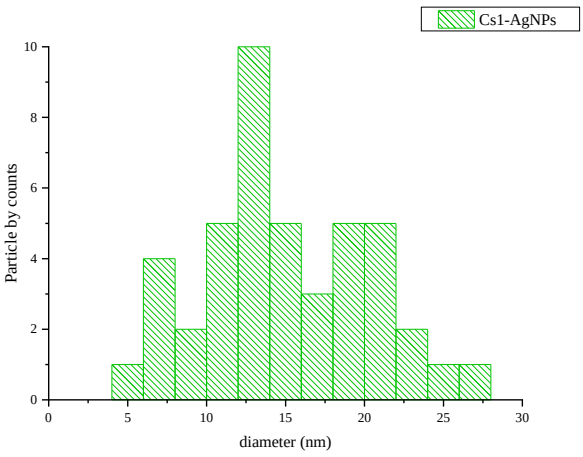

C

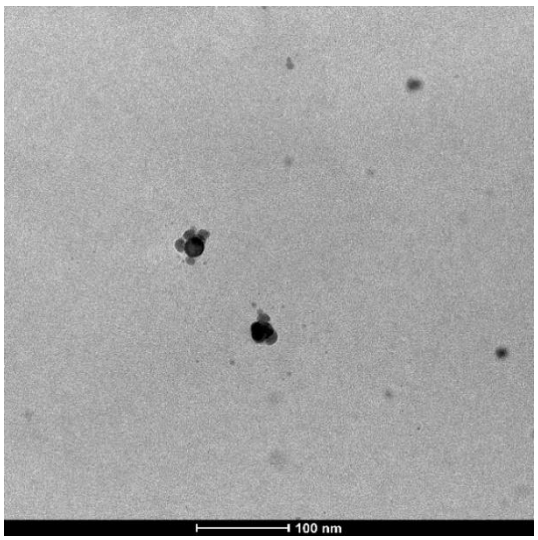

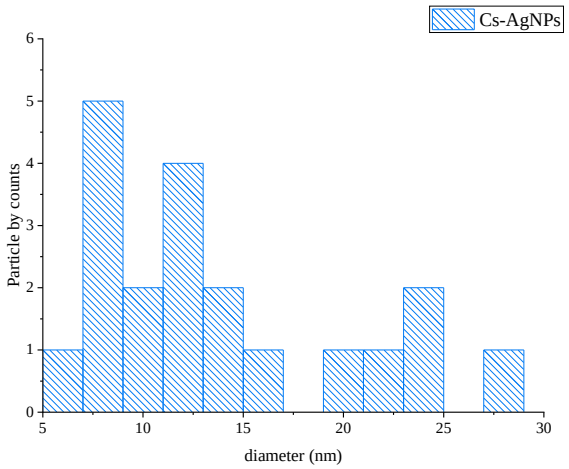

Figure 3.4 TEM images and distribution: A) Hac-AgNPs, B) Cs1-AgNPs, C) Cs-AgNPs

By analysing the high-resolution images, it was also possible to identify the presence of crystalline domains. The reticular distance, estimated by the fast Fourier transform (FFT), is 0.25 nm. This value can be attributed to the planes (111) of metallic silver in the cubic face-centred structure (fcc).[183] (Figure 3.5)

A B

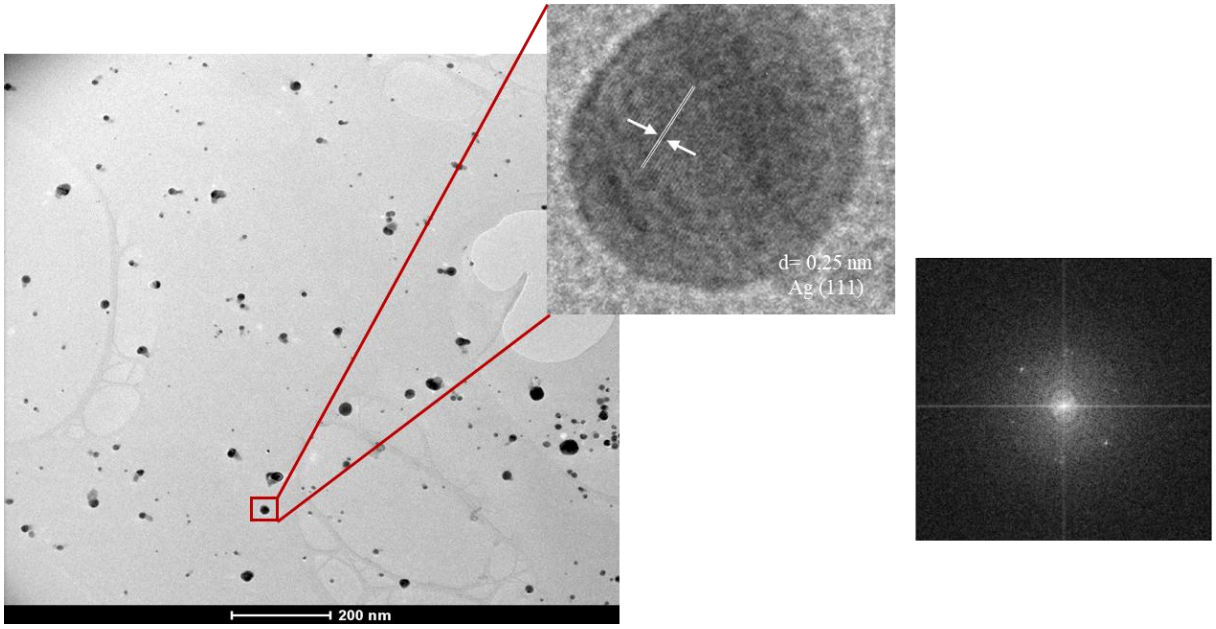

Figure 3.5 A) magnification of a silver nanoparticle showing the presence of crystalline domains, B) image FFT operated in the area of the planes visible on the nanoparticle.

Table 3.4 presents a comparative analysis of the synthesized colloidal solutions, showing data on particle size, process yield and rate of decrease in maximum absorbance, measured at about 400 nm, over time. These data allow the influence of chitosan on the process of laser ablation in liquid of a silver target to be highlighted. Maintaining constant the laser beam power and ablation time, the solutions demonstrate an increase in the average size of nanoparticles in relation to the increase in chitosan concentration. The average size of nanoparticles increases from about 11 nm in the absence of the polymer to about 18 nm at the highest concentration of the polymer tested. In addition, the yield of the process, expressed in terms of silver concentration present in the system, is significantly related to the chitosan concentration. The yield is higher in solutions where the polymer is absent or present in low concentrations. A further important distinction concerns the stability of colloidal solutions. Monitoring of maximum absorbance at about 400 nm over time revealed that the solution containing the highest concentration of chitosan shows a low decrease in absorbance, around 19%, indicating good stability of the system after 12 weeks. In contrast, the other systems show a decrease of about 50%, suggesting lower stability.

Table 3.4 List of colloidal solutions with their component concentrations, mean diameter of the nanoparticles and percentage of maximum absorbance decrease to 400nm, for stability evaluation.

Name sample	[Cs]	[Ag]	Diameter	Decrease max-Abs(400nm)
Cs-AgNPs	1g/l Cs	8.9±0.3 μg/ml	18.46 nm	19%
Cs5-AgNPs	0,5g/l Cs	8.5±0.9 μg/ml	/	53%
Cs1-AgNPs	0,1g/l Cs	10.7±0.5 μg/ml	14.92 nm	58%
Hac-AgNPs	0,1% Hac	10.1±1 μg/ml	11.53 nm	59%

The XRD spectrum shown in Figure 3.6 provides a comparative analysis between a sample of Cs and the composite material Cs-AgNPs. The Cs spectrum shows a wide and diffuse diffraction band centred around 20° 2θ. This characteristic is typical of semi-crystalline polymers such as chitosan and indicates a low degree of crystallinity. The predominant amorphous nature is attributable to the presence of intra and intermolecular hydrogen bonds which hinder a regular arrangement of polymer chains, [184]. From the analysis of the Cs-AgNPs spectrum it is observed that besides presenting the characteristic band of chitosan, it shows a clear and well-defined diffraction peak at about 38° 2θ. This peak can be attributed to the crystalline planes (111) of metallic silver. [185] The presence of this peak clearly indicates the incorporation of silver nanoparticles into the polymer matrix of chitosan. The comparative analysis of the XRD spectra of the Cs samples and the Cs-AgNPs composite reveals that the angular position of the characteristic diffraction peak of chitosan, centred at about 20° 2θ, remains substantially unchanged in the introduction of silver nanoparticles. However, a slight peak enlargement in the composite is observed compared to the pure sample. This enlargement suggests that interactions are taking place between the polymer chains of chitosan and silver nanoparticles, which could induce slight disturbances in the crystal structure of the polymer. In particular, the increase of the FWHM of the peak is indicative of a decrease in crystallite size or an increase in crystal disorder, resulting in an increase in the amorphous component in the composite material.[186]

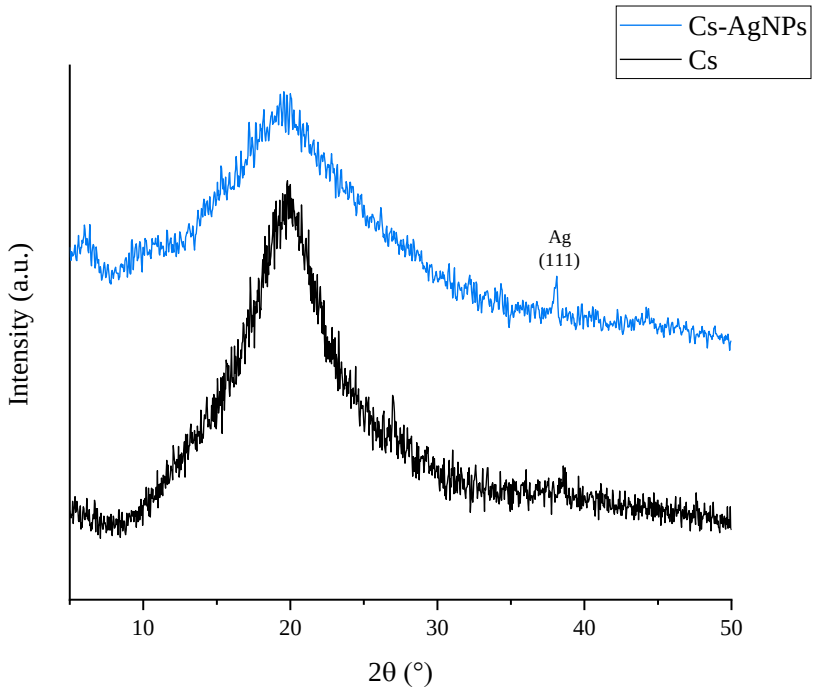

Figure 3.6 XRD Cs spectra (black) and composite Cs-AgNPs (blue), comparison.

Figure 3.7 reports the FTIR for two samples analysed, Cs and Cs-AgNPs. The CS spectrum shows the typical bands of glucosamine-based polymers, that is the broad and intense band around 3400 cm^{-1} is assigned to the stretching vibrations of the OH and NH groups involved in intra- and intermolecular hydrogen bonds; the bands in the 1650-1550 cm^{-1} are associated with the stretching vibrations of the C=O bond of the amide group and the deformations of the NH bond; bands at lower frequencies are related to the vibrations of the carbon skeleton and other functional groups present in the chitosan molecule. The Cs-AgNPs spectrum presents a spectrum with the same characteristic bands as CS, but a significant difference, one can observe a decrease in intensity of the band around 1670 cm^{-1} and a corresponding increase in intensity 1560 cm^{-1}, which could be attributed to the interaction between the amide groups of chitosan and silver ions. [187] From the comparison of the two spectra, it can be assumed that the synthesis process by laser ablation in liquid does not change the structure of chitosan, whose characteristic bands are perfectly visible in the composite spectrum, Furthermore, the observed differences between the two spectra suggest that silver nanoparticles and the chitosan matrix interact, probably involving the functional groups of the polymer.

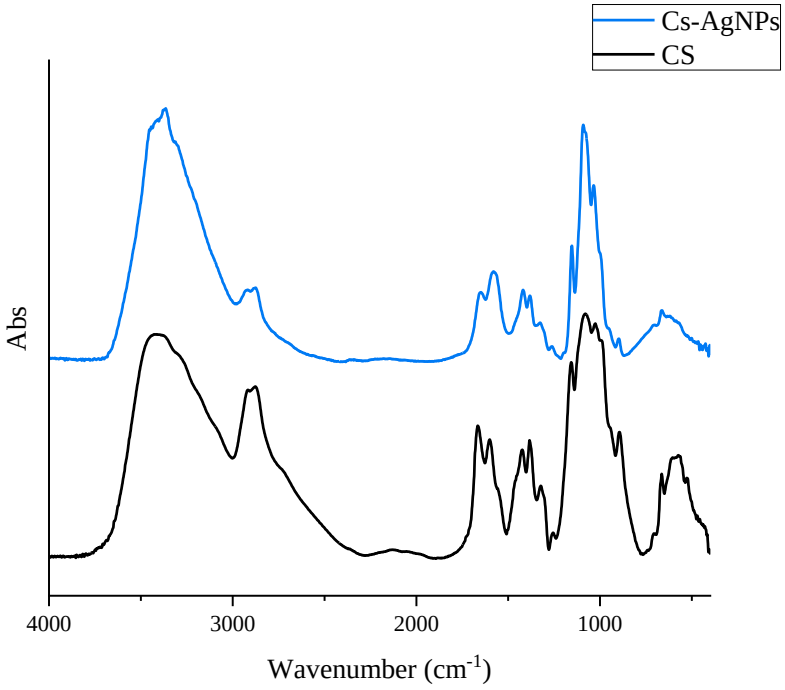

Figure 3.7 Chitosan (black) and Cs-AgNPs (blue) FTIR spectra, comparison.

The chemical composition of the composite material obtained from laser ablation was analysed by XPS analysis, a technique which provides information on chemical species and their abundance, compared with that obtained by analysing chitosan.

XPS analysis of Cs-AgNPs and Cs revealed characteristic peaks associated with nitrogen, oxygen and carbon elements. The N1s peak reveals the presence of two components at 399.4 eV and 400.3 eV assigned respectively to the NH_2 and -NH-CO- bond, groups present in chitosan. The deconvoluted analysis of the C1 peaks revealed three main components at 285.0 eV, 286.4 eV and 288.0 eV, is attributable respectively to the C-C, C-N and C=O bonds present in the composite. Similarly, the O1s peaks were deconvoluted into two components at 531.7 eV and 533.0 eV. The shift towards higher bond energies of the O1s peaks indicates a decrease in electron density on the oxygen atom, suggesting the formation of covalent bonds between oxygen and other atoms.

A

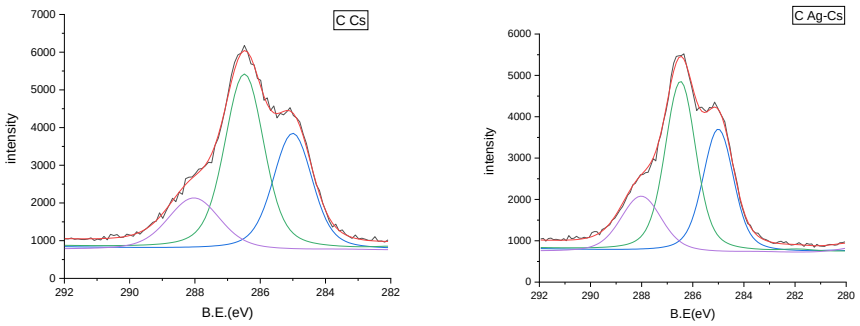

B

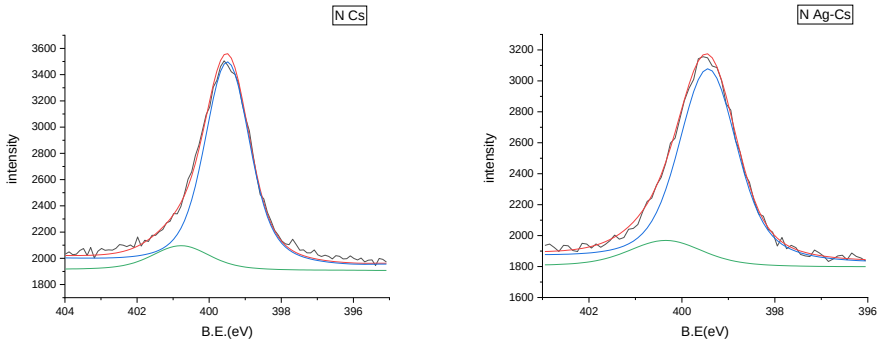

C

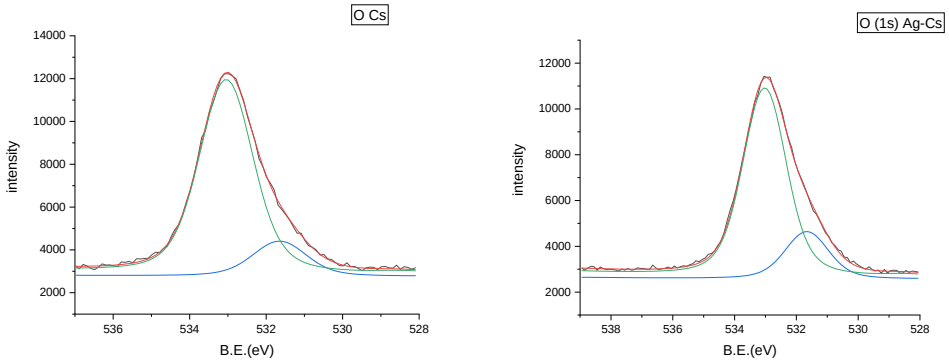

Figure 3.8 XPS spectra A) C1s region spectra; B) N1s region spectra; C) O1s region spectra Cs and Cs-AgNPs, comparison.

From this analysis, the C/N and C/O ratios of chitosan present in the post-ablation colloidal solution were calculated which were found to be quite comparable to those of chitosan in pre-ablation (Table 3.5), the slight increase in the C/O ratio and the slight decrease in the C/N ratio could be due to a partial modification of chitosan, loss of hydroxyl groups (-OH) or amines (-

NH_2) due to oxidation or hydrolysis processes could lead to an increase in the C/O ratio and a decrease in the C/N ratio.[188]

Table 3.5 C/N and C/O ratio for Cs-AgNPs and Cs.

	Cs-AgNPs	**Cs**
C/N	4.88	5.41
C/O	1.94	1.35

It is important to point out that no silver signal could be observed from the XPS analysis, confirming that the metal nanoparticles are completely embedded in the polymer matrix in the composite material.

After evaluating the properties of the synthesized composite materials, the Cs-AgNPs sample emerged as the most promising formulation. Given the excellent stability and good concentration yield, the same synthetic protocol was chosen to obtain a new composite, replacing conventional chitosan with a polymer derived from an alternative biomass. This choice was motivated by the intention to explore the potential of chitosan in Hermetia Illucens and to evaluate the impact of the different origin of the biopolymer on the final properties of the composite material.

The UV-Visible spectrum of the CsE-AgNPs composite, of Figure 3.9, shows an absorption band centred at about 400 nm, typical of the localized surface plasmonic resonance (LSPR) of AgNPs. This spectral characteristic confirms the presence and dispersion of AgNPs within the composite matrix.

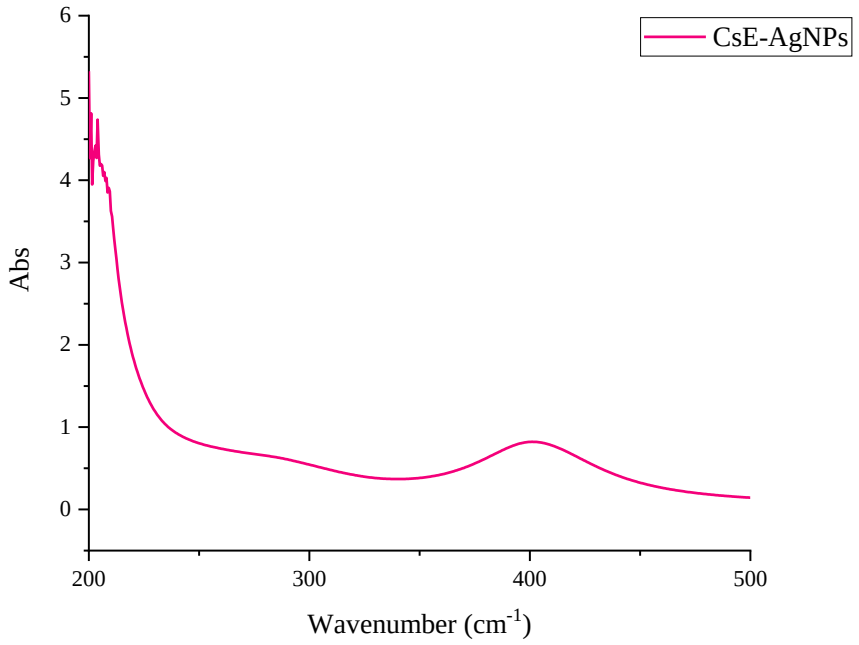

Figure 3.9 UV spectrum of CsE-AgNPs.

CsE has been shown to be an effective stabilizer for AgNPs, allowing time-stable colloidal systems. The analysis of UV-Vis spectra (Figure 3.10) showed a slight decrease in absorbance over time (about 30%), due to growth and aggregation phenomena of nanoparticles that cause precipitation. The final concentration of AgNPs in colloidal solutions was quantified at about 8 µg/mL, a value comparable to that obtained using commercial chitosan.

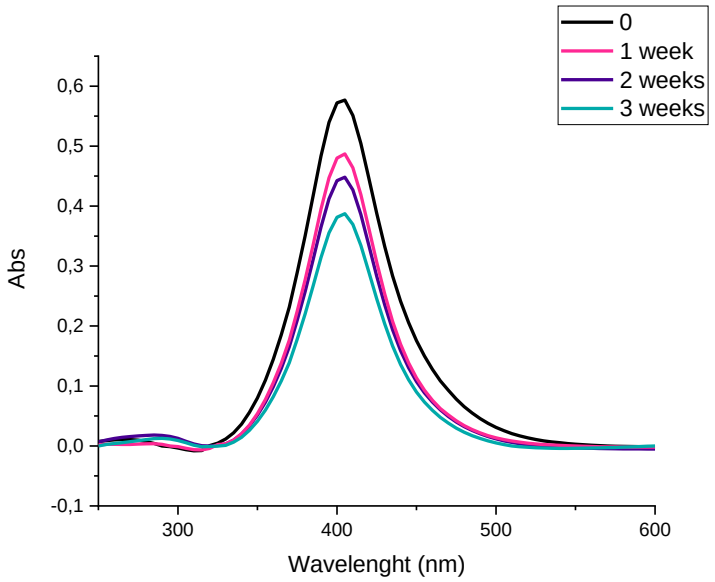

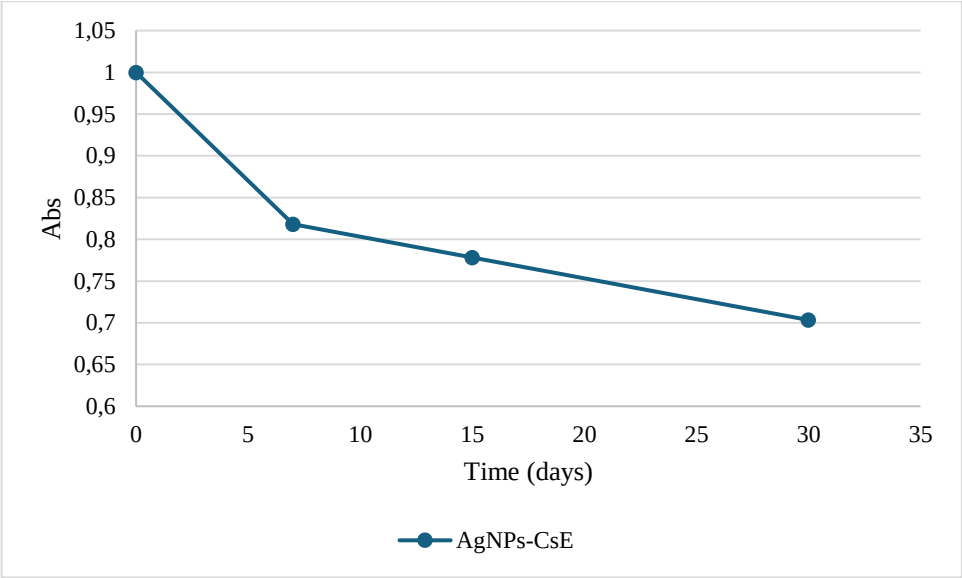

Figure 3.10 A) CsE-AgNPs UV-Visible spectra at different times, B) Graph with time-recorded absorption pattern for CsE-AgNPs.

The analysis of TEM micrographs presented in Figure 3.11 (A) reveals a predominantly spherical morphology of synthesized AgNPs. The dimensional analysis showed an average particle diameter of about 18.5 nm (Table 3.6). However, the size histogram shows a high-sized tail, with a minority of AgNPs between 50 and 90 nm.

A B

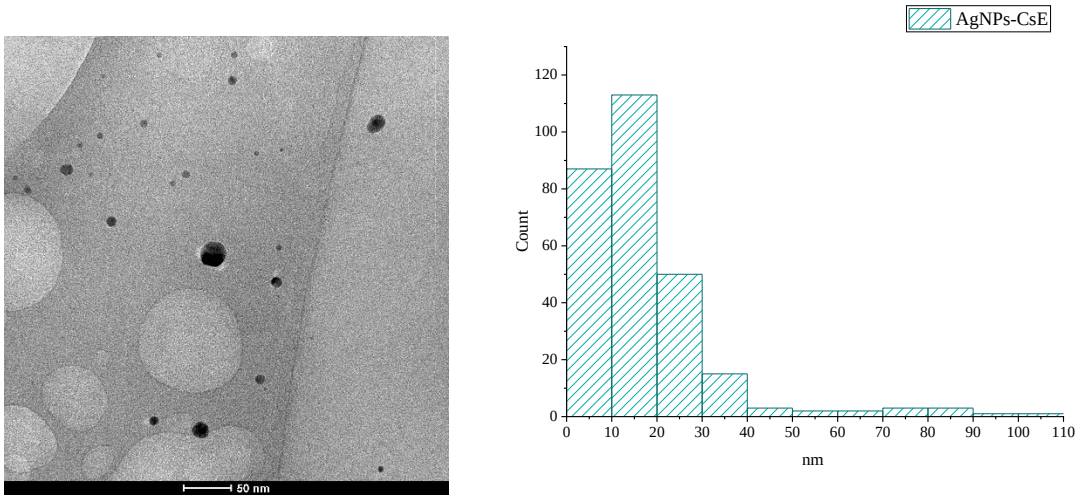

Figure 3.11 A) TEM images AgNPs-CsE, B) AgNPs size distribution.

Table 3.6 AgNPs size and concentration

Name sample	Average	Median	[AgNPs]
CsE-AgNPs	18.5 nm	12.3nm	8.4 μg/ml

The FTIR spectra of Figure 3.12 A, show CsE-AgNPs and CsE in comparison, it can be seen that the characteristic bands of chitosan are also present in the spectrum of the composite, indicating that the basic structure of the polymer has not been substantially altered by the introduction of silver nanoparticles. One can notice some significant differences, especially in the region of about 1570 cm^{-1}. In this region, there is a decrease in the intensity of the band associated with amide II and a slight shift to lower frequencies in the composite compared to pure chitosan. These changes can be attributed to the interaction between the functional groups of chitosan and the surface of silver nanoparticles. In particular, the decrease of intensity and the shift of the amide II band suggest a reduction of the vibrational freedom of the N-H groups, as a result of the formation of interactions with the surface of nanoparticles. In Figure 3.12 B, the ray diffraction spectra of CsE and CsE-AgNPs samples are presented in comparison; both samples show the characteristic diffraction peaks of the crystal structure of chitosan, located at approximately 10° and 20° 2θ. Unlike the observed for commercial chitosan, it was not possible to identify the characteristic peak (111) of metallic silver in CsE-AgNPs. This absence could be attributed to the formation of a polymeric shell of chitosan around silver nanoparticles during ablation, which would act as a shield by attenuating the diffraction signal from the metal

A B

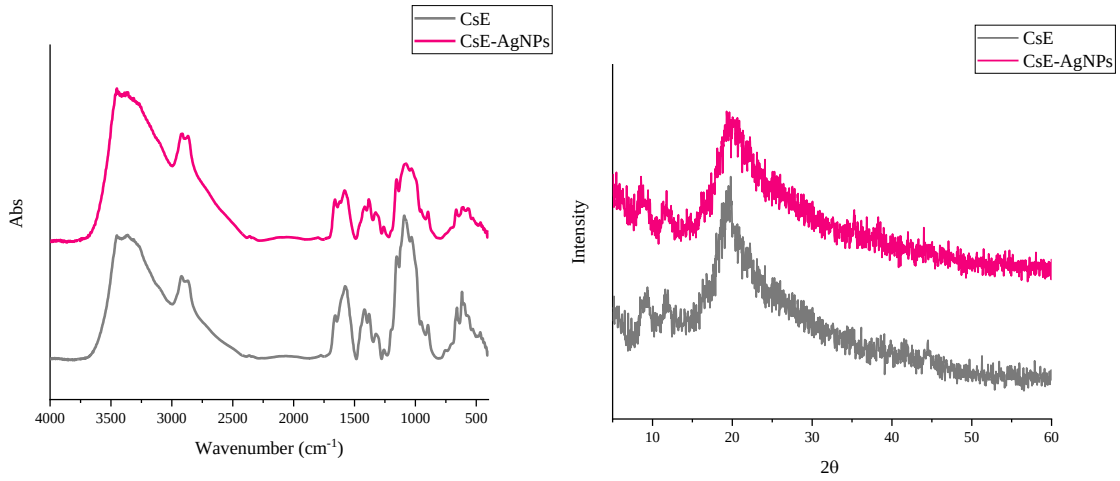

Figure 3.12 Chitosan (grey) and CsE-AgNPs (pink) A) FTIR spectra and B) XRD comparison.

3.3.1.1 Antibacterial tests

Agar diffusion test

The tested solutions, Cs-AgNPs, CsE-AgNPs, induced the formation of inhibition zones on both Gram positive and Gram negative strains, respectively *M. flavus* and *E. Coli*, the inhibition rings are shown in Figure 3.13 Cs and CsE were also evaluated and showed to inhibit in a comparable way on both bacterial strains. Distilled water, used as negative control, did not induce inhibition zones; acetic acid as well as Hac-AgNPs and acetic acid did not induce inhibition zones. This test does not show a substantial difference in antibacterial capacity between composite materials and biopolymer solution. The results of the agar diffusion test are shown in Figure 3.13, the data are reported in Table 3.7.

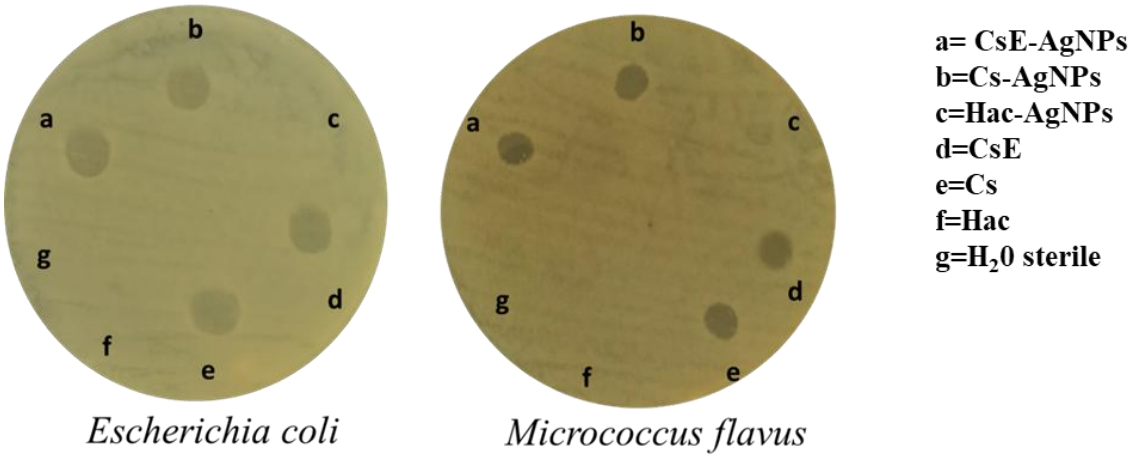

Figure 3.13 Inhibition zones of silver sample experiments on *E. coli* (A) and *M. flavus* (B) resulting from the agar diffusion test are reported. Silver nanoparticles combined with chitosan from pupal exuviae of *H. illucens* (a), silver nanoparticles combined with commercial chitosan (b), silver nanoparticles in acetic acid (c), *H. illucens* chitosan sample (d), commercial chitosan (e), acetic acid (f) and distilled water (g).

Table 3.7 Diameters (mm) of inhibition zones formed by samples on *E. coli* and *M. flavus*. Distilled water was tested as negative control. Results are expressed as mean ± standard deviation of diameters measured with agar diffusion test of three independent biological replicates.

Solution	**Diameter**	
	E. Coli	*M. flavus*
CsE- AgNPs	8±0,3 mm	8±0,3 mm
Cs- AgNPs	8±0,5 mm	7±0,5 mm
Hac- AgNPs	/	/
CsE	8±0,2 mm	8,5±0,2 mm
Cs	8,5±0,4 mm	8±0,3 mm
H_20 distilled	/	/
Hac	/	/

Microdilution Assay

The results of the microdilution test are shown in Figure 3.14 Cs-AgNPs, CsE-AgNPs, analysed at concentrations of 1, 0,5, 0,25, 0,125, 0,06, 0,03, 0,015, 0,006, 0,003 mg/ml and the MIC, the minimum inhibitory concentration, was determined for each sample; The Cs, CsE and Hac-AgNPs samples were analysed under the same conditions to allow comparison with the results obtained from composite materials and to assess the possible synergistic effect of the components.

At the highest concentration, 1 g/L, all samples showed significant inhibition of growth on both *E. coli* and *M. flavus*. However, the antimicrobial effect could be due not only to the biopolymer itself or nanoparticles, but also to acetic acid, the solvent, which has antimicrobial properties at these concentrations. As can be clearly seen from the absorbance levels in the figure, at

concentrations of 0.25 g/L and below, acetic acid loses its antimicrobial capacity, reported to concentrations below 200 ppm, equivalent to 0.04% acetic acid in solution,[189] it is therefore possible to exclude a possible influence on the bactericidal activity by evaluating the inhibition of growth obtained from samples at lower concentrations.

The image shows that the MIC, on *E. coli* bacterial culture, for both composite materials, CsE-AgNPs and Cs-AgNPs, was determined in 0,006 g/L. However, it is evident that the effectiveness of silver nanoparticles combined with chitosan from H. illucens is higher than that of silver nanoparticles combined with crustacean chitosan. In addition, in the concentration range between 0.5 g/L and 0.006 g/L, CsE-AgNPs showed significantly higher antimicrobial activity than silver nanoparticles in acid solution. The presence of CsE seems to positively influence the antibacterial capacity of nanoparticles, which have lower MIC than their counterparts produced with commercial chitosan. Cs and CsE show a comparable trend at all dilutions, maintaining an antibacterial activity always lower than the corresponding composite materials. Silver composite materials show a strong inhibitory capacity of almost 50% in the concentration range between 0,5 and 0.03 mg/ml, the combination of the antimicrobial capacity of chitosan would seem to be conjugated with that of metal nanoparticles and lead to an increase in antibacterial activity due to a synergy of action.

When tested against *M. flavus* under the same conditions, CsE-AgNPs C-AgNPs s showed good inhibitory activity, although not statistically significant compared to silver nanoparticles in acid solution. In particular, at higher concentrations of 1, 0.5 and 0.25 g/L, the inhibitory effect was found to be greater for silver nanoparticles in acetic acid, probably due to a synergistic action of the acid itself. By further reducing the concentration from 0.125 to 0.015 g/L, no significant differences between the two formulations were observed. The MIC obtained on *M. flavus* with CsE-AgNPs and Cs-AgNPs was determined at a concentration of 0.006 g/L. The inhibition Cs and CsE is comparable to the three lowest concentrations from 0.015 to 0.003 g/L, while at higher concentrations CsE inhibits more markedly than Cs.

A

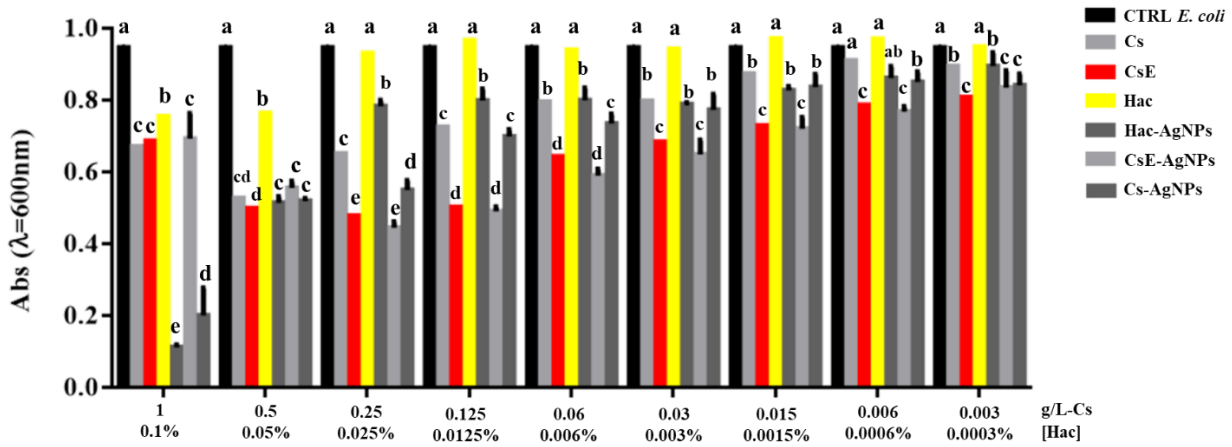

B

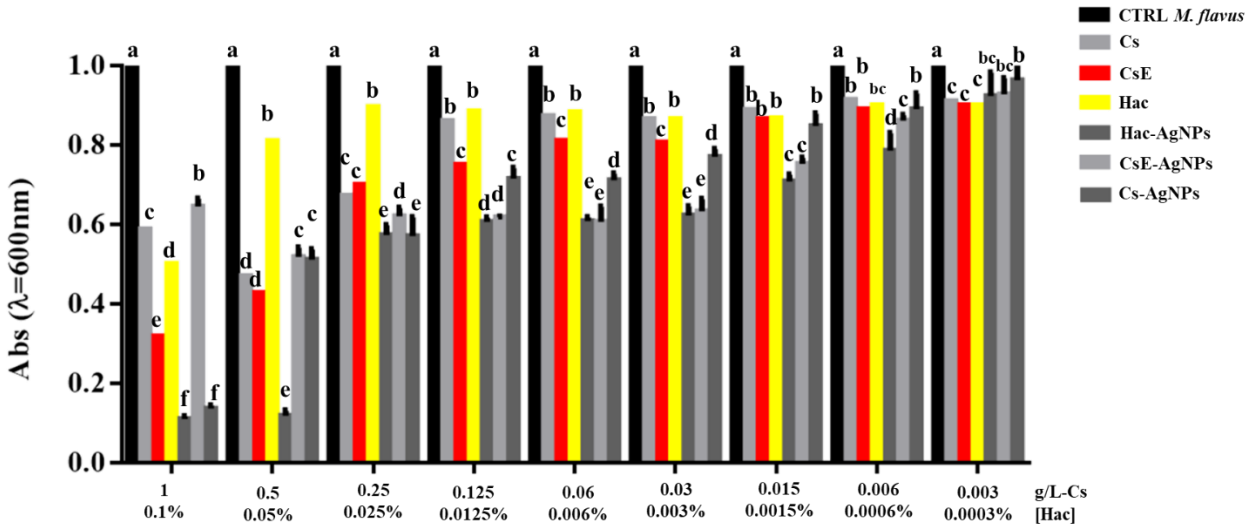

Figure 3.14 Results of microdilution assay for silver nanoparticles combined with chitosan from pupal exuviae of *H. illucens*, silver nanoparticles combined with commercial chitosan, silver nanoparticles in acetic acid, H. illucens chitosan sample, commercial chitosan, acetic acid and distilled water at the nine concentrations of 1, 0.5, 0.25, 0.125, 0.06, 0.03, 0.015, 0.006 and 0.003 g/L against *E. coli* and *M. flavus*. Bars indicate the absorbance of the bacterial culture (black bars), the culture treated with commercial chitosan (light grey bars), *H. illucens* chitosan (red bars), acetic acid (yellow bars), silver nanoparticles in acetic acid (grey bars), silver nanoparticles combined with chitosan from pupal exuviae of H. illucens (silver grey) and silver nanoparticles combined with commercial chitosan (dark grey). Data are expressed as mean ±

standard deviation. Different letters indicate significant differences ($p<0.05$) between absorbance values of the bacterial culture alone and that of bacteria treated with the different concentrations of each treatment (data were analyzed with one-way Anova and Bonferroni post-hoc test).

3.3.2 Laser ablation of copper in chitosan solution

Copper is highly sensitive to oxidation, and studies have shown that the ablation of a Cu target in water by a nanosecond green laser source leads to the formation of Cu nanoparticles with varying degrees of oxidation and stability.[190] Composite solutions Cs-CuNPs and CsE-CuNPs were prepared operating with the experimental conditions optimized for the preparation of Cs-AgNPs.

Table 3.8 List of colloidal solution and Copper nanoparticles concentration.

Name Sample	[Polymer]	[CuNPs]
Cs-CuNPs	1g/l Cs	15,7 μg/ml
CsE-CuNPs	1g/l CsE	11,7 μg/ml
Hac-CuNPs	0,1% HAc	18μg/ml

The UV-Vis absorption spectrum CuNPs synthesized in Cs and CsE solutions, of Figure 3.15-3.16 (A), shows a low intensity band centred at about 580 nm immediately after the laser ablation process. This band, shown in the magnification of Figure 3.15-3.16(B), is attributable to the plasmonic surface resonance of metallic copper, suggesting an effective stabilizing action by the Cs and CsE compounds against oxidation of nanoparticles during synthesis.

However, a subsequent spectroscopic analysis, conducted one week after preparation, reveals a significant evolution of the system in both cases. The characteristic band of metallic copper at 580 nm disappears completely, leaving room for two new spectral shoulders, centred around 250-300 nm and 300-400 nm respectively. The latter are typical of the electronic transitions typical of copper oxides, CuO and Cu_2O respectively.[190]

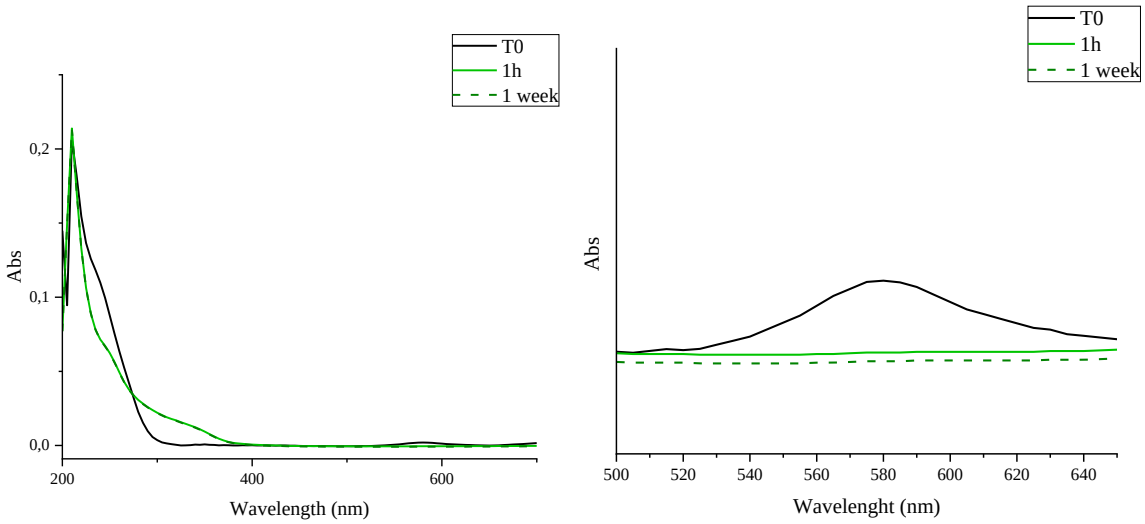

Figure 3.15 UV-Visible spectra: A) Cs-CuNPs, B) magnification on the signal at about 560 nm of metallic copper.

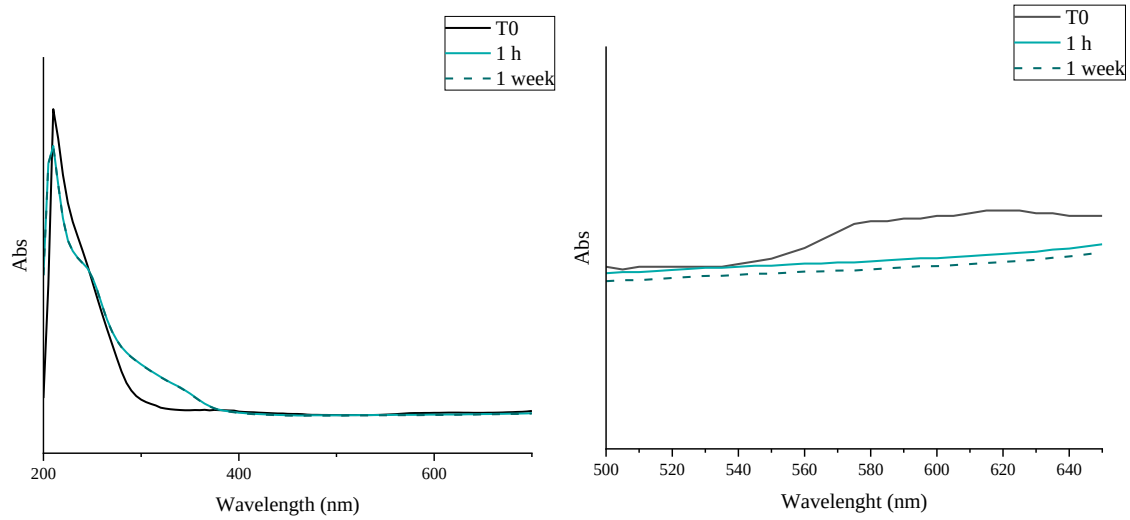

Figure 3.16 UV-visible spectra: A) CsE-CuNPs, B) magnification on the signal at about 560 nm of metallic copper.

Therefore, it can be concluded that CuNPs initially present in metallic form, in both synthesized systems, undergo a complete oxidation process over time, leading to the formation of a mixture of CuO and Cu_2O. The presence of Cu_2O was further confirmed by TEM analysis (Figure 3.17). The Fast Fourier Transform (FFT) of the TEM images showed a predominant reticular spacing of about 0.24 nm, in excellent agreement with the expected theoretical value for the cubic phase of Cu_2O.[190]

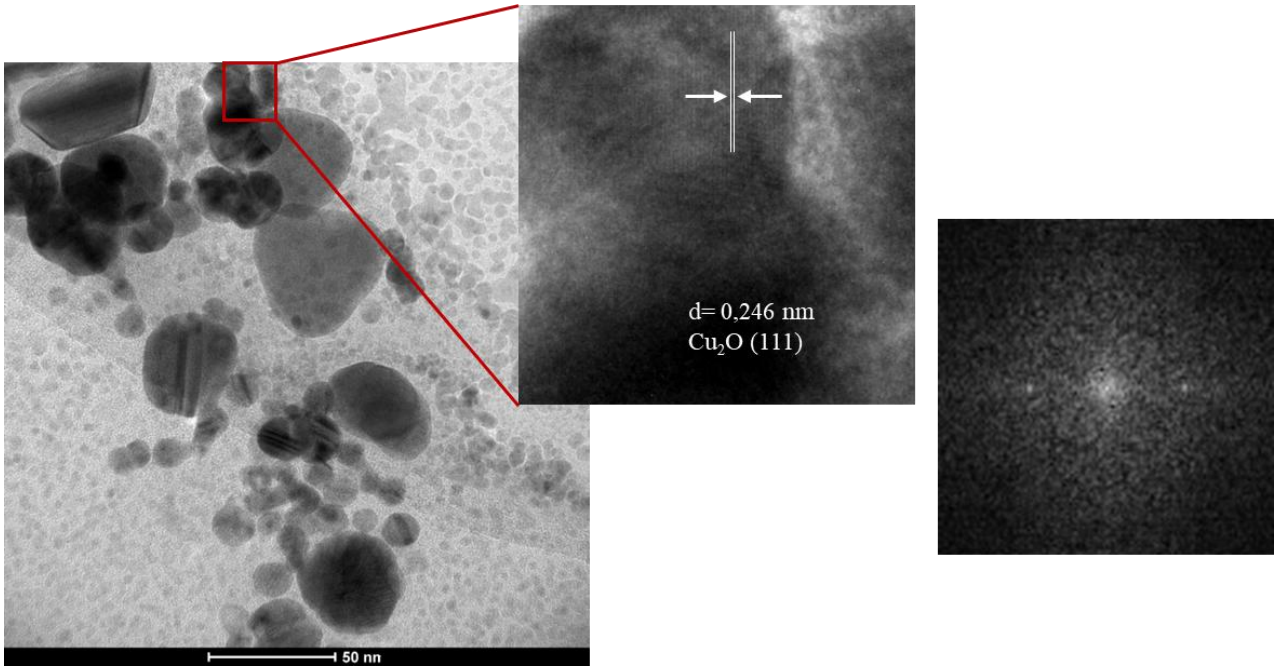

Figure 3.17 TEM image of Cu nanoparticles obtained by laser ablation. Magnification of the measured interplanar distances and corresponding FFT from a single nanoparticle.

The TEM images allowed for accurate morphological and dimensional analysis of synthesised nanoparticles. The micrograph of Figure 3.18 shows that most particles have a spherical geometry and dimensions not exceeding 10nm. However, it is evident that a minority of nanoparticles are present with significantly larger sizes, ranging from 40nm to 50nm. This dimensional heterogeneity could be attributed to melting phenomena occurring during the laser ablation process, which have favoured the growth of some particles.[182] A quantitative analysis of the size of nanoparticles revealed an average diameter of about 5 nm.

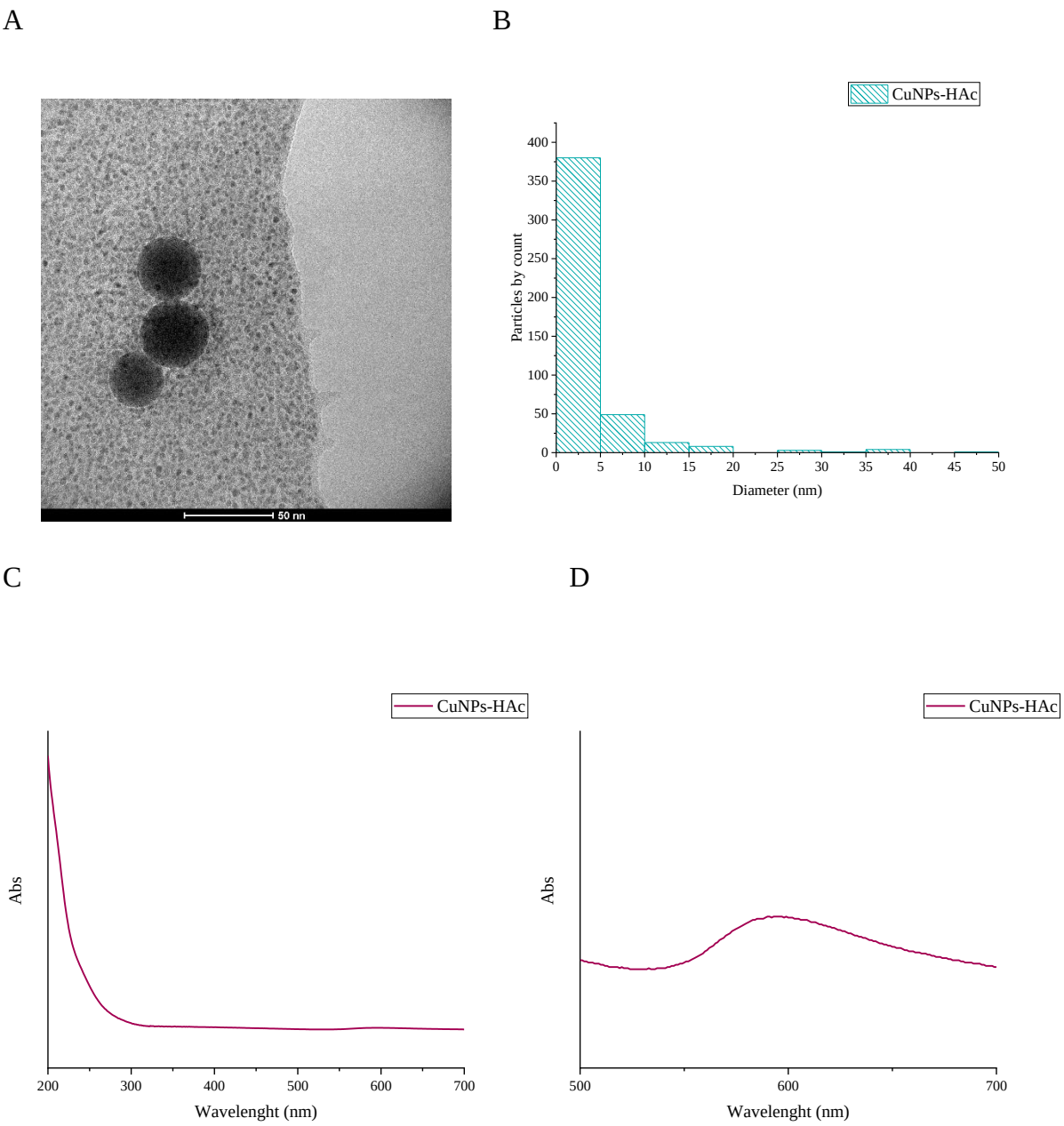

Figure 3.18 A) TEM image of the CuNPs of the Hac-CuNPs sample, B) CuNPs size distribution, C) UV-Visible spectra of CuNPs-HAc, D) magnification on the signal at about 560 nm of metallic copper.

The FTIR spectra of the Cs-CuNPs and CsE-CuNPs samples compared with Cs and CsE (Figure 3.19) as for silver, have characteristic bands of chitosan, typical of the OH 3400 cm^{-1} stretching vibration, of the stretching of C=O of amide I at about 1650 cm^{-1} and of the deformation of N-H of amide II at about 1590 cm^{-1}. These bands confirm the presence and basic structure of the natural polymer in all samples analysed, however, it is possible to observe some significant differences, particularly in samples containing nanoparticles of CuO. The frequency variations of the characteristic bands of chitosan, particularly in the region at 1550 cm^{-1}. In this region, a decrease in intensity and a slight shift to the right in copper-content composites compared with

chitosan can be observed. These variations suggest the formation of bonds between the amino groups of chitosan and the surface of CuO nanoparticles, the presence of which causes changes in the strength of the bonds involved in the interactions and variations in the local chemical environment of the functional groups.

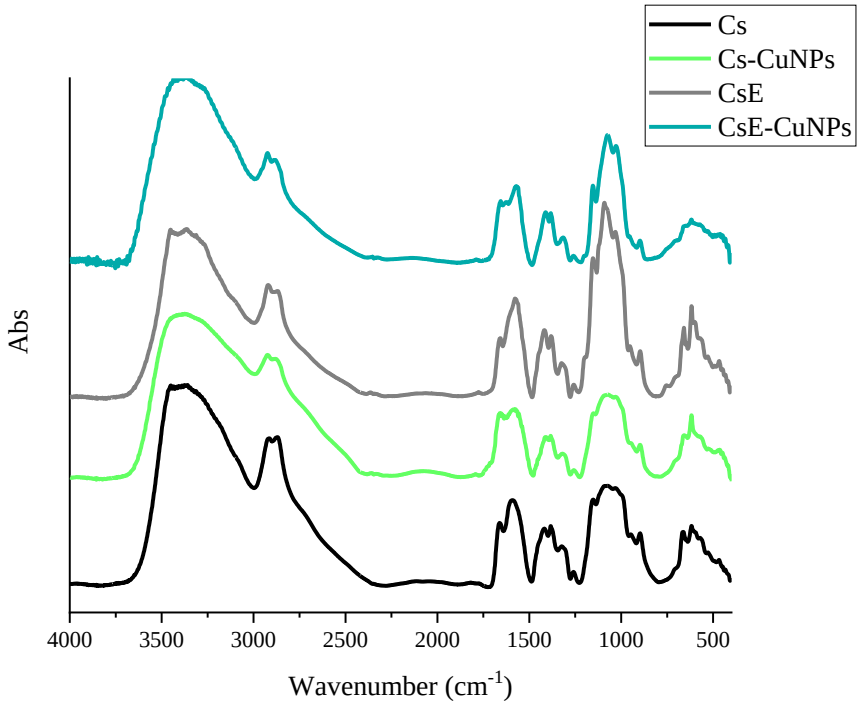

Figure 3.19 Chitosan (black), Cs-CuNPs (green), Exuviae Chitosan (grey) and CsE-CuNPs (dark green) FTIR spectra, comparison.

3.3.2.1 Antibacterial tests

Agar diffusion test

The antibacterial activity of different solutions, including CsE-CuNPs and Cs-CuNPs, on Gram-positive, *M. flavus* and Gram-negative, *E. coli* bacterial strains was evaluated. The results, of Figure 3.20, show the formation of inhibition halos, indicating significant antimicrobial activity. Cs and CsE solutions have shown comparable effectiveness in inhibiting the growth of both tested bacterial strains. In contrast, neither the distilled water, negative control, Hac-CuNPs and Hac showed any inhibitory effect. This experiment suggests that CsE-CuNPs and Cs-CuNPs have obvious antibacterial properties, but no significant difference in the

antibacterial activity between these composite materials and the base biopolymer solution was observed.

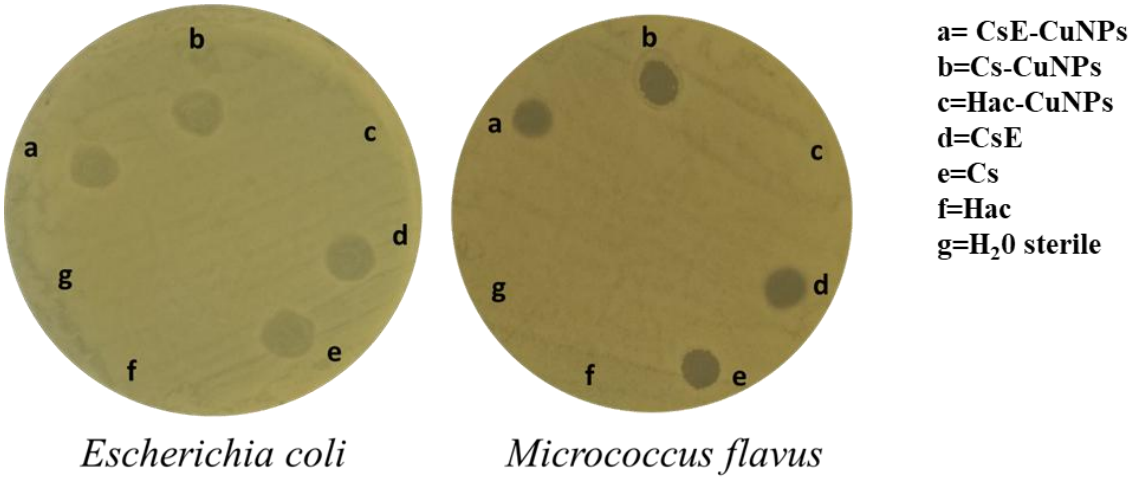

Figure 3.20 Inhibition zones of copper sample experiments on *E. coli* (A) and *M. flavus* (B) resulting from the agar diffusion test are reported. Copper nanoparticles combined with chitosan from pupal exuviae of *H. illucens* (a), copper nanoparticles combined with commercial chitosan (b), copper nanoparticles in acetic acid (c), *H. illucens* chitosan sample (d), commercial chitosan (e), acetic acid (f) and distilled water (g).

Table 3.9 Diameters (mm) of inhibition zones formed by samples on *E. coli* and *M. flavus*. Distilled water was tested as negative control. Results are expressed as mean ± standard deviation of diameters measured with agar diffusion test of three independent biological replicates

Solution	**Diameter**	
	E.Coli	*M.flavus*
CsE-CuNPs	7±0,4 mm	7±0,4 mm
Cs- CuNPs	8±0,4 mm	8.5 cm± 0.4 mm
Hac- CuNPs	/	/
CsE	8±0,2 mm	8,5±0,2 mm
Cs	8,5±0,4 mm	8±0,3 mm
H_20 distilled	/	/
Hac	/	/

Microdilution assay

The results of the microdilution test for copper nanoparticles combined with chitosan and chitosan derived from Hermetia illucens are shown in Figure 3.21; the CsE-CuNPs, Cs-CuNPs, Hac-CuNPs, CsE, Cs and Hac samples were analyzed at nine concentrations: 1, 0.5, 0.25, 0.125, 0.06, 0.03, 0.015, 0.006 and 0.003 g/L.

Both *E. coli* and *M. flavus* at the highest concentrations, i.e., 1 and 0.5 g/L, in all tested solutions produced a valuable inhibition effect, probably due to the intrinsic activity of acetic acid present in all, with established antimicrobial capabilities. The need to use acetic acid for the dissolution of chitosan, limits the attribution of antimicrobial capacity of tested solutions. This limitation is easily exceeded at the first dilution, as clearly shown by the values shown in Figure 3.21, in fact at concentrations of 0.25 g/L and below acetic acid loses its antimicrobial capacity. This is in line with the literature, where it has been seen that at concentrations below 200 ppm, equivalent to 0.04% acetic acid in solution, this loses its bactericidal activity [191]. Therefore, experiments conducted at concentrations below 0.5 g/L (0.05% Hac) report antibacterial activity performed without the addition of acetic acid.

On *E. coli* CsE-CuNPs and Cs-CuNPs showed good antibacterial activity showing a statistically significant inhibition compared to Hac-CuNPs at the same concentration. CsE-CuNPs show to have the lowest inhibitory concentration at 0.003g/l, similarly Cs-CuNPs showed an inhibitory activity even at the lowest concentration tested, 0.003 g/l, although to a lesser extent than the corresponding levels of exuviae. On the negative gram CsE shows a higher inhibitory activity than Cs at all concentrations below 0.5g/l evaluated.

Observing the graph (Figure 3.21 B) for *M. flavus*, it is possible to see that at concentrations below 0.5g/l the inhibition of CsE-CuNPs and Cs-CuNPs is always greater than that of the individual components tested under the same conditions. CsE-CuNPs and Cs-CuNPs have a MIC at the lowest head concentration, 0.0003 g/l.

A

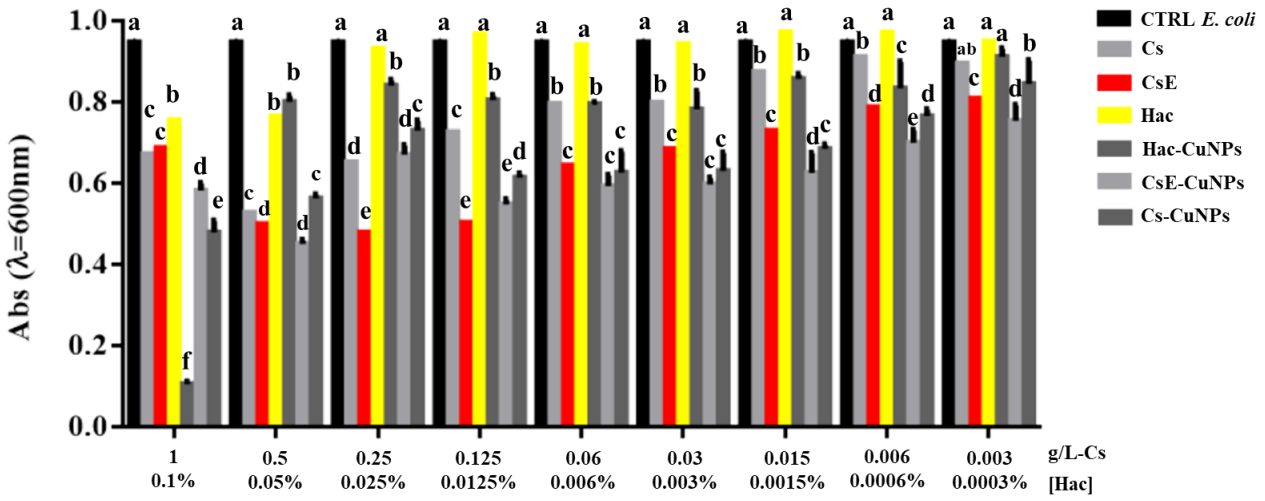

B

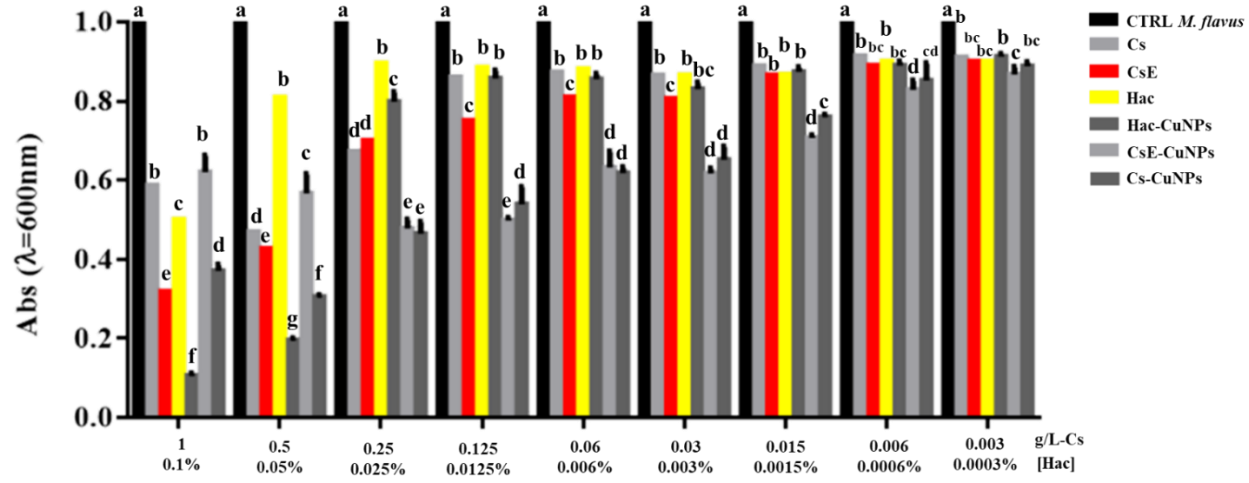

Figure 3.21 Results of microdilution assay for copper nanoparticles combined with chitosan from pupal exuviae of *H. illucens*, copper nanoparticles combined with commercial chitosan, copper nanoparticles in acetic acid, *H. illucens* chitosan sample, commercial chitosan, acetic acid and distilled water at the nine concentrations of 1, 0.5, 0.25, 0.125, 0.06, 0.03, 0.015, 0.006 and 0.003 g/L against *E. coli* (a) and *M. flavus* (b). Bars indicate the absorbance of the bacterial culture (black bars), the culture treated with commercial chitosan (light grey bars), *H. illucens* chitosan (red bars), acetic acid (yellow bars), copper nanoparticles in acetic acid (grey bars), copper nanoparticles combined with chitosan from pupal exuviae of *H. illucens* (silver grey) and copper nanoparticles combined with commercial chitosan (dark grey). Data are expressed

as mean ± standard deviation. Different letters indicate significant differences ($p<0.05$) between absorbance values of the bacterial culture alone and that of bacteria treated with the different concentrations of each treatment (data were analyzed with one-way Anova and Bonferroni *post-hoc* test).

The results shown are consistent with other studies on chitosan copper composites. The copper-chitosan nanocomposite has shown considerable potential as a broad-spectrum antibacterial agent, effective against both Gram-negative and Gram-positive bacteria. In particular, increased inhibitory activity against Gram-negative bacteria was observed, a phenomenon attributable to the intrinsic differences in cell wall composition between the two types of bacteria.[192]

Other studies have shown the effectiveness of the nanocomposite against multidrug-resistant clinical strains of Staphylococcus aureus and Escherichia coli, with considerable activity against MRSA (methicillin-resistant Staphylococcus aureus) strains at a minimum concentration of 0.17 μg/ml. This result underlines the potential of the nanocomposite to counter infections caused by antibiotic-resistant bacteria. [193]

Furthermore, in other studies the nanocomposite has shown a significant inhibitory effect on Gram-negative bacteria already after one hour of exposure, surpassing the effect of copper ions alone. This evidence suggests a synergistic action between chitosan and copper oxide nanoparticles (nano-CuO). Chitosan, in fact, seems to promote the interaction between the nanocomposite and bacterial cells, facilitating the release of copper ions near the cell surface and enhancing the overall antibacterial effect.[194]

3.3.3 Film

The colloidal solutions studied in the previous paragraphs, which were carefully characterized and evaluated for their biological activities, have been further investigated in this research. With the aim of exploring the persistence of antimicrobial properties in solid form, the possibility of obtaining solid systems from the same colloidal solutions was evaluated. In particular, as described in detail in paragraph 3.2.5, thin films were produced from colloidal dispersions. This methodological choice was motivated by the growing relevance of solid release systems in biomedical applications and tissue engineering. The analysis of the antimicrobial properties of the films obtained allowed to assess the impact of the transition from liquid to solid state on the bioactivity of colloidal systems, providing important indications for future applications.

Colloidal solutions of Cs-AgNPs, CsE-AgNPs, Cs-CuNPs and CsE-CuNPs were used for the preparation of self-supporting thin films of AgNPs-Cs, AgNPs-CsE, CuNPs-Cs and CuNPs-CsE respectively. The colloidal solutions were deposited on disposable weighing boats (3.5 x 3.5 cm) and left to air dry. The films were then subjected to a neutralization treatment in 0.05 M sodium hydroxide aqueous solution, followed by thorough washing with distilled water until neutrality was achieved and finally let air dried.

3.3.3.1 Preliminary Agar diffusion tests

The antimicrobial capacity of all films produced was evaluated by means of agar diffusion test on gram negative bacteria, *E. coli*, and on gram positive bacteria, *M. flavus*.

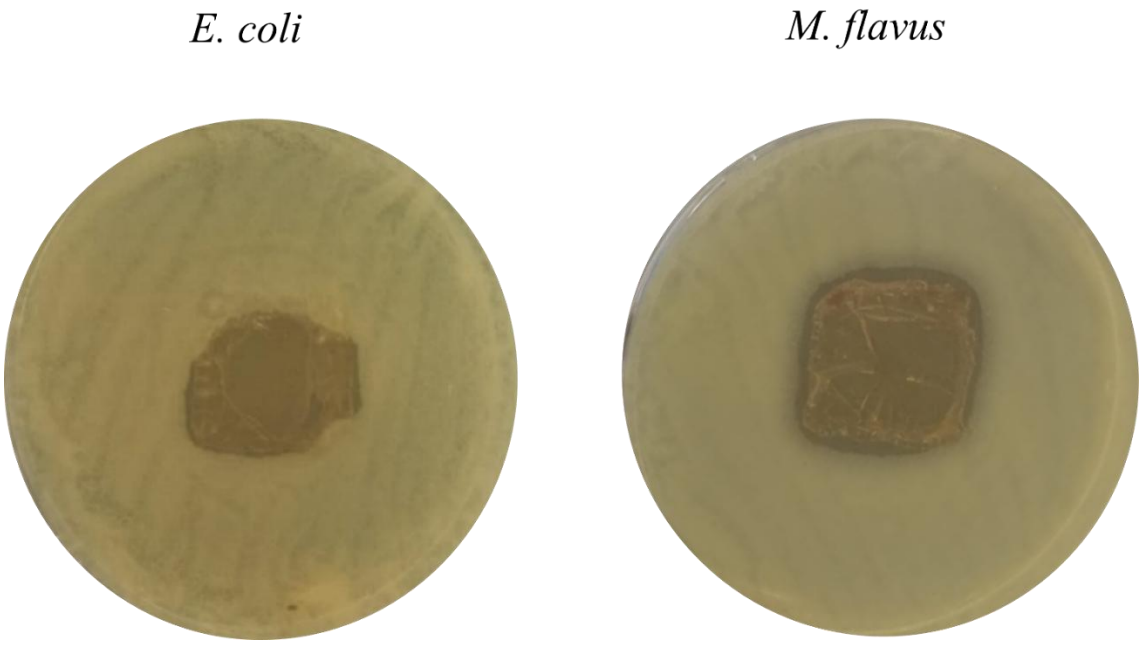

Figure 3.22 AgNPs-Cs film inhibition zones on *E. coli* and *M. flavus*.

The analysis of the images from the agar diffusion test of AgNPs-Cs composite films shows antimicrobial activity against the two microorganisms tested, *E. coli* and *M. flavus*. Figure 3.22 indicates the formation of a poorly defined inhibition zone around the composite film in *E. coli*, which is nevertheless characterized by a slight absence of bacterial growth. This indicates moderate antimicrobial activity of the material tested against *E. coli*. When *M. flavus* is analysed, an inhibition zone is observed, with a well-defined appearance and larger than that observed for *E. coli*. The size and clarity of this zone suggest an effective release of silver ions

from the film, which, interacting with bacterial cellular components, inhibit their growth and proliferation. The lower sensitivity of *E. coli* could be attributed to several factors, including an increased intrinsic resistance or a different mode of interaction with silver ions.

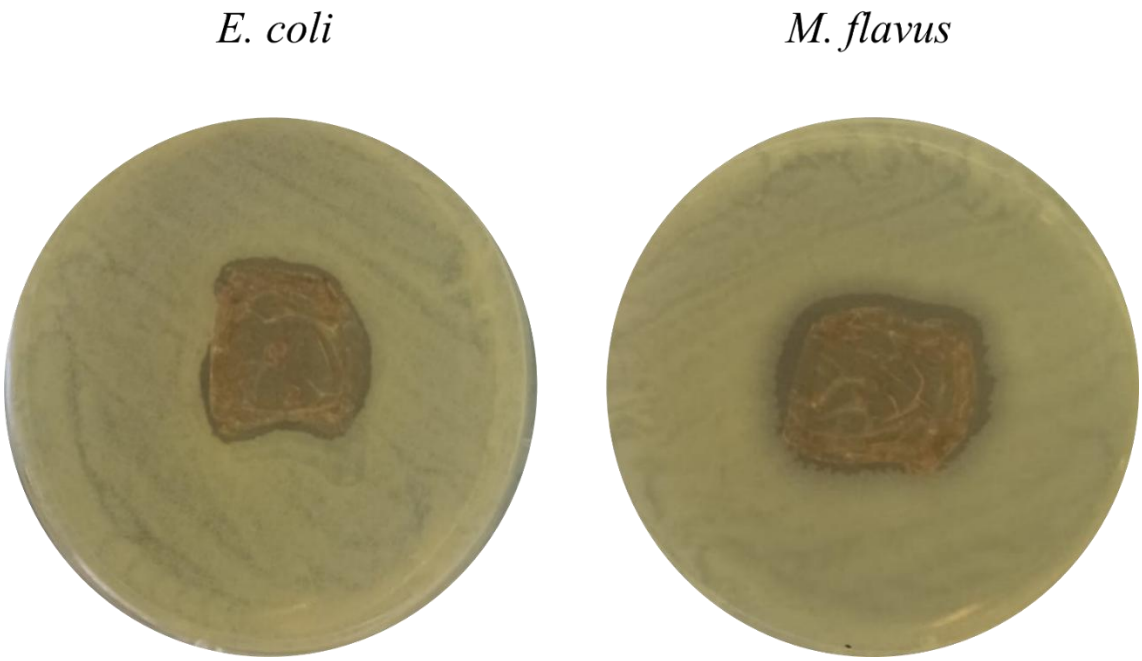

Figure 3.23 AgNPs-CsE film inhibition zones on *E. coli* and *M. flavus*.

Analysis of the images obtained by agar diffusion assay of AgNPs-CsE films revealed a promising antimicrobial activity against the tested micro-organisms, *E. coli* and *M. flavus*. In the case of *E. coli*, Figure 3.23, there is a well-defined inhibition zone around the composite film, characterized by a clear absence of bacterial growth. This result suggests antimicrobial activity of the material tested against *E. coli*. As for *M. flavus*, it also shows an inhibition zone, slightly larger than that found for *E. coli*.

The mechanisms underlying the antimicrobial activity of composite films can be traced to the interaction of silver ions with cellular biomolecules, in particular with the thiol groups of proteins and phospholipids of the plasma membrane. This interaction induces a disruption of membrane permeability, resulting in the leakage of essential intracellular compounds and denaturation of proteins, leading to cell death.[195] The increased effectiveness of CsE-based composites could be related to a different affinity of chitosan for silver nanoparticles, or to a higher permeability of the film, favouring a faster and longer release of silver ions. The results

suggest that composite films based on AgNPs and chitosan represent a promising alternative to traditional antibiotics, offering an innovative approach for controlling microbial infections in different sectors, medicine, agriculture and food industry.

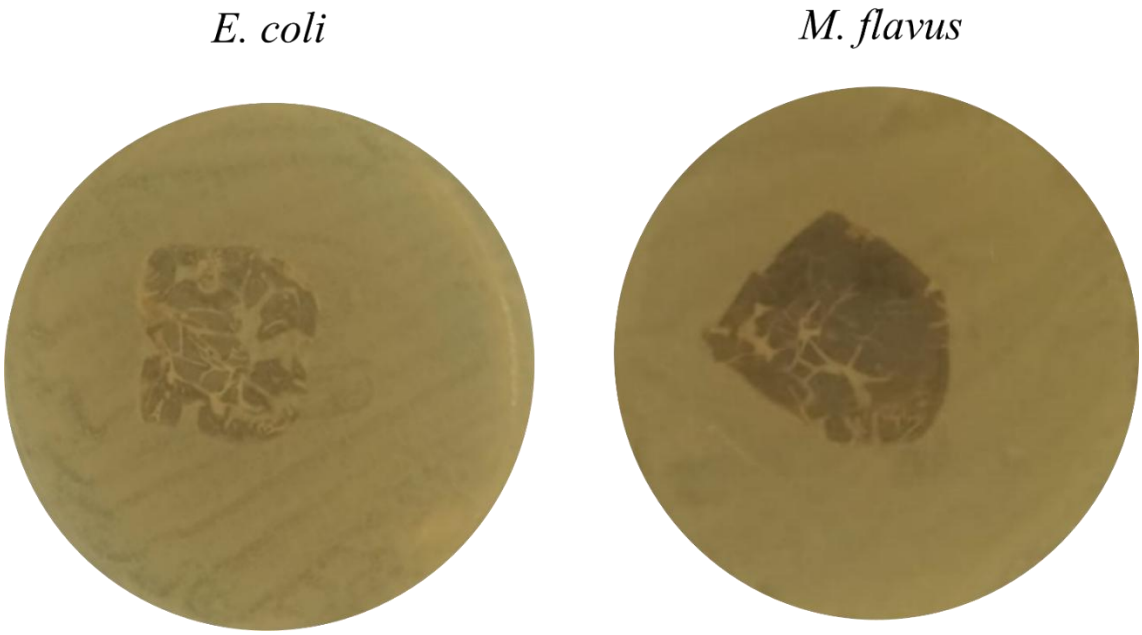

Figure 3.24 Cs-CuNPs film inhibition zones on *E. coli* and *M. flavus*.

Analysis of the agar diffusion tests of CuNPs-Cs composite films did not reveal significant antimicrobial activity against bacterial strains *E. coli* and *M. flavus*. In particular, the absence of inhibition zones around the composite films, as shown in Figure 3.24, suggests a marked reduction or even loss of bacteriostatic activity compared to previously tested CuNPs-Cs colloidal solutions.

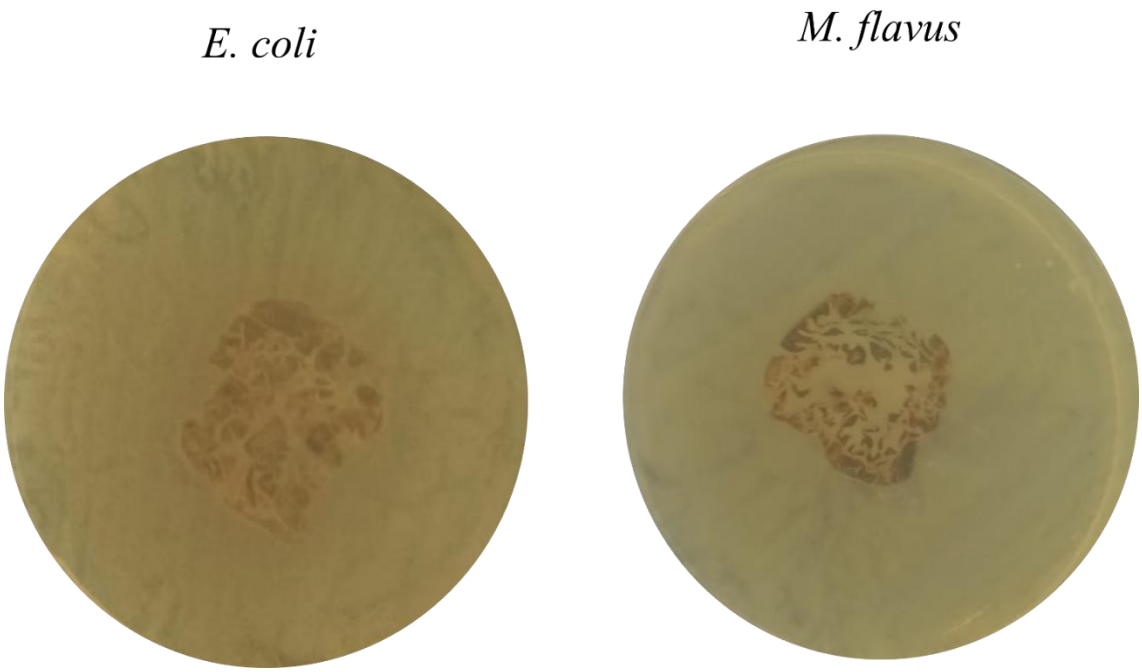

Figure 3.25 CsE-CuNPs film inhibition zones on *E. coli* and *M. flavus*.

Analysis of agar diffusion tests (Figure 3.25) conducted using CuNPs-CsE films showed a different susceptibility of the microorganisms tested. While *E. coli* showed no inhibition zone around the composite film, *M. flavus* exhibited a modest inhibition zone, suggesting an increased sensitivity to the antimicrobial agent. These results contrast with those previously obtained using colloidal solutions of the same nanoparticles, which have shown a more pronounced antimicrobial activity against both micro-organisms. This discrepancy can be attributed to the different physical nature of the two systems. The solid form of the composite could significantly limit the release of copper ions, chemical species responsible for bactericidal activity, in the culture medium.

3.3.3.2 Films characterization

Preliminary results obtained by agar diffusion tests showed a marked antimicrobial activity in the compound films AgNPs-Cs and AgNPs-CsE. In contrast, copper nanoparticle films Cs-CuNPs and CsE-CuNPs did not show significant antimicrobial activity. Based on these promising results, it was decided to focus further investigations on AgNPs-Cs films in order to characterize their chemical-physical and biological properties in depth. In parallel, pure chitosan films, both commercial and derived from exuviae, have been analysed to assess the impact of nanoparticles on the polymer matrix and to compare the properties of biopolymers obtained from different sources. The aim of this study is twofold: on the one hand, it aims to understand the mechanisms underlying the antimicrobial activity of AgNPs-Cs films,

correlating it to their structural and compositional characteristics; on the other hand, it is intended to assess the application potential of these innovative materials in the biomedical and food. Cs, AgNPs-Cs and CsE films were prepared by drop casting method, the solutions Cs, Cs-AgNPs and CsE, as described in paragraph 3.2.5.

Morphological characterization

The morphological analysis of the thin films, shown in Figure 3.26, revealed a significant variation in surface characteristics following the neutralisation process; before neutralisation, the films had a smooth and homogeneous surface, with clearly defined edges and a ductile appearance. After neutralisation, a substantial change in surface morphology was observed, characterized by the appearance of ripples and an irregularity of the edges.

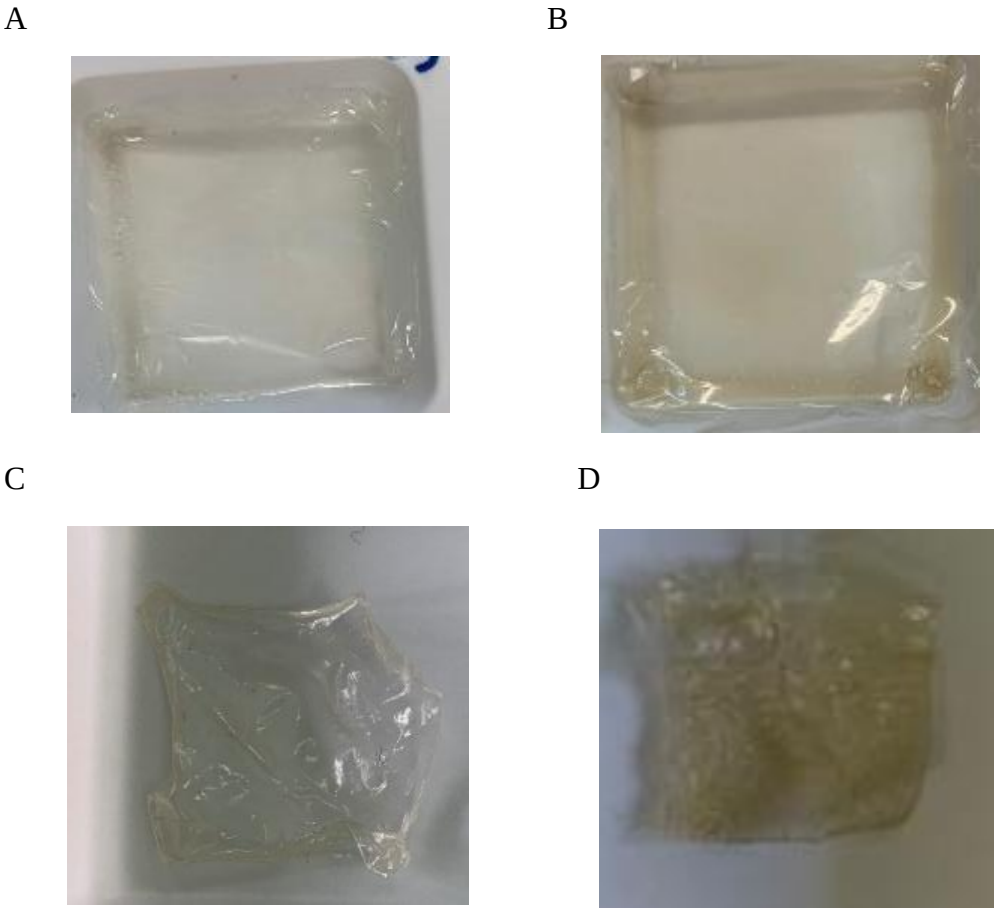

Figure 3.26 Images of A) Cs, B) CsE films, as prepared and C) Cs, D) CsE films, after the neutralization step.

SEM analysis was conducted to assess film thickness before and after the neutralization process. The results obtained indicate that the Cs and CsE films had average thicknesses of 9 μm and 10 μm respectively in their initial state. After the neutralization treatment, a significant increase in thickness was observed, with values reaching 35 μm and 27 μm respectively (Figure 3.27). This

increase in thickness can be attributed to the possible formation of a more compact three-dimensional lattice between the polymer chains of chitosan following the elimination of protonated amino groups. These results suggest that the neutralisation process has a significant impact on the morphology and mechanical properties of films, affecting their internal structure and permeability.

A B

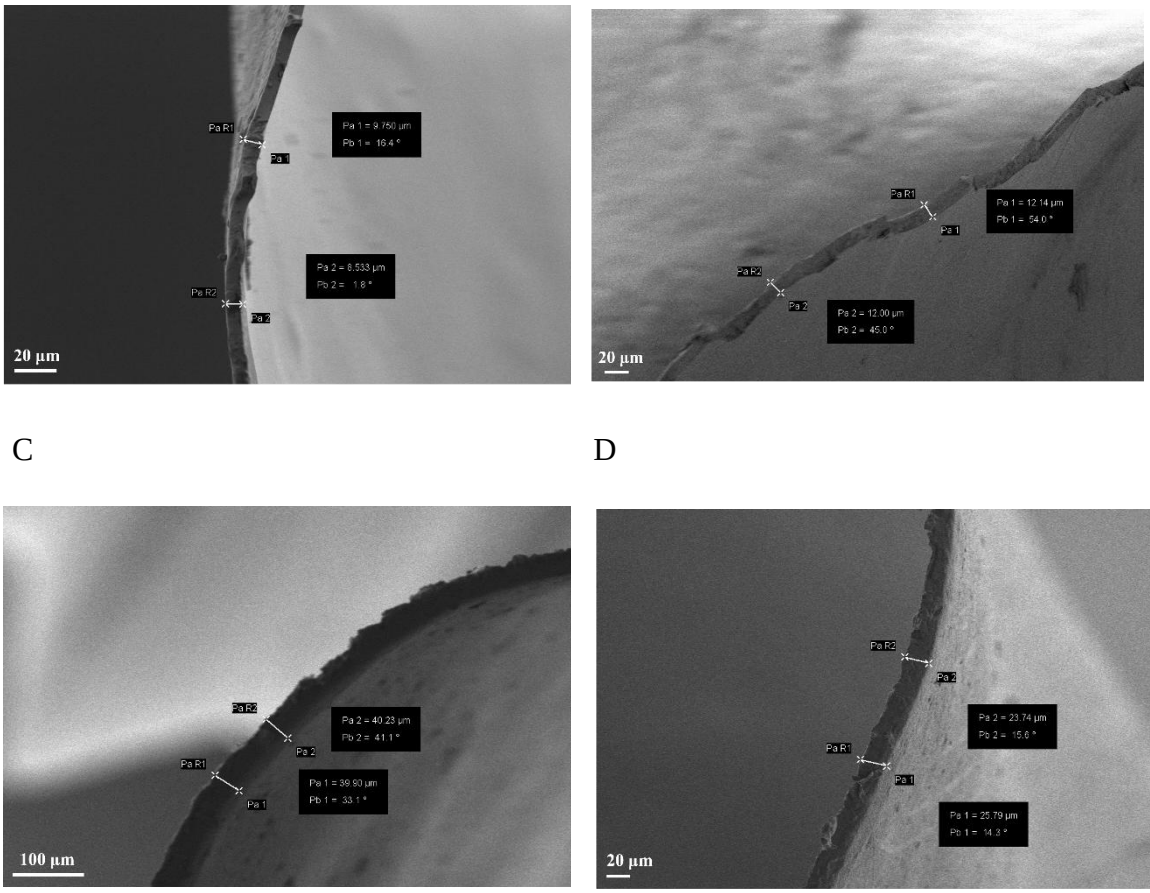

C D

Figure 3.27 SEM cross section images of A) Cs, B) CsE films, as prepared and C) Cs, D) CsE films, after the neutralization step.

The surface morphology analysis performed by SEM detects a surface of the Cs and CsE films characterized by significant roughness, with the presence of numerous micropores and irregularities. (Figure 3.28) The morphology is quite heterogeneous, with areas of higher density of pores alternating with more smooth areas. It is possible notice some micro-fractures or surface defects, which could be due to the film preparation process or mechanical stress. The neutralization process does not seem to change substantially the surface morphology.

A B

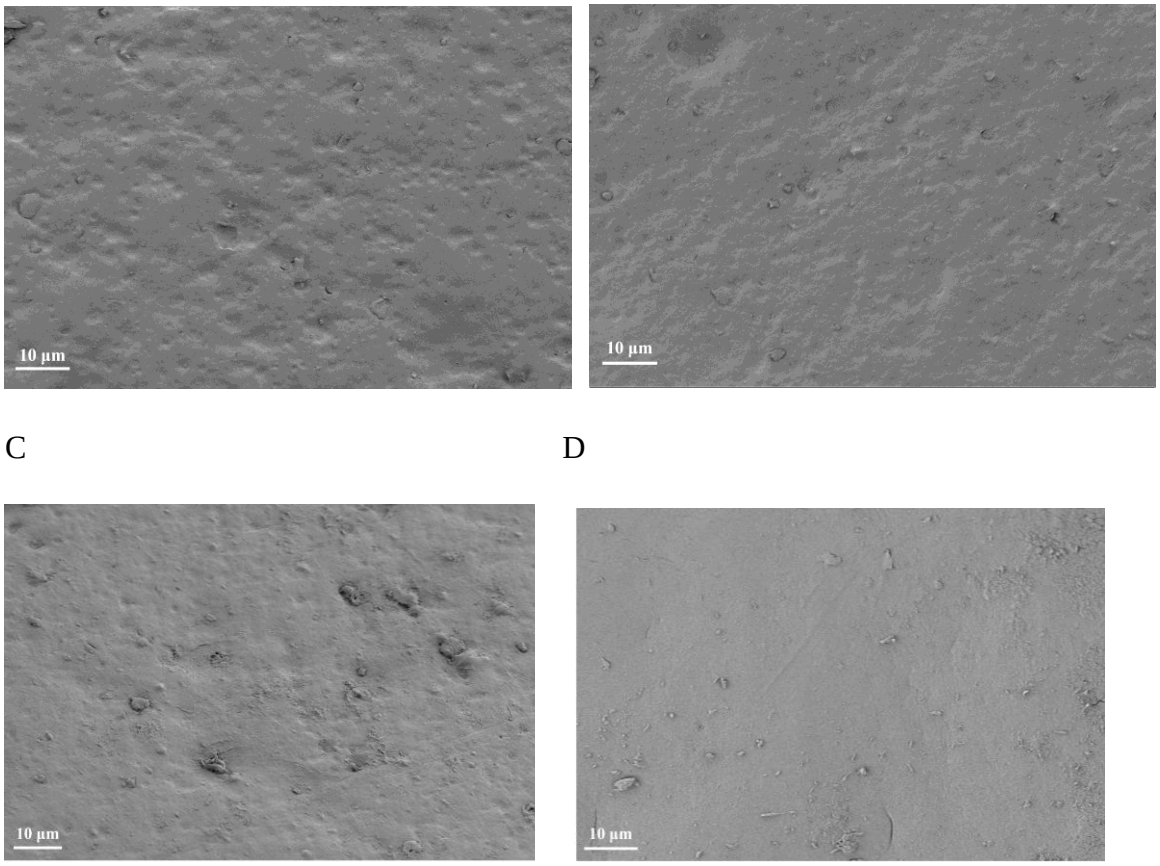

Figure 3.28 Surface SEM images of A) Cs, B) Cs E, as prepared and C) Cs and D) CsE, after the neutralization step.

Visual analysis of AgNPs-Cs films, shown in Figure 3.29, reveals a characteristic yellow-gold coloration, attributable to the presence of AgNPs within the chitosan matrix. This colour makes these films clearly different from those made exclusively of chitosan. Before the neutralization process, as seen for Cs and CsE films, it displays a homogeneous morphology with well defined edges and a ductile appearance. At the end of the neutralization process, a significant morphological variation is observed in AgNPs-Cs films, characterized by curly and not well defined edges and the presence of folds.

A B

Figure 3.29 AgNPs-Cs films, A) as prepared and B) after the neutralization step.

The cross-section SEM analysis (Figure 3.30) confirms this observation, showing a considerable increase in film thickness following neutralization from about 8 μm to about 33 μm.

A B

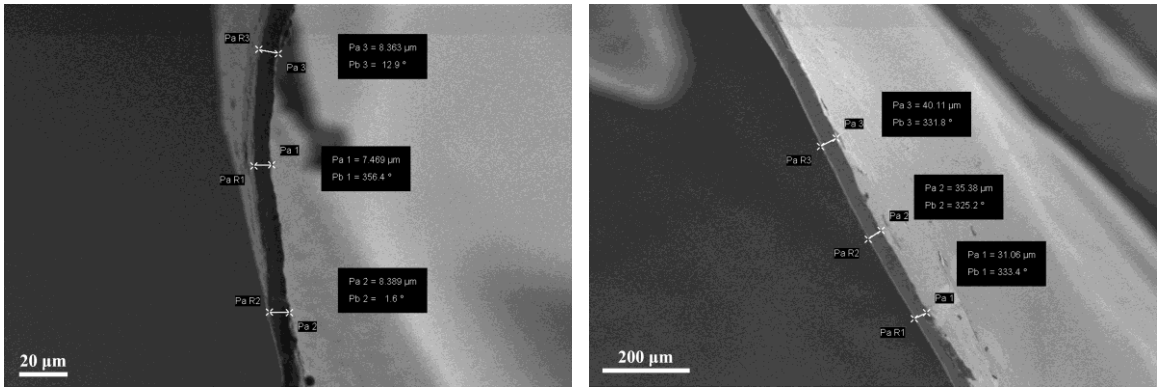

Figure 3.30 SEM cross section images of AgNPs-Cs A) as prepared and B) after the neutralization step.

SEM analysis of the AgNPs-chitosan composite film before and after neutralization (Figure 3.31) reveals significant surface morphological differences. Before neutralisation, the surface has a marked roughness, characterised by an uneven distribution of bumps and depressions. In contrast, the neutralized film shows a less rough surface morphology, although there are superficial inclusions attributable to the rearrangement of the chitosan matrix induced by the loss of the acetyl group.

A B

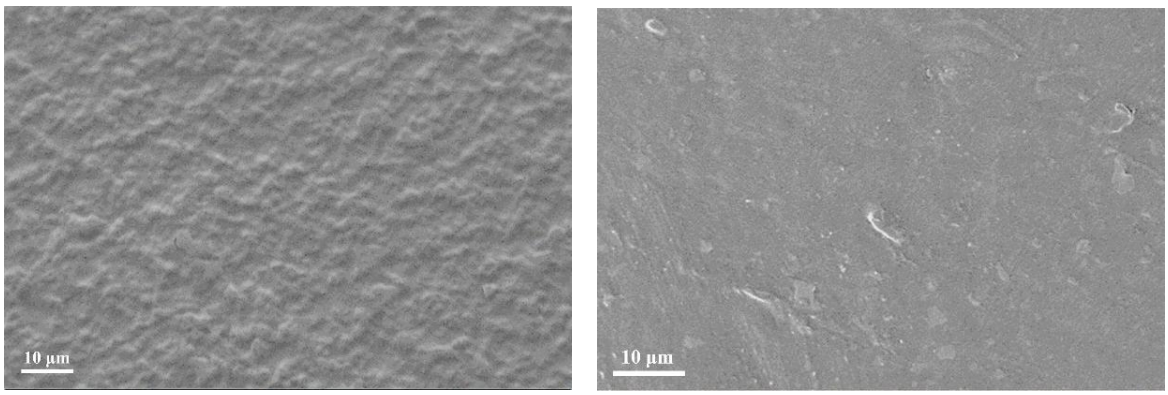

Figure 3.31 Surface SEM images of AgNPs-Cs A) as prepared and B) after the neutralization step.

Physico-chemical characterization

FTIR analysis of films before and after the neutralisation process shows that the band of the carboxylic group of acetic acid, visible at 1540 cm^{-1}, present before neutralisation disappears after neutralisation. In the films Cs and CsE (Figure 3.32) there was distinctive peaks at 3400 cm^{-1} associated with the overlapping stretching vibrations between the groups O-H and N-H. The peaks at 2870 cm^{-1} and 1374 cm^{-1} correspond to the asymmetric stretching vibrations of the aliphatic groups CH and the symmetric deformation vibrations of the groups CH_3, respectively. Other distinctive peaks of the chitosan include the OH bending vibration at 1430 cm^{-1} and the C=O stretching peaks of amides I and IIa 1673 cm^{-1} and 1590 cm^{-1} respectively.

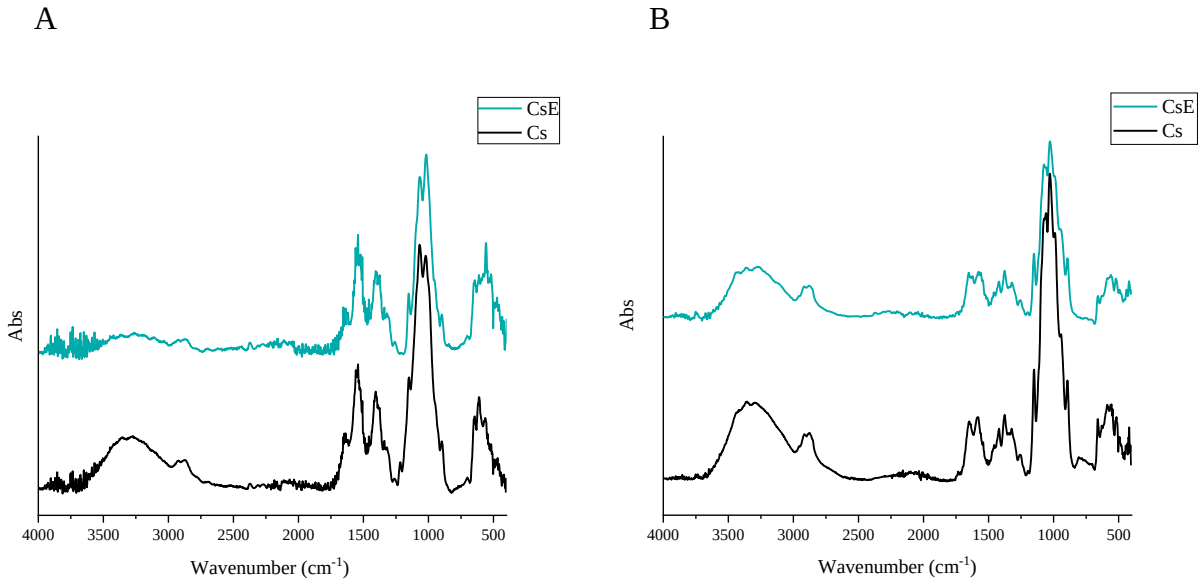

Figure 3.32 FTIR spectra of Cs and CsE A) as prepared and B) after the neutralization step.

In the FTIR analysis of the AgNPs-Cs sample, shown in Figure 3.33, all chitosan characteristic bands are observed, although with some differences in intensity. In particular, there is a significant increase in the intensity of the band at 1651 cm^{-1}, assigned to the bending of the C=O amidate bond. In parallel, there is a slight decrease in the intensity of the band at 1585 cm^{-1}, also associated with the bending of the amino group. These spectral variations suggest a specific interaction between the nitrogen atoms of chitosan and the surface of silver nanoparticles.[187] Also in this case it is possible to notice the decrease the intensity of the typical carboxylic group of acetic acid at 1540 cm^{-1}, following the neutralization process.

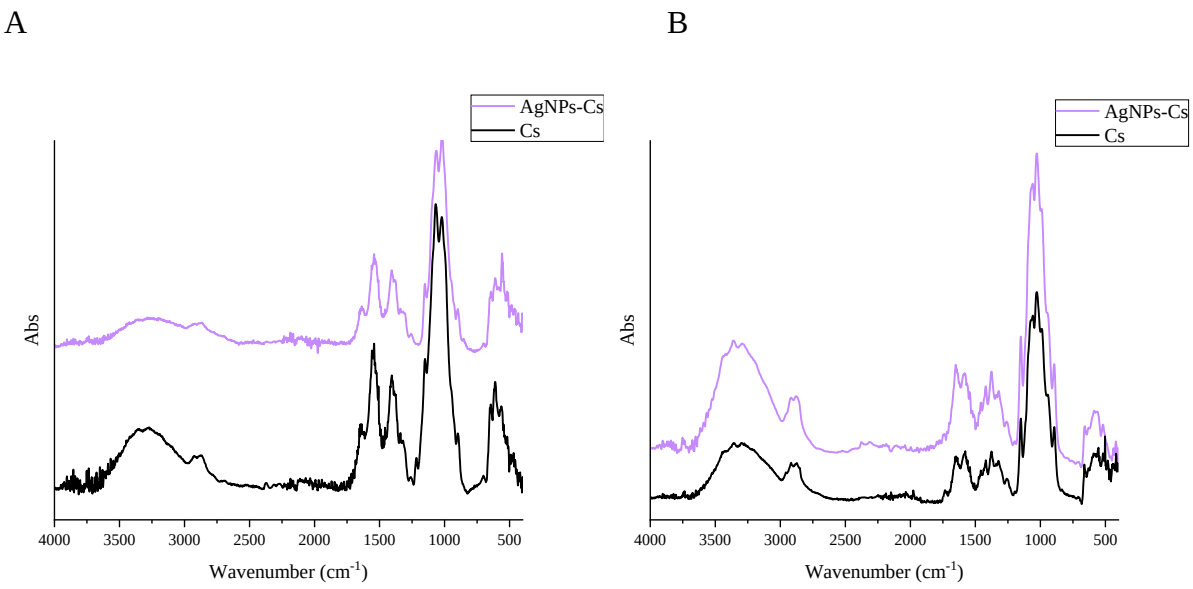

Figure 3.33 FTIR spectra of Cs and AgNPs-Cs films, A) as prepared and B) after the neutralization step.

The X-ray diffractometric analysis, of Figure 3.34, showed two characteristic diffraction peaks for chitosan: a low intensity peak at 2θ 14° and a more pronounced and enlarged peak at 2θ 17°. This last peak, assigned to chitosan, indicates the presence of a semi-crystalline crystal structure and suggests the formation of an intense network of intermolecular hydrogen bonds between the polymer chains, giving the material a certain structural rigidity. [184]

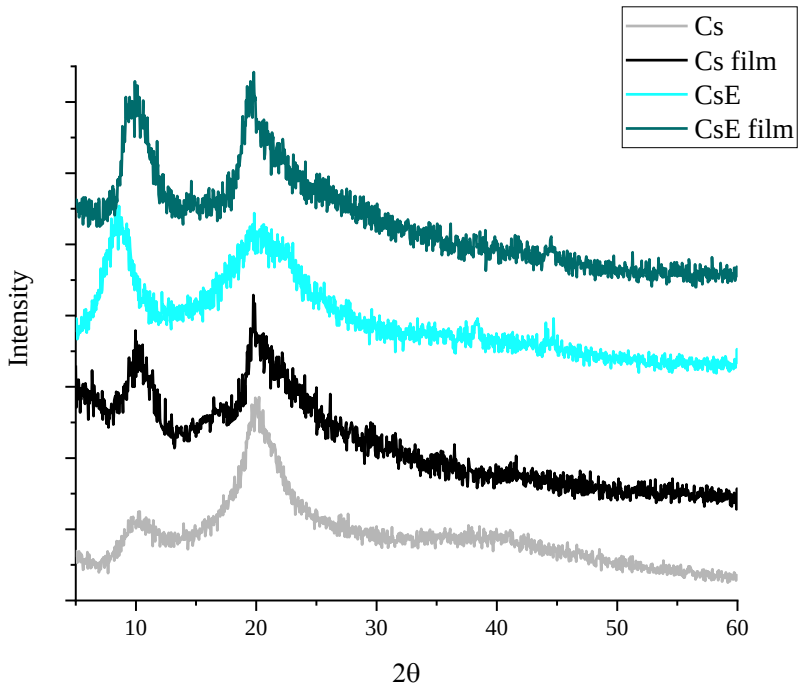

Figure 3.34 XRD spectra of Cs (black), CsE (green) films after the neutralization step, compared with chitosan (grey) and exuviae chitosan (light blue) powder.

In the XRD spectrum of AgNPs-chitosan nanocomposite films, shown in Figure 3.35, a new peak at 2θ 37.8° was observed, corresponding to the crystal reflection (111) of metallic silver. The presence of this peak confirms the presence of silver nanoparticles within the polymer matrix and suggests that nanoparticles have a cubic, face-centred crystal structure (fcc) typical of metallic silver. [185]

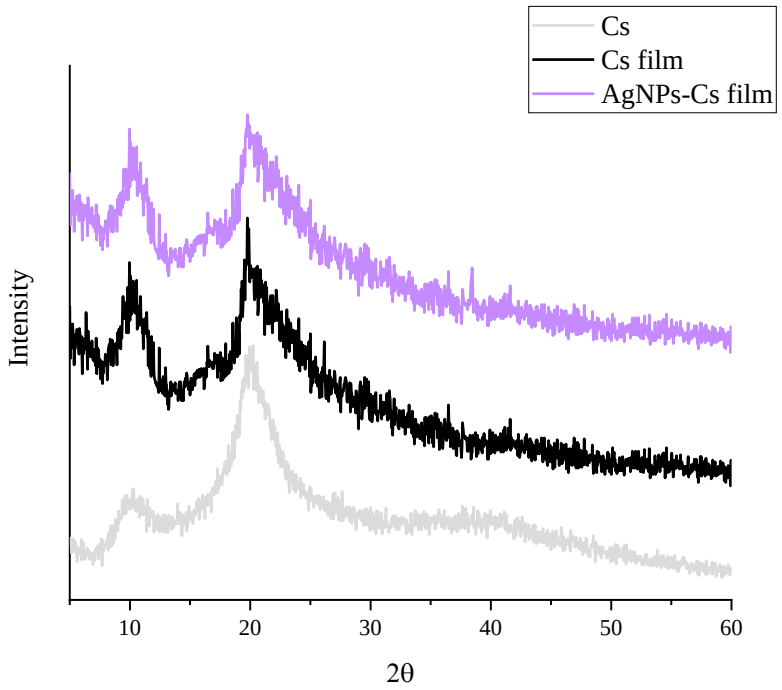

Figure 3.35 XRD spectra of Chitosan powder (grey), Cs (black) and AgNPs-Cs (purple) films, after the neutralization step.

Wetting and hydrophobicity properties of materials can be evaluated by measuring of static water contact angle. Usually, lower contact angles indicate lower hydrophobicity or better wettability of water. From Figure 3.36, the film Cs display a contact angle of 75° to 80°, while the film CsE shows a contact angle of 75° to 85°. Although the error bars overlap, a slight trend towards higher hydrophobicity for CsE than for Cs can be observed, possibly due to variations in their composition or surface structure. However, this difference is relatively small and may not be statistically significant.

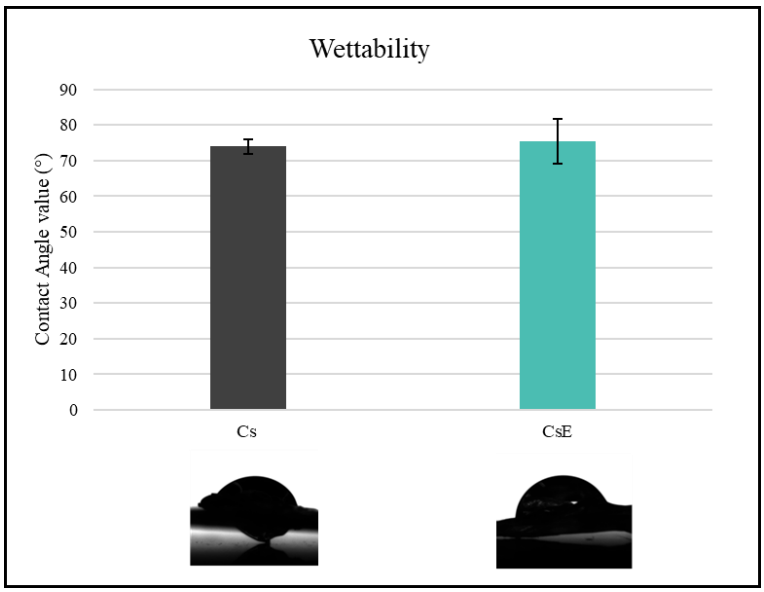

Figure 3.36 Static water contact angle results for all the samples with the related images, reported as example. The error bar is reported as ±SD.

In the Figure 3.37, the measurement of the contact angle of the AgNPs-Cs film is shown, whose value is between 70° and 80° comparable to that reported for Cs; this suggests that Cs that AgNPs-Cs have similar hydrophobic properties and that the presence of nanoparticles does not affect the hydrophobicity of the material.

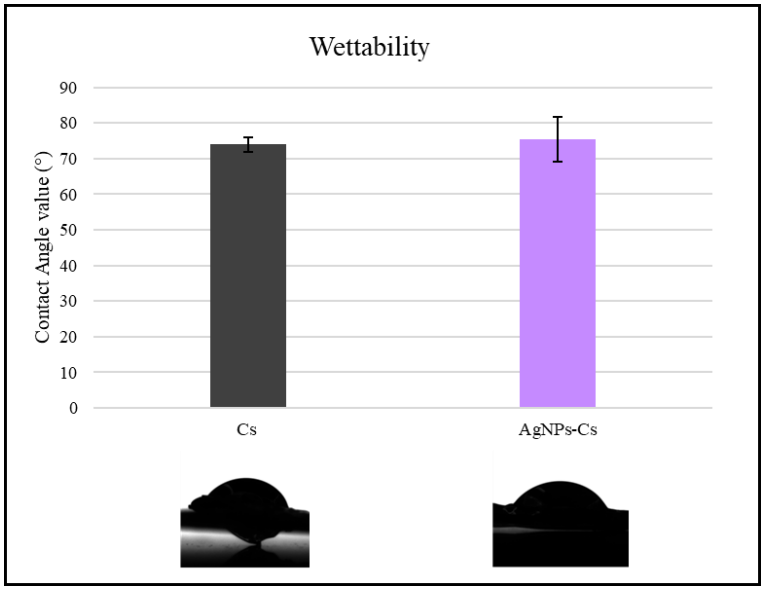

Figure 3.37 Static water contact angle results for all the samples with the related images, reported as example. The error bar is reported as ±SD.

The polymer films obtained showed an exceptional water absorption capacity, from a mean dry weight of 0.0230 g to a mean wet weight of 0.0750 g, corresponding to a swelling index of more than 200% (Figure 3.38). This behaviour suggests a significant affinity of the material for water. Interestingly, the three film types analysed Cs, CsE, AgNPs-Cs showed very similar swelling values. This result indicates that the incorporation of nanoparticles did not significantly affect the intrinsic ability of the polymer to absorb water. In addition, CsE showed a swelling behaviour comparable to that of Cs, suggesting that the extraction process did not impair the hygroscopic properties of the natural polymer.

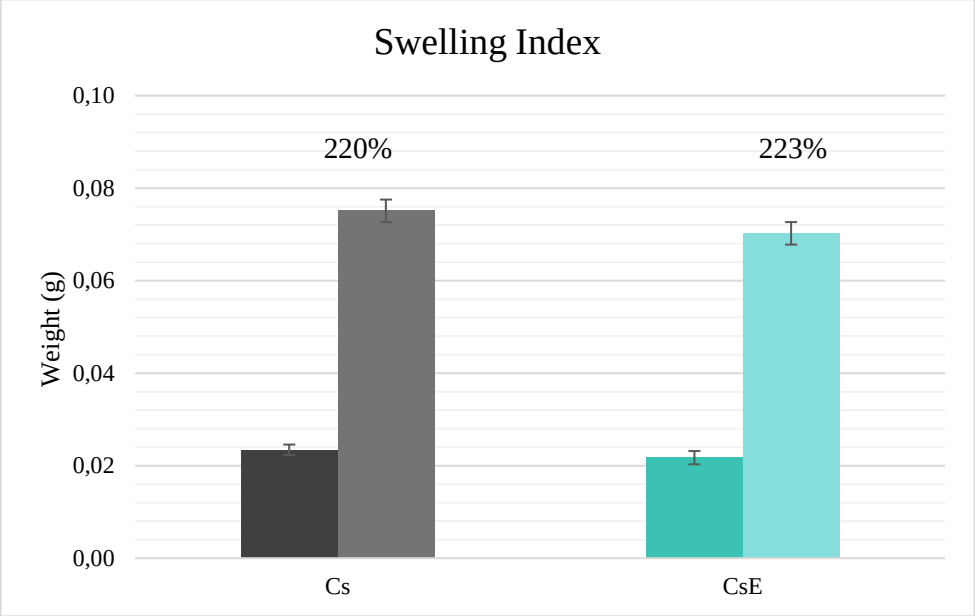

Figure 3.38 Swelling index of the films, in figure are shown, as average value, the weights of the films Cs and CsE dry and the average weights of the films after immersion in water for 2h. The error bar is reported as ±SD.

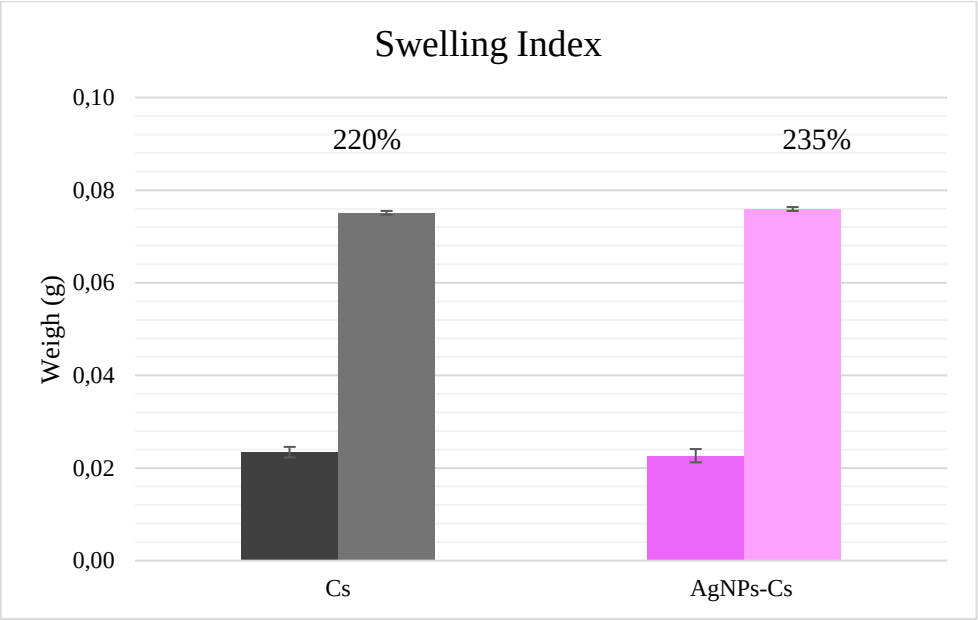

Figure 3.39 Swelling index of the films, in figure are shown, as average value, the weights of the films Cs and AgNPs-Cs dry and the average weights of the films after immersion in water for 2h. The error bar is reported as ±SD.

3.3.3.3 Antibacterial activity

The antimicrobial efficacy of polymer films against two bacterial reference strains: *S. aureus* (Gram-positive) and *E. coli* (Gram-negative) was studied. The test provided significant inhibition of bacterial growth for all films. Figure 3.40 shows a 20% reduction in bacterial growth for both *S. aureus* and *E. coli* when exposed to Cs and CsE films, compared to the control. These data indicate similar antimicrobial efficacy of the two films against both bacterial strains tested.

A B

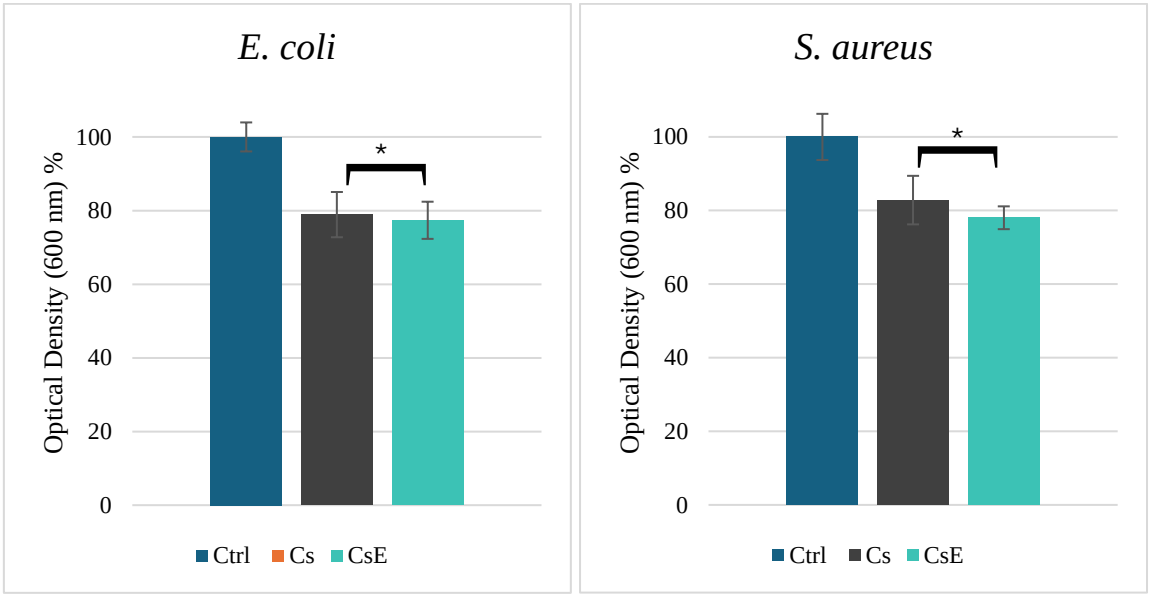

Figure 3.40 Antimicrobial test results for A) *E. coli* and B) *S. aureus*. The bars indicate the bacterial culture absorbance (blue) and the culture absorbance in the presence of Cs (grey) and CsE (green). Data are presented as the mean standard error of three independent biological experimental replicates. (*) indicates significant differences ($p<0,05$) between the absorbance values of the bacterial culture alone and those of the bacteria grown in the presence of the samples.

The analysis of the antimicrobial activity of AgNPs-Cs nanocomposites, presented in Figure 3.41, showed a significant inhibition of bacterial growth for both *S. aureus* and *E. coli* compared to control and Cs film. In particular, a reduction of bacterial growth of about 30% was observed against both bacterial strains tested. These results suggest that the incorporation of silver nanoparticles into the polymer matrix of chitosan has resulted in a significant enhancement of the antimicrobial activity of the material. This synergy is attributable to the known antibacterial properties of AgNPs, which, by interacting with components of the bacterial cell membrane, compromise its integrity and inhibit life processes.[195]

A B

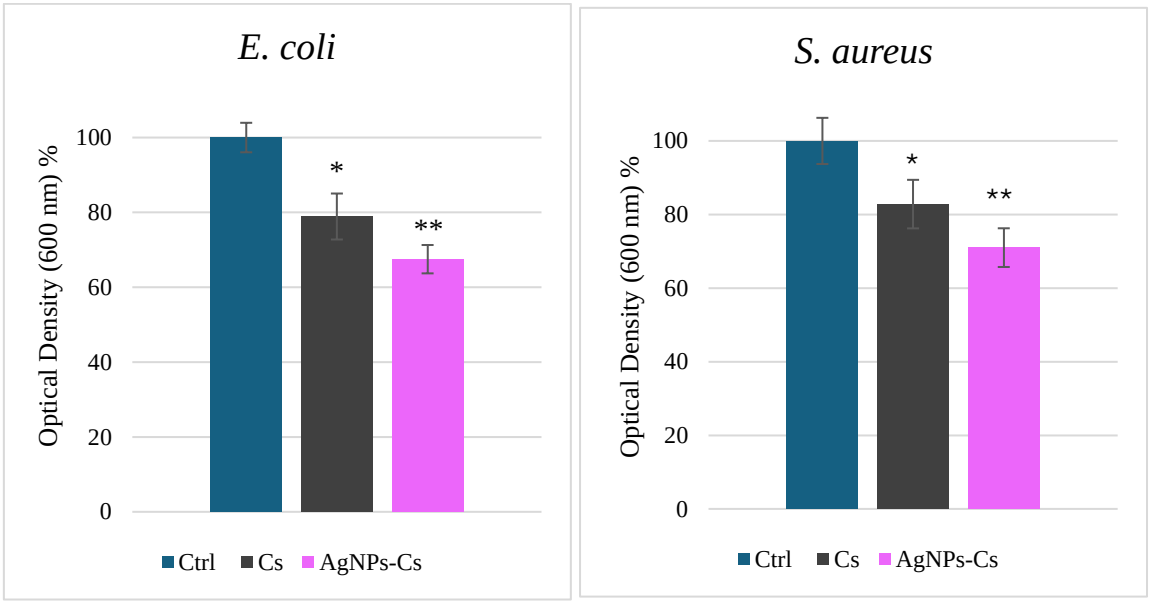

Figure 3.41 Antimicrobial test results for A) *E. coli* and B) *S. aureus*. The bars indicate the bacterial culture absorbance (blue) and the culture absorbance in the presence of Cs (grey) and AgNPs-Cs (purple). Data are presented as the mean standard error of three independent biological experimental replicates. (*) indicates significant differences ($p<0,05$) between the absorbance values of the bacterial culture alone and those of the bacteria grown in the presence of the samples.

These results are in line with other studies where chitosan-based scaffolds enriched with silver nanoparticles (AgNPs) have shown a marked antimicrobial activity against pathogenic bacteria, including *Staphylococcus aureus*, *Escherichia coli*, *Pseudomonas aeruginosa* and *Methicillin-resistant Staphylococcus aureus* (MRSA). In vitro antibacterial tests, conducted using agar diffusion methods and growth inhibition tests, revealed that the incorporation of AgNPs into chitosan-based biomaterials showed a synergistic effect, improving antibacterial properties compared to nanoparticle-free materials. The uniform distribution of AgNPs in the scaffold also allowed a controlled release of silver ions, which improved long-term antimicrobial activity, reducing the risk of bacterial resistance.[196][197]

3.3.3.4 Cytotoxicity test

The biocompatibility of films was tested by WST-8. The cell line chosen to evaluate cytotoxicity was NIH 3T3, murine fibroblasts. NIH 3T3 cells were sown on the films at the bottom of the wells and incubated for several days (1,2 and 3 days) after which viability was assessed by analysis of formazan conversion by mitochondrial enzyme. The conversion of formazan takes place only in cells that have metabolically active mitochondria, which consequently indicates the good health of the cell. From the data shown in the Figure 3.42, we observe an initial slowdown of cell proliferation of cells attached to the Cs and CsE films, where the viability values are about 50% compared to the control in the first two times tested, 24h and 48h; in the last time tested, 72h, a cell viability of more than 90% compared to the control is observed. It is therefore assumed that the observed reduced cell viability is related to low cell adhesion. [198] Cell adhesion is known to be a multiphasic process, initially mediated by non-specific physical interactions (e.g. electrostatic forces and van der Waals forces) and subsequently by specific bonds between cellular receptors and substrate ligands. [199] Chitosan, lacking cell recognition sequences (such as RGD) and receptor-specific interaction domains, has limited adhesion potential. Therefore, it is suggested that cell adhesion to chitosan surfaces occurs mainly through weak electrostatic interactions between the protonated amino groups of chitosan and the anionic (carboxylate and sulphate) groups of membrane proteoglycans. The absence of specific and stronger interactions may justify a lower number of adherent cells and, as a result, lower viability. [200]

A B

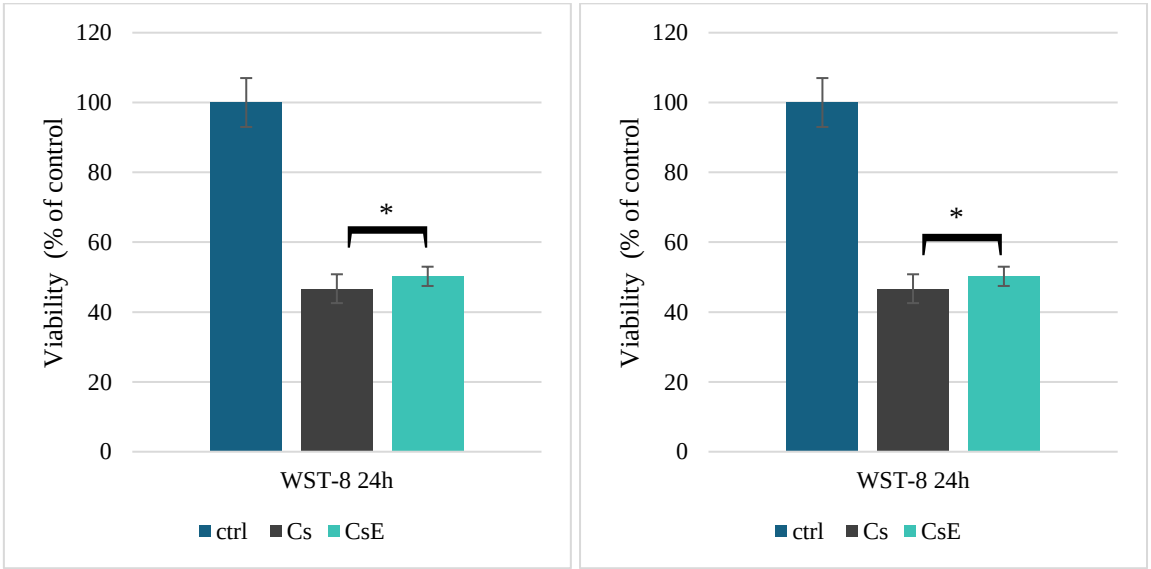

C

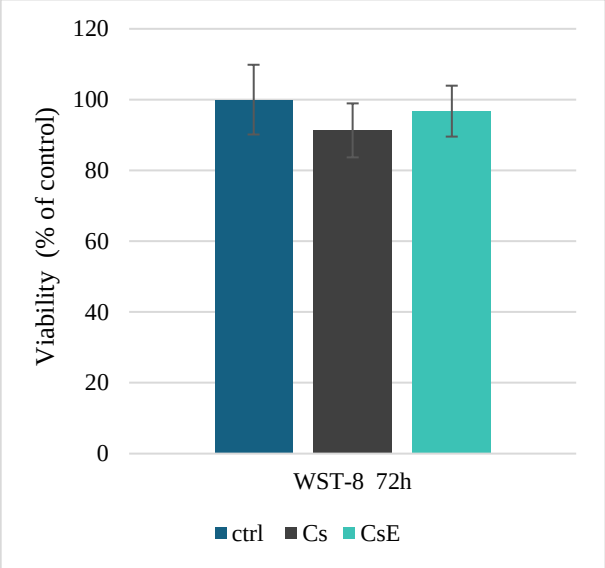

Figure 3.42 Cell viability of mouse embryonic fibroblasts (NIH 3T3) cultured coatings after A) 24h, B) 48h and C) 72h of incubation. Well without sample was used as control. The bars indicate the viability percentage of cells control (blue), in the presence of Cs (grey) and CsE (green). Asterisks (*) denote significant differences ($p < 0.05$).

From the analysis of cell viability in the presence of AgNPs-Cs, shown in Figure 3.43, it is observed that at 24h there is a significant reduction in cell viability, about 20% compared to the control, suggesting an initial limiting impact on the adhesion of the tested material. However, already 48 hours, a partial recovery of viability is noted, with a value of about 30% compared to the control, indicating a possible beginning of proliferation. Finally, at 72 hours, a marked recovery in viability was observed, with the value being about 80% of that of the control. These results indicate that although the material induces initial cellular stress, fibroblasts are able to adapt and proliferate in the long term in the presence of film, demonstrating that the films tested are non-toxic and can be used for biomedical applications.

A

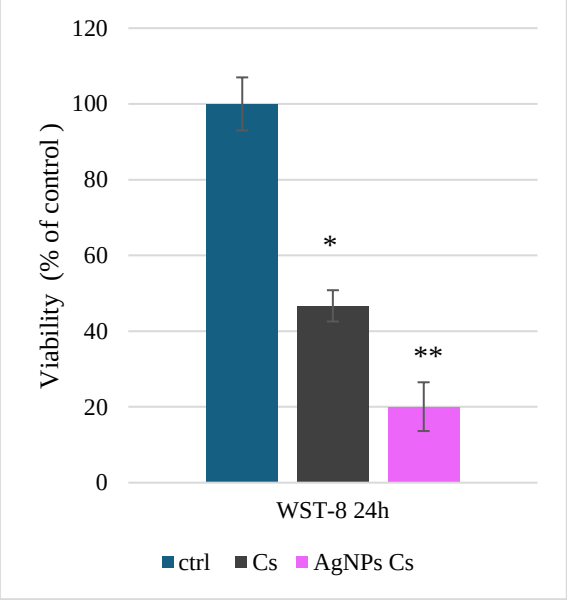

B

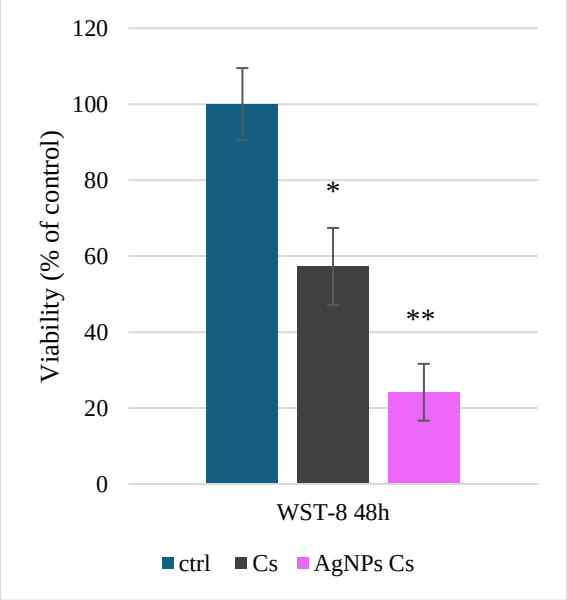

C

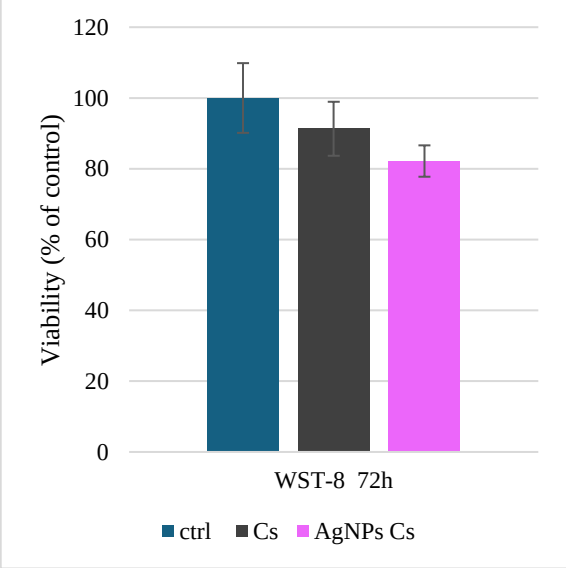

Figure 3.43 Cell viability of mouse embryonic fibroblasts (NIH 3T3) cultured coatings after A) 24h, B) 48h and C) 72h of incubation. Well without sample was used as control. The bars indicate the viability percentage of cells control (blue), in the presence of Cs (grey) and CsE (purple). Asterisks (*) denote significant differences ($p < 0.05$).

The results obtained are consistent with what has been seen in other studies on the same polymer metal scaffolds, where the biocompatibility of chitosan-based scaffolds incorporated with silver nanoparticles (AgNPs) has been amply demonstrated through numerous in vitro studies, which used different cell lines to assess toxicity and cellular response. In particular, cell viability of more than 70% was observed in several skin cell lines, confirming the non-toxicity of these

scaffolds. Human dermal fibroblasts (HDF), responsible for the production of collagen and extracellular matrix components crucial to wound healing, showed no impairment of viability and proliferation in the presence of scaffolds. Similarly, human keratinocytes (HaCaT), which are essential for re-epithelialization of wounds, did not show cytotoxicity and showed increased migration, a process essential for wound closure. In addition, human umbilical vein endothelial cells (HUVEC), involved in angiogenesis, were not interfered with viability and showed a promotion of capillary tube formation, suggesting the potential of these scaffolds in supporting new blood vessel formation [196], [197]

3.4 Conclusion

Colloidal solutions containing silver nanoparticles were produced by laser ablation in liquid, using different concentrations of chitosan. Analysis of the produced nanoparticles showed that the concentration of chitosan present in solution during ablation affects the number and size of particles. In particular, a higher concentration of chitosan reduces the number of larger nanoparticles but at the same time ensures greater stability of the solution, preventing precipitation and aggregation. The physic-chemical characterization of the resulting composite materials showed that the functional groups of chitosan remain unchanged without undergoing structural changes during the synthesis of silver nanoparticles (AgNPs). Among the various concentrations analyzed, the colloidal solution with 1 g/L of chitosan was selected for further studies due to its excellent stability characteristics. Using the same laser ablation technique, spherical nanoparticles of silver and copper, were also produced in both commercial chitosan and chitosan extracted from the exuviae Hermetia illucens, at a concentration of 1 g/L. This procedure led to the synthesis of a biopolymer-nanometallic composite. The biological properties of composites showed higher antibacterial activity than the individual components, biopolymers and nanoparticles, used separately. In composite materials, the antimicrobial activities of the components are combined, increasing the antibacterial effect and causing the death of bacteria through different mechanisms. Finally, the properties of films made from both composite material and chitosan alone were evaluated. Morphological analyses showed no significant differences between the films, with very similar surfaces, thicknesses and swelling capacities in contact with water. However, differences emerge in terms of antimicrobial capacity: silver nanoparticle films inhibit bacterial proliferation to a greater extent for both Gram-positive and Gram-negative species than only chitosan films. On the biocompatibility front, it was found that the presence of silver nanoparticles slightly affects short-term cell proliferation, slowing it down compared to chitosan films; However, this difference is reduced

with the extension of the observation period. The study also focused on the physic-chemical characteristics and biological properties of chitosan obtained from alternative sources, in particular from the exuviae of Hermetia illucens. This type of chitosan has shown chemical properties, such as swelling index and contact angle, and biological activities, including antimicrobial properties and biocompatibility, comparable to those of marine chitosan. As a result, chitosan extracted from the exuviae of Hermetia illucens presents itself as a viable alternative to traditional fish-derived chitosan.

Chapter 4 Electrophoretic deposition (EPD) of composite biopolymers for bone implants applications

4.1 EPD Coating for bone implants

4.1.1 Bone Tissue

Bone tissue is a specialized type of connective tissue that forms the skeleton of vertebrates. It is characterized by a mineralised extracellular matrix, characterized by an organic component composed mainly of type I collagen, which gives flexibility and tensile strength, and an inorganic hydroxyapatite component (a calcium phosphate mineral), which gives hardness and compressive strength.[201] The main functions of this particular tissue are: support and protection, providing a structure for the body and protecting the internal organs; movement; mineral reserve, especially calcium and phosphorus; haematopoiesis, bone marrow is in fact the site of blood cell production. [202] Bone tissue consists of three types of cells each with a specific function. Osteoblasts are cells responsible for the production of the bone matrix, synthesizing and secreting collagen and other proteins that form the osteoid, a non-mineralized matrix. The osteocytes, are osteoblasts that remained trapped in the bone matrix they produced, are essential for the maintenance of the bone matrix and for communication with other bone cells through cytoplasmic extensions called canaliculi. Osteoclasts, large multinucleated cells, reabsorb bone tissue, releasing enzymes and acids that decompose the mineralized bone matrix.[203] Bone tissue undergoes a continuous process, known as remodelling, in which old bone tissue is replaced with new bone tissue; this process involves the coordinated activity of osteoclasts (bone resorption) and osteoblasts (bone formation). This process is essential for repairing microfractures, adjusting blood calcium and adapting to mechanical requirements Bone tissue is therefore a highly dynamic tissue, continuously renewed and shaped to meet the mechanical and metabolic needs of the body.[202]

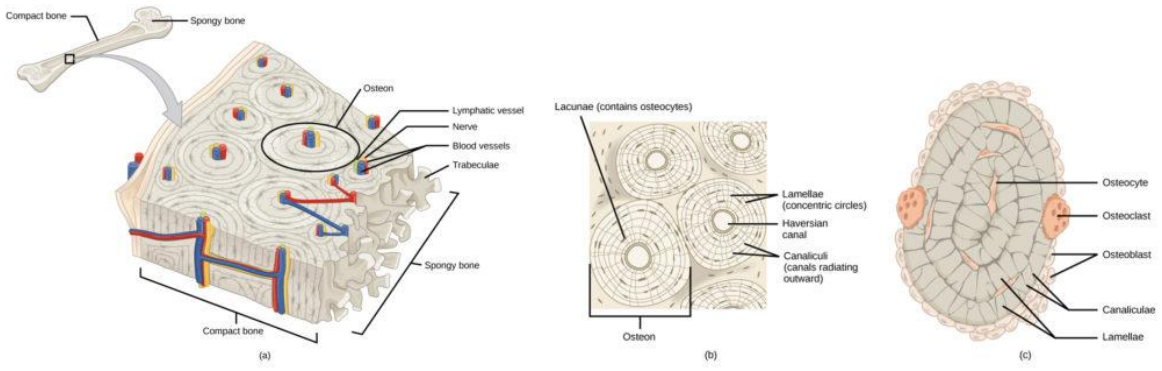

Figure 4.1 Graphical representation of bone tissue. [202]

The process of bone remodelling sometimes fails to repair too extensive damage, as in the case of broken fractures, major osteoporosis, compromised joints, and the use of bone implants to replace or stabilize the damaged bone tissue is necessary. The use of implants is made possible by the ability of bone tissue to integrate the implant, through the process of osteointegration. Osteointegration is the formation of a mechanically solid interface between biomaterial and bone. The implant fuses with the bone to the point that separation is impossible without causing fractures, and there is no relative movement between them.[204] Preimplant osteogenesis can occur at contact or at a distance from the implant. In remote osteogenesis, peri-implant bone trabeculae take place from the host bone to the implant surface. Existing bone tissues provide a population of osteogenic cells that deposit the new bone matrix that, as osteogenesis progresses, approaches the implant itself. In contact osteogenesis, peri-implant bone develops from the surface of the implant to the healing bone. Previously, the surface of the plant was colonized by a population of osteogenic cells.[205] Generally, the process of bone healing around an implant includes three phases: osteoconduction, formation of new bone (De novo bone formation) and bone remodelling. During osteoconduction, undifferentiated osteogenic cells migrate to the implant surface. If cells differentiate before reaching the implant surface, they will synthesize a bone matrix that will not be in contact with the implant; if they do not differentiate, a mineralized matrix will be synthesized on the implant (contact osteogenesis) during the formation phase of the new bone.[206] The ability of bone cells to attach to the surface of the implant implies specific interactions with adsorbed proteins, extracellular matrix and cytoskeleton proteins, including collagen type I and V, osteocalcin, serum albumin, fibronectin or vitronectin. This interaction takes place through cadherins and integrins and results in internal signals that induce cell diffusion or migration, as well as cell growth and differentiation.[207]

During the process of osteointegration there is intervention and modulation by the immune system. The temporary matrix acts as a scaffold for the migration of bone cells to the surface of the implant. Neutrophils and leukocytes clean the wound area of damaged bone tissue, along with osteoclasts (cells that reabsorb bone), so that "new" bone can be deposited. Platelets and immune cells release chemoattractant such as transforming growth factor beta (TGF-β), vascular endothelial growth factor (VEGF), or platelet-derived growth factor (PDGF), which affect bone cell migration.[208] In addition, the distribution between the M1 and M2 macrophage phenotype will determine between fibrous encapsulation or osseointegration. M1 macrophages, known as pro-inflammatory, secrete oncostatin M, a cytokine that induces osteogenic differentiation of bone cells. M2 macrophages, also known as anti-inflammatory or

pro-healing, secrete osteogenic/angiogenic molecules and serve as precursors of osteoclasts, the cells responsible for bone resorption (active in bone remodelling processes).[209]

4.1.2 Coating bone implant

To improve their integration with bone and prevent complications such as infections or implant failures, bone implants often have coatings. The coatings used today vary greatly according to the material of which they are made, each material guarantees particular advantages to the coated prosthesis; for example the hydroxyapatite (HA) coating improves bone integration due to its chemical similarity with natural bone tissue; the extracellular matrix coating (collagen), is used to coat implants in order to promote adhesion and proliferation of bone cells; magnesium coating helps to improve bone formation and reduce inflammation; antibiotic-loaded hydrogel coating used to release antimicrobial agents in a controlled manner; improving the effectiveness against infections without compromising biocompatibility; finally, the chitosan coating is valued for its broad-spectrum antimicrobial properties, is used to prevent implant-associated infections and promote bone regeneration.[210]

The properties of chitosan, such as biocompatibility, biodegradability, allergenicity, and especially its broad-spectrum antimicrobial activity make it an ideal, innovative and very promising material for the application of coatings for bone implants.[211] Several studies have been conducted to assess the use of chitosan in bone implant coatings, and the results showed that this polymer prevents the formation of bacterial biofilm by exerting an antibacterial action and promotes bone regeneration by promoting the adhesion and proliferation of osteoblasts allowing the incorporation of the implant in a shorter time.[212], [213] Chitosan is often used in combination with other materials such as hydroxyapatite, collagen or metal nanoparticles.[211]

The proven antibacterial capacity of silver nanoparticles has earned significant attention in bone implant coatings research. The use of silver nanoparticles as an additive in bone implant coatings has been shown to provide long-term protection against infections, reducing bacterial proliferation and preventing infectious complications.[214]–[216] The major limitation of the use of silver nanoparticles in bone implant coatings is the possible toxic effect due to excessive release of silver ions. Some studies have therefore investigated the use of AgNPs associated with chitosan as a bone implant coating, acting both as an antimicrobial agent and as a matrix that moderates the release of silver ions, mitigating the potential cytotoxic effect.[217]

4.2 Electrophoretic deposition

Electrophoretic deposition (EPD) is a technique for creating coatings, laminated structures or functional gradient materials from a stable powder suspension in an aqueous or organic medium. This method uses two electrodes, one of which has the shape of the desired piece, immersed in the suspension of the solid to be deposited. By applying an electric potential difference (V) between the electrodes, the positively or negatively charged particles move towards the opposite electrode to be coated. The electrode on which the deposition takes place can act as a support or be an integral part of the final product (reinforcing fabric, fibres, surfaces to be covered, decorated or protected). In the first case, the material must be electrically conductive and have the desired shape. After deposition, the product should be carefully removed to avoid cracks or leaching of the deposit. If the electrode is part of the final product, it must be made of the required material, preferably conductor. The EPD has several advantages: uniformity of deposition even on complex surfaces, the ability to adjust the thickness of the deposit by changing the parameters of the process, versatility, speed and the possibility of realizing the process at room temperature. The most obvious limit of the EPD is found with the use of aqueous suspensions, in the deposition of which the electrolysis of water takes place, which can cause large and irregularly distributed defects. In addition, electrochemical reactions may occur on the surface of the metal electrode when current passes. For these reasons, many researchers prefer the use of organic solvents, even if they are not environmentally friendly.[218]

4.2.1 Deposition mechanism

The electric field of EPD induces electrophoretic movement of the charged particles in suspension, causing them to move towards the oppositely charged electrode, where they form a coherent coating. EPD is usually carried out in a two-electrode cell (Figure 4.2).[218]

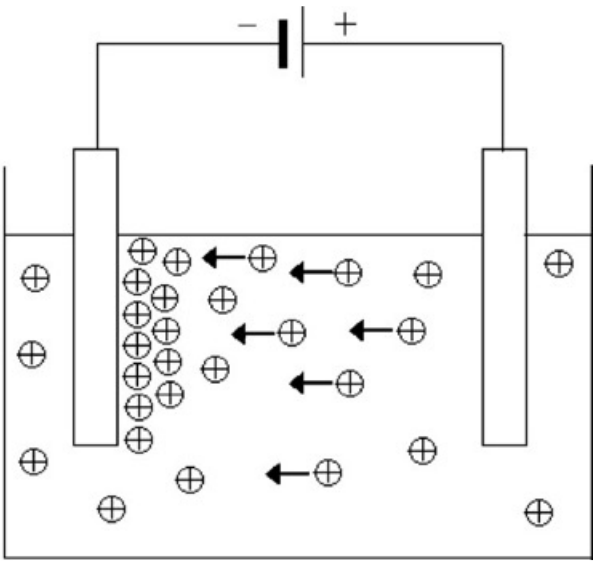

Figure 4.2 typical EPD set-up

The mechanism of electrophoretic deposition involves two phases. In the first phase, an electric field is applied between two electrodes, causing the charged particles suspended in a suitable liquid to move towards the oppositely charged electrode (electrophoresis). In the second phase, the particles accumulate on the deposition electrode, creating a relatively compact and homogeneous film (deposition). To effectively apply this technique, it is essential to produce a stable suspension with charged particles free to move when an electric field is applied. Therefore, EPD can be applied to any solid available as a fine powder (e.g., particle size <∼30 μm) or as a colloidal suspension, including metals, polymers, ceramics, and glasses.[218]

4.2.2 Kinetics

One of the first study on the kinetics of EPD was conducted by Hamaker, who observed that the deposition yield of EPD varies linearly with the applied charge , therefore, in the 1940 he published his first kinetic model,[219] in which the deposit yield (Y, Kg) was proportional to the electrophoretic mobility (μ, m^2 / (V*s)), the electric field strength (E, V/m), the surface area (A, m^2) of the electrode and the particle concentration in suspension (Cs, kg/m^3), integrated over the time of the deposition (t, s):

$$Y = \int_{t_1}^{t_2} \mu E A C_S dt$$

The equation is usually integrated implicitly, assuming μ, E, A and Cs constant during the deposition time. Furthermore, the efficiency factor (f≤1) is often included, in order to considering the possibility that not all the particles delivered to the electrode are incorporated into the deposit; however is considered f≈1 for colloidal stable suspension.[220] Thus the equation becomes

$$Y = f\mu E A C_S t$$

4.4

However, the equation does not consider the decreasing of the Cs during the EPD process. Later Biesheuvel and Verweij[221] conduced a more accurate study. They considered EPD as a undisturbed sedimentation process, describing only the transport phenomena close to the interface suspension-deposit and neglecting all the possible movement in the suspension and the counter electrode. The concentration of the particle in the suspension (s), Cs and the concentration in the deposit (d), Cd are:

$$C_s = \phi_s \rho_p \qquad C_d = \phi_d \rho_p$$

4.5

Where ϕ is the volumetric concentration and ρ is the intrinsic particles density. Thus, the deposition rate is related to the particles velocity and their volumetric concentration by the equation:

$$\frac{\mathrm{d}\delta}{\mathrm{d}t} = -v_c \frac{\phi_s}{\phi_d - \phi_s}$$

4.6

Where δ is the deposit thickness and v_c is the particle velocity at the suspension-deposit boundary. Considering that the velocity of particles in an electrical field is the product of their mobility and the field strength, it is possible to solve equation 4.6 for δ=0 at initial condition:

$$\delta = \mu E \frac{\phi_s}{\phi_d - \phi_s} t$$

4.7

If the deposition yield is written as a functional of the film thickness, it becomes:

$$Y = \delta A \phi_d \rho_p$$

4.8

By the substitution of the equations 4.5 and 4.7 into 4.8 the result is:

$$Y = \mu E A C_d \frac{\phi_s}{\phi_d - \phi_s} t$$

4.9

If $\phi_s << \phi_d$ so if the suspension is sufficiently diluted, ϕ_s is neglected in the denominator in equation 4.9, considering equation 4.5; thus, it is possible to obtain the Hamaker's law equation 4.4.

In all the other cases, generally observed, the correction factor for the concentration (X) is obtainable by the division of equation 4.9 by 4.4:

$$X = \frac{\phi_d}{\phi_d - \phi_s}$$

4.10

X is normally >1; as ϕ_s approaches to zero and *X* approaches to 1.

Another important factor that can affect the deposition yield is the particles charged, because of its influence on the particle mobility. In fact , charged particles in suspension repel ions with same charge (co-ions) and are surrounded by ions with opposite charge (counter-ions), forming a lyosphere.[220] When an electrical field is applied, ions with opposite charge should move in the opposite direction, however the attractive force ions/counter-ions keep them together in the so called Stern layer. Externally to the Stern layer a second diffuse layer of the co-ions and counter-ions takes place, in which the concentration of ions decreases gradually with the distance until the reaching of the equilibrium condition. The resulting particle mobility, called the slipping plane, is related to the dielectric constant, the viscosity of the suspending liquid. As it is shown in the Figure 4.11, the electrical potential at the slipping plane corresponds to the zeta potential ζ. Therefore, particles mobility is related to ζ by the following Henry law [221]:

$$\mu = \frac{2\varepsilon\zeta f_1(ka)}{3\eta}$$

4.11

Where ε is the dielectric constant, η is the viscosity $f_1(ka)$ is the Henry's function, that is function of the double layer thickness (1/k) and the particles core radius (a).

ζ is an indicator of the charge distribution in the suspension, hence the particles velocity does not depend directly on their charge, but on the net charge enclose the lyospherse.[222] Accordingly, the ζ is an indicator of the suspension stability: the higher ζ the thicker the double layer, more stable is the suspension, because the colloids whit low zeta potential tends to coagulate or flocculate.

4.2.3 Parameters Governing EPD

Suspension Parameters	**Process Parameters**
Particle size	Applied electric field
Dielectric constant, conductivity, and viscosity	Deposition time
Zeta potential	Conductivity of the substrate
Stability	
Concentration of solids	

Effect of the Applied Electric Field

The colloidal suspension has a composition with presence of both particles of interest and free ions. This ionic presence results in a partial dissipation of the applied electric field, which constitutes the driving force of the electrodeposition process (EPD), resulting in a reduction of the efficiency of the field itself. However, if the amount of current carried by free ions is insignificant, the applied electric field should be fully utilized for the stable advancement of electrophoresis, as deposition increases directly with the applied potential. While fields that are too low cannot trigger electrophoresis, fields that are too high compromise the quality of the

deposits. It has been suggested that the best quality deposits are obtained with moderate applied fields. Additionally, a high electric field can cause turbulence in the suspension, compromising the deposit quality, and increasing particle speed, preventing them from settling in the best position, which affects negatively the formation of a dense, compact structure of the deposit. [218]

Effect of Deposition Time

The electrophoretic deposition process has two distinct time patterns. Initially, a decreasing trend is observed, predominant at the beginning of the process, when the electrophoretic force exerted on the particles exceeds the forces of viscous and gravitational resistance. This dynamic results in a rapid accumulation of deposited mass, with a rate of deposition that decreases progressively over time. Subsequently, the system evolves towards a constant asymptotic trend, in which the rate of deposition approaches zero. This behaviour is determined by the progressive balance between the electrophoretic force and the resistance and gravitational forces.[218]

Conductivity of the Substrate

In EPD, the quality of the deposited film strongly depends on the conductivity of the substrate. Low substrate conductivity leads to both slow deposition and lack of its uniformity.[218]

4.2.3 EPD of chitosan

The electrophoretic deposition mechanism of chitosan provides that protonated amine groups of chitosan lose their charge in the high pH region at the cathode surface, forming an insoluble deposit. In solution, the salt form of chitosan dissociates into polycations with a charge that depends on its molecular weight and degree of deacetylation (DA), as well as negatively charged counterions. [223], [224]

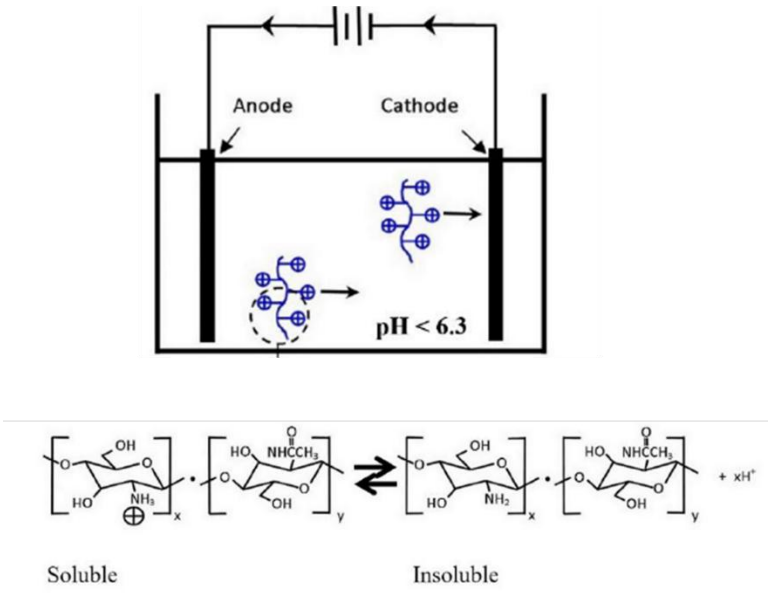

Figure 4.3 Schematic representation of electrophoretic deposition of chitosan.[224]

Several studies on the deposition of chitosan for bone implant coatings have been conducted. In the study, conducted by Pawłowski, the chitosan coatings combined with Eudragit E 100 and silver nanoparticles have shown particular efficacy in inflammatory environments, due to their ability to release silver ions in a controlled way when exposed to reduced pH conditions, typical bacterial infections. This property makes chitosan a promising material for developing "smart" coatings that can dynamically adapt to the body's condition, offering proactive treatment against infections.[225] Finally, in a study conducted by Bartmanski, it assesses the better surface bioactivity and the introduction of antibacterial properties due to the deposition of chitosan and silver nanoparticles on titanium (alloy $Ti_{13}Zr_{13}Nb$); Titanium due to its excellent biocompatibility and bone-like modulus of elasticity, is the material of choice for bone and dental implants. The study found that the surfaces obtained had high roughness and good dispersion of nanoparticles, and that the release of silver ions was sufficient to ensure an antibacterial effect, keeping concentrations below the safe limit for the human organism. Furthermore, nanoscratch tests have shown that chitosan coatings with AgNPs possess adequate mechanical properties, good wear resistance and significant hardness. The use of the polymer combination metal nanoparticles has therefore been shown to be effective.[226]

This chapter will describe the production and physical chemical characterization of chitosan deposits, exuviae chitosan and composite material obtained by electrophoretic deposition; the tests to determine the antibacterial capacity and biocompatibility of the deposits obtained will be explained.

4.3 Experimental

These tests have been carried out at Institute of Biomaterials, Department of Materials Science and Engineering, University of Erlangen-Nuremberg, Heated Prof. Dr.-Ing. habil. Aldo R. Boccaccini.

4.3.1 Preparation of solutions and deposition set-up

The suspensions Cs, CsE and Ag-Cs were magnetically stirred for 30 minutes and then ultrasonicated (using an ultrasonic bath, Bandelin Sonorex, Germany) for 5 minutes. 25 ml of each suspension was taken and placed in a glass beaker for subsequent deposition.

The EPD setup consists of a power supply (TTI EX752M Miltu-mode PSU 75V/150V 300W) with an amperemeter (TTI 1906) connected to the electrodes by copper cables. The electrodes consist of stainless-steel foil AISI 316L (thickness 0.12 mm), are attached to a spacer adjustable by clamps, and immersed in the suspension to be deposited. The suspension EPD is inserted into a glass beaker and positioned at the right height by means of a manually elevator platform. Deposition occurs at constant voltage, with an accuracy of about 0.1V, and deposition time is monitored by timer. The parameters, such as deposition time, electrode distance and applied voltage, were varied until a homogeneous and crack-free deposit was obtained.

Figure 4.4 picture of EPD set up employed.

4.3.2 Film deposition

AISI 316L stainless steel was cut to the dimensions of 30 mm length and 15 mm width, to obtain the substrate suitable for deposition, this was subsequently washed in isopropanol for 5 minutes in the ultrasonic bath, then rinsed in ultrasonic bath for 10 minutes with water and in the end dried. Two SS substrates, one on which the deposit was deposited and the other acting

as an electrode, were placed immersed 15 mm in the solution in order to be coated and insure the connection to the constant voltage power source. The deposition time and electrode distance parameters were varied to obtain the best deposit in terms of homogeneity.

Table 4.1 List of coating produced, with name, origin solution and deposition parameters.

Sample	**Suspension**	**ddp**	**Electrode distance**	**Dep. time**
Cs	Chitosan (1g/L)	10 V	1 cm	1 min
CsE	Exuviae Chitosan (1g/L)	20 V	1 cm	1 min
Ag-Cs1	Cs-AgNPs (1g/L- 8,9µg/ml)	10 V	1 cm	1 min
Ag-Cs2	Cs-AgNPs (1g/L- 8,9µg/ml)	10 V	1 cm	2 min

4.3.3 Physico-chemical characterization

Fourier transformed infra-red spectroscopy (FTIR)

Infrared spectra were collected with a Nicolet 6700 spectrometer operating in ATR mode, by collecting 64 scans at 4 cm^{-1}, in the 4000 to 400 cm^{-1} wavenumber range.

X-ray diffraction

The XRD patterns were obtained using the Rigaku, (MiniFlex 600) diffractometer, using Cu-Kα radiation at 40 kV and 32 mA. Diffraction patterns were acquired in the 2θ range of 5°-60°, with a step size of 0.040° and a time per step of 4 s.

Contact angle measurement

The wetting behaviour of coatings was evaluated by contact angle measurement for each coating using the KRÜSS DSA30 drop shape analyser. Five drops of distilled water with a volume of 3 µl were dropped on the centre of each sample to avoid any effects from the edges. Then a mean value and the standard deviation of the contact angle were calculated.

SEM-EDX

A scanning electron microscopy (SEM) equipped with an energy dispersive X-ray (EDX) analyser (SEM Carl Zeiss Auriga with EDS, X-MaxN Oxford Instruments) was used to study the surface morphology and elemental composition of coatings. Before the observation the samples were coated with gold layer (around 15nm) by QUORUM model Q150T, to prevent sample charging during images acquisition.

High-definition optical microscope

High-definition optical microscope LEICA DM6M operated with the software LEICA LAS X Materials Science (version 5.2.0.26130), with automatic control of its various components has been employed. The images reported were acquired using an external EL6000 fluorescence UV source, a motorized table (Scanning stage mot., DM4-6, 100x100,2 mm with 10 nm resolution) and a HC PL FLUOTAR 100 lens (NA 0.90). 3D images of the samples were obtained by capturing 28 x, y-plane images with a difference in height between one and 72 nm. The scan range of images acquired along the z-axis was equal to 2,016 nm. In order to highlight the 3D characteristics of the images obtained, the values associated along the z-axis were amplified by a factor of 10 and represented with the associated dimensions by the false colour bars shown.

Atomic force microscopy AFM

The AFM analysis of deposits obtained on stainless steel was carried out with the atomic force microscope PARK XE-120 of the Park System in the "no contact mode" and processed with the XEI software. The roughness was calculated as Surface Area Ratio:

$$Surface\ Area\ Ratio(\%) = \frac{Area_{eff} - Area_{geom}}{Area_{eff}} x\ 100$$

This value is the percentage increase of the area actually scanned from the tip of the instrument compared to the geometric one. From each deposit 4 different magnifications 20µm x 20µm, 10µm x 10µm, 5µm x 5µm, 3µm x 3µm were acquired for 3 different sites of the coating in order to mediate the measured roughness values.

Bending test for qualitative adhesion evaluation

The mechanical properties of the coating were evaluated qualitatively through cyclic bending test. During this test, the coated substrate was bent around an axis of 180° until the coated surface became parallel to the other half of the substrate. Subsequently, the substrate was folded back to its original position before starting the next bending cycle. Over the entire process, the

distance between the two halves of the folded substrate was maintained constantly less than 2 mm.[227] SEM images have been acquired in the region of maximum tensile strength.

4.3.4 Biological test

Antimicrobial test

The antimicrobial activity of coatings against the gram-positive bacteria Staphylococcus aureus (S. aureus) and gram-negative Escherichia coli (E. coli) was evaluated. A suspension of S. aureus and E. coli bacteria was inoculated into a sterile Lysogeny broth (LB) medium overnight. The optical density was then adjusted to 0.015. Aliquots of the bacterial suspensions were added to the samples, that were previously sterilized by UV, immersed in sterile LB; the stainless steel uncoated that was used as a control group. After a 24-hour incubation at 37 ºC, these extracts were completely homogenised and rates from 100 µl to 96 wells (n = 3) were added.

This test was also performed by incubating the coating for 24 h at 37 °C in sterile culture medium before the next inoculation of bacterial strains.

The optical density measurements were performed on a microplate reader (PHOmo, anthos Mikrosysteme GmbH, Germany) at 600 nm.

Viability: WST-8 test

Commercially available MG63 human osteoblast-like cells were cultured in dulbecco's modified eagle medium (Gibco) supplemented with 10% (v/v) heat inactivated FBS, 200mM L-glutamine, 100 units/mL penicillin and 100 µg/mL of streptomycin, at 37°C in a humidified atmosphere of 5% CO_2. The growth media was changed every 2 days. The cells were washed with PBS and isolated from the culture flask through trypsinization (0.25% trypsin-EDTA), suspended in fresh culture media, and used to access the bone cell viability on bare.

Prior to these assays, the samples were sterilized with UV 1h per side and washed with sterile PBS. In order to assess the cytotoxicity of the samples, the cells were seeded at a density of $1x10^4$ cells/well, and incubated for 24, 48 and 72h, at 37°C in a humidified atmosphere of 5% CO_2. Negative controls were assigned to cells cultured on stainless steel without coating. Each coating has been tested in triplicate. At the end of the incubation time, the culture medium was removed and washed with phosphate buffer solution (PBS), then 300 µl of WST-8 reagent (1% reagent solution WST-8 (Sigma-Aldrich) and 99% complete fresh medium) have been added to each well and the cells have been incubated for ~2 hours at 37 ºC and 5% CO2. During the incubation WST-8 (water-soluble tertrazolium salt) was reduced to an orange-coloured formazan by mitochondria. After incubation, 100 µl of the solution was transferred from each

well to a 96-well plate. The absorbance was measured at 450 nm using an Omega FLUO star microplate reader (BMG Labtech) UV-Vis spectrometer.

4.4 Results and Discussion

4.4.1 Optimization EPD parameter

A deposit can be considered optimal if it meets some requirements: homogeneous distribution, good adhesion to the substrate, good wettability and lack of superficial imperfections. With the aim of obtaining good coating the EPD parameters have been optimized from those considered optimal in the work of Bartmański, that is 1 minute 10V and 1 cm distance of the electrode, in which unlike was in the different substrate used [226]. The first step was to vary the potential difference (ddp) (10 V , 20 V and 30 V) while maintaining stable deposition time and electrode distance, it emerged that with the applied ddp increase there was an increase in the formation of surface imperfections in the deposit, in particular in the field obtained at 20 V has surface ripples of circular nature on the surface of the deposit was obtained, conversely at 30 V has the same ripples but more marked way were observed. The second step was to evaluate the influence on the coating of the deposition time (1, 2 and 3 minutes), kept constant the ddp and the distance of the electrodes. Very similar to what has been seen for the ddp with the increase of the deposition time there has been an increase of the presence of superficial ripples on the deposits. The presence of these superficial imperfections is due to the electrolysis of the water that leads to the formation of gas to the electrodes during deposition, with subsequent incorporation of gas bubbles in the deposits and consequential formation of low-quality deposits; these deposits have in fact holes, lack of adhesion to the substrate and poor homogeneity. The best deposition parameters were found to be 1 minute, 10 V and 1 cm, the deposit obtained in this condition does not in fact have superficial imperfections that can compress subsequent applications.

Table 4.2 Optical microscope images of coating surfaces.

Suspension	**ddp**	**Electrode distance**	**Dep. time**	
Chitosan	30 V	1 cm	1 min	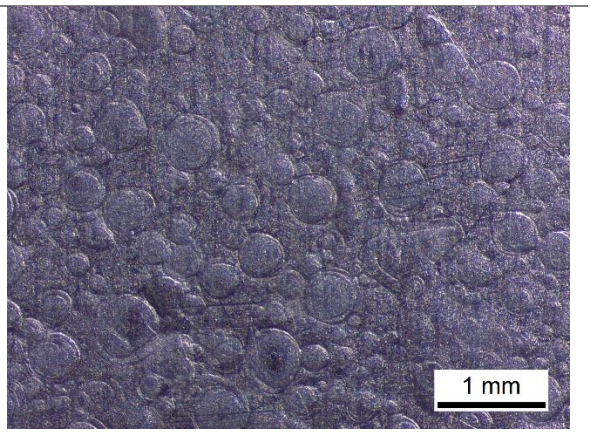
Chitosan	20 V	1 cm	1 min	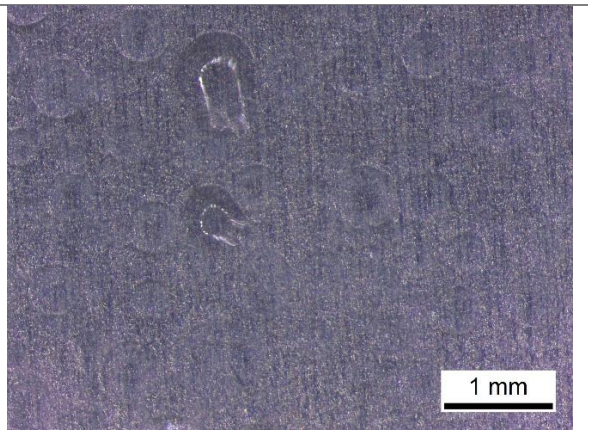
Chitosan	10 V	1 cm	1 min	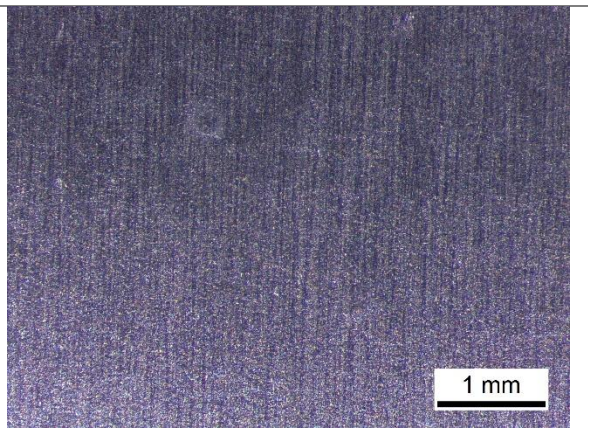

Chitosan	10 V	1 cm	2 min	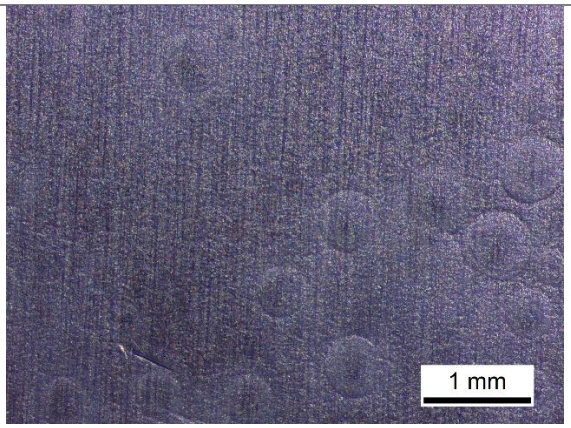
Chitosan	10 V	1 cm	3 min	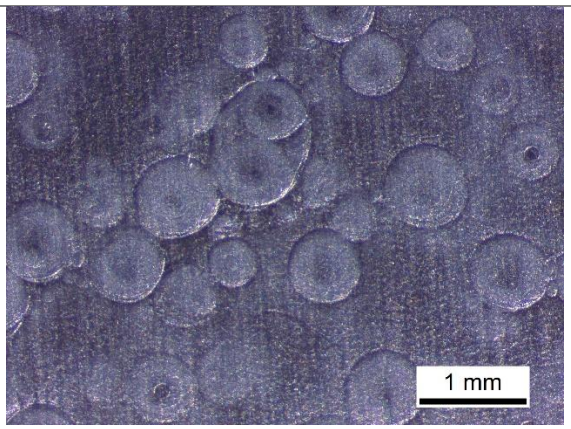

4.4.2 Physico chemical characterizations

All coatings prepared by EPD as described in Table 4.1 were characterized by FTIR, XRD and SEM techniques. FTIR and XRD spectra of commercial Cs powder (C-Cs) are reported for comparison. FTIR spectra of Cs, CsE, Ag-Cs1, Ag-Cs2 and C-Cs are reported in Figure 4.5. All coatings present all the signal characteristic of the Cs functional groups. In particular, the broad band at 3400 cm^{-1} is associated with the stretching vibrations of O-H and N-H groups. The peaks at 2870 cm^{-1} and 1374 cm^{-1} correspond to the asymmetric stretching vibrations of the aliphatic CH groups and the symmetric deformation vibrations of the CH_3 groups, respectively, whereas other distinctive peaks are the OH bending vibration at 1430 cm^{-1} and the C=O stretching peaks of amides I and II at 1673 cm^{-1} and 1590 cm^{-1} respectively.

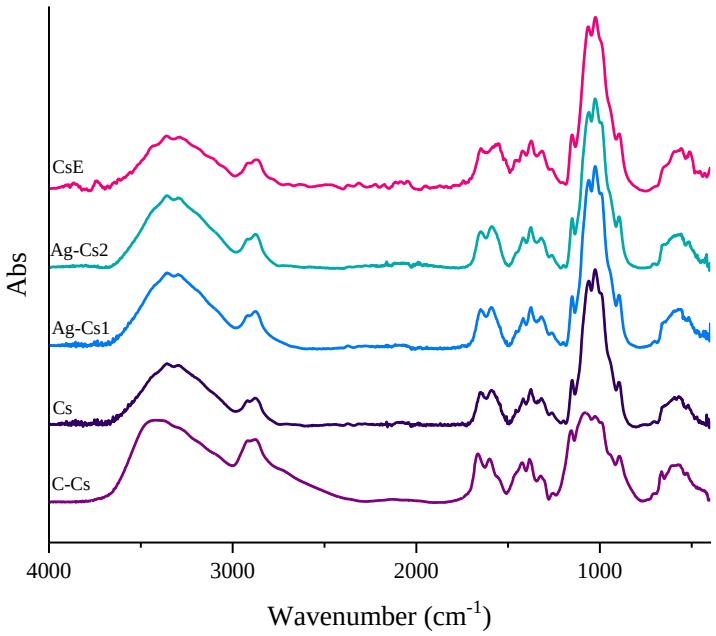

Figure 4.5 FTIR spectra of CsE, Ag-Cs2, Ag-Cs1 and Cs respectively pink, green, light blue and blue, comparted with C-Cs, purple.

X-ray diffraction spectra Cs, CsE, Ag-Cs1, Ag-Cs2 and C-Cs are reported in Figure 4.6. All coatings present the broad band of Cs centred at 20° .[228] In the Ag-Cs coatings, it can be observed a weak signal at 37.8° that can be associated to the (111) crystal planes of Ag. This band is more visible in Ag-Cs2 spectrum.

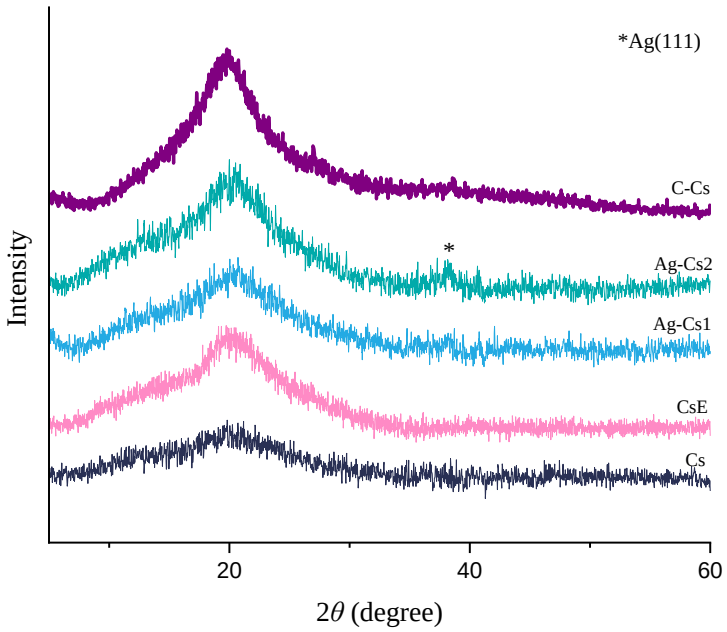

Figure 4.6 XRD spectra Cs, CsE, Ag-Cs1 and Ag-Cs2 respectively blue, pink, light blue and green comparted with C-Cs, purple.

Wetting and hydrophobicity properties of materials can be evaluated through the water contact angle. Usually, lower contact angles indicate lower hydrophobicity or better wettability of water. The steel used as substrate has a contact angle of between 90° and 100°, the presence of the deposits improves wettability by lowering the contact angle. More specifically, the coatings Cs and CsE have a contact angle between 60° and 70°. The deposits obtained from AgNPs@Cs solution show a trend in agreement with the deposition time, as time increases there is a lowering of the contact angle values, ranging from 80°±5° and 70°±7° for depositions of 30 and 45 sec, to 65°± 5° for deposits obtained with deposition of 1min, as shown in Figure 4.7. Several studies indicate that to achieve the best cellular adhesion, the contact angle of the coatings should fall within the range of 40° to 70°.[229] However, it is important to note that this range may vary depending on the type of cell considered [230]. In the context of bone cells, specifically, it has been suggested that the ideal range is between 35° and 85°, with an optimal value of 55°[231]. As a result, it emerged that Ag-Cs1 and Ag-Cs2 tended to approach the upper limit of this requirement.

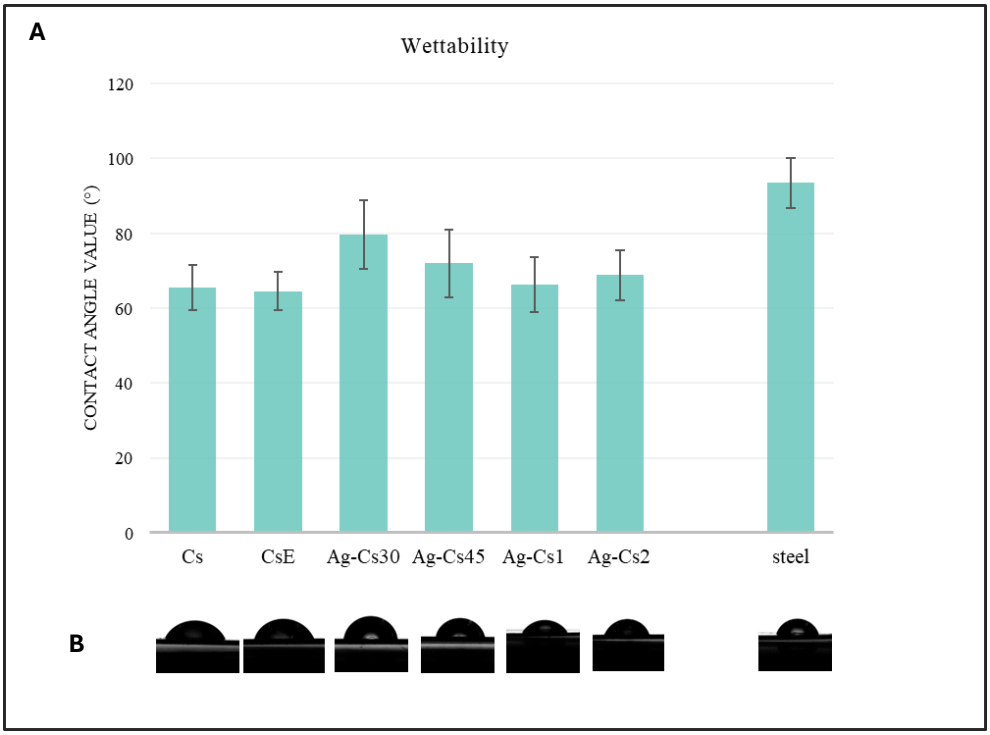

Figure 4.7 A) Average contact angle of water droplets coating, B) Profiles of water droplets Cs, CsE, Ag-Cs30, Ag-Cs45, Ag-Cs1, Ag-Cs2 and steel immediately after deposition.

SEM images (Figure 4.8) show a very similar surface morphology for all coatings produced that result almost compact and homogeneous. It is also noted the presence of shallow cracks in all deposits except the CsE and Ag-Cs2 in which the cracks are sharper and deeper. By SEM cross section (not shown) it was possible to evaluate the thicknesses of the various coatings, (Table 4.3), form which emerges the clear correlation between deposition time and thickness.

Table 4.3 Deposition thickness

Sample	thickness
Cs	4,1 µm
Ag-Cs30	2,9 µm
Ag-Cs45	5,1 µm
Ag-Cs1	7,1 µm
Ag-Cs2	14,4 µm
CsE	4,1 µm

A

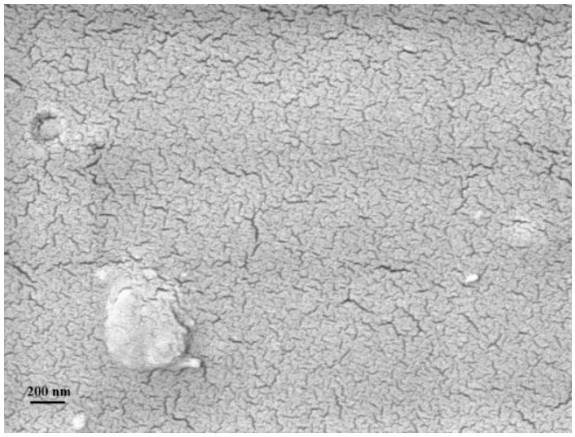

B

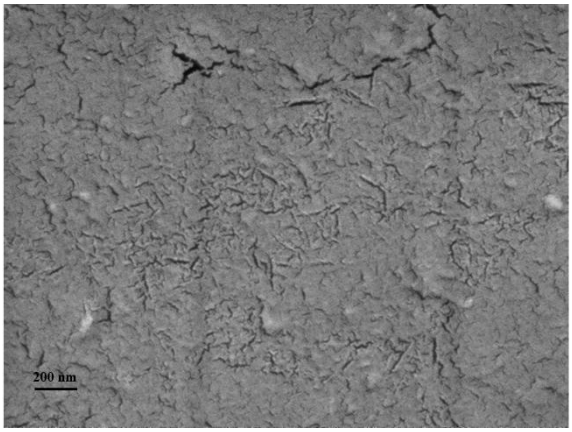

C

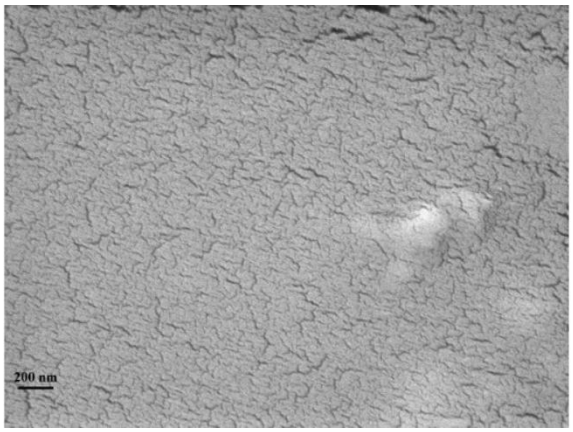

D

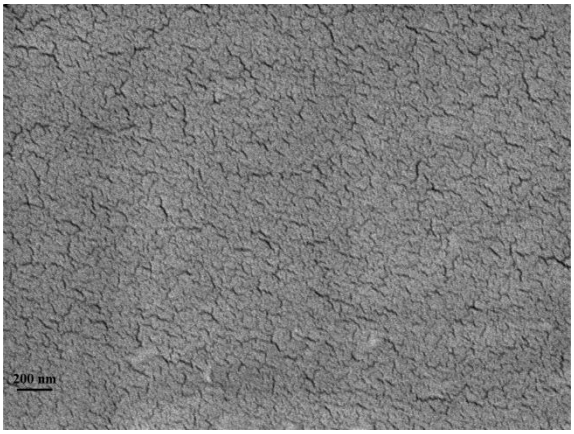

E F

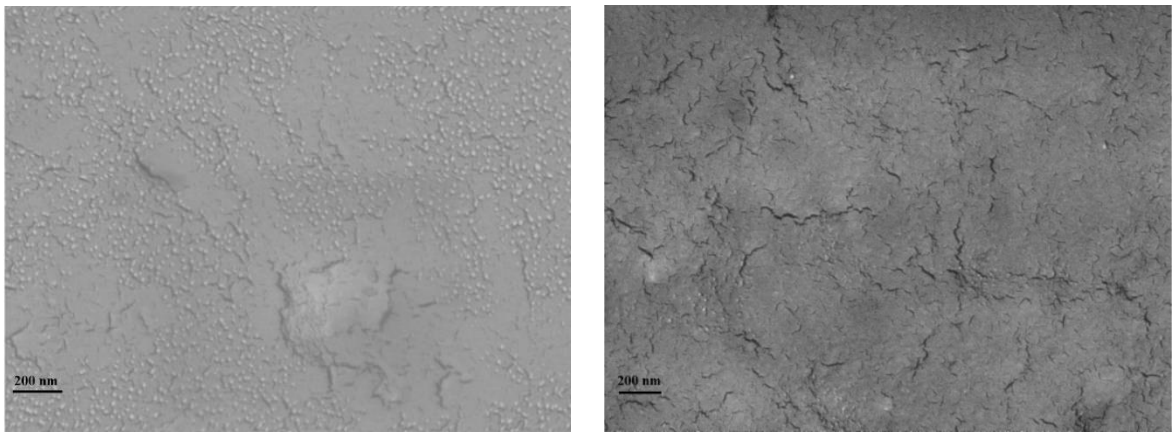

Figure 4.8 SEM images of, A) Cs, B) CsE, C) Ag-Cs30, D) Ag-Cs45, E) Ag-Cs1, F) Ag-Cs2.

Optical microscopy was used to obtain 3D images of the deposit surface, specifically the Cs, Ag-Cs1 and Ag-Cs2 deposits were analysed. Three-dimensional images, obtained by processing several images, provide a detailed representation of the surface of the samples analysed. The Cs deposit (Figure 4.9 A) shows a relatively uniform surface morphology, with a roughness distribution appearing constant. The absence of particular irregularities or inclusions suggests a compact and homogeneous structure of the material. The AgNPs-Cs1 sample (Figure 4.9 B) has a slightly more complex morphology, with variation in surface morphology compared to Cs deposit. In particular, there is an increase in surface roughness and a greater heterogeneity of the structure, with areas of different density and more pronounced morphological micro-characteristics. These morphological differences can be attributed to the presence of silver nanoparticles, which influence the growth and organization of the polymer matrix of chitosan during deposition. The AgNPs-Cs2 sample (Figure 4.9 C) shows a marked variation in surface morphology compared to the Cs and AgNPs-Cs1 deposits. In particular, there is a decrease in surface roughness and greater homogeneity of the structure. This difference, particularly marked in the sample, can be attributed to the longer deposition time.

A

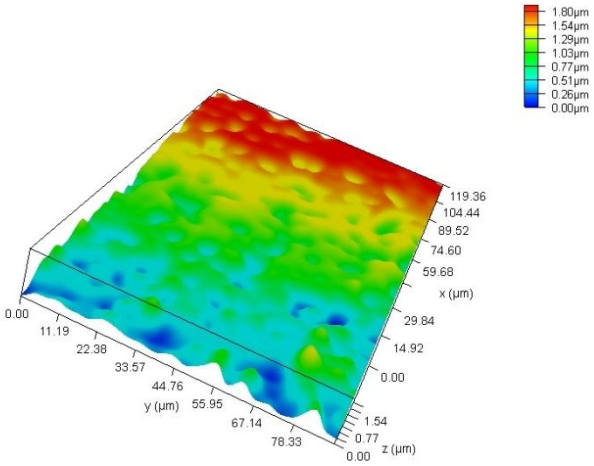

B

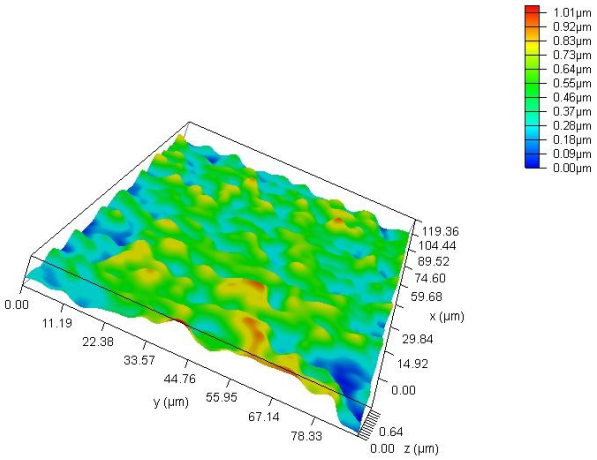

C

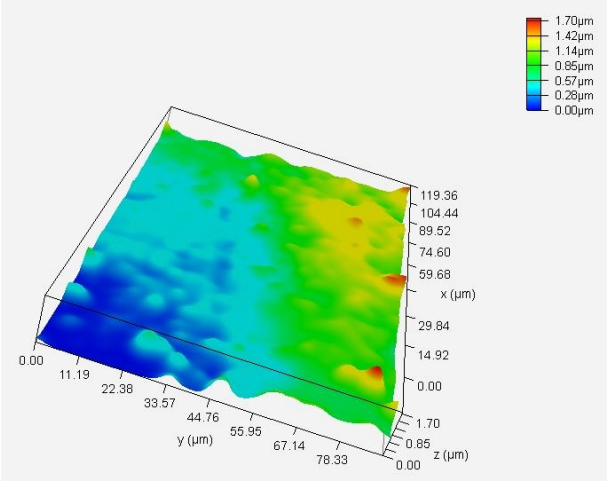

Figure 4.9 coating surface images: A) Cs, B) Ag-Cs1, C) Ag-Cs2.

The surface and more specifically the roughness of the deposits Cs, CsE, Ag-Cs1 and Ag-Cs2 were analysed by AFM and compared with SS, Figure 4.10, where 5µm x 5µm acquisitions are shown, it is possible to note as Cs, Ag-Cs1 and Ag-Cs2 have a similar surface with material deposited uniformly in larger globules than those visible in the CsE deposit, which on the contrary has agglomerates of material always laid out homogeneously as in the others, but of smaller size. The roughness of all the deposits analysed, expressed as area ratio (%), data reported in the Table 4.4, appear to be comparable with each other and with the roughness of the uncoated substrate, the deposits thus seem to adhere to the surface without substantially changing its surface morphology.

A

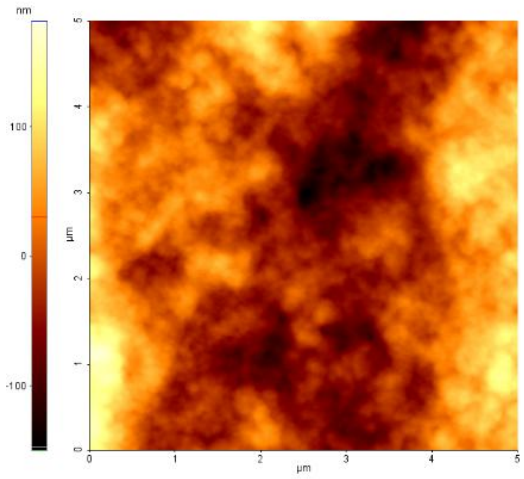
nm
100
0
-100
µm
0
1
2
3
4
5

B

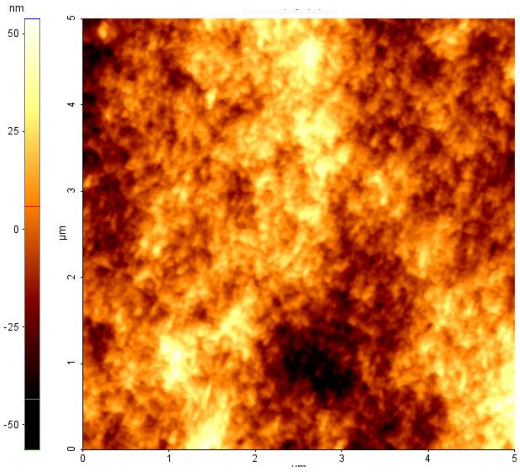
nm
50
25
0
-25
-50
µm
0
1
2
3
4
5

D

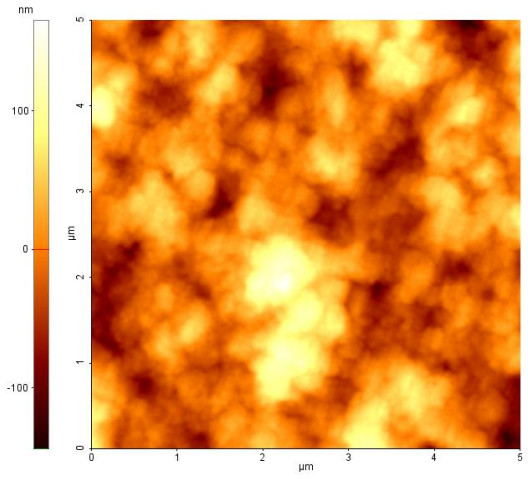
nm
100
0
-100
µm
0
1
2
3
4
5

E

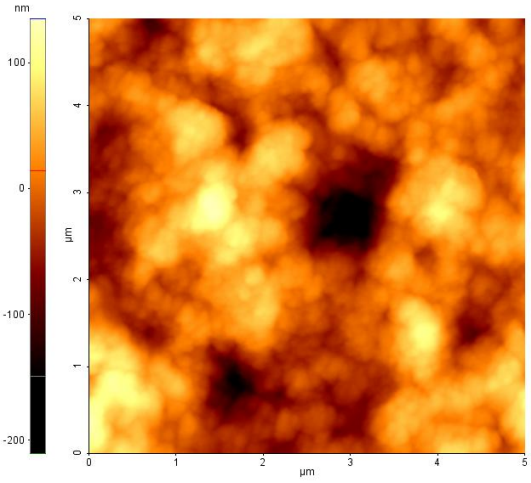
nm
100
0
-100
-200
µm
0
1
2
3
4
5

F

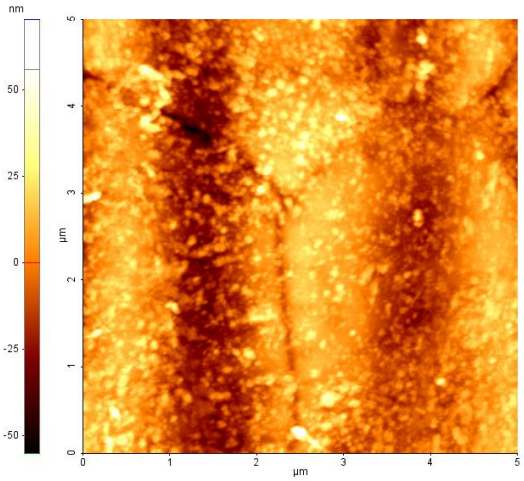
nm
50
25
0
-25
-50
µm
0
1
2
3
4
5

Figure 4.10 AFM coating surface images: A) Cs, B) CsE, C) Ag-Cs1, D) Ag-Cs2, F) SS

Table 4.4 Roughness value of deposits obtained from AFM analysis.

Sample	Surface Area Ratio (%) 5μm x 5μm
SS	5.17
Cs	5.30
CsE	3.19
Ag-Cs1	5.79
Ag-Cs2	4.07

The composition of the coatings, determined by EDX analysis, data reported in table 4.5, shows the presence of the polymer elements (C, O, N) in all deposits; from the figure it is possible to see the presence of silver which, indicates that the AgNPs have been successfully transferred during the EPD process.

Table 4.5 EDX elemental analysis

Element	**Cs**	**CsE**	**Ag-Cs30**	**Ag-Cs45**	**Ag-Cs1**	**Ag-Cs2**
C	32,5	32,6	34,7	34,8	33,05	31,8
O	12,6	13,42	7,7	10,2	11,1	12,2
N	54,8	53,9	56,9	54,2	55,07	54.96
Ag	/	/	0,51	0,67	0,80	0,89

All the elements concentrations are expressed in wt%

The cyclic bending test assess the quality of adhesion between the coating and the substrate [227]. Figure 4.11 shows the cyclically bent surfaces of the coatings in the region where the tensile strength is at the maximum. Cs and CsE after 10 bending cycles show a relatively compact surface with few micro-cracks and loose areas on the edge of the coating. No visible cracks or detachments of the Ag-Cs45 coating were observed after 10 bending cycles. Ag-Cs30 and Ag-Cs1, after the test, have cracks and some slight lifting of the coating layer. The Figure 4.11 (F) clearly shows cracks and lifting of the Ag-Cs2 coating after 10 bending cycles. Detachment of the coating during the cyclic bending test can be attributed to the thickness of the polymer leading to less flexibility of the coating. Therefore, reduce the deposition time to

reduce the thickness of the deposit, could be an ideal compromise to achieve high adhesion to the substrate and reduce the formation of cracks.

A

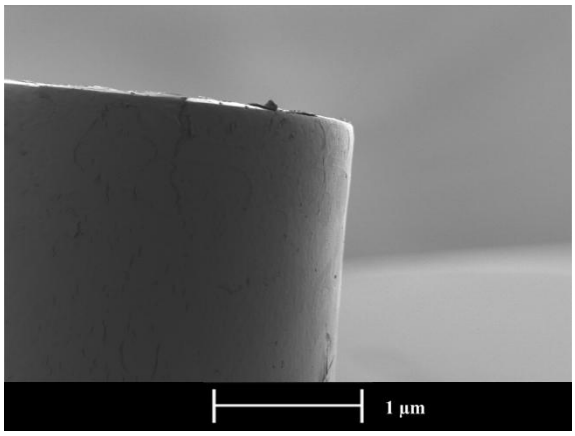

B

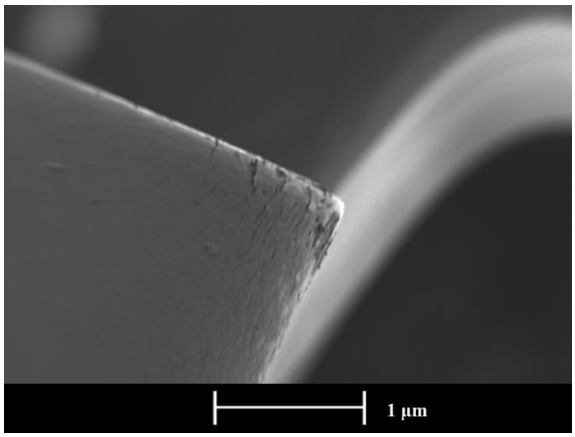

C

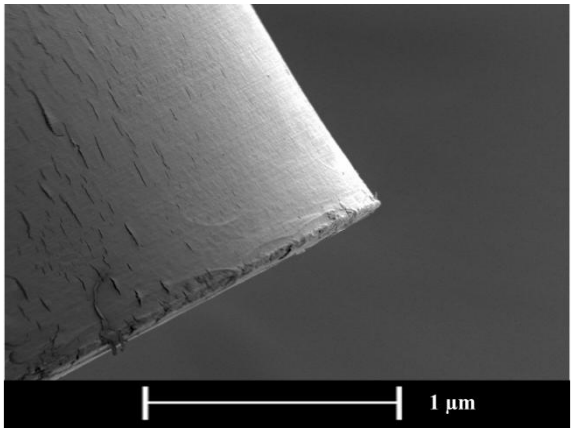

D

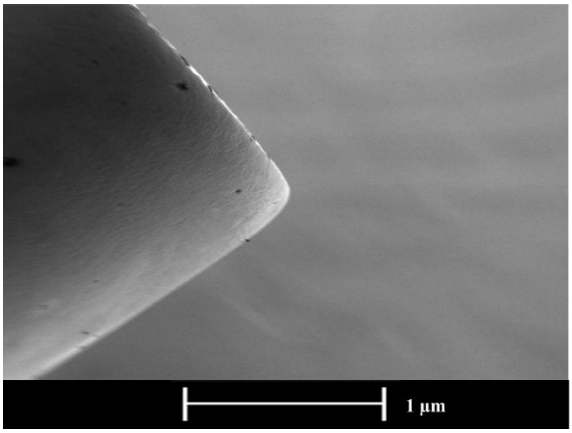

E

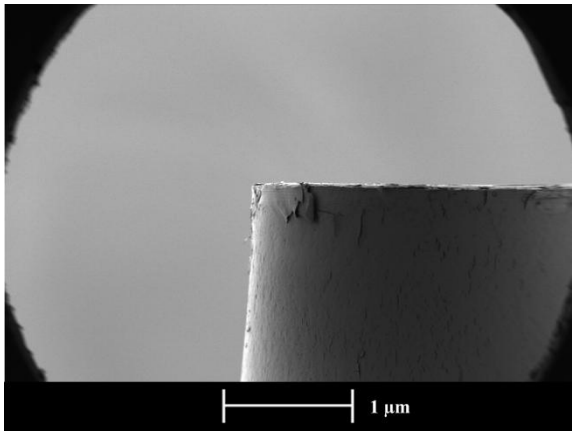

F

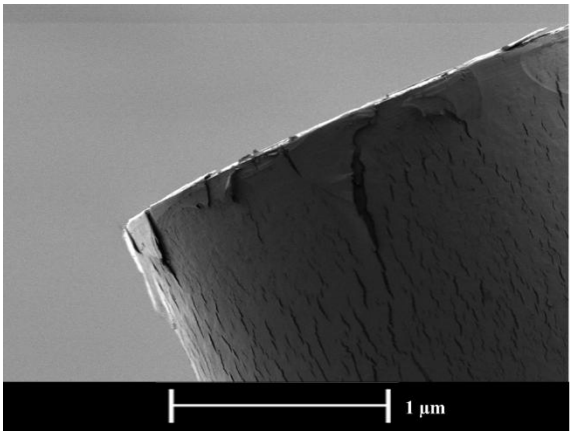

Figure 4.11 SEM images of A) Cs, B) CsE, C) Ag-Cs30, D) Ag-Cs45, E) Ag-Cs1, F) Ag-Cs2.

4.4.2 Antibacterial activity

The results of the antimicrobial test showed that all coatings tested have an inhibitory effect on bacterial proliferation, both on *S. Aureus* gram-positive and on *E. Coli* gram-negative bacteria. From the Figure 4.12 A in which the data obtained from the test in the first variant are reported, an antimicrobial activity emerges, in both bacterial strains, with a decrease in growth of 15% for all coatings except Ag-Cs1 that shows 25% inhibitory activity. From the figure 4.12 B, which reports the data obtained from the test performed in the second variant, emerges an increase in the limitation of proliferation that exceeds 20% for all the coating tested, except for the coating Ag-Cs1 that confirms the best one showing an inhibition of 35%.

It appears, therefore, evident that a contact coating-medium more prolonged allows the deposits to exert a stronger inhibitory action against bacterial strains tested; the coating Ag-Cs1 proves to be the most performing in both tests. It also emerges that CsE have antimicrobial activities comparable to that of Cs.

A

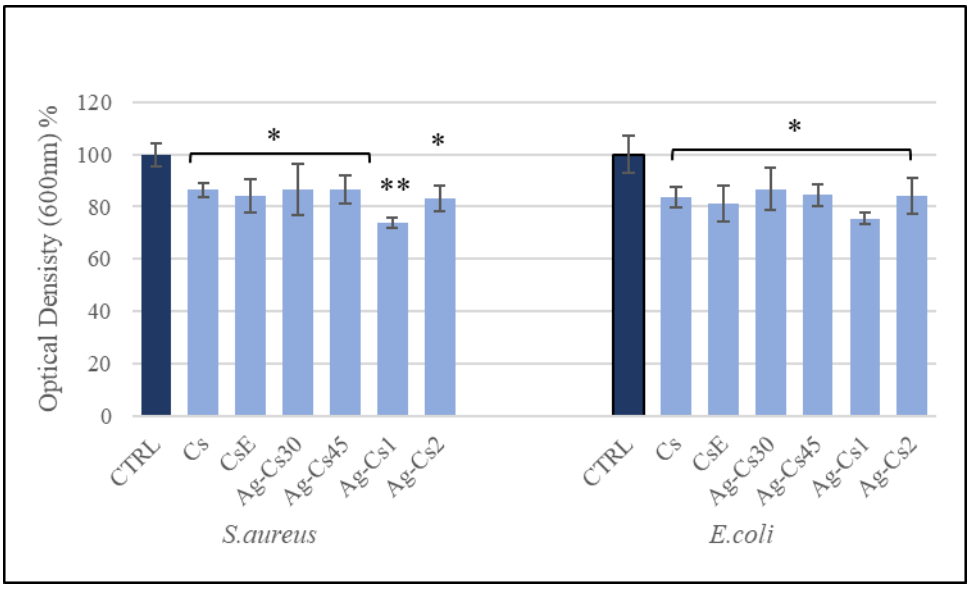

B

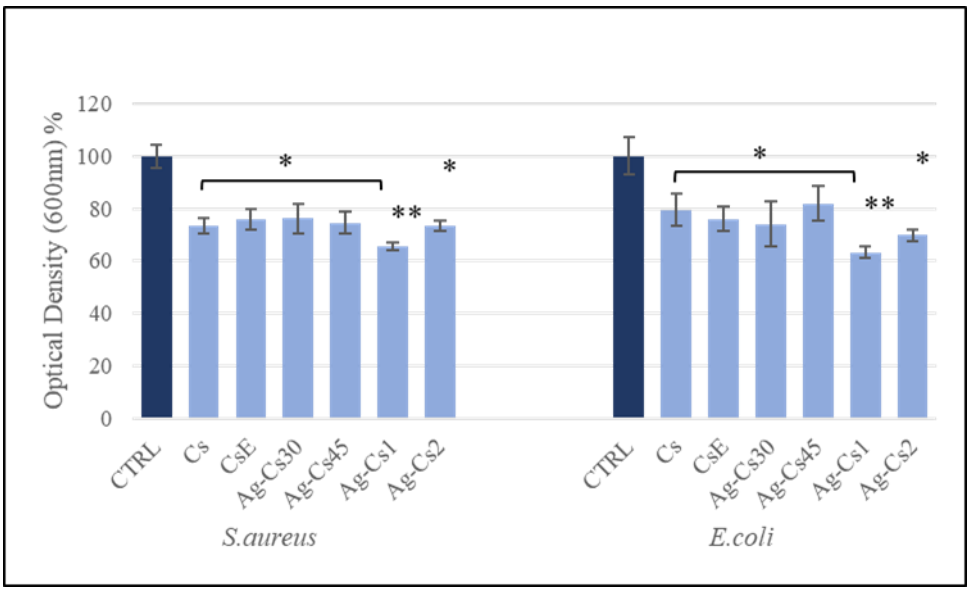

Figure 4.12 A) Antibacterial activity of coatings relative to stainless steel against Escherichia coli and Staphylococcus aureus after 24 h of incubation. B) Antibacterial activity of coatings relative to stainless steel, preincubated 24h, against E. coli and S. aureus after 24 h of incubation. Asterisks (*) denote significant differences ($p < 0.05$) vs. control.

4.4.3 Viability test

The cell viability test was performed on human osteoblasts (MG-63) at three different times, 24h, 48h and 72h using uncoated stainless steel as control. In the 24 h test, the data show reductions of 10-15% in mitochondrial cell activity in samples Cs and CsE compared to control. Chitosan has shown to be not toxic to MG-63 cells [232], so it is assumed that the reason for this decrease in viability may be related to the relatively low number of cells attached. It is known that cellular adhesion first involves non-specific forces, such as electrostatic or van der Waals ones, followed by specific interactions, mediated by cell receptors, with the substrate[198]. However, chitosan lacks specific domains, mediated by integration receptors or cell recognition sequences (such as RGD) that promote cellular adhesion [199]. As a result, fewer cells are likely to attach to the coating surfaces only through non-specific electrostatic interactions between the protonated amine groups of the glucosamine unit in chitosan and the negatively charged groups of the carboxylate and sulphate in proteoglycans on the cell surface. [200] Ag-Cs30, Ag-Cs45 and Ag-Cs show values of vitality ranging from 80% to 75%, these coatings prove to be not toxic to the MG-63 cell line. Conversely, the deposit Ag-Cs2, shows a cellular viability below 60%, which is probably due to an excessive release of silver ions in the culture medium that by interacting with cellular metabolism slows down cell proliferation. [233]

In the 48h test, Cs and CsE provide a substrate of adhesion and proliferation slightly better than the control with a cell viability value of about 117% and 119% respectively; Ag-Cs30, Ag-Cs45, Ag-Cs1 deposits show values comparable to the control; whereas Ag-Cs2 shows a cell viability value of 80%.

In the 72h test, Cs and CsE show cell proliferation, with viability values of 110% and 120% respectively; at the same time, the deposits Ag-Cs30, Ag-Cs45, Ag-Cs1 and Ag-Cs2 show values comparable to the control.

Cs and CsE deposits show at times 48h and 72h to be suitable substrates for cell growth compared to control, this is partly due to a contact angle within the optimal range for cellular adhesion (40 someone-70 someone) (40°-70°) [229] and in part the ability of chitosan to stimulate cell growth.[234] The comparison also shows how the CsE deposit stimulates proliferation more strongly than Cs at all times considered, this is probably linked to the degree of acetylation; one study showed that the degree of acetylation affects cell adhesion and proliferation, it follows that low degrees of acetylation are the best substrates for the line MG-63. [235]

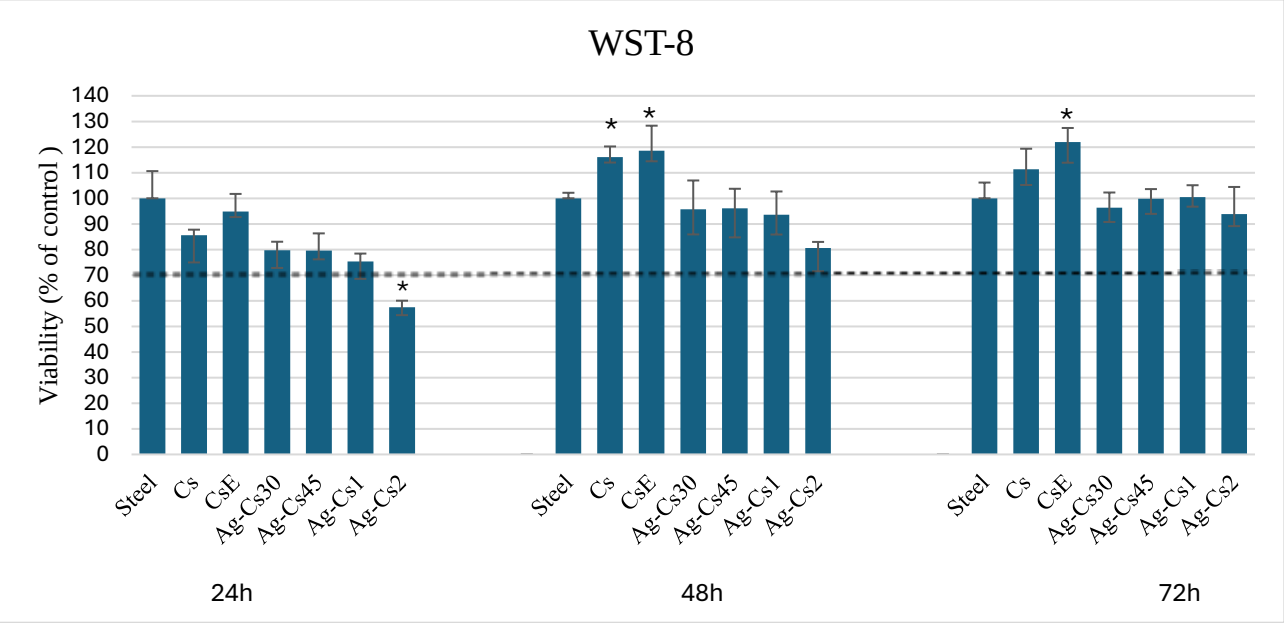

Figure 4.13 Cell viability of osteoblast-like cells (MG-63) cultured coatings after 24h, 48h and 72h of incubation. Stainless steel was used as a control. Asterisks (*) denote significant differences ($p < 0.05$) vs. control.

4.5 Conclusion

Chitosan, chitosan exuviae derived (Hermetia Illucens) and composite obtained from the direct generation of AgNPs in polymeric solution (AgNPs-Cs) have been considered for coating 316L stainless steel by EPD. The optimization of the deposition parameters has allowed the deposition of adherent and uniform coatings of controlled thicknesses. All coatings showed antibacterial properties resulting in effective restriction of bacterial growth on both gram-positive and gram-negative strains, S. aureus and E. coli respectively. Ag-Cs1 showed the highest antibacterial activity, while Cs and CsE showed comparable inhibitory capacity. All coatings used as growth substrates for the human osteoblast cell line were found to be non-toxic to this cell line; the presence of silver nanoparticles in deposits if bacterial proliferation is limited, in contact with eukaryotic cells, although better tolerated a slight slowdown in growth in the hours immediately after sowing, a phenomenon disappears after 24 hours. Cs and CsE have revealed not only the absence of toxicity but also the ability to promote proliferation compared to steel alone. [236] It is therefore possible to imagine a possible use of composite deposits as coating for biomedical implants and one can also think replacing the chitosan from marine source with chitosan extracted from insects, specifically the one Hermetia illucens.

The data obtained and analyzed in this chapter have been used as a basis for the article "Enhancing the Antibacterial Properties of Chitosan Coatings: Ag@Chitosan and Chitosan from Insects" published in June 2024.

Chapter 5 Silver/chitosan composite for photocatalytic degradation applications

5.1 Wastewater treatment

Organic dyes are widely used in different field of industry, the main sources are the textile and tanning industry, but also the paper, cellulose and dye industry, so that they can be easily found in various industrial wastewater even at high concentrations.[237] Recent studies have reported that, annually, about $7x10^7$ tons of synthetic dyes are produced worldwide, of which about 10,000 tons of such dyes used by the textile industry.[238] In addition, there is a significant increase in the global textile market every year. From the analysis carried out, the concentration of organic dyes in textile wastewater can be as high as 250 mg/L, posing serious risks to the environment.[239] Due to the very high concentrations the dyes can change the colour of the water causing increased biochemical and chemical demand for oxygen, limiting the penetration of light and compromising the photosynthesis and growth of plants; even at low concentrations, can cause numerous damages, in fact they promote toxicity, mutagenicity and carcinogenicity, entering the food chain and causing accumulation and secondary pollution. In addition, they can cause skin irritation, allergies or gastrointestinal and respiratory diseases.[240]

Synthetic organic dyes vary enormously in chemical structure: for example, azo dyes, which are the most common class (over 60% of textile dyes), are characterized by the presence of at least one azo group, acid dyes are water soluble anions and basic dyes are water soluble cations.[241] In spite of the structural variability, all synthetic dyes are combined with a high solubility in water and excellent stability both in sunlight and environmental oxidation, which prevent a possible bioremediation of the environment from these pollutants.[242]

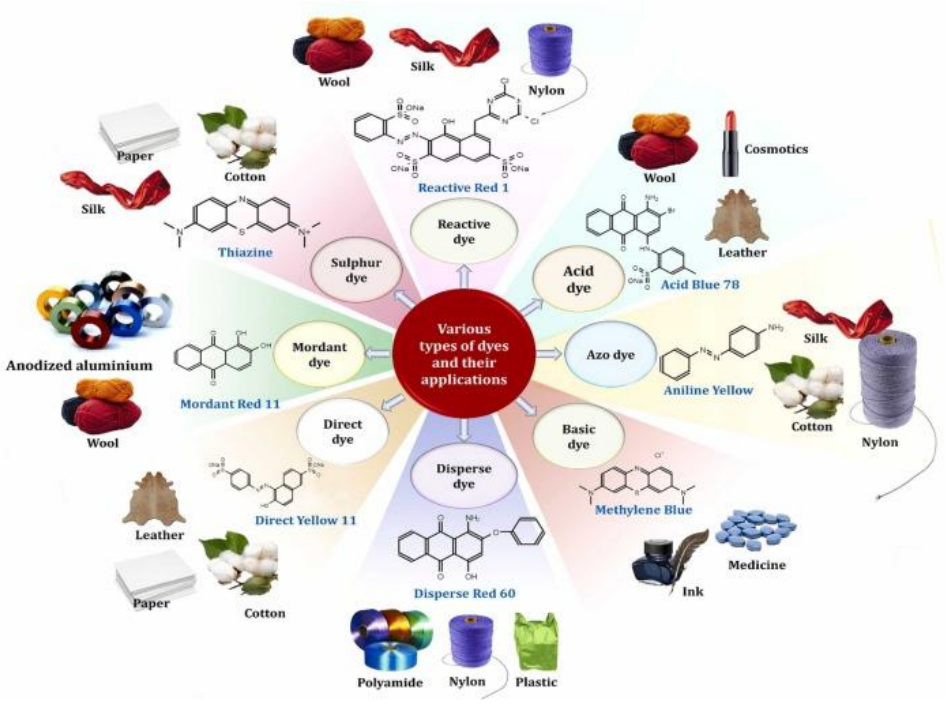

Figure 5.1 Classification of different types of organic dyes with their fields of application.[241]

Another common denominator of synthetic organic dyes is that their structure can be difficult to degrade without the formation of dangerous intermediate species. For these reasons, conventional treatment options are often ineffective and innovative advanced decontamination approaches are needed. Among the different strategies proposed in the literature are coagulation, flocculation, advanced oxidation (Fenton or photo-Fenton), ion exchange, electrochemical treatments, adsorption and biological degradation (assisted by bacteria, enzymes, fungi or algae)[243]. Fenton-like reactions are a variant of the Fenton reactions, processes used primarily for the degradation of organic pollutants through the production of highly reactive species such as hydroxyl radicals (•OH). Whereas in the classical Fenton reaction hydrogen peroxide (H_2O_2) and an iron-based catalyst (usually Fe^{2+}) are used, in Fenton-like reactions non-ferrous catalysts (such as copper, manganese, vanadium) are introduced or oxidized forms of iron are used, as Fe^{3+}. Figure 5.2

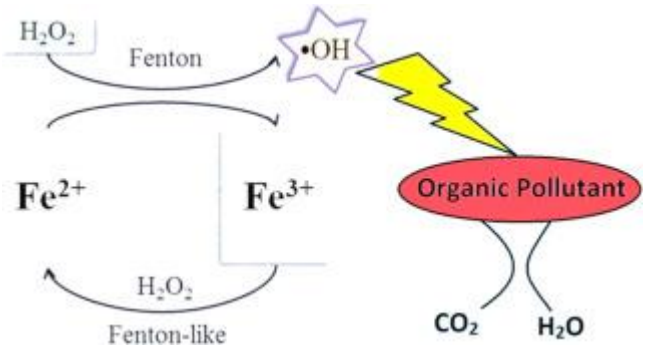

Figure 5.2 Graphical representation of the Fenton reaction. [244]

The ideal decontamination system should be characterised by ease of preparation and use, stability, fast removal of dyes and low cost, a system based on the adsorption process, surface-based process where adsorbed molecules or ions are attracted to the surface of an adsorbent solid, is often considered the best option. The standard currently used for adsorption systems for industrial wastewater treatment is activated carbon, but its production and regeneration are characterized by high costs and require treatments at very high temperatures. Moreover, the derivation from fossil fuels poses limits and doubts about their extensive use.[245] On the contrary, the preparation and use of the adsorption system should be characterized by a low environmental impact, suggesting that the use of natural materials, which can be treated according to sustainable chemical processes, is a virtuous strategy. In this perspective, the use of chitosan, as the main component of multifunctional systems capable of adsorbing pollutants, is particularly interesting.[246]

Multifunctional systems usually consist of [247]:

- An adsorbent unit: a component with a high-water retention capacity which can be easily recovered after use and which is easy to handle. Obviously, it should not release toxic compounds into the surrounding aquatic environment and should possibly be obtained through a simple, sustainable and low-cost procedure.

- A unit of recognition: molecular species capable of interacting in a specific way with the analyte or class of analytes, favouring their capture and reducing their desorption.

- Photocatalyst: consisting of plasma nanoparticles or dielectric nanoparticles capable of promoting the photodegradation of pollutants through the capture of UV-visible light.[248]

The idea behind this work is to use chitosan as a matrix and adsorbent unit in combination with silver nanoparticles, used as a photocatalyst, in multifunctional systems created to remove dyes from wastewater.[249] The advantages of such a system are closely linked to the proposed system: chitosan is a biocompatible and biodegradable natural polymer, the preparation of the adsorbent system in film form is extremely simple and ensures the removal of the adsorbent simply by using a common filtration system or tweezers. In addition, chitosan is characterized by antimicrobial activity that can be exploited for further improvement of water quality.

AgNPs show strong surface plasmon resonance (SPR), which makes them excellent absorbers of visible light. Surface plasmon resonance is caused by collective and consistent oscillations of free electrons in the metal, induced by the oscillation of the electromagnetic field of the incident light on the surfaces of metal nanoparticles. The charge separation is caused by this oscillation, which then leads to a dipole oscillation in the direction of the magnetic field. When

this oscillation reaches a maximum value at a certain specific frequency, surface plasmon resonance (SPR), which causes a strong adsorption and diffusion of light.[250] The same phenomenon is at the basis of the photocatalytic capacity of these nanoparticles against synthetic organic dyes. The photocatalytic process of AgNPs involves several phases: in the first phase of light absorption, during irradiation with visible light, the electrons in the conduction band are excited, creating electron-gap pairs; the second phase involves reactive species generation. In this phase the excited electrons can react with the molecular oxygen adsorbed on the surface of the nanoparticles, forming reactive oxygen species (ROS), such as superoxide radicals (O_2^-) and hydrogen peroxide (H_2O_2). Finally, the third phase or degradation of dyes, when the highly reactive ROS generated can attack organic dye molecules, breaking down chemical bonds and decomposing dyes into less toxic or harmless substances. For this reason, AgNPs are interesting in the field of environmental remediation.[251], [252]

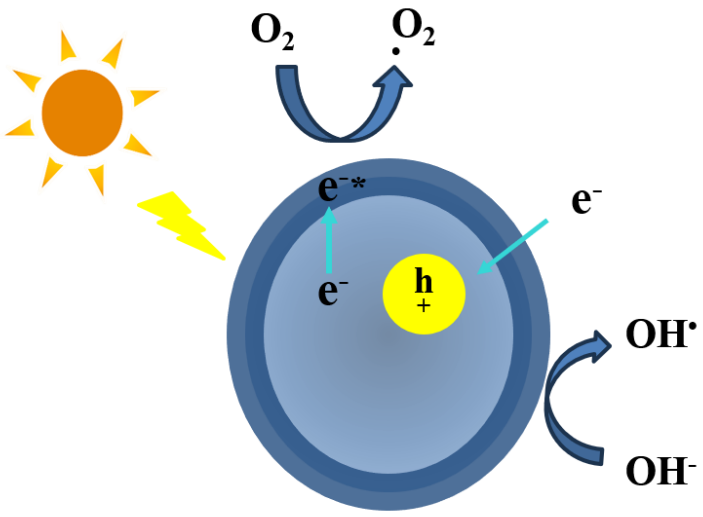

Figure 5.3 Photocatalysis mechanism of AgNPs under UV and visible light radiation for dye degradation.

This chapter discusses the evaluation of the composite materials prepared, (Cs-AgNPs and CsE-AgNPs) as photocatalysts for an organic dye, methylene blue, used as dye- model for environmental pollutants. The composite materials have been tested in both liquid and solid forms.

5.2 Experimental

The colloidal solution Cs-AgNPs and CsE-AgNPs were prepared and characterized as described in paragraph 3.2.1 the films Cs, CsE, AgNPs-CS and AgNPs-CsE were prepared as described in paragraphs 3.2.2.

5.2.1 Mechanism of methylene Blue degradation

Photocatalytic degradation of methylene blue (MB) is a process using light, usually UV or solar, and a photocatalyst to degrade the dye into less harmful compounds, this process can lead to mineralization where MB is completely degraded into end products such as carbon dioxide (CO_2), water (H_2O), and other inorganic ions, such as, NO_3^- e SO_4^{-2}.

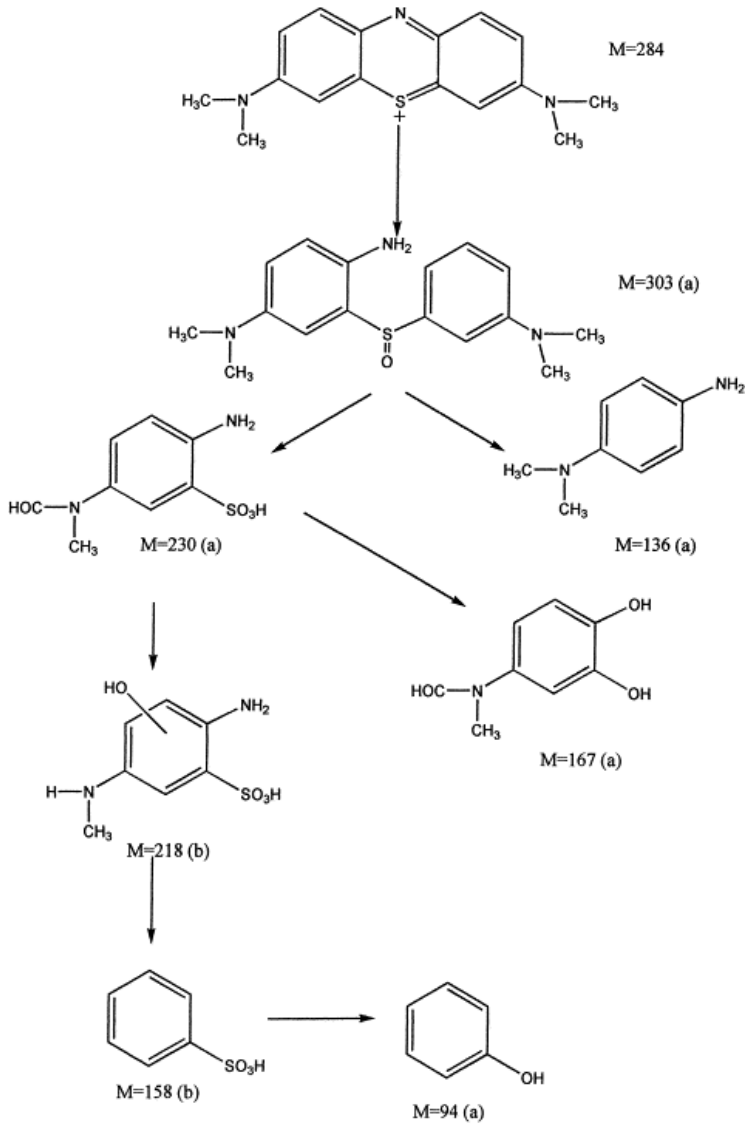

Figure 5.4 Photocatalytic degradation pathway of MB.[253]

The degradation of methylene blue is described by pseudo first order kinetics. This means that the rate of degradation is proportional to the residual concentration of the dye[254]. The kinetic law can be expressed by the following equation:

$$v = k[C]$$

where:

C is the concentration of methylene blue;

k is the degradation kinetic constant (min^{-1} or s^{-1});

by integrating this equation, the following velocity kinetic law is obtained:

$$\ln \frac{C}{C0} = -kt$$

where:

C0 is the initial concentration of methylene blue;

C is the residual concentration at a given time t;

t is the exposure time;

k is the speed constant;

By plotting the value of $ln\left(\frac{C}{C0}\right)$ as a function of time, we obtain a graph whose slope of the line represents the value of the kinetic constant.

The calculated kinetic constant value can also be used to calculate half-life, which is the time required for MB concentration to decrease by half. The half-life is calculated with the following equation, bearing in mind that the reaction is pseudo first order:

$$t_{1/2} = \frac{ln2}{k}$$

Finally, to assess the percentage of colour degraded over time, the degradation efficiency is calculated (η %):

$$\eta(\%) = \left(\frac{CO - Ct}{CO}\right) x\ 100$$

where C0 is the initial concentration and Ct is final concentration at t (time).

5.2.2 Photocatalytic assesment set-up

Methylene blue (MB) solutions (Sigma-Aldrich) were prepared by dissolving the dye in 50 ml of solvent, obtaining concentrations ranging from 50 to 6.25 mg/l.

Before irradiation, the solutions were kept in dark stirring for 10 minutes to allow the adsorption equilibrium to be reached. The photocatalytic process was then initiated by exposing the solutions to an Osram Ultra Vitalux 300 W lamp with a radiation intensity of 10.7 mW/cm^2, designed to simulate sunlight. The lamp was placed about 15 cm from the solutions, which were constantly stirred during the whole experiment. To prevent evaporation of the solvent, the

degradation reactions were carried out in an ice bath, maintained at a controlled temperature of 10 °C.

The residual concentration of methylene blue was measured at regular intervals using a UV-vis spectrophotometer, monitoring the maximum absorbance at 633 nm, characteristic of MB. All experiments were conducted in triplicate to ensure a minimum reproducibility of results.

5.3 Results

Methylene blue's absorption peak is located at around 664 nm, which is connected to the monomer MB, and it has a shoulder at around 612 nm, which is linked to the dimer MB, as shown in Figure 5.5 A. During the photo-degradation process, the decrease in the maximum absorbance value due to the decrease in the concentration of MB can be observed over time. Figure 5.5 B

A B

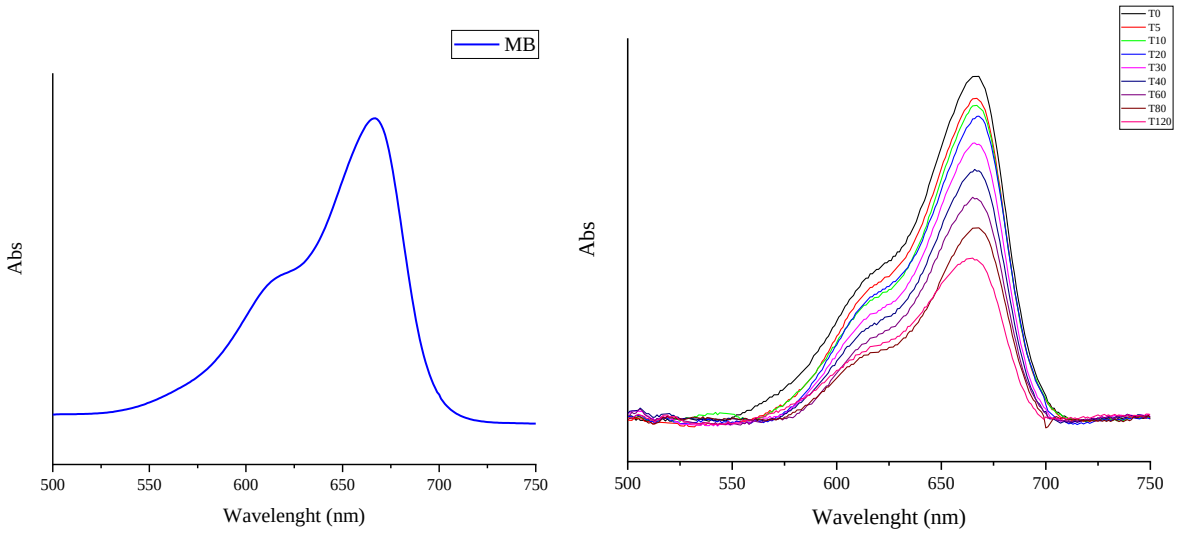

Figure 5.5 A) UV-Vis spectrum MB; B) UV-Vis spectrum of MB photodegradation with time going from time 0 (t0) to 120 minutes (t120).

The first step in the study was to evaluate the synergistic capacity between chitosan (CS) and silver nanoparticles (Ag NPs) in the catalysis of the photodegradation reaction. To better understand the contribution of each component, the rate constant for the degradation of MB, in the presence of CS (1 g/L) and Ag NPs (8 µg/mL), was measured separately. The results showed that the rate constant for photodegradation of MB at a concentration of 50 mg/L is 0.0013 min^{-1} for CS and 0.0031 min^{-1} for Ag NPs. The difference between the two rate constants highlights

the importance of the Ag NPs catalyst in the dye degradation process, with a rate more than twice that obtained with CS alone, Figure 5.6.

A

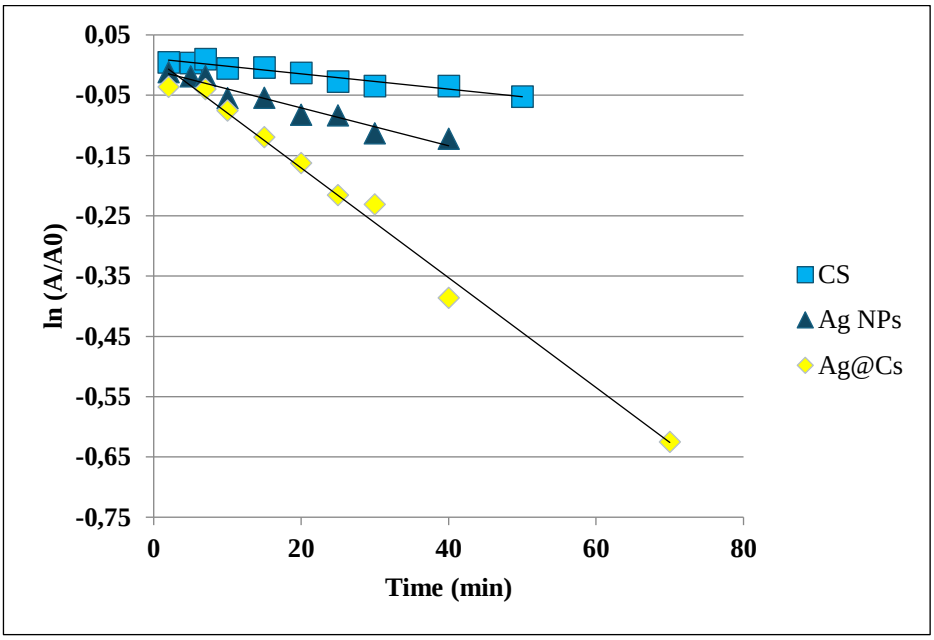

B

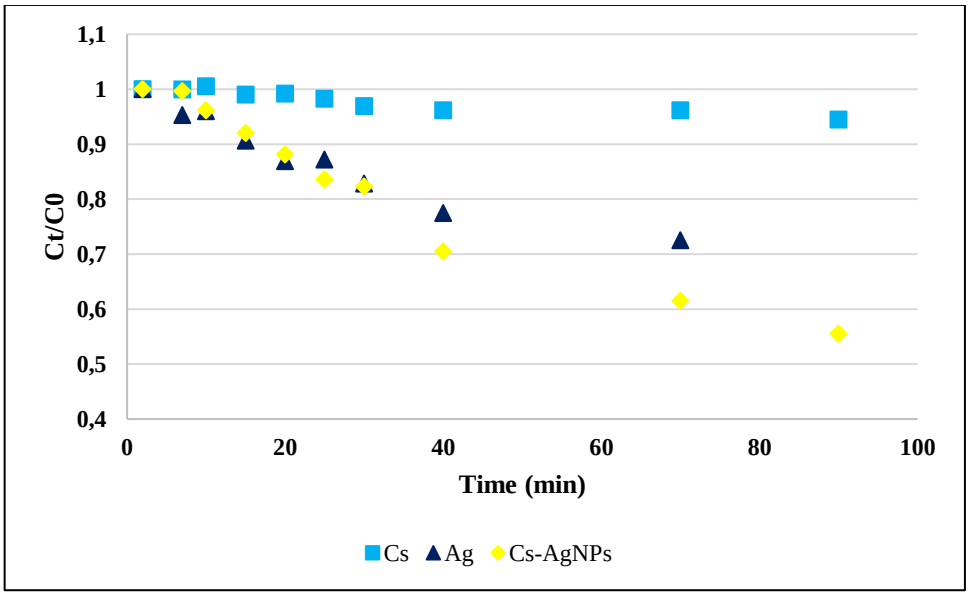

C

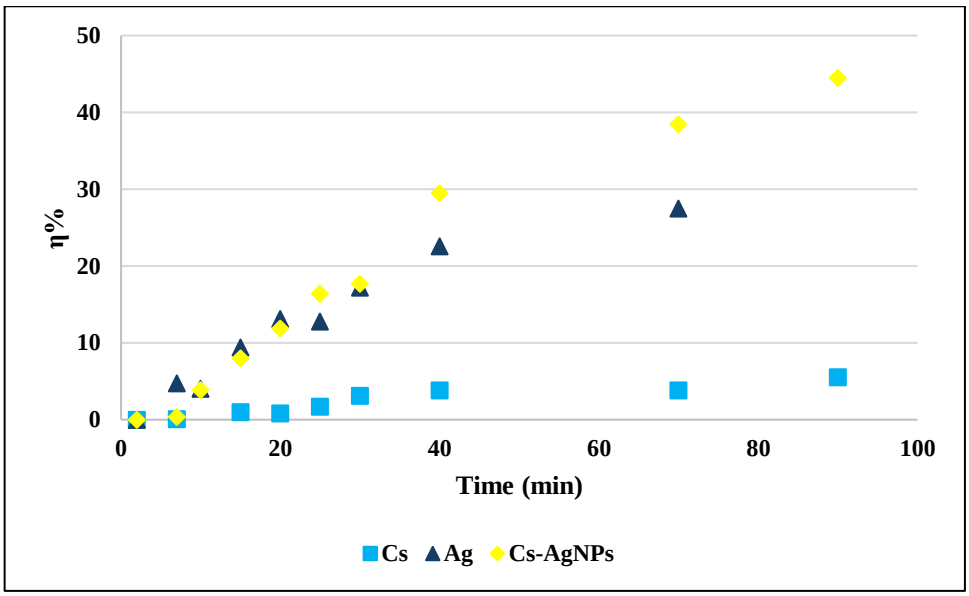

Figure 5.6 A) plots of the slope of ln(A/Ao) vs time for the reduction of MB (50mg/l), B) plots of the slope of C/C0 vs. time for the reduction of MB (50mg/l), C) plots of the slope of degradative efficiency vs. time for the reduction of MB (50mg/l) in CS (light blue), AgNPs (blue), and Cs@Ag (yellow) solutions.

The rate constant of the composite material CS@Ag for the degradation reaction MB 50mg/l was then measured. The obtained constant of speed is 0.064 min^{-1}, with a degradation efficiency greater than 40% during the first 90 minutes, highlighting the synergistic activity between AgNPs and CS in the composite. This synergistic behaviour suggests that the combination of the two components greatly improves catalytic performance compared to using each separately.

As the concentration of the dye significantly affects the kinetics of degradation, a study was conducted to assess the catalytic capacity of the Cs-AgNPs composite at different concentrations of MB ranging from 50 mg/L to 6,25 mg/L. The results showed that kinetic constants increase from 0.064 min^{-1} for the highest concentration of MB (50 mg/L) to 0.098 min^{-1} for the lowest concentration (6.25 mg/L). This increase in the rate constants with decreasing dye concentration is indicative of a higher catalytic efficiency under lower concentration conditions, in line with the pseudo-first-order kinetics that characterize this reaction.[254] The rate constants, degradation efficiency and half-life ($t_{1/2}$) for all experimental conditions are given in Table 5.1, providing a complete description of the catalytic performance of Cs-AgNPs at different concentrations of MB.

Table 5.1 kinetic constant (k), half time ($t_{1/2}$) and efficiency (η%) for the MB photodegradation reaction at different conditions.

	k(min-1)	$t_{1/2}$ (min)	η %
CS_MB (50mg/l)	0.0013	533	5
Ag _MB (50mg/l)	0.0031	223	27
Cs-AgNPs_MB_(50mg/l)	0.0064	108	44
Cs-AgNPs_MB_(25mg/l)	0.0086	80	65
Cs-AgNPs_MB_(12.5mg/l)	0.024	29	94
Cs-AgNPs _MB_(6.25mg/l)	0.098	7	94

The effectiveness of photocatalytic degradation decreases by increasing MB concentration. This is because at higher concentrations the adsorbed dye molecules saturate the photocatalyst surface and the amount of photons reaching the catalyst decreases. As a result, fewer hydroxyl radicals (•OH) are generated, reducing the efficiency of the degradation process.[255]

A

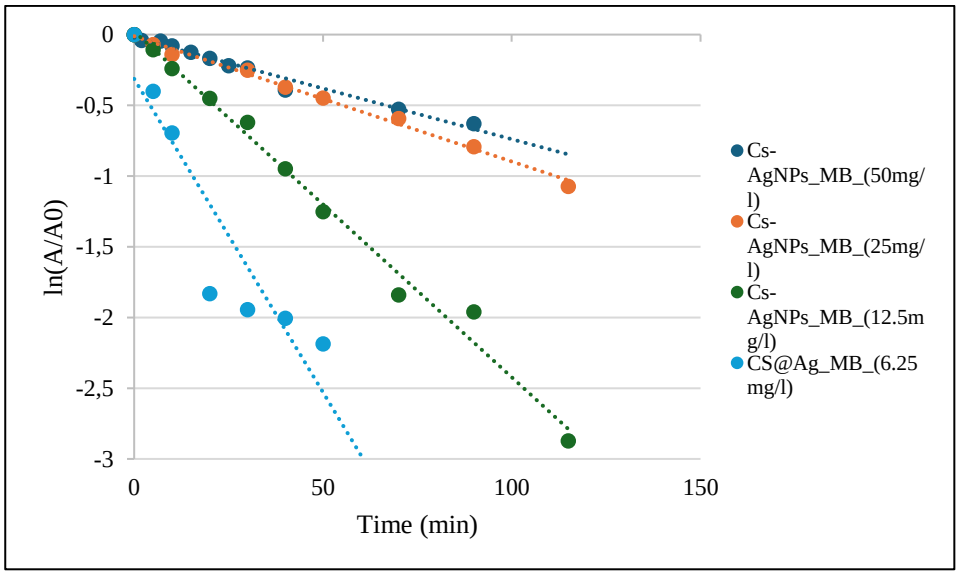

B

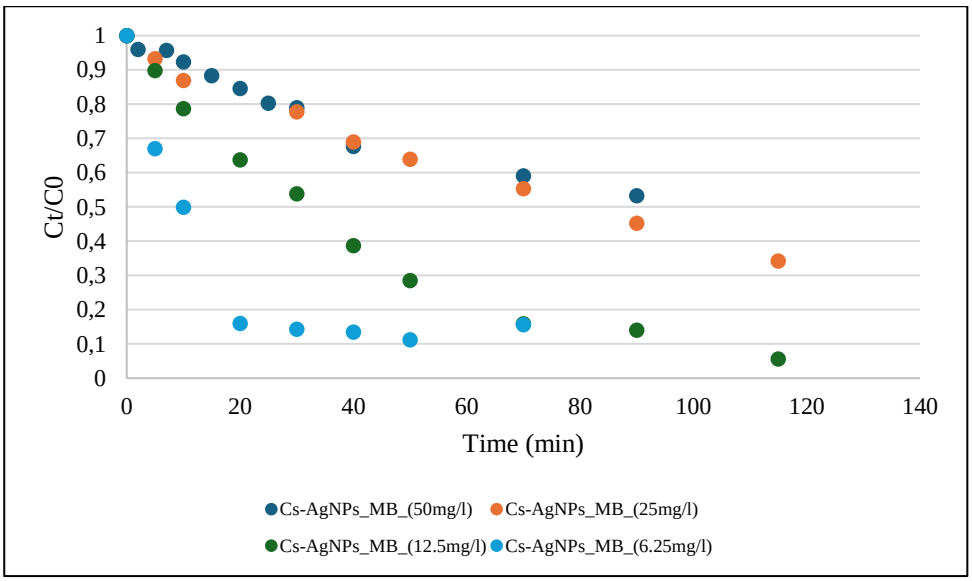

C

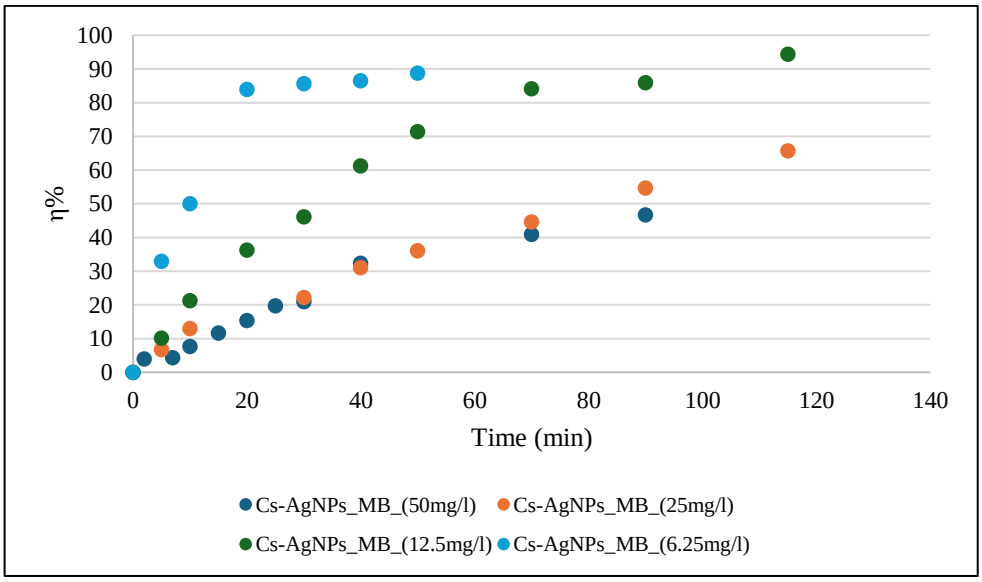

Figure 5.7 A) plots of the slope of ln(A/Ao) vs. time for the reduction of MB, B) plots of the slope of C/C0 vs. time for the reduction of MB (50mg/l), C) plots of the slope of degradative efficiency vs time for the reduction of Cs-AgNPs_MB_(50mg/l) light blue, Cs-AgNPs_MB_(25mg/l) orange, Cs-AgNPs_MB_(12.5mg/l) green, Cs-AgNPs_MB_(6.25mg/l) solutions blue solutions.

In the case of the CSE system, the rate constants and efficiency measured with the highest concentration of MB for the CsE, and with the lowest concentration of MB for CsE-AgNPs, are comparable to those obtained with the CS under the same experimental conditions (as shown in the Table 5.2). These results suggest that CsE could be a viable alternative, both economically and environmentally sustainable, to commercial sources of chitosan.

Table 5.2 Shows the kinetic constant (k), half time ($t_{1/2}$) and efficiency (η %) for the MB photodegradation reaction at different conditions.

	k(min-1)	**$t_{1/2}$ (min)**	**η %**
Cs_MB (50mg/l)	0.0013	533	5
CsE_MB (50mg/l)	0.0008	866	8
Cs-AgNPs_MB_(6.25mg/l)	0.098	7	94
CsE-AgNPs_MB_(6.25mg/l)	0.0421	16	96

Considering the catalytic capacity of the composite synthesized in solution, the photocatalytic degradation of MB in presence of the films was studied. In particular, the kinetic constants for the degradation of MB at concentration of 6.25 mg/L were measured using the Cs and CsE films separately. The results show that the rate constants are 0.0021 min^{-1} for Cs film and 0.0027 min^{-1} for CsE film, showing a comparable performance of chitosan from alternative sources compared to commercial. Subsequently, the analysis of the photocatalytic capacity of composite films in the degradation of the dye MB (6.25 mg/l) revealed rate constants of 0.0054 min^{-1} for AgNPs-Cs and 0.0057 min^{-1} for AgNPs-CsE, whose data are shown in Table 5.3. These data confirm the close similarity between commercial chitosan and exuviae, demonstrating their interchangeability as both films catalyzed the reaction with almost identical efficiency. In addition, it has been shown that the composite material retains its catalytic properties even in solid form, confirming its effectiveness.

Table 5.3 shows the kinetic constant (k), half time ($t_{1/2}$) and efficiency (η%) for the MB photodegradation reaction using CS, CSE, AgNPs-Cs and AgNPs-CsE films as catalyst.

Film	**k(min-1)**	**$t_{1/2}$ (min)**	**η %**
CS_MB (6.25mg/l)	0.0021	330	23
CSE_MB (6.25mg/l)	0.0027	256	26
AgNPs-Cs_MB_(6.25mg/l)	0.0054	128	48
AgNPs-CsE_MB_(6.25mg/l)	0.0057	121	45

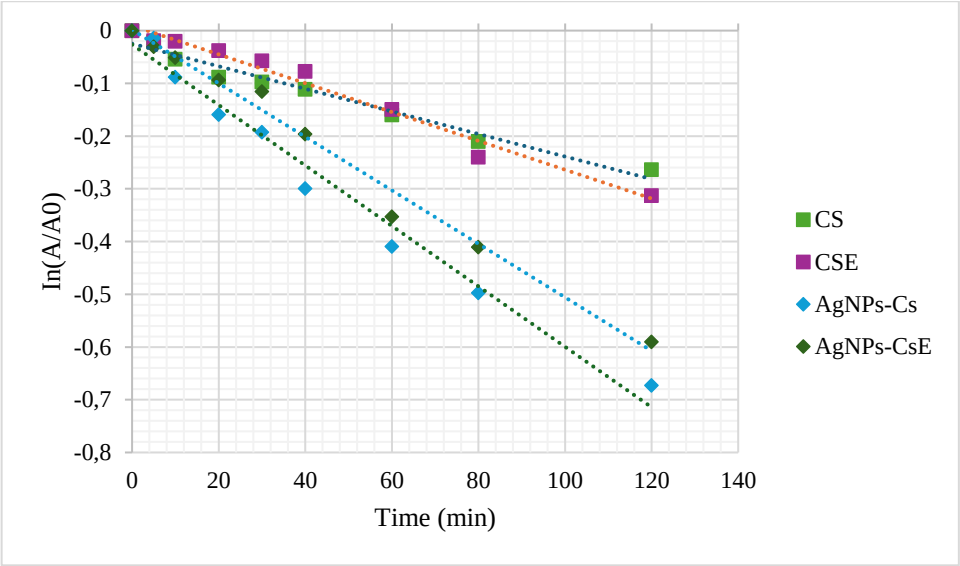

Figure 5.8 reports the plots of ln(A/Ao) vs. time for reduction of MB (6.25mg/l) in presence of CS, CSE, AgNPs-Cs and AgNPs-CsE films.

The AgNPs-Cs films were subjected to five cycles of degradation of low-concentration (6.25 mg/l) methylene blue, washed in distilled water between cycles, to assess their potential reuse. During the first cycle, the degradation efficiency reached 60%, and while slightly decreasing with the passing of cycles, as reported in figure 5.9 the film maintained an efficiency of 50% at the fifth cycle. This behaviour highlights the advantages of the composite film over its solution counterpart: its solid form can be easily recovered at the end of the reaction, maintains a significant catalytic efficiency even after several cycles making it reusable and so improving the sustainability and cost-effectiveness of the process.

A

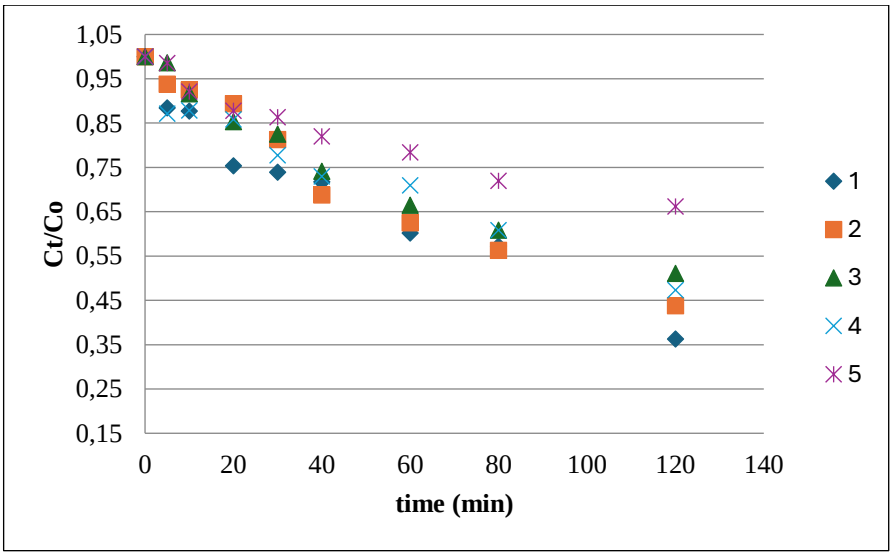

B

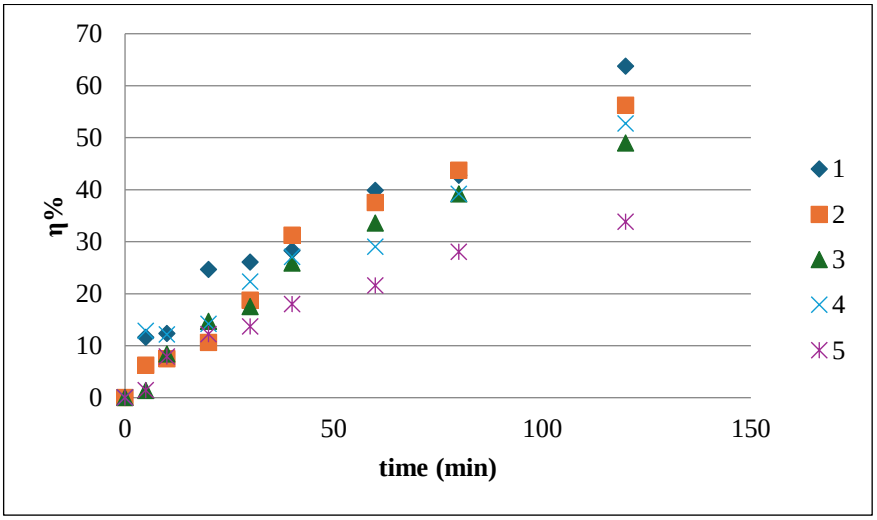

C

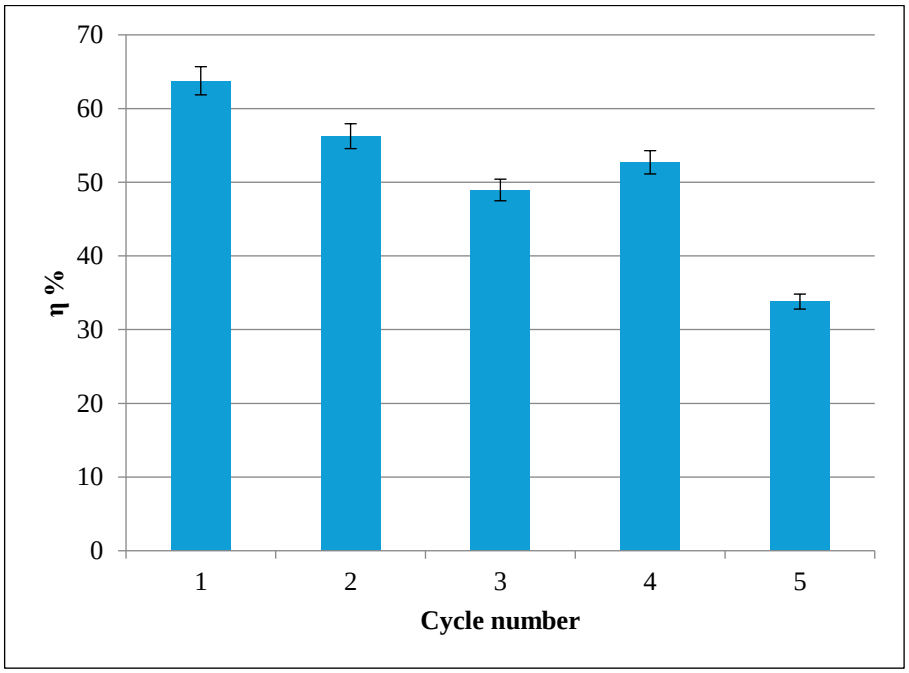

Figure 5.9 A) Degradation of MB in presence of AgNPs-Cs film at different usage cycle; B) Photodegradation efficiency of AgNPs-Cs film; C) Total photodegradation efficiency of AgNPs-Cs at different photodegradation cycles.

5.4 Conclusions

The study demonstrated the significant potential of chitosan-based composite materials and silver nanoparticles in decontaminating wastewater containing organic dyes. The results obtained, in both liquid and solid form, confirm the effectiveness of these materials in the photodegradation of methylene blue, a model dye used to represent environmental pollutants. The analysis revealed an effective synergy between chitosan and silver nanoparticles. In particular, the composite material Cs-AgNPs has shown to have a significantly higher degradation rate constant than the individual components. The results also confirmed that the catalytic performance of exuviae chitosan is comparable to commercial chitosan. This suggests that chitosan from exuviae is an economically and environmentally sustainable option for the development of decontamination materials. Finally, the re-use test of AgNPs-Cs films showed that even after five degradation cycles, the film maintained a catalytic efficiency of 50%. This result highlights the advantage of composite materials over liquid solutions, as the film can be easily recovered and reused, thus reducing operating costs and environmental impact. In conclusion, chitosan-based composite materials and silver nanoparticles emerge as a promising solution for photodegradation of organic dyes. Their high efficiency, combined with sustainability and re-usability, makes them particularly suitable for industrial wastewater treatment, offering a viable alternative to conventional methods.

Conclusions

This work has shown that the integration of biocompatible and biodegradable materials, such as chitosan, with advanced production technologies, such as liquid laser ablation, represents an innovative and sustainable approach to the development of nanostructured materials. The choice of chitosan, in particular comparing that derived from marine sources with that derived from alternative sources such as Hermetia illucens, proved to be a valid strategy for promoting environmental sustainability. The use of chitosan produced by Hermetia illucens, has shown characteristics and properties quite similar to the commercial polymer.

The first experiments carried out allowed a detailed analysis of the processes characterizing LAL in the presence of chitosan solution, and the results showed that the polymer significantly influences the processes involved during laser ablation, modulating the formation, growth of nanoparticles and improving the stability of the obtained colloidal solutions. The characterization of composite materials has made it possible to differentiate their intrinsic properties and assess their application potential.

Chitosan and copper composites showed strong antibacterial activity in solution, while this was absent in solid form. On the contrary, chitosan-silver composites have demonstrated antimicrobial efficacy in both liquid and solid forms, such as films and self-supporting coatings, suggesting their use in biomedical applications, For example, as coatings for bone implants or antibacterial films. In particular, the biocompatibility of the thin coating chitosan-silver composite, evaluated on osteoblast cell lines, supports its use in biomedical applications.

The films made from these composites have shown great versatility, which could be applied in various sectors such as the food industry or water treatment. Simulations of dye catalysis calculations have shown a significant increase in the degradation of these organic compounds, underlining the potential of these materials for treating contaminated water.

However, further studies will be needed to examine the long-term effects of the nanoparticles produced and to optimise the mechanical properties of chitosan composites, which are often inferior to those of other synthetic materials. Research could focus on the development of new processing techniques, the use of innovative reinforcements (such as cellulose nanofibers), or the chemical modification of chitosan to increase its strength and stiffness.

In addition, the development of multi-functional composites is a promising direction, exploiting the ability of chitosan to incorporate different functionalities into a single material. The creation of composites with combined properties, such as antibacterial activity and release controlled of drugs, or mechanical properties and tissue regeneration capabilities, could lead to the

development of "smart" materials for advanced biomedical applications. When evaluating its use for biomedical applications, it will then be crucial to further study the interaction with biological tissues, understanding the mechanisms of interaction at the molecular level, assessing immune response and inflammation, and studying the degradation of the material over time. Finally, assessing its application in tissue engineering, with the possibility of developing three-dimensional scaffolds with complex architectures, incorporating growth factors and stem cells, and evaluating its effectiveness in the regeneration of specific tissues.

In addition to this, however, it should be considered that the industrial scalability of liquid laser ablation is hampered by several factors. Production costs are a significant challenge, as the implementation of high-power laser systems and the need for pure chemical precursors can have a major impact on costs. In addition, scalability requires optimizing process parameters to maximize yield and minimize waste, a balance not always easy to achieve. Large-scale production is made difficult by the complexity of the LAL process, which requires precise control of process parameters. Variation in these parameters can lead to considerable heterogeneity in the properties of nanoparticles produced, making it difficult to produce consistent batches. Regulatory regulations are another hurdle, as the use of nanoparticles in commercial applications is subject to strict regulations, especially in the biomedical and food sectors. Other obstacles include the complexity of the LAL process, which is a multi-physical process involving complex interactions between the laser, target material and liquid, requiring specialist expertise and advanced equipment. The heterogeneity of nanoparticles produced with LAL can affect their properties and performance. Despite these challenges, LAL offers unique advantages such as the ability to synthesise nanoparticles with customized properties and the production of nanoparticles in a single step. With continued research and development of new technologies, LAL is likely to become an increasingly important nanoparticle production technique for a wide range of industrial applications.

In conclusion, this research represents a step forward in the field of sustainable composite materials, proposing an integrated model combining technological innovation and environmental sustainability. The results help to open up new perspectives for the application of advanced techniques such as LAL in the production of nanocomposite materials, At the same time, it provides a good example of how scientific and technological choices can be directed towards a more responsible and sustainable future.

References

[1] K. K. Chawla, *Composite Materials: Science and Engineering*. 2016.

[2] R. F. Gibson, *Principles of Composite Material Mechanics, Third Edition*. 2011.

[3] K.Joseph , K. Oksman, G. Gejo, R. Wilson, S. Appukuttan, *Fiber Reinforced Composites Constituents, Compatibility, Perspectives, and Applications*. Woodhead Publishing Series in Composites Science and Engineering, 2021.

[4] M. K. Egbo, "A fundamental review on composite materials and some of their applications in biomedical engineering," *J. King Saud Univ. - Eng. Sci.*, vol. 33, no. 8, pp. 557–568, 2021.

[5] P. Bovio, "Technological District on Engineering of polymeric and composite Materials and Structures," 2015.

[6] S. N. Gorb and W. Krings, "Editorial: Composite materials in biological and bioinspired systems: Part II, Biological and bioinspired composites," *Interface Focus*, vol. 14, no. 3, pp. 2–4, 2024.

[7] D. K. Rajak, D. D. Pagar, R. Kumar, and C. I. Pruncu, "Recent progress of reinforcement materials: A comprehensive overview of composite materials," *J. Mater. Res. Technol.*, vol. 8, no. 6, pp. 6354–6374, 2019.

[8] I. A. Ibrahim, F. A. Mohamed, and E. J. Lavernia, "Particulate reinforced metal matrix composites - a review," *J. Mater. Sci.*, vol. 26, no. 5, pp. 1137–1156, 1991.

[9] P. Bharathy and P. V. Thanikachalam, "Recent Advances and Future Prospects in Polymer-Mediated Drug Delivery Systems: A Comprehensive Review," *Int. J. Drug Deliv. Technol.*, vol. 14, no. 3, pp. 1896–1907, 2024.

[10] Y. Xu, J. Zhu, Z. Wu, Y. Cao, Y. Zhao, and W. Zhang, "A review on the design of laminated composite structures: constant and variable stiffness design and topology optimization," *Adv. Compos. Hybrid Mater.*, vol. 1, no. 3, pp. 460–477, 2018.

[11] D. Li, "Layerwise Theories of Laminated Composite Structures and Their Applications: A Review," *Arch. Comput. Methods Eng.*, vol. 28, no. 2, pp. 577–600, 2021.

[12] M. H. Mobarak, M. A. Islam, N. Hossain, Z. Al Mahmud , T. Rayhan, N. Jahan Nishi, M Asaduzzaman Chowdhury "Recent advances of additive manufacturing in implant fabrication – A review," *Appl. Surf. Sci. Adv.*, vol. 18, no. September, p. 100462, 2023.

[13] B. S. Ghuman, “Nanocomposites – A Review,” *Journal of Chemistry and Chemical Sciences* June,2020

[14] P. M. Ajayan, Linda S. Schadler, and Paul V. Braun, *Nanocomposite Science and Technology*. 2003.

[15] J. H. Koo, *Polymer Nanocomposites: Processing, Characterization, and Applications*, Second edi. McGraw Hill, 2019.

[16] B. Aaliya, K. V. Sunooj, and M. Lackner, “Biopolymer composites: a review,” *Int. J. Biobased Plast.*, vol. 3, no. 1, pp. 40–84, 2021.

[17] A. Kumar, R.K. Mishra, K. Verma, S.M. Aldosari, C.K. Maity, S. Verma, R. Patel and V.K. Thakur, “A comprehensive review of various biopolymer composites and their applications: From biocompatibility to self-healing,” *Mater. Today Sustain.*, vol. 23, p. 100431, 2023.

[18] R. Hsissou, R. Seghiri, Z. Benzekri, M. Hilali, M. Rafik, and A. Elharfi, “Polymer composite materials: A comprehensive review,” *Compos. Struct.*, vol. 262, no. November 2020, pp. 0–3, 2021.

[19] A. M. Díez-Pascual, “Biopolymer Composites: Synthesis, Properties, and Applications,” *Int. J. Mol. Sci.*, vol. 23, no. 4, pp. 10–13, 2022.

[20] S. Kou, L. Peters, and M. Mucalo, “Chitosan: A review of molecular structure, bioactivities and interactions with the human body and micro-organisms,” *Carbohydr. Polym.*, vol. 282, p. 119132, 2022.

[21] J. Kluczka, “Chitosan: Structural and Chemical Modification, Properties, and Application,” *Int. J. Mol. Sci.*, vol. 25, no. 1, pp. 1–5, 2024.

[22] D. Alemu, E. Getachew, and A. K. Mondal, “Study on the Physicochemical Properties of Chitosan and their Applications in the Biomedical Sector,” *Int. J. Polym. Sci.*, vol. 2023, 2023.

[23] M. Pakizeh, A. Moradi, and T. Ghassemi, “Chemical extraction and modification of chitin and chitosan from shrimp shells,” *Eur. Polym. J.*, vol. 159, no. May, p. 110709, 2021.

[24] M. Rinaudo, “Chitin and chitosan: Properties and applications,” *Prog. Polym. Sci.*, vol. 31, no. 7, pp. 603–632, 2006.

[25] E. El-hefian and A. H. Yahaya, “Rheological study of chitosan and its blends: An overview,” *Maejo Int. J. Sci. Technol.*, vol. 4, no. 02, pp. 210–220, 2010.

[26] J. Cho, M. C. Heuzey, A. Bégin, and P. J. Carreau, “Viscoelastic properties of chitosan solutions: Effect of concentration and ionic strength,” *J. Food Eng.*, vol. 74, no. 4, pp. 500–515, 2006.

[27] M. Koralewski and K. Bodek, “Temperature and metal ions influence on optical properties of chitosan in aqueous solution Progress on Chemistry and Application of Chitin and its derivates ,” no.1, pp. 79-86, 2007.

[28] H. Huang, F- López, L. J. Borrero-González, T. Terencio, M. Caetano, C. Reinoso, G.González, “Enhanced fluorescence of chitosan based on size change of micelles and application to directly selective detecting Fe3+ in human serum,” *Biosens. Bioelectron.*, vol. 42, no. 1, pp. 539–544, 2013.

[29] M. Ul-Islam, K. F. Alabbosh, S. Manan, S. Khan, F. Ahmad, and M. W. Ullah, “Chitosan-based nanostructured biomaterials: Synthesis, properties, and biomedical applications,” *Adv. Ind. Eng. Polym. Res.*, vol. 7, no. 1, pp. 79–99, 2024.

[30] K. K. Ahmed, D. Q. Muheddin, P. A. Mohammed, G. S. Ezat, A. R. Murad, B. Y. Ahmed, S. A. Hussen, T. Y. Ahmed, S. M. Hamad, O. G. Abdullah and S. B. Aziz , “A brief review on optical properties of polymer Composites: Insights into Light-Matter interaction from classical to quantum transport point of view,” *Results Phys.*, vol. 56, no. December 2023, p. 107239, 2024.

[31] S. Beier and S. Bertilsson, “Bacterial chitin degradation-mechanisms and ecophysiological strategies,” *Front. Microbiol.*, vol. 4, no. JUN, pp. 1–12, 2013.

[32] W. Xia, P. Liu, and J. Liu, “Advance in chitosan hydrolysis by non-specific cellulases,” *Bioresour. Technol.*, vol. 99, no. 15, pp. 6751–6762, 2008.

[33] E. L. Mcconnell, S. Murdan and A- W. Basit, “An Investigation into the Digestion of Chitosan (Noncrosslinked and Crosslinked) by Human Colonic Bacteria,” *J. Pharm. Sci.*, vol. 97, pp. 3820–3829, 2008.

[34] R. de Sousa Victor, A. M. da Cunha Santos, B. Viana de Sousa, G. de Araújo Neves, L. Navarro de Lima Santana and R. R. Menezes, “A Review on Chitosan ’ s Uses as Biomaterial : Tissue Engineering , Drug Delivery Systems and Cancer treatment”, Materials (Basel), vol. 13, no. 21,pp 4995-5023, 2020.

[35] A. Abarrategi, Y. Lópiz-Morales, V. Ramos, A.Civantos, L. López-Durán, F. Marco and J. L. López-Lacomba, “Chitosan scaffolds for osteochondral tissue regeneration,” *J. Biomed. Mater. Res. - Part A*, vol. 95, no. 4, pp. 1132–1141, 2010.

[36] H. Y. Atay, "Antibacterial Activity of Chitosan-Based Systems", *Functional Chitosan*, vol 6, pp. 457-489, 2020.

[37] J. Li and S. Zhuang, “Antibacterial activity of chitosan and its derivatives and their interaction mechanism with bacteria: Current state and perspectives,” *Eur. Polym. J.*, vol. 138, no. September, p. 109984, 2020.

[38] R. Teixeira-Santos, M. Lima, L. C. Gomes, and F. J. Mergulhão, “Antimicrobial coatings based on chitosan to prevent implant-associated infections: A systematic review,” *iScience*, vol. 24, no. 12, 2021.

[39] C. L. Ke, F. S. Deng, C. Y. Chuang, and C. H. Lin, “Antimicrobial actions and applications of Chitosan,” *Polymers (Basel).*, vol. 13, no. 6, 2021.

[40] A. R. Egorov, A. A. Kirichuk, V. V. Rubanik, V. V. Rubanik, A. G. Tskhovrebov, and A. S. Kritchenkov, “Chitosan and Its Derivatives: Preparation and Antibacterial Properties,” *Materials (Basel).*, vol. 16, no. 18, 2023.

[41] N. Desai, D. Rana, S. Salave, R. Gupta, P. Patel, B. Karunakaran, A. Sharma, J. Giri, D. Benival and N. Kommineni, “Chitosan: A Potential Biopolymer in Drug Delivery and Biomedical Applications,” *Pharmaceutics*, vol. 15, no. 4, 2023.

[42] H. Yadav, R. Malviya, and N. Kaushik, “Chitosan in biomedicine: A comprehensive review of recent developments,” *Carbohydr. Polym. Technol. Appl.*, vol. 8, no. 2, p. 100551, 2024.

[43] S. M. Mawazi, M. Kumar, N. Ahmad, Y. Ge, and S. Mahmood, “Recent Applications of Chitosan and Its Derivatives in Antibacterial, Anticancer, Wound Healing, and Tissue Engineering Fields,” *Polymers (Basel).*, vol. 16, no. 10, 2024.

[44] M. M. Islam, M. Shahruzzaman, S. Biswas, M. Nurus Sakib, and T. U. Rashid, “Chitosan based bioactive materials in tissue engineering applications-A review,” *Bioact. Mater.*, vol. 5, no. 1, pp. 164–183, 2020.

[45] K. Kulka and A. Sionkowska, “Chitosan Based Materials in Cosmetic Applications: A Review,” *Molecules*, vol. 28, no. 4, 2023.

[46] P. Mura, F. Maestrelli, M. Cirri, and N. Mennini, “Multiple Roles of Chitosan in Mucosal

Drug Delivery: An Updated Review," *Mar. Drugs*, vol. 20, no. 5, 2022.

[47] A. El Hadrami, L. R. Adam, I. El Hadrami, and F. Daayf, "Chitosan in plant protection," *Mar. Drugs*, vol. 8, no. 4, pp. 968–987, 2010.

[48] A. Basem, D. J. Jasim, H. Sh Majdi, R. M. Mohammed, M. Ahmed, A. H. Al-Rubaye and E. Kianfar, "Adsorption of heavy metals from wastewater by chitosan: A review," *Results Eng.*, vol. 23, no. June, p. 102404, 2024.

[49] K. Stefanowska, M. Woźniak, R. Dobrucka, and I. Ratajczak, "Chitosan with Natural Additives as a Potential Food Packaging," *Materials (Basel).*, vol. 16, no. 4, 2023.

[50] M. Barik, G. V. S. BhagyaRaj, K. K. Dash, and R. Shams, "A thorough evaluation of chitosan-based packaging film and coating for food product shelf-life extension," *J. Agric. Food Res.*, vol. 16, pp. 101164, 2024.

[51] K. Klinkhammer, H. Hohenbild, M. T. Hoque, L. Elze, H. Teshay, and B. Mahltig, "Functionalization of Technical Textiles with Chitosan," *Textiles*, vol. 4, no. 1, pp. 70–90, 2024.

[52] L. Huamg, L. Xiao and G. Yang, "Chitosan Application in Textile Processing," *Curr. Trends Fash. Technol. Text. Eng.*, vol. 4, no. 2, 2018.

[53] S. Vílchez, A. M. Manich, P. Jovancic, and P. Erra, "Chitosan contribution on wool treatments with enzyme," *Carbohydr. Polym.*, vol. 71, no. 4, pp. 515–523, 2008.

[54] M. Azmana, S. Mahmood, A. R. Hilles, A. Rahman, M. A. Bin Arifin, and S. Ahmed, "A review on chitosan and chitosan-based bionanocomposites: Promising material for combatting global issues and its applications," *Int. J. Biol. Macromol.*, vol. 185, no. July, pp. 832–848, 2021.

[55] D. A. Newfang, G. T. Johnson, and R. D. Harbison, "Nanoparticles," *Hamilt. Hardy's Ind. Toxicol. Sixth Ed.*, vol. 5, no. June, pp. 1025–1028, 2015.

[56] K. A. Altammar, "A review on nanoparticles: characteristics, synthesis, applications, and challenges," *Front. Microbiol.*, vol. 14, no. April, pp. 1–20, 2023.

[57] N. Baig, I. Kammakakam, W. Falath, and I. Kammakakam, "Nanomaterials: A review of synthesis methods, properties, recent progress, and challenges," *Mater. Adv.*, vol. 2, no. 6, pp. 1821–1871, 2021.

[58] G. Magdy, E. Aboelkassim, S. M. Abd Elhaleem, and F. Belal, "A comprehensive review

on silver nanoparticles: Synthesis approaches, characterization techniques, and recent pharmaceutical, environmental, and antimicrobial applications," *Microchem. J.*, vol. 196, no. November, p. 109615, 2024.

[59] C. Pechyen, B. Tangnorawich, S. Toommee, R. Marks, and Y. Parcharoen, "Green synthesis of metal nanoparticles, characterization, and biosensing applications," *Sensors Int.*, vol. 5, no. March, p. 100287, 2024.

[60] D. D. Evanoff and G. Chumanov, "Synthesis and optical properties of silver nanoparticles and arrays," *ChemPhysChem*, vol. 6, no. 7, pp. 1221–1231, 2005.

[61] R. Das, S. S. Nath, D. Chakdar, G. Gope, and R. Bhattacharjee, "Synthesis of silver nanoparticles and their optical properties," *J. Exp. Nanosci.*, vol. 5, no. 4, pp. 357–362, 2010.

[62] H. Barabadi, K. Jounaki, E. Pishgahzadeh, H. Morad, S. Sadeghian-Abadi, H. Vahidi and C. M. Hussain., "Antiviral potential of green-synthesized silver nanoparticles," *Handb. Microb. Nanotechnol.*, pp. 285–310, 2022.

[63] S. A. Ahmad, S. Sachi Das, A. Khatoon, M. Tahir Ansari, Mohd. Afzal, M. Saquib Hasnain and A. Kumar Nayak, "Bactericidal activity of silver nanoparticles: A mechanistic review," *Mater. Sci. Energy Technol.*, vol. 3, pp. 756–769, 2020.

[64] P. Allawadhi, V. Singh, Amit Khurana, I. Khurana, S. Allwadhi, P. Kumar, A. Kumar Banothu, S. Thalugula, P. J. Barani, R. R. Naik and K. Kumar Bharani, "Silver nanoparticle based multifunctional approach for combating COVID-19," *Sensors Int.*, vol. 2, no. March, p. 100101, 2021.

[65] L. Li, H. Pan, L. Deng, G. Qian, Z. Wang, W. Li and C. Zhong, "The antifungal activity and mechanism of silver nanoparticles against four pathogens causing kiwifruit post-harvest rot," *Front. Microbiol.*, vol. 13, no. August, pp. 1–16, 2022.

[66] K. J. Kim, W. S. Sung, B. Kyoung Suh, S. Moon, J. Choi, J. G. Kim and D. G. Lee, "Antifungal activity and mode of action of silver nano-particles on Candida albicans," *BioMetals*, vol. 22, no. 2, pp. 235–242, 2009.

[67] Z. A. Ratan, F. R. Mashrur, A. P. Chhoan, S. Md. Shahriar, M. Faisal Haidere, N. Jahan Runa, S. Kim, D. Kweon, H. Hosseinzadeh and J. Youl Cho, "Silver nanoparticles as potential antiviral agents," *Pharmaceutics*, vol. 13, no. 12, pp. 1–25, 2021.

[68] W. A. Al-Onazi and M. A. Abdel-Lateef, "Catalytic oxidation of O-phenylenediamine

by silver nanoparticles for resonance Rayleigh scattering detection of mercury (II) in water samples," *Spectrochim. Acta - Part A Mol. Biomol. Spectrosc.*, vol. 264, p. 120258, 2022.

[69] S. S. Ahmad, O. Yousuf, R. U. Islam, and K. Younis, "Silver nanoparticles as an active packaging ingredient and its toxicity," *Packag. Technol. Sci.*, vol. 34, no. 11–12, pp. 653–663, 2021.

[70] A. Istiqola and A. Syafiuddin, "A review of silver nanoparticles in food packaging technologies: Regulation, methods, properties, migration, and future challenges," *J. Chinese Chem. Soc.*, vol. 67, no. 11, pp. 1942–1956, 2020.

[71] A. Scroccarello, F. Della Pelle, M. Del Carlo, and D. Compagnone, "Optical plasmonic sensing based on nanomaterials integrated in solid supports. A critical review," *Anal. Chim. Acta*, vol. 1237, no. November, p. 340594, 2023.

[72] I. Ivanišević, S. Milardović, and P. Kassal, "Recent advances in (Bio)chemical sensors for food safety and quality based on silver nanomaterials," *Food Technol. Biotechnol.*, vol. 59, no. 2, pp. 216–237, 2021.

[73] L. Xu, Y. Y. Wang, J. Huang, C. Y. Chen, Z. X. Wang, and H. Xie, "Silver nanoparticles: Synthesis, medical applications and biosafety," *Theranostics*, vol. 10, no. 20, pp. 8996–9031, 2020.

[74] C. Mendes, A. Thirupathi, M. E. A. B. Corrêa, Y. Gu, and P. C. L. Silveira, "The Use of Metallic Nanoparticles in Wound Healing: New Perspectives," *Int. J. Mol. Sci.*, vol. 23, no. 23, 2022.

[75] N. Ivanova, V. Gugleva, M. Dobreva, I. Pehlivanov, S. Stefanov, and V. Andonova, "Silver Nanoparticles as Multi-Functional Drug Delivery Systems," *Nanomedicines*, 2019.

[76] M. A. Raheem, M. Ajwad Rahim, I. Gul, X. Zhong, C. Xiao, H. Zhang, J. Wei, Q. He, M. Hassan, C. Yang Zhang, D. Yu, V. Pandey, K. Du, R. Wang, S. Han, Y. Han, P. Qin, "Advances in nanoparticles-based approaches in cancer theranostics," *OpenNano*, vol. 12, no. April, 2023

[77] A. Loiseau, V. Asila, G. Boitel-Aullen, M. Lam, M. Salmain, and S. Boujday, "Silver-based plasmonic nanoparticles for and their use in biosensing," *Biosensors*, vol. 9, no. 2, 2019.

[78] M. Khazaei, M. S. Hosseini, A. M. Haghighi, and M. Misaghi, “Nanosensors and their applications in early diagnosis of cancer,” *Sens. Bio-Sensing Res.*, vol. 41, no. January, p. 100569, 2023.

[79] I. Salah, I. P. Parkin, and E. Allan, “Copper as an antimicrobial agent: Recent advances,” *RSC Adv.*, vol. 11, no. 30, pp. 18179–18186, 2021,

[80] M. Raffi, S. Mehrwan, T. M. Bhatti, J. I. Akhter, A. Hameed, W. Yawar and M. M. Ul Hasan, “Investigations into the antibacterial behavior of copper nanoparticles against Escherichia coli,” *Ann. Microbiol.*, vol. 60, no. 1, pp. 75–80, 2010.

[81] M. C. Vestergaard, Y. Nishida, L. T. T. Tran, N. Sharma, X. Zhang, M. Nakamura, A. F. Oussou-Azo and T. Nakama, “Antifungal Activity and Molecular Mechanisms of Copper Nanoforms against Colletotrichum gloeosporioides,” *Nanomaterials*, vol. 13, no. 23, 2023.

[82] X. Fan, L. Yahia, and E. Sacher, “Antimicrobial properties of the Ag, Cu nanoparticle system,” *Biology (Basel).*, vol. 10, no. 2, pp. 1–37, 2021.

[83] R. Khursheed, K. Dua, S. Vishwas, M. Gulati, N. Kumar Jha, G. M. Aldhafeeri, F. Ghadeer Alanazi, B. Hing Goh, G. Gupta, K Raj Paudel, P. M. Hansbro, D. Kumar Chellappan, S. Kumar Singh, “Biomedical applications of metallic nanoparticles in cancer: Current status and future perspectives,” *Biomed. Pharmacother.*, vol. 150, no. February, p. 112951, 2022.

[84] N. B. Varukattu, R. Vivek, C. Rejeeth, R. Thangam, T. Ponraj, A. Sharma, S. Kannan, "Nanostructured pH-responsive biocompatible chitosan coated copper oxide nanoparticles: A polymeric smart intracellular delivery system for doxorubicin in breast cancer cells,” *Arab. J. Chem.*, vol. 13, no. 1, pp. 2276–2286, 2020.

[85] R. Gulati, S. Sharma, and R. K. Sharma, “Antimicrobial textile: recent developments and functional perspective,” *Polym. Bull.*, vol. 79, no. 8, pp. 5747–5771, 2022.

[86] K. M. Flores-Rábago, D. Rivera-Mendoza, A. R. Vilchis-Nestor, K. Juarez-Moreno, and E. Castro-Longoria, “Antibacterial Activity of Biosynthesized Copper Oxide Nanoparticles (CuONPs) Using Ganoderma sessile,” *Antibiotics*, vol. 12, no. 8, 2023.

[87] S. Bonthula, S. R. Bonthula, R. Pothu, R. K. Srivastava, R. Boddula, A. B. Radwann and N. Al-Qahtani, “Recent Advances in Copper-Based Materials for Sustainable Environmental Applications,” *Sustain. Chem.*, vol. 4, no. 3, pp. 246–271, 2023.

[88] J. B. Fathima, A. Pugazhendhi, M. Oves, and R. Venis, “Synthesis of eco-friendly copper nanoparticles for augmentation of catalytic degradation of organic dyes,” *J. Mol. Liq.*, vol. 260, pp. 1–8, 2018.

[89] R. Teghil, A. De Bonis, A. Galasso, A. Santagata, G. Albano. P. Villani, D. Spera and G.P. Parisi, “Applications of ultra-short pulsed laser ablation: thin films deposition and fs/ns dual-pulse laser-induced breakdown spectroscopy,” *Phys. Scr.*, vol. 78, no. 5, p. 058113, 2008.

[90] R. F. Miller, J.C. Haglund, *Laser Ablation and Desorption*, Academic. 1st ediction,New York, 1988.

[91] H. Zeng, X. Du, S.C. Singh, S. A. Kulinich, S. Yang, J. He, W. Cai, “Nanomaterials via laser ablation/irradiation in liquid: A review,” *Adv. Funct. Mater.*, vol. 22, no. 7, pp. 1333–1353, 2012.

[92] G. W. Yang, “Laser ablation in liquids: Applications in the synthesis of nanocrystals,” *Prog. Mater. Sci.*, vol. 52, no. 4, pp. 648–698, 2007.

[93] L. Berthe, R. Fabbro, P. Peyre, and E. Bartnicki, “Wavelength dependent of laser shock-wave generation in the water-confinement regime,” *J. Appl. Phys.*, vol. 85, no. 11, p. 7552, 1999.

[94] S. M. Huang, Y. F. Lu, and Z. Sun, “Conversion of diamond clusters from a polymer by Nd:YAG pulsed laser (532 nm) irradiation,” *Appl. Surf. Sci.*, vol. 151, no. 3, pp. 244–250, 1999.

[95] W. Inoue, M. Okoshi, and N. Inoue, “Fabrication of diamond-like carbon thin films by femtosecond laser ablation of frozen acetone,” in *Applied Physics A: Materials Science and Processing*, vol. 79, no. 4–6, pp. 1457–1460, 2004.

[96] H. Zeng, X. Du, S. C. Singh, S. A. Kulinich, S. Yang, J. He and W. Cai, “Nanomaterials via laser ablation/irradiation in liquid: A review,” *Adv. Funct. Mater.*, vol. 22, no. 7, pp. 1333–1353, 2012.

[97] H. Zeng, Z. Li, W. Cai, B. Cao, P. Liu, and S. Yang, “Microstructure control of Zn/ZnO core/shell nanoparticles and their temperature-dependent blue emissions,” *J. Phys. Chem. B*, vol. 111, no. 51, pp. 14311–14317, 2007.

[98] H. Zeng, W. Cai, Y. Li, J. Hu, and P. Liu, “Composition / Structural Evolution and Optical Properties of ZnO / Zn Nanoparticles by Laser Ablation in Liquid Media,”

Society, pp. 18260–18266, 2005.

[99] Q. X. Liu, C. X. Wang, and G. W. Yang, "Formation of silver particles and silver oxide plume nanocomposites upon pulsed-laser induced liquid-solid interface reaction," *Eur. Phys. J. B*, vol. 41, no. 4, pp. 479–483, 2004.

[100] V. Amendola and M. Meneghetti, "What controls the composition and the structure of nanomaterials generated by laser ablation in liquid solution?," *Phys. Chem. Chem. Phys.*, vol. 15, no. 9, pp. 3027–3046, 2013.

[101] K. Y. Niu, J. Yang, S. a. Kulinich, J. Sun, H. Li, and X. W. Du, "Morphology control of nanostructures via surface reaction of metal nanodroplets," *J. Am. Chem. Soc.*, vol. 132, no. 28, pp. 9814–9819, 2010.

[102] K. Y. Niu, J. Yang, S. a. Kulinich, J. Sun, and X. W. Du, "Hollow nanoparticles of metal oxides and sulfides: Fast preparation via laser ablation in liquid," *Langmuir*, vol. 26, no. 22, pp. 16652–16657, 2010.

[103] A. V. Kabashin and M. Meunier, "Synthesis of colloidal nanoparticles during femtosecond laser ablation of gold in water," *J. Appl. Phys.*, vol. 94, no. 12, pp. 7941–7943, 2003.

[104] W. T. Nichols, T. Sasaki, and N. Koshizaki, "Laser ablation of a platinum target in water. II. Ablation rate and nanoparticle size distributions," *J. Appl. Phys.*, vol. 100, no. 11, p. 114912, 2006.

[105] C. Momma, B. N Chichkov, S. Nolte, F. von Alvensleben, A. Tünnermann, H. Welling and B. Wellegehausen, "Short-pulse laser ablation of solid targets," *Opt. Commun.*, vol. 129, no. 1–2, pp. 134–142, 1996.

[106] B. N. Chichkov, C. Momma, S. Nolte, F. von Alvensleben, and A. Tünnermann, "Femtosecond, picosecond and nanosecond laser ablation of solids," *Appl. Phys. A Mater. Sci. Process.*, vol. 63, no. 2, pp. 109–115, 1996.

[107] A. Miotello and R. Kelly, "Laser-induced phase explosion: new physical problems when a condensed phase approaches the thermodynamic critical temperature," *Appl. Phys. A Mater. Sci. Process.*, vol. 69, no. S1, pp. S67–S73, Dec. 1999.

[108] M. Hashida, H. Mishima, S. Tokita, and S. Sakabe, "Non-thermal ablation of expanded polytetrafluoroethylene with an intense femtosecond-pulse laser," *Opt. Express*, vol. 17, no. 15, pp. 1850–1852, 2009.

[109] F. Giammanco, E. Giorgetti, P. Marsili, and A. Giusti, “Experimental and Theoretical Analysis of Photofragmentation of Au Nanoparticles by Picosecond Laser Radiation,” *J. Phys. Chem. C*, vol. 114, no. 8, pp. 3354–3363, 2010.

[110] A. Vogel, N. Linz, S. Freidank, and G. Paltauf, “Femtosecond-laser-induced nanocavitation in water: Implications for optical breakdown threshold and cell surgery,” *Phys. Rev. Lett.*, vol. 100, no. 3, pp. 1–4, 2008.

[111] Y. Tomita, M. Tsubota, and N. An-naka, “Energy evaluation of cavitation bubble generation and shock wave emission by laser focusing in liquid nitrogen,” *J. Appl. Phys.*, vol. 93, no. 5, p. 3039, 2003.

[112] T. Tsuji, Y. Tsuboi, N. Kitamura, and M. Tsuji, “Microsecond-resolved imaging of laser ablation at solid–liquid interface: investigation of formation process of nano-size metal colloids,” *Appl. Surf. Sci.*, vol. 229, no. 1–4, pp. 365–371, 2004.

[113] T. E. Itina, “On Nanoparticle Formation by Laser Ablation in Liquids,” *J. Phys. Chem. C*, vol. 115, no. 12, pp. 5044–5048, 2011.

[114] M. Barberio and P. Antici, “In situ study of nucleation and aggregation phases for nanoparticles grown by laser-driven methods,” no. August 2016, pp. 85–87, 2017.

[115] A. Subhan and A. I. Mourad, “Influence of Laser Process Parameters , Liquid Medium , and External Field on the Synthesis of Colloidal Metal Nanoparticles Using Pulsed Laser Ablation in Liquid : A Review,” *Nanomaterials*,vol. 12, no. 13, 2022.

[116] L. V. Zhigilei, “Dynamics of the plume formation and parameters of the ejected clusters in short-pulse laser ablation,” *Appl. Phys. A Mater. Sci. Process.*, vol. 76, no. 3, pp. 339–350, 2003.

[117] A. De Giacomo, M. Dell’Aglio, O. De Pascale, and M. Capitelli, “From single pulse to double pulse ns-Laser Induced Breakdown Spectroscopy under water: Elemental analysis of aqueous solutions and submerged solid samples,” *Spectrochim. Acta Part B At. Spectrosc.*, vol. 62, no. 8, pp. 721–738, 2007.

[118] S. Ibrahimkutty, P. Wagener, A. Menzel, A. Plech, and S. Barcikowski, “Nanoparticle formation in a cavitation bubble after pulsed laser ablation in liquid studied with high time resolution small angle x-ray scattering,” *Appl. Phys. Lett.*, vol. 101, no. 10, 2012.

[119] Z. Yan, R. Bao, Y. Huang, and D. B. Chrisey, “Hollow particles formed on laser-induced bubbles by excimer laser ablation of Al in liquid,” *J. Phys. Chem. C*, vol. 114, no. 26,

pp. 11370–11374, 2010.

[120] R. Zhao, R. Xu, Z. Shen, J. Lu, and X. Ni, “Experimental investigation of the collapse of laser-generated cavitation bubbles near a solid boundary,” *Opt. Laser Technol.*, vol. 39, no. 5, pp. 968–972, 2007.

[121] T. K. Fumitaka Mafune, Jun-ya Kohno and Yoshihiro Takeda, “Formation of Gold Nanoparticles by Laser Ablation in Aqueous Solution of Surfactant,” *J. Phys. Chem. B*, vol. 105, pp. 5114–5120, 2001.

[122] F. Mafune, J. Kohno, Y. Takeda, T. Kondow, and H. Sawabe, “Formation and size control of sliver nanoparticles by laser ablation in aqueous solution,” *J. Phys. Chem. B*, vol. 104, no. 39, pp. 9111–9117, 2000.

[123] V. Amendola, S. Polizzi, and M. Meneghetti, “Laser Ablation Synthesis of Gold Nanoparticles in Organic Solvents,” *J. Phys. Chem. B*, vol. 110, no. 14, pp. 7232–7237, 2006.

[124] A. Menéndez-Manjón, *Metal nanoparticle formation by laser ablation in liquids*, *Tredition*, 2012.

[125] E. Stratakis, V. Zorba, M. Barberoglou, C. Fotakis, and G. a Shafeev, “Laser writing of nanostructures on bulk Al via its ablation in liquids,” *Nanotechnology*, vol. 20, no. 10, p. 105303, 2009.

[126] E. Stratakis, M. Barberoglou, C. Fotakis, G. Viau, C. Garcia, and G. a Shafeev, “Generation of Al nanoparticles via ablation of bulk Al in liquids with short laser pulses.,” *Opt. Express*, vol. 17, no. 15, pp. 12650–12659, 2009.

[127] E. Christopher, Brennen, "Cavitation and bubble dynamics", *Oxford University Press*, vol. 9, no. 1. 1977.

[128] D. Faccio, G. Tamošauskas, E. Rubino, J. Darginavičius, D. G. Papazoglou, S. Tzortzakis, A. Couairon, and A. Dubietis, “Cavitation dynamics and directional microbubble ejection induced by intense femtosecond laser pulses in liquids,” *Phys. Rev. E*, vol. 86, no. 3, p. 036304, 2012.

[129] M. S. Plesset and a Prosperetti, “Bubble Dynamics and Cavitation,” *Annu. Rev. Fluid Mech.*, vol. 9, no. 1, pp. 145–185, 1977.

[130] Z. Yan and D. B. Chrisey, “Pulsed laser ablation in liquid for micro-/nanostructure generation,” *J. Photochem. Photobiol. C Photochem. Rev.*, vol. 13, no. 3, pp. 204–223,

2012.

[131] W. Lauterborn and T. Kurz, “Physics of bubble oscillations,” *Reports Prog. Phys.*, vol. 73, no. 10, p. 106501, 2010.

[132] A. Menéndez-Manjón, P. Wagener, and S. Barcikowski, “Transfer-matrix method for efficient ablation by pulsed laser ablation and nanoparticle generation in liquids,” *J. Phys. Chem. C*, vol. 115, pp. 5108–5114, 2011.

[133] X. Liu, Y. Hou, X. Liu, J. He, J. Lu, and X. Ni, “Oscillation characteristics of a laser-induced cavitation bubble in water at different temperatures,” *Opt. - Int. J. Light Electron Opt.*, vol. 122, no. 14, pp. 1254–1257, Jul. 2011.

[134] M. Mucha, “Rheological characteristics of semi-dilute chitosan solutions,” *Macromol. Chem. Phys.*, vol. 198, no. 2, pp. 471–484, 1997.

[135] M. Psarianos, S. Ojha, R. Schneider, and O. K. Schlüter, “Chitin Isolation and Chitosan Production from House Crickets (Acheta domesticus) by Environmentally Friendly Methods,” *Molecules*, vol. 27, no. 15, 2022,.

[136] A. Nafary, S. Mousavi Nezhad, and S. Jalili, “Extraction and characterization of chitin and chitosan from Tenebrio Molitor beetles and investigation of its antibacterial effect against Pseudomonas aeruginosa,” *Adv. Biomed. Res.*, vol. 12, no. 1, pp. 2–7, 2023.

[137] R. Siddiqui, Y. Elmashak, and N. A. Khan, “Cockroaches: a potential source of novel bioactive molecule(s) for the benefit of human health,” *Appl. Entomol. Zool.*, vol. 58, no. 1, pp. 1–11, 2023.

[138] M. Triunfo, E. Tafi, A. Guarnieri, R. Salvia, C. Scieuzo, T. Hahn, S. Zibek, A. Gagliardini, L. Panariello, M. B. Coltelli, A. De Bonis and P. Falabella, “Characterization of chitin and chitosan derived from Hermetia illucens, a further step in a circular economy process,” *Sci. Rep.*, vol. 12, no. 1, pp. 1–17, 2022.

[139] Y. L. Kleden, L. Mukkun, M. H. Ndapamuri, and F. Pramatana, “The migratory locust (Locusta migratoria) as a potential source of protein and biopolymer compounds in the future,” *Biodiversitas*, vol. 24, no. 11, pp. 5979–5987, 2023.

[140] S. V. Nemtsev, O. Y. Zueva, M. R. Khismatullin, A. I. Albulov, and V. P. Varlamov, “Isolation of chitin and chitosan from honeybees,” *Appl. Biochem. Microbiol.*, vol. 40, no. 1, pp. 39–43, 2004.

[141] S. Lievens, G. Poma, J. De Smet, L. Van Campenhout, A. Covaci, and M. Van Der

Borght, “Chemical Safety of Black Soldier Fly Larvae (Hermetia Illucens), Knowledge Gaps and Recommendations for Future Research: a Critical Review,” *J. Insects as Food Feed*, vol. 7, no. 4, pp. 383–396, 2021.

[142] H. Guo, C. Jiang, Z. Zhang, W. Lu, and H. Wang, “Material flow analysis and life cycle assessment of food waste bioconversion by black soldier fly larvae (Hermetia illucens L.),” *Sci. Total Environ.*, vol. 750, p. 141656, 2021.

[143] M. Kaczor, P. Bulak, K. Proc-Pietrycha, M. Kirichenko-Babko, and A. Bieganowski, “The Variety of Applications of Hermetia illucens in Industrial and Agricultural Areas—Review,” *Biology (Basel).*, vol. 12, no. 1, pp. 1–36, 2023.

[144] A. Franco, C. Scieuzo, R. Salvi, A. M. Petrone, E. Tafi, A. Moretta, E. Schmitt and P. Falabella, “Lipids from hermetia illucens, an innovative and sustainable source,” *Sustain.*, vol. 13, no. 18, 2021.

[145] S. A. Siddiqui, L. van Greunen, A. Zeiri, B. Yudhistira, A. Ahmad, and M. Monnye, “The potential of chitin and chitosan from dead black soldier fly (BSF) (Hermetia illucens) for biodegradable packaging material – A critical review,” *Process Saf. Environ. Prot.*, vol. 189, no. February, pp. 1342–1367, 2024.

[146] N. A. Z. Abidin, F. Kormin, N. A. Z. Abidin, N. A. F. M. Anuar, and M. F. A. Bakar, “The potential of insects as alternative sources of chitin: An overview on the chemical method of extraction from various sources,” *Int. J. Mol. Sci.*, vol. 21, no. 14, pp. 1–25, 2020.

[147] A. Khayrova, S. Lopatin, and V. Varlamov, “Obtaining chitin, chitosan and their melanin complexes from insects,” *Int. J. Biol. Macromol.*, vol. 167, pp. 1319–1328, 2021.

[148] A. Das, S. Ghosh, and N. Pramanik, “Chitosan biopolymer and its composites: Processing, properties and applications- A comprehensive review,” *Hybrid Adv.*, vol. 6, no. July, p. 100265, 2024.

[149] C. Ardean, C. M. Davidescu, and N. S. Neme, " Factors Influencing the Antibacterial Activity of Chitosan and Chitosan Modified by Functionalization" , *Int. J. Mol. Sci.*, vol. 22, no. 14, p. 7449, 2021.

[150] I. Aranaz, R. Alc, and M. Concepci, “Chitosan: An Overview of Its Properties and Applications", *Polymers*, vol. 13, p. 3256, 2021.

[151] T. Hahn, E. Tafi, A. Paul, R. Salvia, P. Falabella, and S. Zibek, “Current state of chitin

purification and chitosan production from insects," *J. Chem. Technol. Biotechnol.*, vol. 95, no. 11, pp. 2775–2795, 2020.

[152] L. Segal, J. J. Creely, A. E. Martin, and C. M. Conrad, "An Empirical Method for Estimating the Degree of Crystallinity of Native Cellulose Using the X-Ray Diffractometer," *Text. Res. J.*, vol. 29, no. 10, pp. 786–794, 1959.

[153] P. Scherrer, "Bestimmung der inneren Struktur und der Größe von Kolloidteilchen mittels Röntgenstrahlen," *Kolloidchem. Ein Lehrb.*, vol. 277, no. 1916, pp. 387–409, 1912.

[154] R. D. Biskup, D. Jarosińska, B. Rokita, P. Ulański, J. M. Rosiak "Determination of degree of deacetylation of chitosan - comparision of methods"*Progress on Chemistry and Application of Chitin and Its* Derivates, vol. 17, pp. 5–20, 2012.

[155] A. Z. Hameed, S. A. Raj, J. Kandasamy, M. A. Baghdadi, and M. A. Shahzad, "Chitosan: A Sustainable Material for Multifarious Applications," *Polymers (Basel).*, vol. 14, no. 12, pp. 1–34, 2022.

[156] T. Fromme, S. Reichenberger, K. M. Tibbetts, and S. Barcikowski, "Laser synthesis of nanoparticles in organic solvents – products, reactions, and perspectives," *Beilstein J. Nanotechnol.*, vol. 15, pp. 638–663, 2024.

[157] T. T. V. Phan, D. T. Phan, X. T. Cao, T. C. Huynh, and J. Oh, "Roles of chitosan in green synthesis of metal nanoparticles for biomedical applications," *Nanomaterials*, vol. 11, no. 2, pp. 1–15, 2021.

[158]A.Ancona,M.C. Sportelli, A. Trapani, R.A. Picca, C. Palazzo, E. Bonerba, F.P. Mezzapesa, G. Tantillo, G. Trapani, N. Cioffi, "Synthesis and characterizations of hybryd copper-chitosan nano-antimicrobials by femtosecond laser-ablation in liquids", Materials Letters, vol.136, pp. 397-400, 2014

[159] T. X. Phuoc, "Complete Green Synthesis of Gold Nanoparticles using Laser Ablation in Deionized Water Containing Chitosan and Starch," *J. Mater. Sci. Nanotechnol.*, vol. 1, no. 4, 2014.

[160] M. Tajdidzadeh, B. Z. Azmi, W. Mahmood M. Yunus, Z. Abidin Talib, A. R. Sadrolhosseini, K. Karimzadeh, S. A. Gene and M. Dorraj., "Synthesis of silver nanoparticles dispersed in various aqueous media using laser ablation," *Sci. World J.*, vol. 2014, 2014.

[161] R. Zamiri, B. Z. Azmi, H. A. Ahangar, G. Zamiri, M. S. Husin, and Z. A. Wahab, “Preparation and characterization of silver nanoparticles in natural polymers using laser ablation,” *Bull. Mater. Sci.*, vol. 35, no. 5, pp. 727–731, 2012.

[162] M. C. Sportelli, A. Volpe, R. Anna Picca, A. Trapani, C. Palazzo, A. Ancona, P. M. Lugarà, G. Trapani and N. Cioffi, “Spectroscopic characterization of copper-chitosan nanoantimicrobials prepared by laser ablation synthesis in aqueous solutions,” *Nanomaterials*, vol. 7, no. 1, 2017.

[163] H. H. Lara, G. Guisbiers, J. Mendoza, L. C. Mimun, B. A. Vincent, J. L Lopez-Ribot, K. L. Nash, “Synergistic antifungal effect of chitosan-stabilized selenium nanoparticles synthesized by pulsed laser ablation in liquids against Candida albicans biofilms,” *Int. J. Nanomedicine*, vol. 13, pp. 2697–2708, 2018.

[164] M. Tajdidzadeh, A. Zakaria, Z. A. Talib, A. Nisar, M. B. Kanoun, and S. Goumri-Said, “Improving stability of zinc nanoparticles in chitosan solution with a nanosecond pulsed laser,” *Laser Phys. Lett.*, vol. 16, no. 5, 2019.

[165] O. M. Khubiev, A. R. Egorov, A. A. Kirichuk, V. N. Khrustalev, A. G. Tskhovrebov, and A. S. Kritchenkov, “Chitosan-Based Antibacterial Films for Biomedical and Food Applications,” *Int. J. Mol. Sci.*, vol. 24, no. 13, 2023.

[166] V. G. L. Souza, J. R. A. Pires, C. Rodrigues, I. M. Coelhoso, and A. L. Fernando, “Chitosan composites in packaging industry-current trends and future challenges,” *Polymers (Basel).*, vol. 12, no. 2, pp. 1–16, 2020.

[167] M. Flórez, E. Guerra-Rodríguez, P. Cazón, and M. Vázquez, “Chitosan for food packaging: Recent advances in active and intelligent films,” *Food Hydrocoll.*, vol. 124, 2022.

[168] H. Wang, F. Ding, L. Ma, and Y. Zhang, “Edible films from chitosan-gelatin: Physical properties and food packaging application,” *Food Biosci.*, vol. 40, no. January, p. 100871, 2021.

[169] S. Affes, H. Maalej, I. Aranaz, H. Kchaou, N. Acosta, Á. Heras and M. Nasri, “Controlled size green synthesis of bioactive silver nanoparticles assisted by chitosan and its derivatives and their application in biofilm preparation,” *Carbohydr. Polym.*, vol. 236, no. December 2019, 2020.

[170] A. H. Virgili, D. C. Laranja, P. S. Malheiros, M. B. Pereira, T. M. H. Costa, and E. W. de Menezes, “Nanocomposite film with antimicrobial activity based on gold

nanoparticles, chitosan and aminopropylsilane," *Surf. Coatings Technol.*, vol. 415, no. January, p. 127086, 2021.

[171] K. Pal, P. Sarkar, A. Anis, K. Wiszumirska, and M. Jarzębski, "Polysaccharide-based nanocomposites for food packaging applications," *Materials (Basel).*, vol. 14, no. 19, pp. 1–38, 2021.

[172] H. Ueno, H Yamada, I Tanaka, N Kaba, M Matsuura, M Okumura, T Kadosawa and T Fujinaga, "Accelerating effects of chitosan for healing at early phase of experimental open wound in dogs," *Biomaterials*, vol. 20, no. 15, pp. 1407–1414, 1999.

[173] A. Moeini, P. Pedram, P. Makvandi, M. Malinconico, and G. Gomez d'Ayala, "Wound healing and antimicrobial effect of active secondary metabolites in chitosan-based wound dressings: A review," *Carbohydr. Polym.*, vol. 233, no. January, p. 115839, 2020.

[174] F. S. Rezaei, F. Sharifianjazi, A. Esmaeilkhanian, and E. Salehi, "Chitosan films and scaffolds for regenerative medicine applications: A review," *Carbohydr. Polym.*, vol. 273, no. July, p. 118631, 2021.

[175] C. Pansara, R. Mishra, T. Mehta, A. Parikh, and S. Garg, "Formulation of Chitosan Stabilized Silver Nanoparticle-Containing Wound Healing Film: In Vitro and In Vivo Characterization," *J. Pharm. Sci.*, vol. 109, no. 7, pp. 2196–2205, 2020.

[176] V. Kulikouskaya, T. Zhdanko, K. Hileuskaya, A. Kraskouski, A. Zhura, H. Skorohod, V. Butkevich, K. Pal, S. Tratsyak and V. Agabekov, "Physicochemical aspects of design of ultrathin films based on chitosan, pectin, and their silver nanocomposites with antiadhesive and bactericidal potential," *J. Biomed. Mater. Res. - Part A*, vol. 110, no. 1, pp. 217–228, 2022.

[177] A. D. Nugraheni, D. Purnawati, and A. Kusumaatmaja, "Physical Evaluation of PVA/Chitosan Film Blends with Glycerine and Calcium Chloride," *J. Phys. Conf. Ser.*, vol. 1011, no. 1, 2018.

[178] S. B. Aziz, O. G. Abdullah, D. R. Saber, M. A. Rasheed, and H. M. Ahmed, "Investigation of metallic silver nanoparticles through UV-Vis and optical micrograph techniques," *Int. J. Electrochem. Sci.*, vol. 12, no. 1, pp. 363–373, 2017.

[179] R. Desai, V. Mankad, S. K. Gupta, and P. K. Jha, "Size distribution of silver nanoparticles: UV-visible spectroscopic assessment," *Nanosci. Nanotechnol. Lett.*, vol. 4, no. 1, pp. 30–34, 2012.

[180] R. Emam and N. Eassa, “Synthesis, Characterization and Size Evaluation of Biosynthesized Silver Nanoparticles by UV–Vis Spectroscopy,” *African J. Eng. Technol.*, vol. 1, no. 1, pp. 1–15, 2021.

[181] J. Vega-Baudrit, R. Alvarado-Meza, and F. Solera-Jiménez, “Synthesis of silver nanoparticles using chitosan as a coating agent by sonochemical method,” *Av. en Quim.*, vol. 9, no. 3, pp. 125–129, 2014.

[182] V. Amendola and M. Meneghetti, “Laser ablation synthesis in solution and size manipulation of noble metal nanoparticles,” *Phys. Chem. Chem. Phys.*, vol. 11, no. 20, pp. 3805–3821, 2009.

[183] M. A. M. Khan, S. Kumar, M. Ahamed,S. A. Alrokayan, M.S. Alsalhi, M. Alhoshan and A.S. Aldwayyan, “Structural and spectroscopic studies of thin film of silver nanoparticles,” *Appl. Surf. Sci.*, vol. 257, no. 24, pp. 10607–10612, 2011.

[184] S. Hajji, I. Younes, O. Ghorbel-Bellaaj, R. Hajji, M. Rinaudo, M. Nasri and K. Jellouli, “Structural differences between chitin and chitosan extracted from three different marine sources,” *Int. J. Biol. Macromol.*, vol. 65, pp. 298–306, 2014.

[185] M. H. Ali, M. A. K. Azad, K. A. Khan, M. O. Rahman, U. Chakma, and A. Kumer, “Analysis of Crystallographic Structures and Properties of Silver Nanoparticles Synthesized Using PKL Extract and Nanoscale Characterization Techniques,” *ACS Omega*, vol. 8, no. 31, pp. 28133–28142, 2023.

[186] W. Wang and P. Alexandridis, “Composite polymer electrolytes: Nanoparticles affect structure and properties,” *Polymers (Basel).*, vol. 8, no. 11, 2016.

[187] J. Brugnerotto, J. Lizardi, F. M. Goycoolea, W. Argüelles-Monal, J. Desbrières, and M. Rinaudo, “An infrared investigation in relation with chitin and chitosan characterization,” *Polymer (Guildf).*, vol. 42, no. 8, pp. 3569–3580, 2001.

[188] A. Pandit, A. Indurkar, C. Deshpande, R. Jain, and P. Dandekar, “A systematic review of physical techniques for chitosan degradation,” *Carbohydr. Polym. Technol. Appl.*, vol. 2, no. November 2020, p. 100033, 2021.

[189] A. Guarnieri, M. Triunfo, C. Scieuzo, D. Ianniciello, E. Tafi, T. Hahn, S. Zibek, R. Salvia, A. De Bonis and P. Falabella, “Antimicrobial properties of chitosan from different developmental stages of the bioconverter insect Hermetia illucens,” *Sci. Rep.*, vol. 12, no. 1, pp. 1–12, 2022.

[190] M. Fernández-Arias, M. Boutinguiza, J. Del Val, C. Covarrubias, F. Bastias, L. Gómez, M. Maureira, F. Arias-González, A. Riveiro and J. Pou, "Copper nanoparticles obtained by laser ablation in liquids as bactericidal agent for dental applications," *Appl. Surf. Sci.*, vol. 507, no. December 2019, p. 145032, 2020.

[191] N. Liu, Xi-Guang Chen, H. Park,C. Liu, C. Liu, X. Meng and L. Yu, "Effect of MW and concentration of chitosan on antibacterial activity of Escherichia coli," *Carbohydr. Polym.*, vol. 64, no. 1, pp. 60–65, 2006.

[192] A. M. Muthukrishnan and M. Sathiyabama, "Green Synthesis of Copper-Chitosan Nanoparticles and Study of its Antibacterial Activity," *J. Nanomed. Nanotechnol.*, vol. 06, no. 01, pp. 1–5, 2015.

[193] V. Holubnycha, M. Pogorielov, V. Korniienko, "Antibacterial activity of the new copper nanoparticles and Cu NPs/chitosan solution," *Proc. 2017 IEEE 7th Int. Conf. Nanomater. Appl. Prop. N. 2017*, vol. 2017-January, pp. 2–5, 2017.

[194] J. Laanoja, M. Sihtmae, S. Vihodceva, M. Iesalnieks, M. Otus, I, Kurvet, A. Kahru and K. Kasemets, "Synthesis and synergistic antibacterial efficiency of chitosan-copper oxide nanocomposites," *Heliyon*, vol. 10, no. 15, 2024, doi: 10.1016/j.heliyon.2024.e35588.

[195] E. O. Mikhailova, "Silver Nanoparticles: Mechanism of Action and Probable Bio-Application," *J. Funct. Biomater.*, vol. 11, no. 4, 2020, doi: 10.3390/jfb11040084.

[196] C. You, Q. Li, X. Wang, P. Wu, J.K. Ho, R. Jin, L. Zhang,H. Shao and C. Han, "Silver nanoparticle loaded collagen/chitosan scaffolds promote wound healing via regulating fibroblast migration and macrophage activation," *Scientific Reports.*, vol. 7, no. 1, pp. 1–11, 2017.

[197] S. Alven and B. A. Aderibigbe, "Chitosan-Based Scaffolds Incorporated with Silver Nanoparticles for the Treatment of Infected Wounds," *Pharmaceutics*, vol. 16, no. 3, pp. 1–28, 2024.

[198] A. A. Khalili and M. R. Ahmad, "A Review of cell adhesion studies for biomedical and biological applications," Int. J. Mol. Sci., vol. 16, no. 8, pp. 18149–18184, 2015.

[199] Z. Zhang, X. Cheng, Y. Yao, J. Luo, Q. Tang, H. Wu, S. Lin, C. Han, Q. Weib and L. Chen, "Electrophoretic deposition of chitosan/gelatin coatings with controlled porous surface topography to enhance initial osteoblast adhesive responses," J. Mater. Chem. B, vol. 4, no. 47, pp. 7584–7595, 2016.

[200] P. R. Souza, A. C. de Oliveira, B. H. Vilsinski, M. J. Kipper, and A. F. Martins, "Polysaccharide-based materials created by physical processes: From preparation to biomedical applications," Pharmaceutics, vol. 13, no. 5, 2021.

[201] B. Clarke, "Normal bone anatomy and physiology.," Clin. J. Am. Soc. Nephrol., vol. 3 Suppl 3, pp. 131–139, 2008.

[202] R. Florencio-Silva, G. R. D. S. Sasso, E. Sasso-Cerri, M. J. Simões, and P. S. Cerri, "Biology of Bone Tissue: Structure, Function, and Factors That Influence Bone Cells," Biomed Res. Int., vol. 2015, 2015.

[203] V. Šromová, D. Sobola, and P. Kaspar, "A Brief Review of Bone Cell Function and Importance," Cells, vol. 12, no. 21, 2023.

[204] A. F. Mavrogenis, R. Dimitriou, J. Parvizi, and G. C. Babis, "Biology of implant osseointegration," J Musculoskelet Neuronal Interact, vol. 9, pp. 61–71, 2009.

[205] J. Y. Choi, J. H. Sim, and I. S. Luke, "Characteristics of contact and distance osteogenesis around modified implant surfaces in rabbit tibiae," J. Periodontal Implant Sci., vol. 47, no. 3, pp. 182–192, 2017.

[206] P. R. T. Kuzyk and E. H. Schemitsch, "The basic science of peri-implant bone healing," Indian J. Orthop., vol. 45, no. 2, pp. 108–115, 2011.

[207] M. do Nascimento, T. O. Brito, A. M. Lima, and C. N. Elias, "Protein interactions with osseointegrable titanium implants," Brazilian J. Oral Sci., vol. 22, pp. 1–15, 2022.

[208] F. Loi, L. A. Córdova, J. Pajarinen, T.-H. Lin, Z. Yao, and S. B. Goodman, "Inflammation, Fracture and Bone Repair HHS Public Access," Bone, vol. 86, pp. 119–130, 2016.

[209] M. A. A. Wahab, E. M. Yusof, R. Ahmad, M. Z. Salleh, and T. L. Kek, "Peri-implant Bone Healing: Its Basic Osteogenesis and Biomarkers," Malaysian J. Med. Heal. Sci., vol. 18, no. 6, pp. 324–331, 2022.

[210] S. Bohara and J. Suthakorn, "Surface coating of orthopedic implant to enhance the osseointegration and reduction of bacterial colonization: a review," Biomater. Res., vol. 26, no. 1, pp. 1–17, 2022.

[211] N. López-Valverde, A. López-Valverde, and J. M. Ramírez, "Systematic review of effectiveness of chitosan as a biofunctionalizer of titanium implants," *Biology (Basel).*, vol. 10, no. 2, pp. 1–12, 2021.

[212] Y. Zhao, S. Zhao, Z. Ma, C. Ding, J. Chen, and J. Li, “Chitosan-Based Scaffolds for Facilitated Endogenous Bone Re-Generation,” *Pharmaceuticals*, vol. 15, no. 8, pp. 1–25, 2022.

[213] B. M. Alnufaiy, R. N. A. Lambarte, and K. S. Alhamdan, “The osteogenetic potential of chitosan coated implant: An in vitro study,” *J. Stem Cells Regen. Med.*, vol. 16, no. 2, pp. 44–49, 2020.

[214] A. Katariya and G. Bhatia, “Silver as an antimicrobial coating on titanium implants,” *J. Oral Res. Rev.*, vol. 14, no. 1, p. 80, 2022.

[215] H. J. Haugen, S. Makhtari, S. Ahmadi, and B. Hussain, “The Antibacterial and Cytotoxic Effects of Silver Nanoparticles Coated Titanium Implants: A Narrative Review,” *Materials (Basel).*, vol. 15, no. 14, 2022.

[216] S. A. Brennan, C. N. Fhoghlú, B. M. DeVitt, F. J. O’Mahony, D. Brabazon, and A. Walsh, “Instructional review: General orthopaedics silver nanoparticles and their orthopaedic applications,” *Bone Jt. J.*, vol. 97-B, no. 5, pp. 582–589, 2015.

[217] S. Cometa, M. A. Bonifacio, F. Baruzzi, S. de Candia, M. M. Giangregorio, L. C. Giannossa, M. Dicarlo, M. Mattioli-Belmonte, L. Sabbatini and E. De Giglio., “Silver-loaded chitosan coating as an integrated approach to face titanium implant-associated infections: analytical characterization and biological activity,” *Anal. Bioanal. Chem.*, vol. 409, no. 30, pp. 7211–7221, 2017.

[218] L. Besra and M. Liu, “A review on fundamentals and applications of electrophoretic deposition (EPD),” *Prog. Mater. Sci.*, vol. 52, no. 1, pp. 1–61, 2007.

[219] H. C. Hamaker, “Formation of deposit by electrophoresis,” *Trans. Faraday Soc.*, vol. 35, pp. 279–287, 1940.

[220] P. Sarka and P. S. Nicholson, “Electrophoretic Deposition (EPD): Mechanism, Kinetics, and Applications to ceramics,” *j. Am. Ceram. Soc.*, vol. 79, pp. 1987–2002, 1996.

[221] P. M. Biesheuvel and H. Verweij, “Theory of cast formation in electrophoretic deposition,” *J. Am. Ceram. Soc.*, vol. 82, no. 6, pp. 1451–1455, 1999.

[222] O. O. Van der Biest and L. J. Vandeperre, “Electrophoretic deposition of materials,” *Annu. Rev. Mater. Res.*, vol. 29, pp. 327–357, 1999.

[223] E. Avcu, F. E. Baştan, H. Z. Abdullah, M. A. U. Rehman, Y. Y. Avcu, and A. R. Boccaccini, “Electrophoretic deposition of chitosan-based composite coatings for

biomedical applications: A review," *Prog. Mater. Sci.*, vol. 103, no. January, pp. 69–108, 2019.

[224] A. R. Boccaccini, S. Keim, R. Ma, Y. Li, and I. Zhitomirsky, "Electrophoretic deposition of biomaterials," *J. R. Soc. Interface*, vol. 7, no. SUPPL. 5, 2010.

[225] Ł. Pawłowski, M. Bartmański, A. Mielewczyk-Gryń, B. M. Cieślik, G. Gajowiec, and A. Zieliński, "Electrophoretically deposited chitosan/eudragit e 100/agnps composite coatings on titanium substrate as a silver release system," *Materials (Basel).*, vol. 14, no. 16, 2021.

[226] M. Bartmanski, Ł. Pawłowski, A. Zielinski, A. Mielewczyk-Gryn, G. Strugała, and B. Ciselik, "Electrophoretic Deposition and Characteristics of," *Coatings*, vol. 10, no. 245, 2020.

[227] Q. Chen, S. Cabanas-Polo, O. M. Goudouri, and A. R. Boccaccini, "Electrophoretic co-deposition of polyvinyl alcohol (PVA) reinforced alginate-Bioglass® composite coating on stainless steel: Mechanical properties and in-vitro bioactivity assessment," *Mater. Sci. Eng. C*, vol. 40, pp. 55–64, 2014.

[228] P. K. Naito, Y. Ogawa, S. Kimura, T. Iwata, and M. Wada, "Crystal transition from hydrated chitosan and chitosan/monocarboxylic acid complex to anhydrous chitosan investigated by X-ray diffraction," *J. Polym. Sci. Part B Polym. Phys.*, vol. 53, no. 15, pp. 1065–1069, 2015.

[229] Y. Arima and H. Iwata, "Effect of wettability and surface functional groups on protein adsorption and cell adhesion using well-defined mixed self-assembled monolayers," *Biomaterials*, vol. 28, no. 20, pp. 3074–3082, 2007.

[230] S. Heise, C. Forster. S. Heer, H. Qi, J. Zhou, S.Virtanen, T. Lu, and A. R. Boccaccini a, "Electrophoretic deposition of gelatine nanoparticle/chitosan coatings," *Electrochim. Acta*, vol. 307, pp. 318–325, 2019.

[231] Ł. Pawłowski, M. Bartmański, G. Strugała, A. Mielewczyk-Gryń, M. Jazdzewska, and A. Zieliński, "Electrophoretic deposition and characterization of chitosan/eudragit E 100 coatings on titanium substrate," *Coatings*, vol. 10, no. 7, 2020.

[232] Y. Shirosaki, K. Tsuru, S. Hayakawa, A. Osaka, M. Ascensão Lopes, J. D. Santos and M. H. Fernandes, "In vitro cytocompatibility of MG63 cells on chitosan-organosiloxane hybrid membranes," *Biomaterials*, vol. 26, no. 5, pp. 485–493, 2005.

[233] H. Xie, P. Wang, and J. Wu, “Effect of exposure of osteoblast-like cells to low-dose silver nanoparticles: uptake, retention and osteogenic activity,” *Artif. Cells, Nanomedicine Biotechnol.*, vol. 47, no. 1, pp. 260–267, 2019.

[234] M. A. S. Abourehab, S. Pramanik , M. A Abdelgawad, B. M Abualsoud, A. Kadi, M. J. Ansari and A. Deepak, “Recent Advances of Chitosan Formulations in Biomedical Applications,” *Int. J. Mol. Sci.*, vol. 23, no. 18, 2022

[235] I. F. Amaral, A. L. Cordeiro, P. Sampaio, and M. A. Barbosa, “Attachment, spreading and short-term proliferation of human osteoblastic cells cultured on chitosan films with different degrees of acetylation,” *J. Biomater. Sci. Polym. Ed.*, vol. 18, no. 4, pp. 469–485, 2007..

[236] W. Paul and C. P. Sharma, “Chitosan and Alginate Wound Dressings : A Short Review,” *Trends Biometerials Artif. Organs*, vol. 18, no. 1, pp. 18–23, 2004.

[237] B. Lellis, C. Z. Fávaro-Polonio, J. A. Pamphile, and J. C. Polonio, “Effects of textile dyes on health and the environment and bioremediation potential of living organisms,” *Biotechnol. Res. Innov.*, vol. 3, no. 2, pp. 275–290, 2019.

[238] C. Kathing and G. Saini, “A Review of Various Treatment Methods for the Removal of Dyes from Textile Effluent,” *Recent Prog. Mater.*, vol. 4, no. 4, pp. 1–15, 2022.

[239] N. Methneni, J. A. Morales-González, A. Jaziri, H. Ben Mansour, and M. Fernandez-Serrano, “Persistent organic and inorganic pollutants in the effluents from the textile dyeing industries: Ecotoxicology appraisal via a battery of biotests,” *Environ. Res.*, vol. 196, no. February, 2021.

[240] A. K. D. Alsukaibi, “Various Approaches for the Detoxification of Toxic Dyes in Wastewater,” *Application of Environmentally Friendly Technologies in Green Processes*, vol. 10, no. 10, 2022.

[241] V. Vinayagam, K. N, Palani, S. Ganesh, S. Rajesh, V. V. Akula, R. Avoodaiappan, O. S. Kushwaha and A. Pugazhendhi, “Recent developments on advanced oxidation processes for degradation of pollutants from wastewater with focus on antibiotics and organic dyes,” *Environ. Res.*, vol. 240, no. 2, p. 117500, 2024.

[242] R. Al-Tohamy, S. S. Ali, F. Li, K. M. Okasha, Y. A.G. Mahmoud, T. Elsamahy, H. Jiao, Y. Fu and J. Sun, “A critical review on the treatment of dye-containing wastewater: Ecotoxicological and health concerns of textile dyes and possible remediation approaches for environmental safety,” *Ecotoxicol. Environ. Saf.*, vol. 231, p. 113160,

2022.

[243] C. A. Martínez-Huitle, M. A. Rodrigo, I. Sirés, and O. Scialdone, “A critical review on latest innovations and future challenges of electrochemical technology for the abatement of organics in water,” *Appl. Catal. B Environ.*, vol. 328, no. December 2022, 2023.

[244] D. Pal, K. Vijyendra, S. Gamini, and W. Kailas L., *Process intensification in wastewater treatments: advanced oxidation processes for organic pollutants*. 2021.

[245] P. V. Atheena, R. Basawa, and R. Raval, “Advancing wastewater treatment: chitin and derivatives for PPCP contaminant mitigation,” *Polym. Bull.*, no. 0123456789, 2024.

[246] I. Vassalini, M. Maddaloni, M. Depedro, A. De Villi, M. Ferroni, and I. Alessandri, “From Water for Water: PEDOT:PSS-Chitosan Beads for Sustainable Dyes Adsorption,” *Gels*, vol. 10, no. 1, 2024.

[247] M. F. & A. Vassalini, I., Ribaudo, G., Gianoncelli, A., Casula, “Plasmonic hydrogels for capture, detection and removal of organic pollutants.,” *Environ. Sci. Nano*, vol. 7, pp. 3888–3900, 2020.

[248] N. Li, J. Ma, Y. Zhang, L. Zhang, and T. Jiao, “Recent Developments in Functional Nanocomposite Photocatalysts for Wastewater Treatment: A Review,” *Adv. Sustain. Syst.*, vol. 6, no. 7, pp. 1–13, 2022.

[249] S. Jaast and A. Grewal, “Green synthesis of silver nanoparticles, characterization and evaluation of their photocatalytic dye degradation activity,” *Curr. Res. Green Sustain. Chem.*, vol. 4, no. October, p. 100195, 2021.

[250] K. Khurana and N. Jaggi, “Localized Surface Plasmonic Properties of Au and Ag Nanoparticles for Sensors: a Review,” *Plasmonics*, vol. 16, no. 4, pp. 981–999, 2021.

[251] H. M. M. Ibrahim, “Photocatalytic degradation of methylene blue and inactivation of pathogenic bacteria using silver nanoparticles modified titanium dioxide thin films,” *World J. Microbiol. Biotechnol.*, vol. 31, no. 7, pp. 1049–1060, 2015.

[252] E. Hermosilla, M. Díaz, J. Vera, A. B. Seabra, G. Tortella, J. Parada and O. Rubilar, “Molecular Weight Identification of Compounds Involved in the Fungal Synthesis of AgNPs: Effect on Antimicrobial and Photocatalytic Activity,” *Antibiotics*, vol. 11, no. 5, 2022.

[253] A. Houas, H. Lachheb, M. Ksibi, E. Elaloui, C. Guillard, and J. M. Herrmann, “Photocatalytic degradation pathway of methylene blue in water,” *Appl. Catal. B*

Environ., vol. 31, no. 2, pp. 145–157, 2001.

[254] R. F. De Mello Peters, P. A. M. Dos Santos, T. C. Machado, D. A. R. Lopez, Ê. L. Machado, and A. De Assis Lawisch Rodriguez, "Photocatalytic degradation of methylene blue using TiO2 supported in ceramic material," *Eclet. Quim.*, vol. 43, no. 1, pp. 26–32, 2018,

[255] A. S. Abdul Haleem , Mohib Ullah , Saif ur Rehman and I. U. and H. L. 1, "In-Depth Photocatalytic Degradation Mechanism of the Extensively Used Dyes Malachite Green, Methylene Blue, Congo Red, and Rhodamine B via Covalent Organic Framework-Based Photocatalysts", *Water*, vol. 16, no. 11, pp. 1588, 2024.